Universidade de Aveiro
Ano 2017
Departamento de Engenharia de Materiais e Cerâmica

Maria Adelaide Cotovio Salvador

Nano-iónicos: optimização da condução protónica de electrólitos por dopagem heterogénea

Nano-ionics: proton conduction enhancement of electrolytes by heterogeneous doping

Universidade de Aveiro
Ano 2017

Departamento de Engenharia de Materiais e Cerâmica

Maria Adelaide Cotovio Salvador

Nano-iónicos: optimização da condução protónica de electrólitos por dopagem heterogénea

Nano-ionics: proton conduction enhancement of electrolytes by heterogeneous doping

Tese apresentada à Universidade de Aveiro para cumprimento dos requisitos necessários à obtenção do grau de Doutor em Ciência e Engenharia de Materiais, realizada sob a orientação científica do Doutor Filipe Miguel Henriques Lebre Ramos Figueiredo, Equiparado a Investigador Principal do CICECO – Instituto de Materiais de Aveiro da Universidade de Aveiro, e da Doutora Paula Celeste da Silva Ferreira, Equiparada a Investigadora Principal do CICECO – Instituto de Materiais de Aveiro da Universidade de Aveiro.

This work was developed within the scope of the project CICECO-Aveiro Institute of Materials, POCI-01-0145-FEDER-007679 (FCT Ref. UID /CTM /50011/2013), financed by national funds through the FCT/MEC and when appropriate co-financed by FEDER under the PT2020 Partnership Agreement.

FCT is acknowledged for the PhD Grant reference SFRH/BD/60903/2009.

Para a minha mãe com saudade

o júri

presidente

Prof. Doutor Nuno Miguel Gonçalves Borges de Carvalho
professor catedrático da Universidade de Aveiro

Prof. Doutor Jorge Ribeiro Frade
professor catedrático da Universidade de Aveiro

Prof.ª Doutora Verónica Cortés Zea Bermudez
professora catedrática da Escola de Ciências da Vida e do Ambiente da Universidade e Trás-os-Montes e Alto Douro

Doutor Filipe Miguel Henriques Lebre Ramos Figueiredo
equiparado a investigador principal da Universidade de Aveiro (orientador)

Doutora Paula Celeste da Silva Ferreira
equiparada a investigadora principal da Universidade de Aveiro (coorientadora)

Prof.ª Doutora Maria Manuela Silva Pires Silva
professora auxiliar com agregação da Escola de Ciências da Universidade do Minho

Prof. Doutor Moisés Luzia Gonçalves Pinto
professor auxiliar do Instituto Superior Técnico da Universidade de Lisboa

Doutor Diogo Miguel Franco dos Santos
equiparado a investigador auxiliar do Instituto Superior Técnico da Universidade de Lisboa

agradecimentos

Gostava de agradecer a todos que directa ou indirectamente contribuíram para a realização deste sonho e tornaram possível a execução da minha Tese de Doutoramento.
À FCT pelo financiamento através da atribuição de Bolsa de Doutoramento (SFRH/BD/60903/2009).
Ao Doutor Filipe Figueiredo, meu orientador, pela sua dedicação, disponibilidade e por todos os conhecimentos científicos que me transmitiu, ao longo do desenvolvimento desta Tese.
À Doutora Paula Ferreira, minha coorientadora pela indispensável colaboração prestada ao longo da execução deste trabalho e por todos os conhecimentos científicos transmitidos.
À Universidade de Aveiro em particular aos membros, funcionários e técnicos do CICECO, dos departamentos de Engenharia de Materiais e Cerâmica e de Química, pelo apoio técnico e por todos os equipamentos disponibilizados, sem os quais não seria possível a realização desta Tese e claro pela forma agradável como me acolheram durante estes últimos anos.
Ao Doutor Jesús Canales-Vázquez pela realização e análise das imagens de TEM realizadas no Instituto de Investigacion en Energias Renovables.
Ao Doutor Stanislav Ferdov pela realização dos difractogramas de raios-X efetuados na Universidade do Minho.
A todos os meus colegas de laboratório e de “cantina” pela sua amizade e pelos momentos de alegria que me proporcionaram.
Aos meus amigos de “Aveiro” de uma forma especial às duas Famílias Marques que me acolheram como membro da família.
Ao Pedro, por tudo, em particular pela sua paciência e incentivo sobretudo nas horas difíceis, e pela forma como me ajudou a ver o "lado bom das coisas" mesmo quando tudo nos parece mau. Amo-te muito.
Ao André (que nasceu durante a realização da minha Tese de Doutoramento) pela compreensão nas minhas ausências e falta de paciência para as brincadeiras.
À minha família, em particular ao meu pai e avó, por estarem sempre ao meu lado, mesmo estando longe, e claro á minha mãe a quem dedico esta Tese por todo o amor e carinho.

O meu muito obrigada a todos.

palavras-chave

Nano-iónicos, Condutores protónicos, Condutividade protónica, Potencial zeta, Óxidos mesoporosos, Electrólitos fracos

resumo

Condutores protónicos são o cerne funcional de muitos equipamentos de conversão de energia, sensores e controle de luz. Portanto, é muito importante compreender fenómenos interfaciais. O objectivo desta Tese de Doutoramento é o estudo da condutividade protónica de compósitos nano-iónicos obtidos pela dopagem heterogénea de electrólitos fracos com nanopartículas de óxido e materiais mesoporosos, que são essencialmente dieléctricos, através da formação de interfaces condutoras com elevada concentração de protões. Esta investigação baseia-se na dopagem heterogénea de electrólitos fracos tais como imidazol (Iz), benzimidazol (Bz), 1*H*-1,2,4-triazol (Tz) e pirazol (Pz) com nanopartículas de óxidos metálicos e os correspondentes óxidos mesoporosos, CeO_2, TiO_2, ZrO_2 e $BaZrO_3$. O princípio subjacente é o da criação de zonas de carga espacial com elevada concentração de protões na interface entre o electrólito e o óxido, configurando assim novos tipos de materiais interfaciais do tipo nano-iónico.

Numa primeira fase, o trabalho é dedicado à síntese de CeO_2, TiO_2, ZrO_2 e $BaZrO_3$ mesoporosos por nano replicação utilizando SBA-15 ou CMK-3 como moldes. O material molde foi selecionado de forma a minimizar a interacção química entre o molde e os percursores, maximizando assim a pureza da fase de óxido mesoporoso obtido. O óxido de cério foi obtido usando SBA-15, o óxido de zircónio e o óxido de titânio foram preparadas usando ambos os moldes SBA-15 e CMK-3, e o zirconato de bário foi sintetizado unicamente com CMK-3. Numa segunda etapa, medidas de potencial zeta foram usadas para avaliação da carga superficial dos óxidos em contacto com os vários electrólitos, em suspensões aquosas. O potencial zeta diminui com o aumento da fracção do electrólito, o que pode ser explicado assumindo a adsorção selectiva de aniões na superfície dos óxidos.

Este efeito é mais evidente com a adição de Iz e Bz do que com a adição de Tz e Pz, em concordância com a menor constante de dissociação apresentada pelos primeiros electrólitos fracos. O enriquecimento dos aniões à superfície tem de ser compensado pelo estabelecimento de regiões de carga ricas em catiões adjacentes à superfície das partículas, o que leva ao desejado efeito mesoscópico do aumento da condutividade. Este efeito foi verificado pelo estudo detalhado de espectroscopia de impedância, o qual mostra que a condutividade protónica, em condições anidras, para os compósitos óxido/electrólito aumenta com o aumento da fracção volúmica das partículas de óxido e com a mesoporosidade. O aumento da condutividade observado pode alcançar cerca de 3 ordens de magnitude em relação a CeO_2 e ao electrólito Bz puros. Embora os resultados do aumento da condutividade sejam impressionantes são ainda insuficientes para aplicação tecnológica. Evidências para a contribuição interfacial encontram-se nos espectros de impedância com o aparecimento de semicírculos adicionais, que podem ser correlacionados à área interfacial óxido/electrólito através da fracção volúmica do óxido e da mesoporosidade.

keywords

Nano-ionics, Proton conductors, Protonic Conductivity, Zeta potential, Mesoporous oxides, Weak electrolytes

abstract

Proton conductors are the functional core of many devices for energy conversion, sensing and light control. Thus, it is very important to understand interfacial phenomena. The main objective of this PhD Thesis is to study the protonic conductivity of nano-ionic composites obtained by heterogeneous doping of weak electrolytes with oxide nanoparticles and mesoporous materials, which are essentially dielectric, via the formation of conducting interfaces with enhanced proton concentration. This investigation is based on the heterogeneous doping of weak proton conducting electrolytes such as imidazole (Iz), benzimidazole (Bz), 1*H*-1,2,4-triazole (Tz) and pyrazole (Pz) with metal oxide nanoparticles and matching mesoporous counterparts of CeO_2, TiO_2, ZrO_2 and $BaZrO_3$. The underlying principle is the formation of proton-enriched space-charge layers at the electrolyte/particle interface, configuring in this way new types of interfacial materials of nano-ionic type. On a first stage, the work is devoted to the synthesis of mesoporous CeO_2, TiO_2, ZrO_2 and $BaZrO_3$ by nanocasting using suitable SBA-15 silica or CMK-3 carbon hard templates in order to minimize the chemical interaction between the template and the reactant precursors, thus maximizing the phase purity of the obtained mesoporous oxide. Ceria was obtained with SBA-15, zirconia and titania with both SBA-15 and CMK-3, and barium zirconate only with CMK-3. On a second stage, zeta potential measurements were used to assess the oxide surface charge in contact with the various electrolytes, in aqueous suspension. The zeta potential decreases with increasing fraction of electrolyte, which can be explained assuming the selective anion adsorption on the surface of the oxides. This effect is stronger upon addition of Iz and Bz than of Tz and Pz, in agreement with the smaller self-dissociation constants of the former weak electrolytes. The enriched anion surface must be compensated by the establishment of adjacent cation-rich space-charge regions, which produce the desired mesoscopic conductivity enhancement. This effect was verified by detailed impedance spectroscopy studies showing that the proton conductivity in anhydrous conditions of the oxide/electrolyte composites increases with increasing volume fraction of the oxide particle and with the mesoporosity. The observed conductivity enhancement may reach ca. 3 orders of magnitude with respect to pure CeO_2 and Bz. While impressive, the attained conductivities are still insufficient for technological application. Evidence for interfacial contribution is found in impedance spectra by additional semicircles, which can be correlated to oxide/electrolyte interfacial area through the oxide volume fraction and mesoporosity.

List of Figures

List of Tables

Abbreviations and acronyms

2D	2-dimensional
3D	3-dimensional
8YSZ	commercial 8 mol% Y_2O_3 stabilized ZrO_2
Vol. %	volume percent
AC	alternating current
a.u.	arbitrary units
*a*TO	anatase phase of the TiO_2 commercial or/and prepared during this Thesis
ATR	attenuated total reflectance spectroscopy
BCO	$BaCeO_3$ prepared during this Thesis
BET	Brunauer- Emmett -Teller method for the calculation of specific surface area
BJH	Barret- Joyner -Halenda method for the calculation of pore size distribution and pore volume
BPP	bipolar plate
Bz	benzimidazole
BZO	$BaZrO_3$ commercial or/and prepared during this Thesis
BZYO	$BaZrO_3$ doped with 20% of yttrium prepared by mechanosynthesis or/and prepared during this Thesis
CE	counter electrode
CL	catalyst layer
CMK-1	mesoporous carbon obtained using MCM-48 as hard template
CMK-3	mesoporous carbon obtained using SBA-15 as hard template
CMK-5	mesoporous carbon obtained using SBA-15 as hard template obtain only by surface coating
CO	CeO_2 commercial or/and prepared during this Thesis
CP	coordination polymer
CPE	constant phase element
DC	direct current
deg.	degrees
DL	diffusion layer
DTA	differential thermal analysis
e.g.	for example
EC	ethylene carbonate
ECDs	electrochromic devices

EDS	energy dispersive X-ray spectroscopy
EIS	electrochemical impedance spectroscopy
F(α_H)	Henry's function
FDU-12	3-D cage pores mesoporous silica with cubic ($Fm\bar{3}m$) array of pores
FTIR	Fourier transform infrared spectroscopy
FWHM	full width at half maximum
GPE	gel polymer electrolyte
h*	photo-holes
HF	high frequency in EIS
HMTA	hexamethylenetetramine
HRTEM	high resolution transmission electron microscopy
hυ	irradiated light
HUP	hydrogen uranyl phosphate
IF	intermediate frequency in EIS
ITO	indium tin oxide
IUPAC	International Union of Pure and Applied Chemistry
Iz	imidazole
JCPDS-ICDD	Joint Committee on Powder Diffraction-International Centre for Diffraction Data
KIT-6	3-D helix channels mesoporous silica with cubic ($Ia\bar{3}d$) array of pores (with micropores connecting the two channel systems)
KJS	Kruk, Jarionec and Sayari method for the calculation of pore size distribution and pore volume based on BJH, specifically for mesoporous materials
LCDs	liquid crystal displays
LDV	laser doppler velocimetry
LEDs	light emitting diodes
LF	low frequency in EIS
*m*ZO	monoclinic ZrO_2
*t*ZO	tetragonal ZrO_2
m.p.	melting point
M3-PALS	technique patented by Malvern (combined LDV and PALS)
M41S	first family of mesoporous silica prepared
MCM-41	2-D channels mesoporous silica with hexagonal ($p6mm$) array of pores (without micropores connecting the two channel systems)
MCM-48	3-D helix channels mesoporous silica with cubic ($Ia\bar{3}d$) array of pores (without micropores connecting the two channel systems)

MEA	membrane electrode assembly
MOF	metal organic framework
mp	micrometric particle
ms	mesoporous particle
np	nanoparticle
PALS	phase analysis light scattering
PBI	polybenzimidazole
PC	propylene carbonate
PEC	photoelectrochemical cell
PEMFC	proton exchange membrane fuel cell
PEO	poly(ethylene oxide)
PFSA	perfluorosulfonic acid
pH(I)	isoelectric point
PID	proportional-integral-derivative
PILs	protic ionic liquids
P123	Poly(ethylene glycol)-block-poly(propylene glycol)-block-poly(ethylene glycol)
P-4VI	poly(4-vinylimidazole)
PMMA	poly(methylmethacrylate)
PMO	periodic mesoporous organosilicas
PSD	pore size distribution
PSS:H	poly(styrenesulfonic acid)
PTFE	polytetrafluoroethylene
PVA	polyvinyl alcohol
PVAc	polyvinyl acetate
PVdF-HFP	poly(vinylidene fluoride hexafluoropropylene)
PWA	phosphotungstic acid
Pz	pyrazole
r.h.	relative humidity
R||CPE	a resistor and a constant phase element in parallel
RC	resistor and capacitor
RE	reference electrode
Ref.	reference
Rot.	rotations
*r*TO	rutile phase of the TiO_2 commercial or/and prepared during this Thesis
SAED	selected-area electron diffraction

SBA-15	2-D channels mesoporous silica with hexagonal (*p6mm*) array of pores (micropores connecting the two channel systems)
SBA-16	3-D cage mesoporous silica with cubic ($Im\bar{3}m$) array of pores
SEM	scanning electron microscopy
SiWA	silicotungstic acid
SOFC	solid oxide fuel cell
S-PEEK	sulfonated polyether ether ketone
S-PES	sulfonated polyethersulfone
STEM	scanning transmission electron microscopy
STP	standard temperature and pressure: 273.15 K and 1 atm
TEM	transmission electron microscopy
TEOS	tetraethylorthosilicate
TG	thermogravimetry
THF	tetrahydrofuran
Tz	1*H*-1,2,4-triazole
WE	working electrode
XRD	X-ray diffraction

Symbols

a	lattice parameter
a_a	chemical activity of the analyte (in Nernst equation)
c	experimental constant (in Isotherm equation)
A	surface area of the electrodes
C	capacitance
C_0	concentration of charge carriers in the first layer of the space-charge zone adjacent to the adsorption layer (used in calculus for conductivity of space charge regions)
C_a	concentration of analyte (in Nernst equation)
C_{HF}	capacitance of first semicircle at high frequencies in EIS
C_{IF}	capacitance of second semicircle at high frequencies in EIS
C_j	concentration of ionic species (j)
d	interplanar distances
d_p	pore diameter

d_{par}	particle diameter
d_{parBET}	particle diameter determine using S_{BET}
d_{parXRD}	crystallite size using Scherrer equation
d_{pellet}	diameter of the pellet
d_{parSEM}	particle diameter determine using SEM micrograph
d_{parTEM}	particle diameter determine using TEM micrograph
e	charge of the electron
E	potential
E^0	the standard electrode potential
E_a	activation energy
$E_{a,\ HF}$	E_a for first semicircle at high frequencies in EIS
$E_{a,\ IF}$	E_a for second semicircle at high frequencies in EIS
$E_{a,\ total}$	E_a total in EIS
F	Faraday constant
G	Gibbs free energy
H	enthalpy
h	Planck´s constant
$I(t)$	current
I_0	the amplitude of the current
j	ionic species
k	Boltzmann constant
K_a	self-dissociation constant
K_{sf}	dimensionless shape factor in Scherrer Equation
l	thickness of pellet
L	inductance
m	mass of the electron
$m_{electrolyte}$	mass of the of electrolyte
m_{oxide}	mass of the of oxide
m_{pellet}	mass of the of pellet
n	CPE exponent that characterizes the phase shift in EIS
n_{ad}	moles of gas adsorbed (in case of this work N_2) on 1 g of adsorbent
n_e	the number of electrons participating in reaction (in Nernst equation)
n_m	monolayer capacity
n_p	the number of the plane that reflects the X-rays
O_o^x	lattice oxygen (in Kröger-Vink notation)

$OH_o^{\bullet}$	protonic defect (in Kröger-Vink notation)
P	equilibrium vapor pressure (in Kelvin equation for N_2 isotherms)
P^0	saturation vapor pressure (in Kelvin equation for N_2 isotherms)
P_{H_2}	partial pressure of H_2
P_{ref}	reference partial pressure (in Nernst equation)
P_x	the partial pressure of gas in the sample gas mixture (in Nernst equation)
Q	the rate of gas consumption (for sensors)
R	ideal gas constant
R_e	resistance
$R_{electrode}$	resistance of electrode in EIS
R_g	resistance of electrolyte grain
$R_{gb\perp}$	resistance of electrolyte grain boundary perpendicular contribution
$Rg_{b\|\|}$	resistance of electrolyte grain boundary parallel contribution
R_{HF}	resistance of first semicircle at high frequencies in EIS
R_{IF}	resistance of second semicircle at low frequencies in EIS
R_{LF}	resistance of third semicircle at low frequencies in EIS
r_m	the radius of curvature (in Kelvin equation)
R_s	radius of the particle (in zeta potential)
R_t	total resistance
S	entropy
S_{BET}	specific surface area
T	absolute temperature
U_E	electrophoretic mobility
$V(t)$	voltage in EIS
V_0	amplitude of the voltage
$V_o^{\bullet\bullet}$	oxide ion vacancy (in Kröger-Vink notation)
V_{con}	volume contraction of the precursor
$V_{electrolyte}$	volume of the electrolyte
V_L	molar volume of liquid adsorptive
V_{oxide}	volume of the oxide
V_p	pore volume
V_{pellet}	volume of the pellet
V_{pre}	volume of precursors
V_{pro}	volume of the products
Y_0	admittance

Z	impedance
Z’	real part of impedance
Z’’	imaginary part of impedance
Z^0	the amplitude of the impedance
$Z_{CPE}(\varpi)$	impedance of the CPE
$Z_{electrolyte}$	contribution of electrolyte impedance to the total impedance of composites
Z_{HF}	impedance of first semicircle at low frequencies in EIS
Z_{IF}	impedance of second semicircle at low frequencies in EIS
$Z_{interface}$	contribution of space-charge impedance to the total impedance
$Z_{electrolyte/interface}$	contribution of regions separated by thin electrolyte regions to the total impedance of composites
z_{je}	net charge of ionic species j
Z_{oxide}	contribution of oxide impedance for total impedance of composites

Greek symbols

α_H	Henry´s parameter
β_i	constant related to percolation effects used for calculation of the σ_i
β_{sc}	degree of percolation of the oxide particles
δ	oxygen substoichiometry in perovskites
δ_b	bending mode vibration in FTIR
$\delta_{in\text{-}plane}$	in-plane bending vibration mode in FTIR
$\delta_{out\text{-}of\text{-}plane}$	out-of-plane bending vibration mode in FTIR
ε	dielectric constant
ε_0	vacuum dielectric constant
ε_r	dielectric constant of the material
$\phi(x)$	electrostatic potential
ϕ_i	the phase angle between the voltage and the current
γ	surface tension of the liquid adsorptive
η	viscosity
φ_i	volume fraction of thecomponent *i*
φ_{oxide}	volume fraction of the oxide

φ_p	volume fraction of the particles
λ	Debye length
λ_{Cu}	wavelength of the XRD Cu Kα radiation
λ_r	wavelength of the zeta potential red laser
$\mu_j(x)$	chemical potential
$\tilde{\mu}_j(x)$	electrochemical potential
μ_j^0	standard chemical potential
ν	stretching vibration mode in FTIR
ν_{as}	asymmetrical stretching vibration mode in FTIR
ν_s	symmetrical stretching vibration mode in FTIR
θ	Bragg angle
θ_i	depressed angle
ρ	density
$\rho_{electrolyte}$	density of the electrolyte
ρ_{oxide}	density of the oxides
ρ_{pellet}	density of the pellet
ρ_{theo}	theoretical density
σ	electrical conductivity
σ_∞	bulk conductivity
σ_m	total electrical conductivity of the composites
σ_p	electrical conductivity of the particles
σ_{sc}	electrical conductivity of the interfacial space charge regions
υ_∞	mobility of the charge in the bulk
ϖ	angular frequency
ϖ_0	relaxation frequency
Ω	ratio of the surface area to the volume of the insulating phase
ξ	zeta potential

Index

1

Introduction

This Introduction starts by briefly presenting the motivation and objectives of the Thesis. The remaining sections are occupied by a literature review of the most relevant applications and transport mechanisms of proton conductors, an explanation of the underlying concepts of nano-ionics and, finally, a review of the synthesis and properties of mesoporous oxides.

1.1 Motivation and objectives

Proton conductors are the functional core of many devices for energy conversion, sensing and light control.

The main objective of this PhD Thesis is to study the protonic conductivity of nano-ionic composites obtained by heterogeneous doping of weak electrolytes with mesoporous oxide nano-particles, which are essentially dielectric, via the formation of conducting interfaces with enhanced proton concentration.

This objective is grounded in three partial objectives:

i) to synthesize mesoporous nano-powders of simple metal oxides and other complex multimetallic oxides with perovskite structure;

ii) to fabricate composites consisting of mixtures of weak electrolytes and mesoporous oxides;

iii) to investigate the effects of oxide particle morphology, composition and surface features on the protonic conductivity of the composites.

1.2 Proton conductors and its applications

Proton conductors are systems formed by one or more phases that allow proton transport. They are usually applied in the form of proton exchange membranes as the core component of various devices.[1-7] Table 1.1 shows examples and the main applications of proton conductors, including main requirements and the relevant protonic conductivity and operation temperature.

Table 1.1 Applications, main requirements, examples, conductivity values and operation temperature of proton conductors.

Applications	Requirements of proton conductor	Example	Conductivity ($S.cm^{-1}$)	Ref.[a)]
Fuel cells	Proton conductivity higher than 1×10^{-2} $S.cm^{-1}$; No electronic conductivity; Low water cross-over and fuel permeability.	Nafion®	0.13 at 75 ºC, 100% r.h[b)]; 0.05 at 150 ºC, 75% r.h	[4, 8-15]
		SnP_2O_7	0.47 at 250 ºC, pH_2O~0.0075 atm	
		$BaZrO_3$ doped with 20% of yttrium	~0.03 at 900 ºC, pH_2O=0.023atm[c)]	
Electrochemical sensors	Proton conductivity higher than 1×10^{-4} $S.cm^{-1}$; High gas permeability; Able to make a thin membrane.	$Zr(HPO_4)_2.H_2O$[d)]	1.05×10^{-4} at 20 ºC, 90% r.h	[4, 16-20]
		Na_3PO_4	4×10^{-3} at 600 ºC, 2% H_2 in air	
Electrochemical reactors	Proton conductivity higher than 1×10^{-3} $S.cm^{-1}$; High H_2 permeation flux rates, High selectivity towards hydrogen; Able to make a thin membrane.	S-PEEK[e)]	0.04 at 160 ºC, 75% r.h	[21-25]
		$BaCeO_3$ doped with 10% of yttrium	~0.07 at 1000 ºC, pH_2O=0.016 atm[f)]	
Electrochromic devices	Proton conductivity higher than 1×10^{-7} $S.cm^{-1}$; Low electronic conductivity less than 1×10^{-12} $S.cm^{-1}$; Able to make a thin membrane; Good electron donating ability; Wide potential window; Optical transparency.	PVAc [g)]/glycerin gel/ antimonic acid[h)]	2.8×10^{-4} at ~25 ºC; 61% r.h	[26-29]
Batteries and supercapacitors	Proton conductivity higher than 1×10^{-6} $S.cm^{-1}$; No electronic conductivity; Rapid proton transfer between interfaces of components. Able to make thin and flexible membrane.	[PMMA[i)]/PVdF-HFP[j)]]/[NH_4SCN in EC[k)]and PC[l)]][m)]	1.9×10^{-3} at room temperature[n)]	[6, 13, 30-33]
		PSS:H[o)]	1.5×10^{-3} at 20 ºC; 80% r.h[p)]	
Photo-electrochemical cells	Proton conductivity higher than 1×10^{-4}S.c m^{-1}; Low gases cross-over; Able to make thin membrane.	S-PES [q)]+sulfonated mesoporous silica[r)]	1.42×10^{-4} at room temperature	[2, 34-36]

[a)] Reference (Ref.); [b)] relative humidity (r.h.); [c)] by extrapolation from[12]; [d)] pelicular form; [e)] sulfonated polyether ether ketone (S-PEEK); [f)] by extrapolation from[25]; [g)] polyvinyl acetate (PVAc); [h)] in proportions 0.25/0.51/0.24 in by weight; [i)] poly(methylmethacrylate) (PMMA); [j)] poly(vinylidene fluoride hexafluoropropylene) (PVdF-HFP);[k)] propylene carbonate (PC); [l)] ethylene carbonate (EC); [m)] in proportions 35 wt% [10 wt% PMMA/90 wt% PVdF-HFP] / 65 wt% [1M NH4SCN in EC:PC 1:1 v/v)]; [n)] for batteries from[31]; [o)] poly(styrenesulfonic acid) (PSS:H); [p)] for supercapacitors from[32]; [q)] sulfonated polyethersulfone (S-PES); [r)] 0.2 wt% of sulfonated mesoporous silica.

1.2.1 Fuel cells

The fuel cells, in particular the proton exchange membrane fuel cells (PEMFCs), are electrochemical devices which convert the chemical energy of hydrogen into electrical energy. The PEMFCs are constituted by a catalyst layer (CL), a diffusion layer (DL), also called gas diffusion layer or porous backing, the bipolar plate (BPP) and the proton exchange membrane (PEM) (Fig. 1.1). The electrodes (anode or cathode) are composed of DL and catalyst layers CL, which together with the membrane form the Membrane Electrode Assembly (MEA). This set of several piled MEAs separated by the bipolar plates is called the stack.[37]

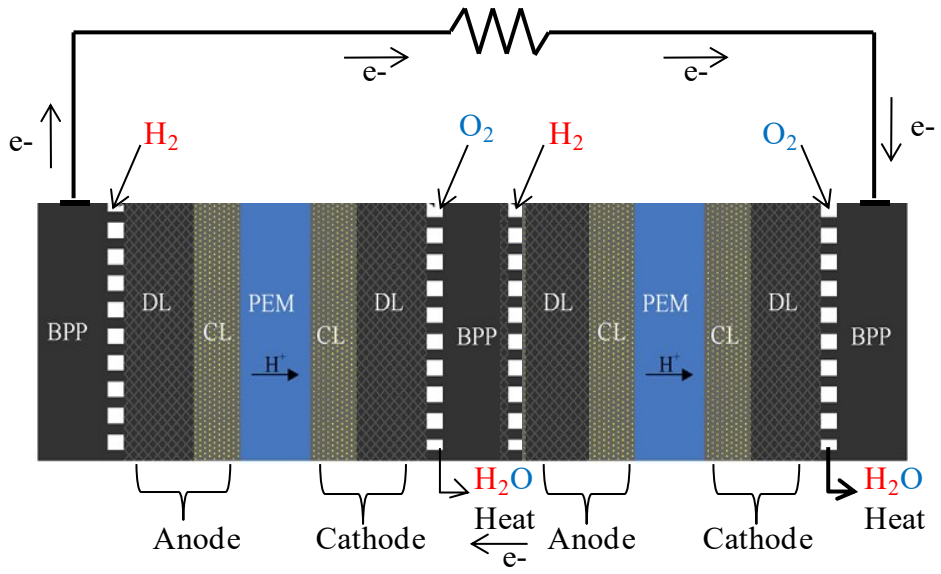

Figure 1.1 Fuel cell stack consisting of two individual PEMFC with conventional planar geometry (adapted from [37]).

The anode side is fed with hydrogen. Each H_2 molecule is dissociated and oxidized in two protons (H^+) (Eq. 1.1) releasing two electrons (e^-) that go through the external electrical circuit, whereas the protons permeate through the membrane to the cathode side. Here they react with oxygen ions, originating water molecules and releasing heat (Eq. 1.2).

$$H_2 \rightarrow 2H^+ + 2e^- \quad (1.1)$$

$$\frac{1}{2}O_2 + 2H^+ + 2e^- \rightarrow H_2O + \text{heat} \quad (1.2)$$

The global equation is

$$H_2 + \frac{1}{2} O_2 \rightarrow H_2O + \text{heat} \qquad (1.3)$$

The operation at temperatures higher than 100 °C and/or low humidity may be desirable for enhanced diffusion/reaction rates. Moreover, at high temperature, the level of CO[1] catalyst poisoning is reduced. As a result, lower loads of the high cost platinum catalyst are needed and the hydrogen fuel purity may be decreased. In addition, the water and temperature management of the cells and stacks is less critical without the need for liquid water in the membrane, hence simplifying the system hardware. The high temperature also facilitates hydrogen sorption from metal hydrides and thus the use of hydrogen solid state storage solutions. The combination of all these factors may significantly reduce the cost of the technology.[8, 38-40]

Some reviews related with application of proton conductors in fuel cells have been published over the years. In 2003, Kreuer [12] described the proton conducting multimetallic oxides (e.g. $BaZrO_3$) for high temperature application (500-800 ºC) in solid oxide fuel cells (SOFCs. Jin *et al.*[11] in 2010 reviewed the metal pyrophosphates materials (e.g. SnP_2O_7) for application at the temperature range 100–400 ºC. Dupuis [41] published a review presenting an overview of proton exchange membrane materials for fuel cells operating at medium temperatures (100–200 ºC) classified in three types: i) polymeric, ii) solid acid membranes such as $RbHSeO_4$ or $CsHSO_4$ and iii) composites membranes such as polymer based composites membranes (e.g. Nafion® with TiO_2) or solid acid composites (e.g. $CsHSO_4$ with polyacrylonitrile). [41] Within the polymeric type, the membranes may be formed by: i) perfluorosulfonic acid (PFSA) [2](e.g. Nafion®), ii) non-fluorinated polymers (e.g. S-PEEK), iii) polymer blends (e.g. S-PEEK with ortho sulfone aminated polysulfone) and iv) anhydrous polymer membranes based on an acid-base pair (e.g. polybenzimidazole (PBI) with phosphoric acid) or composed by polymer matrix containing protic ionic liquids (PILs) (e.g. PBI- phosphoric acid with 1-ethyl-3-methylimidazolium triflate [42]).[41] Bureekaew *et al* [43] reviewed the metal organic frameworks (MOF)/ coordination polymers (CP), e.g. the ferrous oxalate dihydrate, for application in PEMFC for different temperatures.

[1]. The CO is a subproduct of hydrocarbons partial oxidation used in H_2 production.

[2] PFSA membranes operating at low temperature (limited to about 80 ºC) but also present in this review since they can be used but show high conductivity.

1.2.2 Electrochemical sensors

The electrochemical sensors transform chemical information into electrical information. They can detect changes in charge transport or electrical properties due to electrochemical reactions occurring at a working electrode (WE).

The sensors using proton conductors as an electrolyte can be used to detect different components, for example, gaseous components such as CO_2, CO, NH_3, O_2, H_2O_2 [1, 4, 44-47], humidity [48], as well as bio-related compounds such as glucose, insulin (using for example a layer of Nafion®) [1, 49-51] and of course H_2. They can be operated within a large range of temperatures (-30 to 1000 °C). Different electrolytes can be used for example: i) polymeric electrolytes (e.g. Nafion®); liquid basic or acid electrolytes (e.g. NaOH or H_2SO_4), biological materials (e.g. hydrogenases) and solid electrolytes (e.g. Yb doped $SrCeO_3$). The electrochemical sensors can be applied in a broad number of areas, including aerospacial, medical, petrochemical, metal industry and energy.[16, 52-55]

These sensors can be divided in amperometric (Fig. 1.2 A), potentiometric (Fig. 1.2 B) and conductimetric types (Fig. 1.2 C), according to the operating mode.

The amperometric sensor consists of: i) three electrodes, the WE, the counter electrode (CE) and the reference electrode (RE) (however exist sensors without RE), ii) an electrolyte solution (the proton conductor) in which the electrodes are immersed and allows the transport of proton inside of sensor (from WE to CE), iii) a potentiostat used to maintain constant voltage, and iv) a diffusion barrier to maintain the hydration, prevent leakage of the electrolyte and allow the selective permeation of relevant gaseous species (notably hydrogen and oxygen in the case of the hydrogen sensor depicted by Fig. 1.2 A). In the amperometric sensor the current generated by reaction of the analyte is measured and related with the concentration of analyte (C_a) using the Faraday's law equation (Fig. 1.2 A).[17, 52]

The potentiometric sensor shows similar configuration to the amperometric sensor but only with one working electrode and one reference electrode (Fig. 1.2 B). However, the potentiometric sensor operates at zero current or near zero. The electrical potential difference measured between the reference and working electrodes is related with the activity of the analytes through the Nernst equation. Since the activity of the analytes can be approximated to their concentration, the Nernst equation can be rewritten as:[16, 52]

$$E = \frac{RT}{n_e F} \ln \frac{P_x}{P_{ref}} \tag{1.4}$$

where P_x the partial pressure of gas in the sample gas mixture and P_{ref} the reference partial pressure, $P_{H_2(I)}$ and $P_{H_2(II)}$, in Fig. 1.2 B respectively, when the activity of analytes is different of each side of the membrane, a potential can be measured.

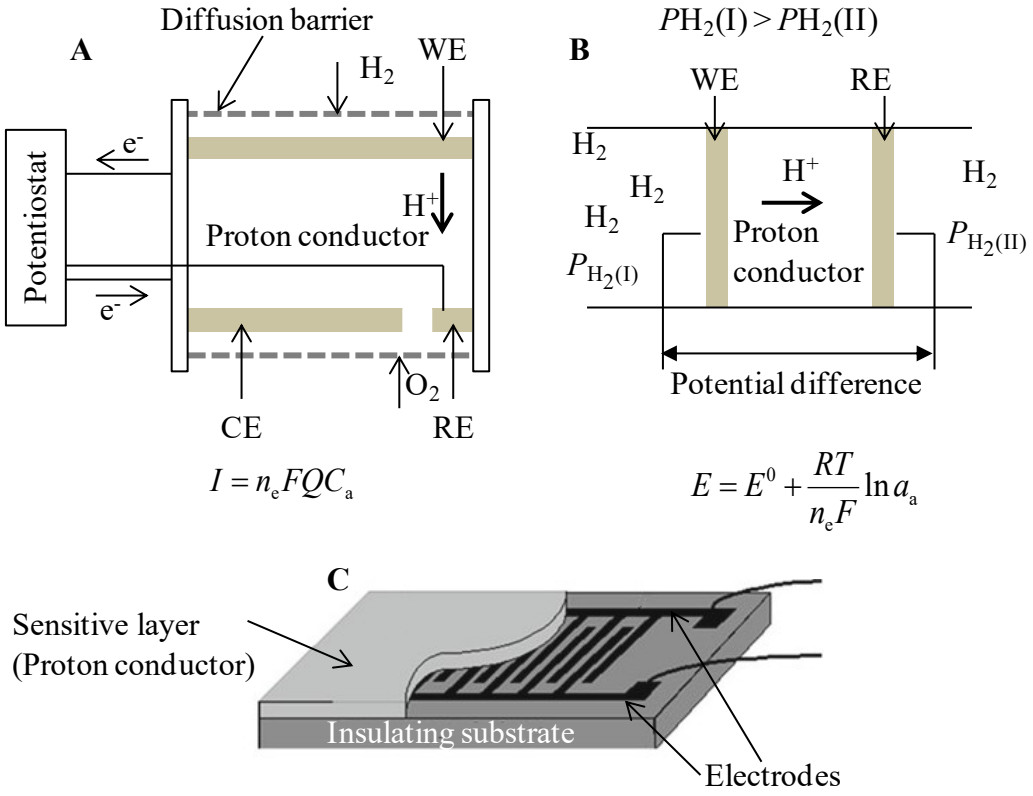

Figure 1.2 Schematic representation of sensors for detection of hydrogen in three different configurations and corresponding equations A) 3-electrode amperometric sensor, B) potentiometric sensor (the equations are taken from[16] [3]) and C) planar thin film for conductimetric sensor (adapted from [20]).

The last type of electrochemical sensor is the conductimetric sensor (Fig. 1.2 C). It is formed by the i) contact electrodes (in which, the change in resistance due to the reaction such as adsorption, chemical reactions, diffusion, catalysis, swelling in sensitive layer is measurable); ii) the sensitive

[3] were I is current in coulombs.s^{-1}, Q is the rate of gas consumption in m^3.s^{-1}, C_a corresponding at analyte concentration in mol.m^{-3}, E and E^0 are the electrode and standard electrode potential respectability in volts, R is ideal gas constant, T temperature in Kelvin, a_a corresponding at activity of the analytes, finally n_e corresponding at number of electrons participating in the reaction, and F is Faraday's constant.

layer (where the reaction occurs) deposited on insulated substrate; and iii) a heater (not presented in Fig. 1.2 C). The concentration of the analyte is determined by measuring the current, which flows between the electrodes before the voltage application. The proton conductors such as perovskites can be used as sensitive layer since they are semiconductors. The most important features are the morphology and crystallographic structure.[16, 20]

There are many different proton conductors used as electrolytes for sensors depending of the operating temperature, as reviewed by Korotcenkov *et al*.[16] For temperatures below 100 ºC, H_2SO_4 liquid electrolyte, or solids such as polymers (e.g. Nafion®) or $H_4SiW_{12}O_{40}\ _{28}H_2O$ can be used. For medium (100-300 °C) and high (400-600 °C) temperatures, solid electrolytes such as Na_3PO_4 or perovskites (e.g. $BaCeO_3$) are envisaged.

1.2.3 Electrochemical reactors

The electrochemical reactors, also called hydrogen pumps, have a proton conducting membrane and are usually used for hydrogenation (Fig. 1.3 A black lines) and dehydrogenation (Fig. 1.3 A red lines) of the organic compounds. The same reactors can be used to for hydrogenation and dehydrogenation reactions simply by reversing the polarity, for electrolysis (Fig. 1.3 B), for methane coupling (Fig. 1.3 C) and for hydrogen separation (Fig. 1.3 D). They can operate at different temperatures however they are mostly used at high temperatures. Proton conducting ceramic material based in perovskite-type oxides (e.g. $SrCeO_3$ or $BaCeO_3$ in which Ce is partly replaced by Yb or Y) are usually used for high temperatures (above 120 ºC) and the polymer membranes such as Nafion® or S-PEEK can be used for low temperatures (up to 120 ºC).[1, 21-23, 55-59]

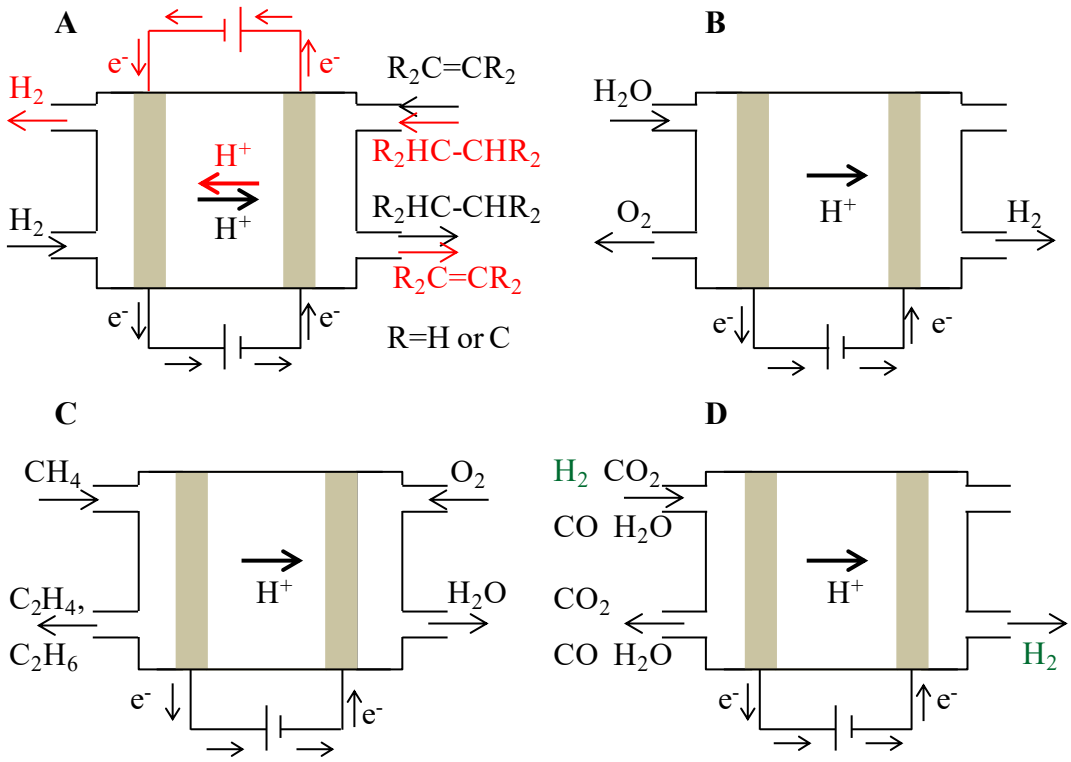

Figure 1.3 Examples of electrochemical reactors for: A) hydrogenation (black arrows)/dehydrogenation (red), B) water electrolysis, C) methane coupling and D) hydrogen separation.

Electrochemical reactors are formed by two electrodes (gray in Fig. 1.3) where the oxidation (anode side) and reduction (cathode side) reactions occur, separated by a proton conducting membrane.

For example Yuan *et al.*[60] performed several hydrogenation reactions of unsaturated organic alcohols (e.g. allyl alcohol) and of unsaturated organic acids (e.g. maleic acid). These reactions did not require any electricity but generated electricity and the operating mode was similar to a fuel cell. A DC stimulus can be applied to promote the oxidation of hydrogen to form protons, which migrate through the membrane from the anode to the cathode as an ionic electric current. In the cathode, the protons can react with unsaturated organic compounds and give saturated compounds (hydrogenation). They may also recombine and form hydrogen again or they can react with oxygen forming water (methane coupling).[23, 56]

The proton conducting membrane reactor shows some advantages compared to other reactors. For example, in hydrogenation and dehydrogenation the hydrogen does not contact with the reagents and the products since they are separated by a membrane. Using this kind of electrolyzers, it is possible to obtain pure H_2 in one step. Like in any electrochemical reactor, the reaction rate can be

controlled by the electric current, whereas the electrode potential can be used to control the selectivity and the catalytic activity.[23, 56]

1.2.4 Electrochromic devices

Electrochromic devices (ECDs) are devices comprising materials characterized by color changes resulting from redox reactions, when a potential difference is applied. The coloration should be reversible by reversing the voltage signal. ECDs are effective if they have: i) high electrochromic efficiency and contrast, ii) short response time for the coloring and bleaching process, iii) good stability and durability and iv) high optical memory also called open-circuit memory (the color should persist after stopping application of potential difference). They can be used in, for example: displays, smart widows, mirrors. Figure 1.4 shows a schematic representation of an electrochromic device with cathodic coloration.[26-28, 61-63]

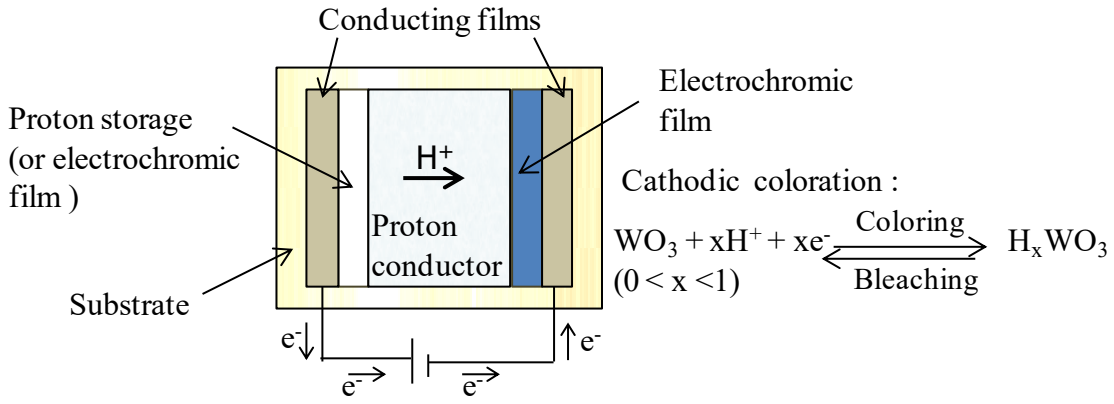

Figure 1.4 Configuration of an electrochromic device with cathodic coloration.

The ECDs are formed by five layers: i) a substrate (e.g. glass), ii) a conducting film (indium tin oxide - ITO, iii) the proton storage (can be electrochromic or not, a Zr-Ni oxide film is typically used), iv) the electrolyte (proton conductor that allows the proton transport) and v) the electrochromic film (responsible for the coloration of ECD, WO_3 is the most studied material).[26-29, 61, 63]

The operation of an electrochromic device is based on the application of a potential difference (few volts) between the conducting films, which leads to the insertion of protons in the electrochromic layer causing a change in the color properties of the device (cathodic coloration, as illustrated in Fig.1.4). Alternatively, protons may be removed and in this case anodic coloration occurs. In these systems, IrO_2 is used instead of WO_3 as electrochromic material.[26-28, 61, 63]

High proton conductivity of the electrolyte is key to achieve short electrochromic response times. The best proton conductors need water to achieve high conductivity. However, the presence of water in the cell should be avoided since its presence increases the occurrence of secondary reactions and the evolution of H_2 and O_2 gases which leads to a decrease of the durability and stability of ECDs. So it is necessary to find a compromise between the presence of water and the electrochromic response time.[6, 62]

The hydrated crystalline phases (such as hydrogen uranyl phosphate (HUP) tetrahydrated) and hydrated polymers like Nafion® are interesting electrolytes. However the most investigated proton conductors for ECDs are anhydrous polymers such as poly(vinyl alcohol) (PVA) and poly(ethylene oxide) (PEO), blended with inorganic acids for example H_2SO_4, H_3PO_4 and H_3SbO_4, or other phosphate (such as $NH_4H_2PO_4$), zirconium phosphate) or the combination of, for example, $NH_4H_2PO_4$ with imidazole (Iz). These proton conductors are very attractive for ECDs application since they can operate without water and show the necessary proton conductivity.[6, 29, 63-66]

ECDs display some advantages compared with liquid crystal displays (LCDs) and light emitting diodes (LEDs) such as wider angle of view than most LCDs and better color contrast than LEDs especially under high levels of ambient light. The ECDs can show large dimensions and show aesthetic appearance. They may exhibit a continuously variable intensity of coloration and possess memory in either the bleached or colored state without power consumption. The drawback is their higher power consumption to operate comparatively to LEDs and LCDs and the slow response time (LCDs~ 1 ms and ECDs ~100 ms).[6, 62]

1.2.5 Batteries and supercapacitors

Batteries and supercapacitors (also called electrochemical capacitors) are two important applications for proton conductors. The batteries share a similar design and manufacturing with supercapacitors, comprising two electrodes, an electrolyte (proton conductor) and a porous separator (to avoid the short circuits in the cell). Figure 1.5 A shows a schematic representation of such devices, depicting discharge (in red) and charge (in black) processes. The main difference between batteries and supercapacitor is the mechanism of charge storage. While a battery stores energy in chemical form and converts it into electrical energy by electrochemical oxidation-reduction process (e.g equations in Fig. 1.5 B), the supercapacitors store energy in an electrostatic field determined by charge stored in electrical double layers (Fig. 1.5 C). There are also supercapacitors which use the redox reactions (Fig.1.5 C) near the surface for charge storage – they are called pseudo-capacitors or redox supercapacitors.[6, 13, 67-69]

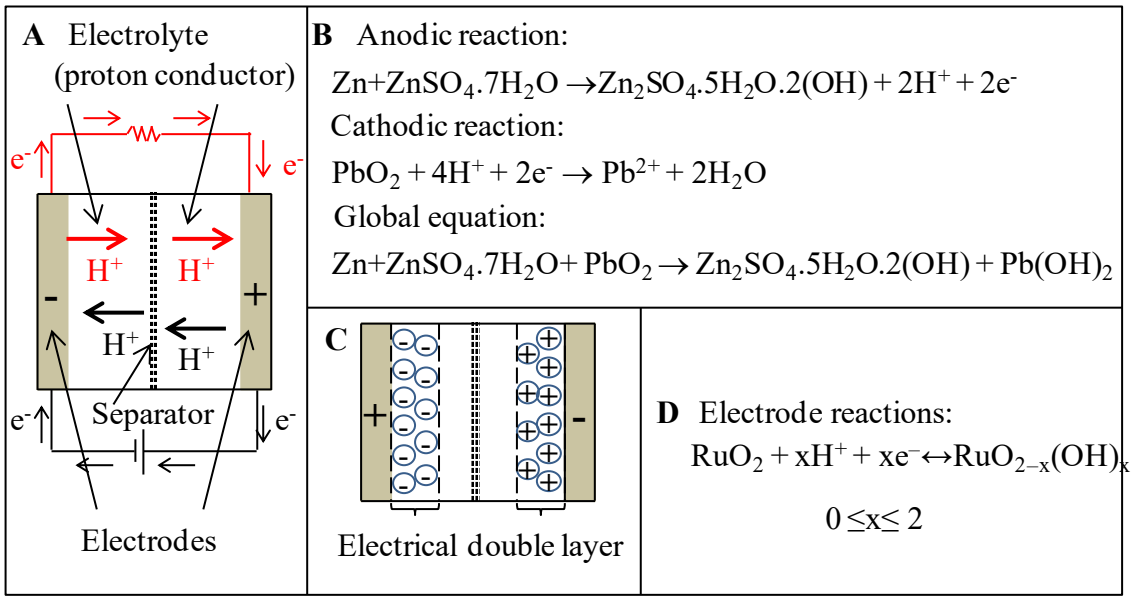

Figure 1.5 A) Schematic representation of supercapacitors or batteries (red part corresponds to discharge phenomena while black part is related to charge processes). B) Chemical equations for type of battery [30, 31]. C) Configuration of supercapacitor with electrical double layer. D) Electrode reactions using RuO_2 as material electrode (adapted from [69]).

The electrolytes for batteries can be liquid (e.g. H_2SO_4) or solids. All solid-state batteries have some advantages when compared to batteries with a liquid electrolyte, namely by minimizing leakage and corrosion problems, thus increasing safety and durability. The first electrolyte used in "all solid batteries" was the HUP which has proton conductivity about 10^{-3} $S.cm^{-1}$ at 25 °C. Polymer electrolytes have great potential for all solid state polymeric rechargeable proton batteries. Polymers such as PEO, PVA, PMMA, PVdF-HFP blended with salt complexes such as $(NH_4)_2SO_4$ or NH_4SCN can be used as proton conductors, and their proton conductivity and mechanical stability improved by addition of ceramic fillers such as SiO_2.[6, 13, 30, 31, 70]

The $Zn/ZnSO_4$ is often used as an anode material while the cathode is usually formed by a combination of materials, for example, PbO_2/V_2O_5/carbon/liquid electrolyte. The carbon provides electronic conductivity and the liquid electrolyte prevents the electrode polarization.[30, 31, 70]

The supercapacitors can be divided according to the energy storage mechanism in: i) double layer capacitors; ii) pseudo-capacitors; and iii) asymmetric supercapacitors, known as "hybrid" capacitors. The latter type is the combination of the first two types, with one electrode being based on the double layer capacitance and the other on the pseudo-capacitance.[13, 33, 69]

For different energy storage mechanisms, different electrodes materials are used. The carbon materials, such as graphitic materials, are the most used in electrodes for supercapacitors based on double layer capacitance, while metal oxides such as RuO_2 or conducting polymers like p-and n-

doped poly(3-arylthiopene) are widely used as electrodes in supercapacitors based on pseudo-capacitance.[13, 71, 72]

Several solid polymeric electrolytes (with or without inorganic fillers) can be used as electrolyte in supercapacitors. Gao and Lian [33] published a review giving an overview on proton conductors and their application in supercapacitors. It is possible to divide them in two main groups: polymer and inorganic/polymer proton conducting electrolytes. Within the first group, the membranes can be formed by PFSA electrolytes (e.g. Nafion®) and sulfonated hydrocarbon electrolytes (e.g. PSS:H). The second group is formed by acid/polymer blend electrolytes such as H_2SO_4/PVA, gel polymer electrolytes such as glutaraldehyde to cross-link PVA in H_2SO_4 and heteropolyacids/polymer composite electrolytes such as silicotungstic acid (SiWA)–PVA-phosphotungstic acid (PWA).[32, 33, 73, 74]

The supercapacitors present advantages comparatively to batteries, like higher power density, fast charge/discharge rate, long life expectancy, high efficiency and wide range of operating temperatures. They are safer and show less environmental impact than batteries. However they are more expensive and show lower energy density and the self-discharging rate is higher than in batteries.[13, 33, 69, 74]

1.2.6 Photoelectrochemical cells

Photoelectrochemical cells (PEC) are usually formed by one photoanode and one cathode separated by an electrolyte, but alternative designs may also include a reference electrode. Fig.1.6 shows an example of a PEC with two electrodes using TiO_2 as photoactive material in the photoanode side, and platinum coated carbon (PT-C) in the cathode side, using carbon paper as support. This cell can be used for water splitting, photocatalytic hydrogen production and air treatment.[75-78]

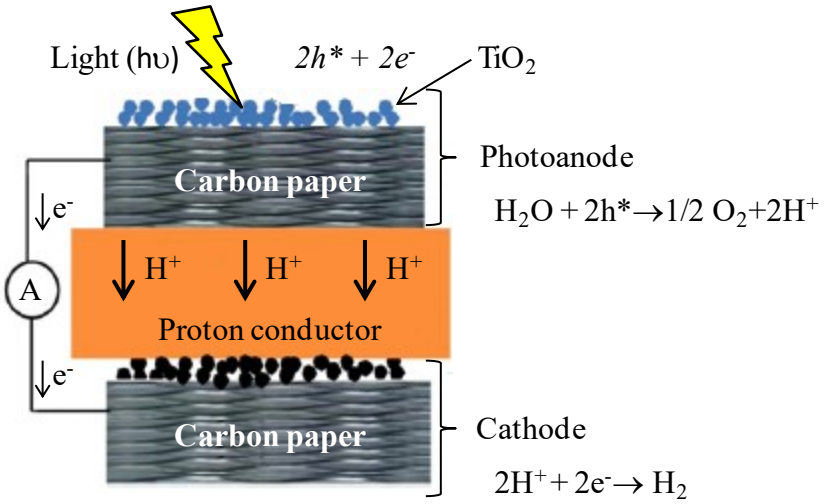

Figure 1.6 Schematic representation of a PEC (adapted from [76]).

In a PEC, the water enters the photoanode side and is combined with the two photo-holes (2h*), generated by the irradiated light (hυ) in the semiconductor (TiO_2 in case of Fig. 1.6). The water is then split into oxygen and two protons. The protons migrate from the anode side to cathode side through the membrane (proton conductor) whereas the electrons go through the electric circuit. In the cathode side the electrons and protons combine, forming a hydrogen molecule.[2, 3, 75-77]

Polymer proton conductors are good candidates for membranes in PECs. In the literature it is possible to find examples of application of Nafion®, Nafion®-based composites (e.g. Nafion® + $Mo_{0.5}W_{0.5}O_3 \cdot 1/3H_2O$) and S-PES and S-PES-based materials (e.g. S-PES +sulfonated MCM-41).[2, 34-36, 76-80]

Taking into account the electrodes, the most studied are the photoanodes. Ahmad *et al.*[75] published a review describing the most used materials for photoanodes, which include TiO_2-based materials[4], metal oxides (e.g. ZnO, α-Fe_2O_3 and WO_3), metal sulfides (e.g. CdS, ZnS), nitrides (e.g. β-Ge_3N_4) oxysulfides and oxynitrides (e.g. TaON and $Sm_2Ti_2S_2O_5$), nanocomposites (e.g. nanoparticles of the TiO_2, CdS, $Cd_{0.8}Zn_{0.2}S$ and Fe_2O_3 intercalated), Z-schemes (e.g. $CaTaO_2N$ with WO_3) and n-p heterojunctions systems of semiconductors (e.g. n-$PbBi_2Nb_{1.9}W_{0.1}O_9$ and p-$CaFe_2O_4$). The PT-C is the most used material for cathode but semiconductors such as CuO or Y-Ba-Cu-O are also widely applied. In the last case, the cathode is also called photocathode.[2, 3, 36, 75-87]

[4] These can have different morphologies (e.g. nanowires,nano-rods, nanotubes, nano-fibers, nano-belts), be used with metal deposition (e.g. Ag_2O), hybridized with carbon nanomaterials (e.g. single-walled carbon nanotubes), have surface modifications with adsorbants (e.g. fluorinated surface), coupled with binary composites such as WO_3, SiO_2, Al_2O_3, ZrO_2, dyes, and also doped with metal (e.g. $Fe^{3+,}$ Ru^{3+},V^{4+}) or non-metallic elements (e.g. N, S, C).

1.3 Mechanisms of proton conduction

From the view point of the mechanisms involved, the proton transport should be considered for the case of homogeneous media (typically when only one phase is present), or for heterogeneous systems (usually involving at least two phases). The latter involves specific interactions at the interface.[9] These are reviewed in this section.

1.3.1 Homogeneous media

Examples of homogeneous media include water or aqueous solutions of weak electrolytes such as imidazole, phosphoric acid, solid acids and also metal oxides with perovskite structure.[9, 88] In the case of water and aqueous solutions, it must be considered the mobility of protons (H^+), typically in acidic conditions, or the mobility of hydroxide ions (OH^-) in basic media. In both cases, the ion transport mechanism is via the so-called structural diffusion, which is an evolution of the Grotthuss mechanism (Fig. 1.7).[9, 89]

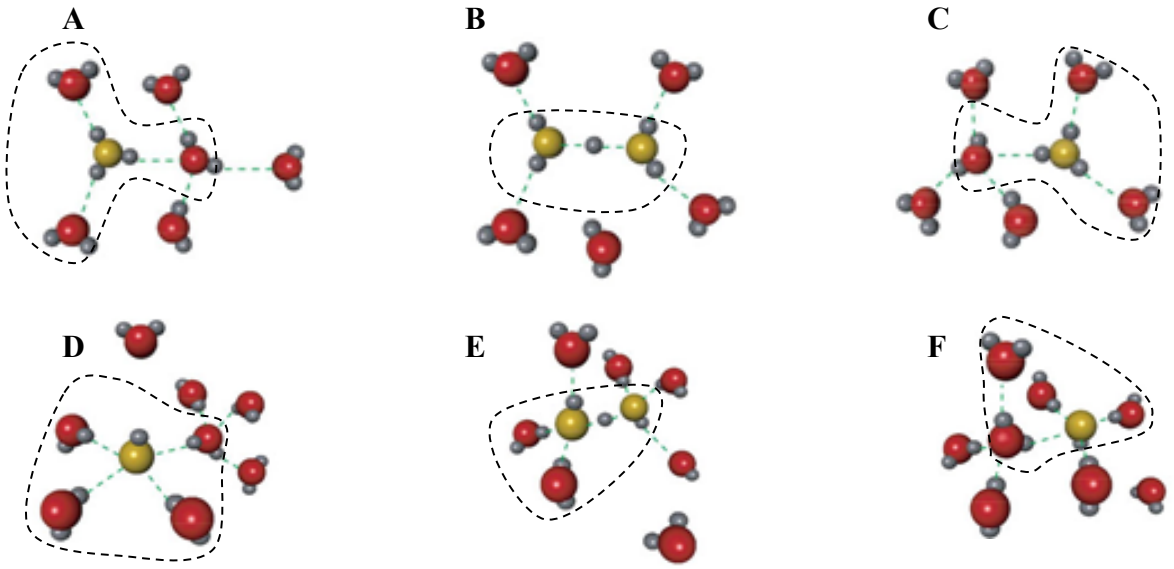

Figure 1.7 Schematic illustration of protons ion transport (A–C) and hydroxide transport ion (D-F). The red and grey spheres are oxygen and hydrogen atoms, respectively, and yellow spheres identify the oxygen in H_3O^+ or OH^-. Dashed green lines denote hydrogen bonds (adapted from [89]).

The underlying mechanism (Figs. 1.7 A-C) assumes excess protons in H_3O^+, which is in a threefold-coordinated $H_9O_4^+$ state (the Eigen-ion), as shown inside the dashed line in Fig. 1.7 A. Thermal fluctuations break the H-bond between the first and second solvation-shell of water of

H_3O^+ to form the $H_5O_2^+$ ion (the Zundel ion) depicted in Fig. 1.7 B. The complete transfer of the proton yields solvated H_3O^+ at a new site in the H-bond network (Fig. 1.7 C) forming a new Eigen-ion, hence allowing the cycle to repeat.[89, 90]

The proposed structural diffusion mechanism of proton holes in the hydrogen bond structure of water (Figs. 1.7 D-F) has obvious similarities to the proton transport. The OH^- ion is shown in a fourfold-coordinated $H_9O_5^-$ state (Fig. 1.7 D). Thermal fluctuations break the H-bond on the first-solvation shell, changing the OH^- to a threefold in $H_7O_4^-$ (Fig. 1.7 E). The complete transfer of the proton causes the migration to a new site in the H-bond network (Fig. 1.7 F) and so on.[89]

The diffusion processes in weak electrolytes such as imidazole or benzimidazole are similar to that of water. Table 1.2 summarizes the principal characteristics of the weak electrolyte compounds explored in this Thesis.

Table 1.2 Principal characteristics of the imidazole, benzimidazole, 1*H*-1,2,4-triazole and pyrazole.

Name	Acronym	Chemical formula	Structure	m.p.[a] (°C)	$\rho_{electrolyte}$ (g.cm^{-3})	pK_a[b]	σ (S.cm^{-1})
Imidazole	Iz	$C_3H_4N_2$	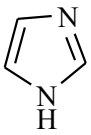	90-91	1.03	6.99	~3 x 10^{-3} [c]
Benzimidazole	Bz	$C_7H_6N_2$	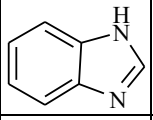	170.5	1.23	5.53	~1 x 10^{-3} [d]
1*H*-1,2,4-Triazole	Tz	$C_2H_3N_3$	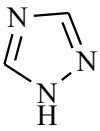	119-121	1.39	2.39	1.5 x 10^{-4} [e]
Pyrazole	Pz	$C_3H_4N_2$	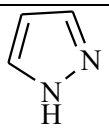	68	0.99	2.61	~3 x 10^{-4} [c]

[a] From[91]; [b] pK_a= -log K_a, $K_a = \frac{[H^+][B^-]}{[HB]}$ for the general proton-transfer reaction: $HB \leftrightarrows H^+ + B^-$. From[91]; [c] at 100°C, from[92]; [d] at 150°C, from[92]; [e] at 115°C, from[93].

These electrolytes are weak due to the covalent binding of hydrogen to the nitrogen. The electrolytes do not completely dissociate in solution, having a low intrinsic charge carrier concentration which implies moderated or low proton conductivity.[9, 94] The mechanism of proton transport can be explained using the kinetic Monte Carlo simulations. This model is based on reorientation and diffusion processes.[95] Figure 1.8 shows in detail the mechanism for proton transport in Iz.

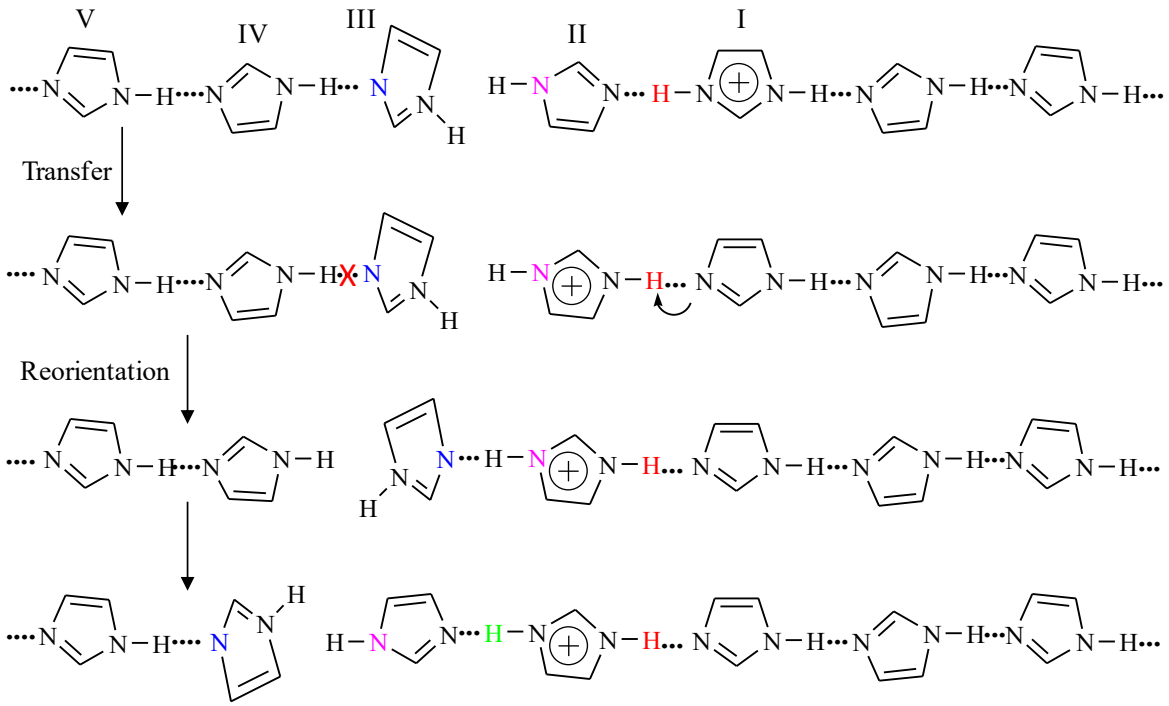

Figure 1.8 Simulated diffusion mechanism of an excess proton in Iz molecule chains.

The process begins by transferring the proton in the hydrogen bridge from molecule I to II (the "red" H in the transfer step), followed by a reorientation step. The distance between the "blue" and "pink" nitrogen atoms decreases and a hydrogen bridge between molecules II and III is formed. The proton in this bridge (green proton) is equivalent to the "red" proton, meaning the availability of the latter proton to start a new transfer.

A Grotthuss-type mechanism has also been proposed to explain proton transport in phosphoric acid through the dissociation of hydrogen-bonded protons and its transfer from one solvated acid molecule to another, as schematized in Fig. 1.9. This mechanism assumes four steps: i) formation of a contact ion pair $H_2PO_4^-$ and $H_4PO_4^+$ (Fig. 1.9 B); ii) solvation and separation of the charge carriers (Figs. 1.9 C and D); iii) migration (Fig. 1.9 E) and; subsequent, iv) neutralization (Fig. 1.9 F).[9, 96, 97]

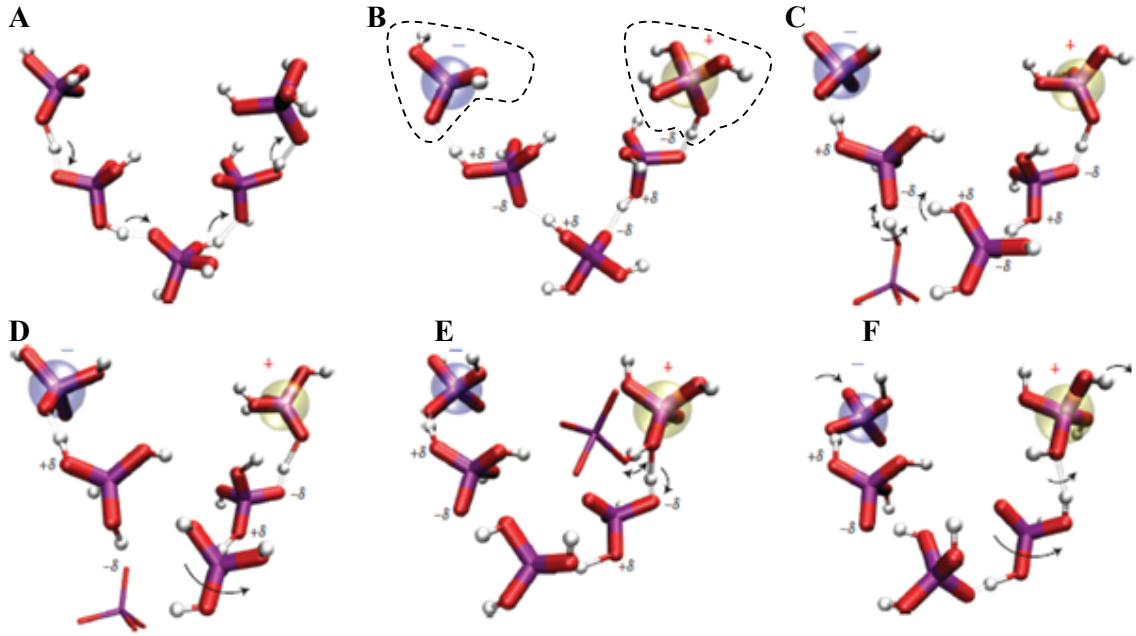

Figure 1.9 Steps of the proton conduction mechanism proposed for H_3PO_4. The white, red and purple are hydrogen, oxygen and phosphorus atoms respectively.[97]

Other example of proton transport in homogeneous media is the proton transport in solid acids of general formula $A_nH_m(XO_4)_{(n+m)/2}$, where A = K^+, Rb^+, Cs^+, Tl^+, Li^+, or NH_4^+ and X = P^{6+}, S^{6+}, As^{6+} or Se^6 which have structure XO_4^{2-} tetrahedra bound to the hydrogen. These acids are often referred to as ‘‘superprotonic conductors’’ since they show an increase in protonic conductivity by 2–3 orders of magnitude associated to a phase transition between 200 and 500 K. There are two possible models to explain the proton transfer.[41, 88] The first model considers the polymerization reaction (Eq. 1.5) with water loss at high temperature. The conductivity increases due the formation of water at the surface of the crystal, which is responsible for the proton conduction.[41, 88, 98]

$$n\,(MH_2PO_4) \rightarrow M_nH_{2n-2}P_nO_{3n+1} + (n-1)H_2O \qquad (1.5)$$

The second model occurs at temperatures above the structural phase transition. The protons are able to migrate through hydrogen bonds and go from one molecule to another by Grotthuss mechanism, based in the rotation of XO_4^{2-} tetrahedral.[41, 88, 98, 99]

Other examples of homogeneous proton conductors with a Grotthuss-type mechanism are cubic perovskites $ABO_{3-\delta}$, where A is typically an alkaline-earth metal ion such as Sr^{2+} or Ba^{2+}, and B is Ce^{+4} or Zr^{4+}, partially substituted by a trivalent cation (e.g. Y^{3+} or Yb^{3+}) in order to increase the concentration of oxygen vacancies (and thus the oxygen substoichiometry δ). Protonic defects in

the crystal lattice of these materials are formed by incorporation of water from the gas phase, which dissociates into a hydroxide ion and a proton. The hydroxide ion fills an oxide ion vacancy, and the proton forms a covalent bond with the lattice oxygen. In Kröger-Vink notation, this reaction can be written as stated in Eq. 1.6:[12, 100-102]

$$H_2O + V_o^{\bullet\bullet} + O_o^x \Leftrightarrow 2OH_o^{\bullet} \tag{1.6}$$

where, $V_o^{\bullet\bullet}$ represents an oxide ion vacancy, O_o^x is the lattice oxygen and $OH_o^{\bullet}$ represents the protonic defect. The key point here is the rotational diffusion of the protonic defect and the subsequent proton transfer towards a neighboring oxide ion, which keeps on its crystallographic position (Fig. 1.10).[12, 100, 101]

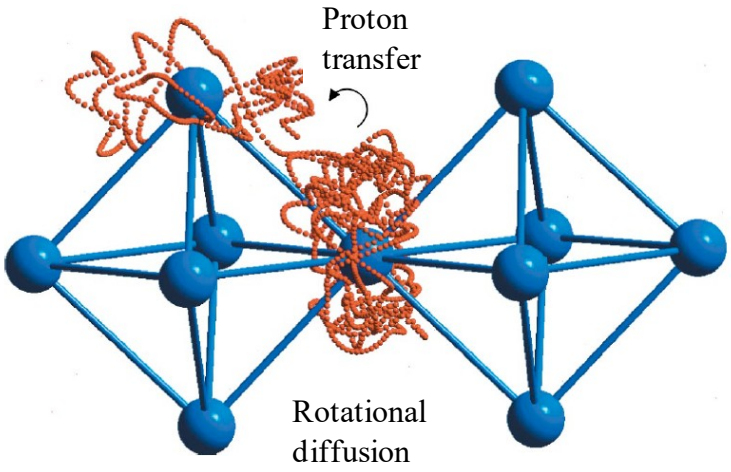

Figure 1.10 Simulation of the structural diffusion path of a proton in the cubic $BaCeO_3$ perovskite.[12]

1.3.2 Heterogeneous systems

Heterogeneous systems are those comprising more than one phase, which include: i) conventional composites (where the two phases are not chemically bound); or ii) systems displaying some level of chemical interaction. In heterogeneous materials, a homogeneous proton conductor is usually confined within a second non-conducting phase that provides other functionalities (e.g. mechanical integrity to the membrane). Examples of heterogeneous systems are: i) hydrated acidic polymers; ii) adducts of basic polymers with oxo-acids or immobilized proton solvents; and iii) composites.[9]

The hydrated acidic polymers, from which Nafion® is the best known example, are the most commonly used separator material for low-temperature fuel cells. The structure of these polymers

consists of hydrophilic (typically side chains terminated by sulfonic acid groups) and hydrophobic domains (such as polytetrafluoroethylene (PTFE) in Nafion®) (Fig. 1.11). The hydrophobic part of the structure allows the membrane to be morphologically stable while the hydrated hydrophilic side chains facilitate the conduction of protons.

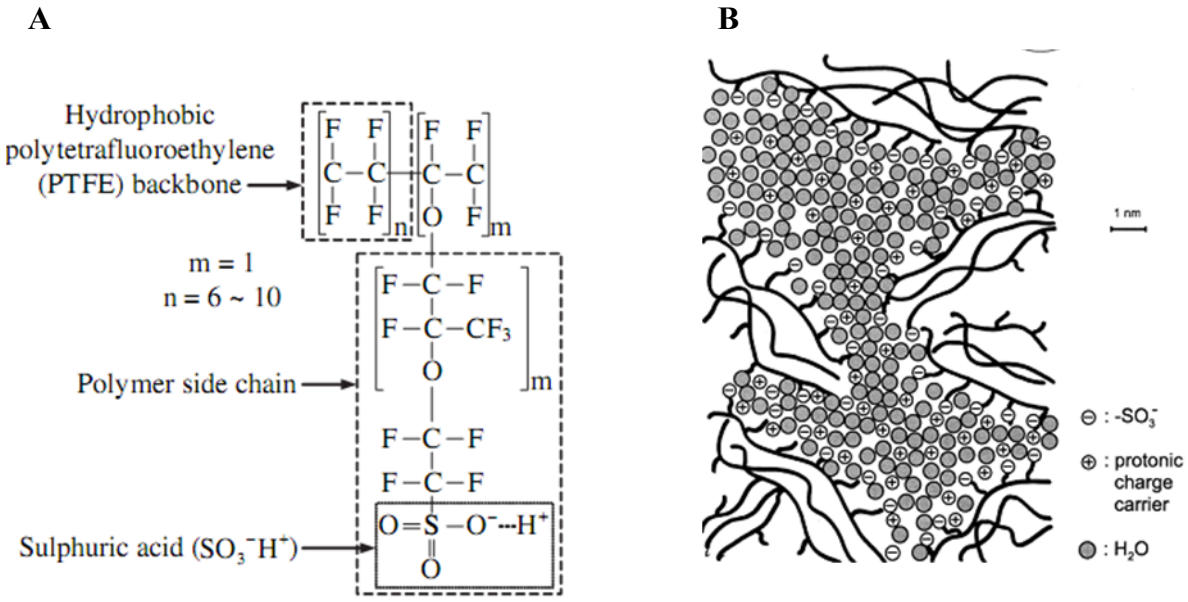

Figure 1.11 Nafion®: A) chemical structure [103] and B) microstructural features of morphology [9].

The protonic conduction in hydrated Nafion® occurs mainly by structure diffusion through water molecules kept inside the polymer structure by the hydrophilic domains. The $-SO_3H$ groups of the polymer can mediate this process, but it is obviously very dependent on the water content of the structure. The structural diffusion is the most important conduction mechanism of Nafion® at high degrees of hydration. Protons can also diffuse by a vehicular mechanism, where they are transported by a molecular diffusion process bound to water molecules (as e.g. hydronium ions) (Fig. 1.12).[9]

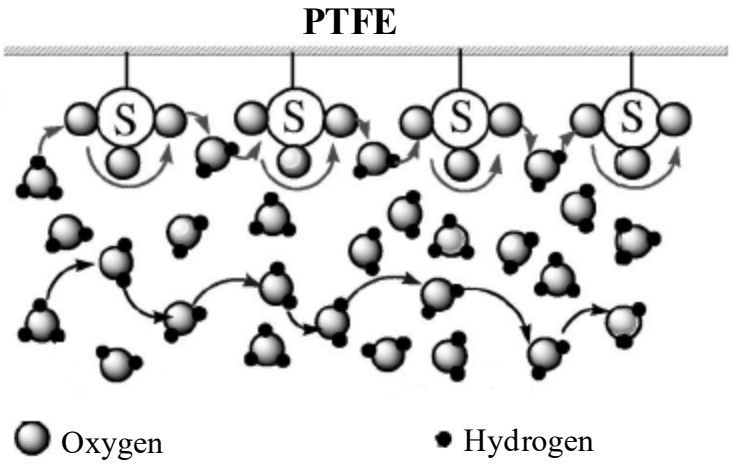

Figure 1.12 Possible mechanisms of structural diffusion of protons in Nafion® (adapted from [104]).

Other heterogeneous systems are adducts of basic polymers with oxo-acids. The most studied adducts are obtained from the various polymers based in poly(4-vinylimidazole) (P-4VI) (Fig. 1.13 A) and PBI (Fig. 1.13 B) with oxo–acids such as H_3PO_4, H_2SO_4, $HClO_4$ and HNO_3. In the latter PBI-based materials the proton conduction occurs via a Grotthuss-type mechanism, where the acid assumes the role of the proton donor (Fig. 1.13 C).[9, 105-109]

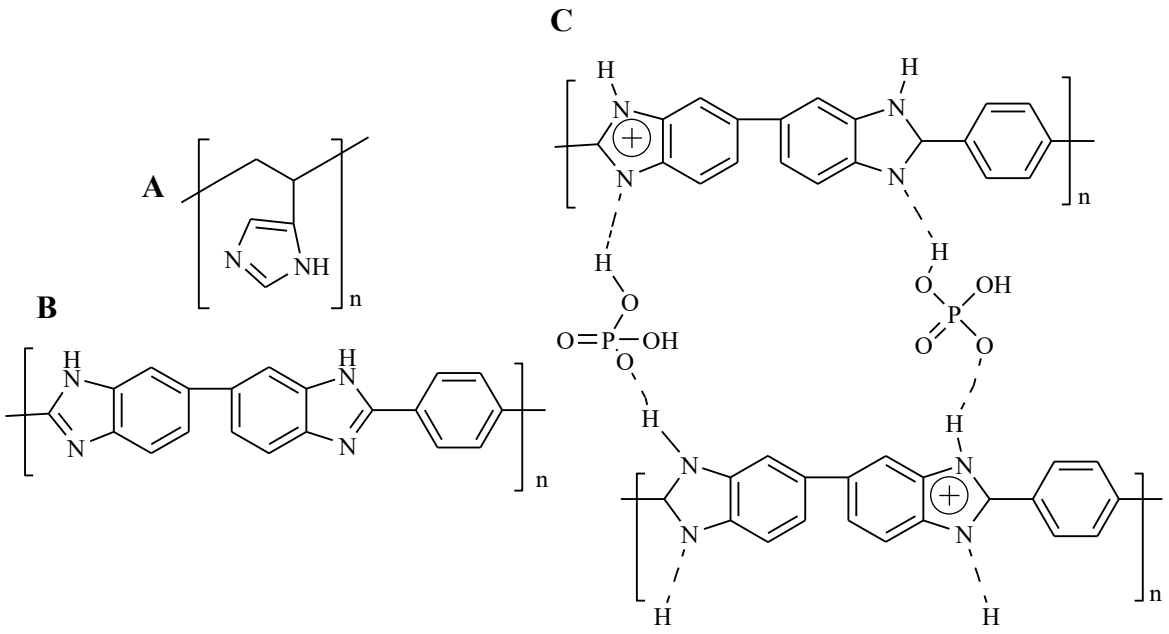

Figure 1.13 Structure of: A) poly(4-vinylimidazole), B) PBI and C) propose conductivity mechanism of H_3PO_4 doped PBI.

Other heterogeneous systems are based on proton solvents such as the Iz, Pz or Bz heterocycles immobilized in a polymeric matrix (Fig. 1.14 A). Here, the heterocycles are used as proton donors

and acceptors through specific sites (N), whereas the additional (C) sites may be used for covalent "grafting" to oligomeric or polymeric structures, thus bridging the nonpolar/polar "interface" and allowing for the immobilization of the proton solvent molecule. This mechanism is based in a structural diffusion of proton and assumes two steps: i) the proton transfer; and ii) ring rotation (Fig. 1.14 B).[9, 110, 111]

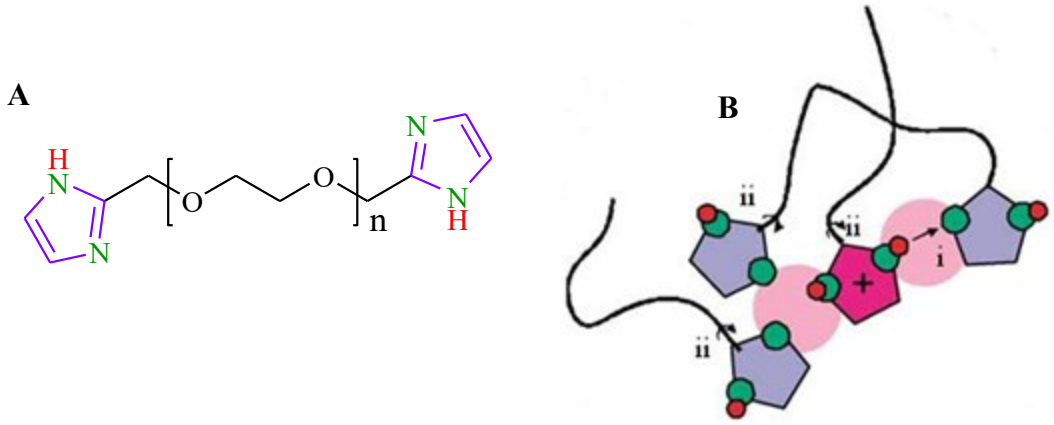

Figure 1.14 Imidazole immobilized in a polymeric matrix: A) structure and B) possible mechanism of proton conduction (adapted from [110]).

The last example of heterogeneous system reviewed here is the conventional composite consisting of one electrolyte matrix containing inorganic particles [38, 41, 112-114]. As summarized by Herring [114], proton conducting composite membranes are designed: i) to increase water retention capacity of an existing membrane; ii) to modify other properties such as the mechanical resistance; or iii) to modify the ionic exchange capacity. The most reported examples are modifications of polymer membranes by a variety of inorganic or organic-inorganic hybrid fillers, namely: i) hygroscopic metal oxides (e.g. $(SiO_2)_n$, ZrO_2, TiO_2, Al_2O_3 or also poly(phenylmethylsilsesquioxane)); ii) clays (the empirical formula is $(Si_2O_5^{2-})_n$; iii) zeolites; iv) mineral acids (HCl, H_2SO_4, H_3PO_4); v) solid acids of general formula $A_nH_m(XO_4)_{(n+m)/2}$, where A = K^+, Rb^+, Cs^+, Tl^+, Li^+, or NH_4^+ and X = P^{6+}, S^{6+}, As^{6+} or Se^{6+}; vi) heteropoly acids (based on clusters of W, Mo, or V or U oxides); and vii) metal (e.g. Zr, Sn, Ca or Cs) phosphates or sulphates.[41, 114] In the case of the acids or inorganic particles with acid surface functionalization, the fillers also provide additional acid sites also favoring proton hopping and structure diffusion in the case of water containing compounds (e.g. Nafion®).[114] Obviously, besides of nature and amount of the ionomer and solid used, the final properties of the composite membranes depend on the dispersion, size and orientation of the solid particles dispersed in the polymeric matrix.

In the above examples, the properties of the composite membrane result from a combination of the properties of the individual components. However, the interaction between the components can

originate new properties or new effects that are not present on either of the individual components. For example, it is possible to increase the crystallite fraction of a polymer by addition of inorganic moieties that strongly interact with the ionomer.[114]
The following section presents a different type of composite effect resulting from the electrostatic interaction between the matrix and the filler that creates space-charge interfacial regions with enhanced proton conductivity in comparison to the original matrix.

1.4 Nano-ionics

As pioneered by Joaquim Maier [115], nano-ionics is an emerging branch of physics that study specific properties, phenomena, effects and processes related to the ion transport at the nanoscale, with a particular focus on understanding and/or manipulating interfaces or junctions in solid state ionic materials.
There are three types of mesoscopic size effects in nano-ionic systems: i) trivial size effects occur when the interfacial properties remain unchanged with increasing amount of interfaces; ii) true size effects occur when the properties of the interfaces change with increasing fraction of interfaces; and iii) capillary effects, which are related to the modification of the interface properties due to their curvature and associated strain.[115, 116] While capillary effects are difficult to explore in a controlled manner, the true mesoscopic size effects can be felt, for example, in engineered heterostructure layers [117], or composites consisting of a ionic conducting matrix (solid or liquid) with dispersed inorganic particles [118-120], which is the relevant case in the context of the present work. The following sections revise the underlying relations describing the formation of space charge layers, and their application in the concept of heterogeneous doping, highlighting the case of heterogeneous doping of a weak electrolyte by inorganic particles as a way to enhance the proton conductivity of such electrolyte.

1.4.1 Space charge properties

The formation of space charge regions is the fundamental principle of the nano-ionic domains. The key point for their characterization is thus to determine the spatial distribution of charged defects at interfaces.[121] A conductor of ionic species j of net charge $z_j e$ (e is the electron charge) is disturbed by the surface of one inorganic particle. This surface breaks the local equilibrium leading to a redistribution of the concentration profiles of all charged species in the space charge layer determined by the space charge potential (Eq. 1.7):

$$\Delta\phi = \phi(0) - \phi(\infty) \tag{1.7}$$

where, $\phi(0)$ is the electrostatic potential at the interface (assumed as the reference location with a spatial coordinate $x=0$) and $\phi(\infty)$ is the potential in the bulk of the ionic conductor (placed at an infinite distance from the surface, $x=\infty$). Once the equilibrium is again established, the electrochemical potential of species j ($\tilde{\mu}_j(x)$[5]), at two different locations x_1 and x_2, will be the same (Eq. 1.8).

$$\tilde{\mu}_j(x_1) = \tilde{\mu}_j(x_2) \tag{1.8}$$

This equilibrium is more useful if written in terms of the defect concentration ($C_j(x)$) and electrostatic potential (Eq. 1.9).

$$\mu_j^0 + kT\ln C_j(x_1) + z_j e\phi(x_1) = \mu_j^0 + kT\ln C_j(x_2) + z_j e\phi(x_2) \tag{1.9}$$

This allows expressing the relation between the defect concentration and the electrostatic potential at the two positions according to Eq. 1.10,

$$\frac{C_j(x_2)}{C_j(x_1)} = \exp\left[-z_j e\left(\frac{\phi(x_2)-\phi(x_1)}{kT}\right)\right] \tag{1.10}$$

or, for any general position x relative to the bulk ($x=\infty$), according to Eq. 1.11.

$$\frac{C_j(x)}{C_j(x_{j\infty})} = \exp\left[-z_j e\left(\frac{\Delta\phi(x)}{kT}\right)\right] \tag{1.11}$$

---

[5] The electrochemical potential ($\tilde{\mu}_j(x) = \mu_j(x) + z_j e\phi(x)$) comprises electrical ($z_j e\phi(x)$) and chemical ($\mu_j(x)$) potential terms. For diluted solutions $\mu_j(x) = \mu_j^0 + kT\ln C_j$, were μ_j^0 is the standard chemical potential (independent of the position) and C_j is the concentration of species j at position x (T is temperature and k is the Boltzmann constant), and thus $\tilde{\mu}_j(x) = \mu_j^0(x) + kT\ln C_j + z_j e\phi(x)$.

This means that a local change of the electrostatic potential is compensated by changes of the chemical concentration profiles in order to maintain the electrochemical equilibrium. In order to find $\Delta\phi(x)$, it is necessary to consider the Poisson's equation (Eq. 1.12),

$$\nabla^2\phi = -\frac{z_j e C_j}{\varepsilon_0 \varepsilon_r} \tag{1.12}$$

where, ε_0 and ε_r are the dielectric constant of the vacuum and material, respectively. Equation 1.12 can be combined with Eq. 1.11 yielding (for the simplest one-dimensional case) the following equation.

$$\frac{d^2\phi}{dx} = -\frac{z_j e C_{j\infty}}{\varepsilon_0 \varepsilon_r} \exp\left[\frac{-z_j e}{kT}\Delta\phi(x)\right] \tag{1.13}$$

Assuming the Gouy–Chapman description of an electrical double layer, according to which the mobility is the same for all positive and negative charged species[6] [119, 122, 123], and assuming ϕ in the bulk as the reference ($\phi_\infty=0$), the spatial variation of the electrostatic potential across the space charge region, $\phi(x)$, can be expressed by Eq. 1.14

$$\phi(x) = \frac{2kT}{z_j e} \ln\left[\frac{1+\Theta\exp(-x/\lambda)}{1-\Theta\exp(-x/\lambda)}\right] \tag{1.14}$$

where,

$$\Theta = \tanh\left(\frac{z_j e \Delta\phi}{4kT}\right) \tag{1.15}$$

and, λ is the Debye length defined by:

$$\lambda = \sqrt{\frac{\varepsilon_0 \varepsilon_r kT}{2z^2 e^2 C_{j\infty}}} \tag{1.16}$$

[6] If the species do not show the same mobility it is necessary to use the Mott-Schottky approximation, where the mobility of one of charged species is assumed to be negligible and hence the corresponding concentration profile should be flat across the space charge thickness and equal to that in the bulk. This would be the case of an oxide conductor at low temperature, where the extremely low cationic mobility determines a frozen-in cation concentration profile, in contrast with the highly mobile anionic defects (oxide vacancies).

The Debye length is the thickness of the double layer formed at the charged surface, usually of a few nanometers. Equation 1.16 shows that λ is inversely proportional to the concentration of defects in the bulk, which means that if the defect concentration is high, for example, for a bulk material with high ionic strength, the Debye length is compressed and the interfacial effects tend to disappear Fig.1.15.[121, 122]

As an example of the application of the above formalism, let us consider the values of $\phi(x)$ plotted in Fig. 1.15 A as a function of the distance (normalized by the Debye length) to the surface, computed for TiO_2 particles with an estimated surface potential of 130 mV [124]. The potential is positive on the TiO_2 particles surface but it decreases exponentially with increasing distance to the interface over a distance equivalent to a few Debye lengths. This means that any positively charged defects are strongly depleted in the vicinity of the surface, whereas negatively charged defects are attracted. The concentration profiles can be quantitatively predicted for both cases by combining the Eq. 1.14 for the spatial dependence of the space charge potential with Eq. 1.11, which correlates the potential with the concentration, as shown in Fig. 1.15 B. This figure shows that the concentration of the negative defects can be enhanced by more than two orders of magnitude in relation to the bulk, whereas the reverse happens for the positive defects.

While Fig. 1.15 is a nice illustration of the mesoscopic effect, the situation may be slightly more complex because of adsorptive interactions of the active oxide surfaces. In the mentioned example of Iz doping, the excess imidazolate anion adsorbed at the particles surface decreases its surface potential. Consequently, there is an enrichment of the space charge layer adjacent to the oxide surface with imidazolium cations, where the anion concentration is depleted by the same factor. This is somewhat the inverse picture of Fig. 1.15, yet phenomenological equivalent.

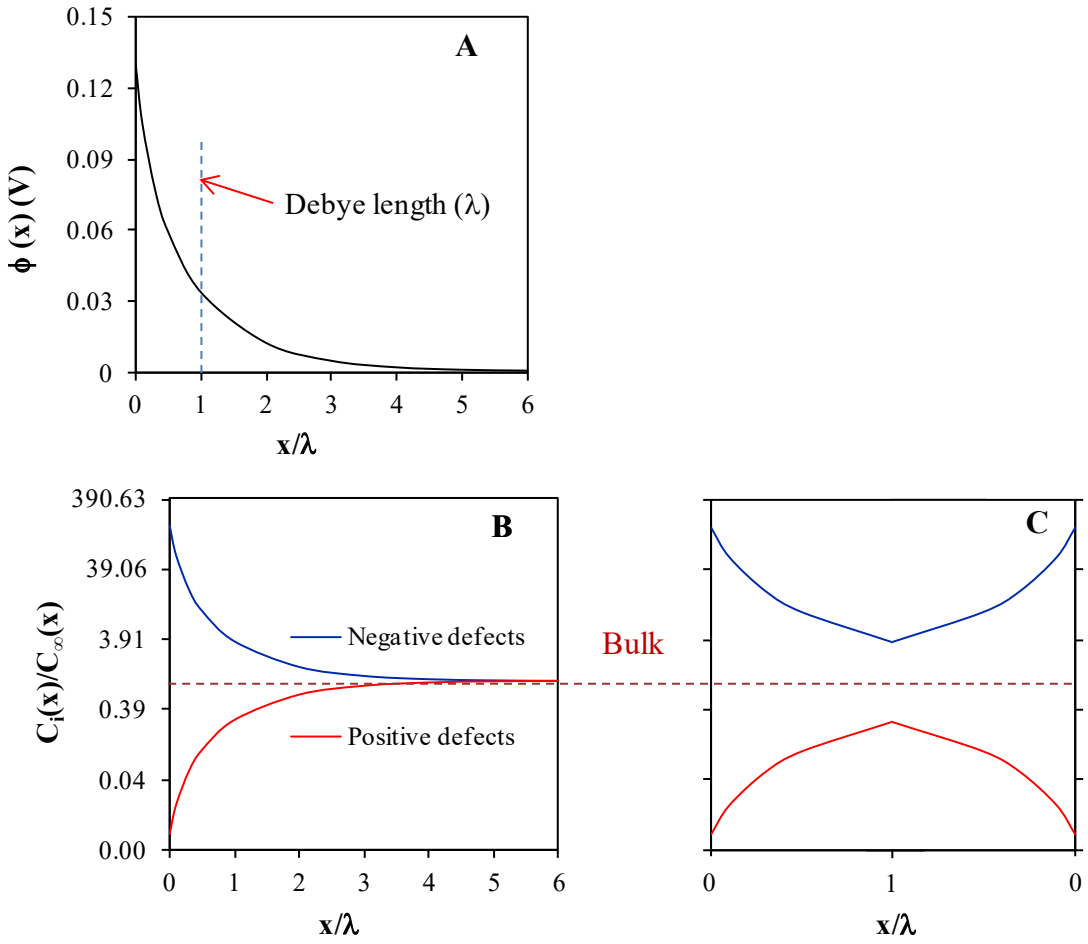

Figure 1.15 Graphical representation of A) electrostatic potential; B) concentration profiles of single charged positive and negative Iz defects plotted as a function of the distance from the surface of TiO_2 particles considering the Gouy–Chapman condition; and C) profile for a region between two surfaces placed at a distance of 2 x/λ to illustrate the mesoscopic effect of the potentially higher defect concentration in this region than in the undisturbed bulk of the electrolyte.

A case of special interest for the present Thesis is when two surfaces are brought sufficiently close (for example the mesoporous materials) so that the entire region between them may display a significant enhancement of the relevant defect concentration, as illustrated in Fig. 1.15 C. The manipulation of interfaces according to the above mentioned principles is the ground for the concept of heterogeneous doping.[116]

1.4.2 Heterogeneous doping

The heterogeneous doping is an example of the application of nano-ionics by adding a second phase to an ionic conducting system leading to an increase of the conductivity by means of interfaces. The main focus of the present Thesis is the addition of oxide particles at weak electrolytes (Iz, Bz, Tz or Pz). When oxide particles with a positive surface charge are added to a weak electrolyte (such as Iz) the negative species are adsorbed to the surface charge inducing a local deviation from electroneutrality that is compensated by the accumulation of protons in the adjacent regions (Fig. 1.16), locally increasing the proton conductivity.[125]

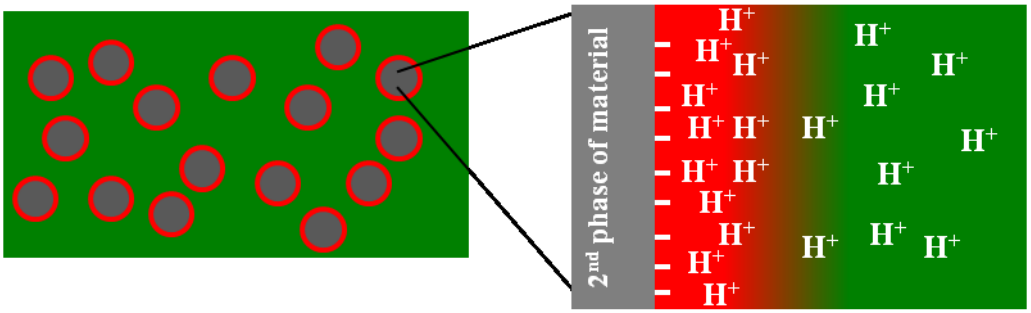

Figure 1.16 Schematic representation of addition the oxide particles (gray) to the weak electrolytes (green), with formation of the interface (red).

The total conductivity of such composites (σ_m) can be approximated by the Eq. 1.17:[121]

$$\sigma_{\mathrm{m}} = \sum \beta_{\mathrm{i}} \varphi_{\mathrm{i}} \sigma_{\mathrm{i}} \qquad (1.17)$$

where, σ_{i} is the specific mean conductivity of a specific region *i* of the composite with a volume fraction φ_{i}, and β_{i} is a constant related to percolation effects. Three different regions are considered in the composite: the bulk of the electrolyte with conductivity σ_{∞}, the oxide particles with σ_{p}, and the interfacial space charge regions with σ_{sc}. For metal oxide particles behaving as insulators at temperatures below 200 °C, the conductivity can be considered nearly zero (Eq. 1.18):

$$\sigma_{\mathrm{p}} \cong 0 \qquad (1.18)$$

The contributions of the bulk and of the space charge regions can be approximated by Eq. 1.19 and Eq. 1.20, respectively.

$$\left(1-\varphi_{\mathrm{p}}\right)\sigma_{\infty} \tag{1.19}$$

$$\beta_{\mathrm{SC}}\Omega\varphi_{\mathrm{p}}\left(2\varepsilon_0\varepsilon_{\mathrm{r}}RT\right)^{1/2}\upsilon_{\infty}C_0^{\,1/2} \tag{1.20}$$

where, φ_p is the volume fraction of particles, β_{sc} is a parameter that accounts for the degree of percolation of the oxide particles, Ω is the ratio of the surface area to the volume of the insulating phase, $\varepsilon_0\varepsilon_r$ is the absolute dielectric permeability, υ_∞ is the mobility of charge in the bulk and C_0 is the concentration of charge carriers in the first layer of the space-charge zone adjacent to the adsorption layer.[121, 124, 126]

An expression for the total conductivity of the composite can thus be expressed by combining Eq. 1.18 through Eqs.1.19 and 1.20, which leads to Eq. 1.21:

$$\sigma_{\mathrm{m}} = \left(1-\varphi_{\mathrm{p}}\right)\sigma_{\infty} + \beta_{\mathrm{SC}}\Omega\varphi_{\mathrm{p}}\left(2\varepsilon_0\varepsilon_{\mathrm{r}}RT\right)^{1/2}\upsilon_{\infty}C_0^{\,1/2} \tag{1.21}$$

This result shows that oxide particles with higher ratios of the surface area to volume lead to enhanced conductivity. Mesoporous materials featuring high values of Ω are thus very attractive to improve the performance of nano-ionic proton conductors, the ultimate goal of this Thesis.

The ionic transport occurs along percolating interfaces and thus the conductivity should increase with increasing oxide volume fraction. Increasing the amount of particles above a certain point forces this increase to be limited up to a maximum. After that the conductivity decreases due to an increasing number of particles touching each other, thus destroying the mesoscopic effect, as confirmed experimentally for mixtures of Iz e with TiO_2, Al_2O_3 and ZrO_2 (Fig. 1.17).[124]

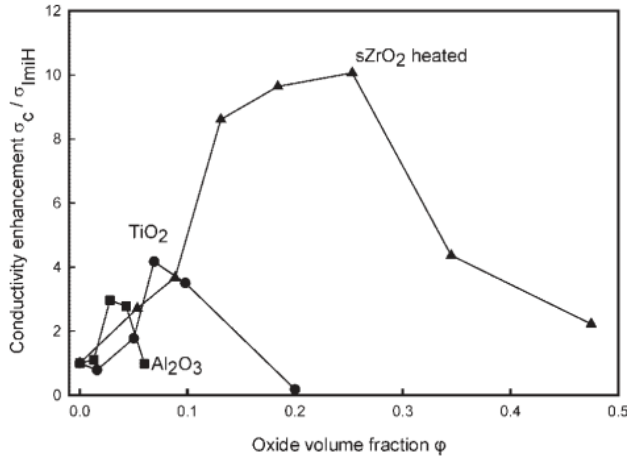

Figure 1.17 Plot of the effective overall conductivity enhancement as a function of volume fraction for various types of oxides at 90 °C in Iz.[124]

Besides Iz, other weak electrolytes with similar structure and properties such as Bz, Tz and Pz could also be used (Table 1.2). A similar effect was observed by Hurd *et al.*[127] in 2009 for a mixture of Tz with a MOF Na_3(2,4,6-trihydroxy-1,3,5-benzenetrisulfonate). Surprisingly, this was not interpreted as mesoscopic size effect.

1.5 Mesoporous materials

Mesoporous materials are materials with pore diameter (d_p) between 2 and 50 nm, according to the definition of the International Union of Pure and Applied Chemistry (IUPAC).[128] These materials feature a high specific surface area (S_{BET}), large pore volume (V_p) and narrow pore size distributions (PSD), which make them interesting for applications in catalysis, adsorption, sensors (e.g. gas sensors, biosensors, etc.), separation (e.g. proteins), enzyme immobilization, drug delivery, dye-sensitized solar cells, lithium-ion batteries or fuel cell.[129-139]

Kresge *et al* [140] in 1992 synthesized for the first time ordered mesoporous SiO_2 materials (M41S family) with a very narrow pore size distribution using a "liquid crystal templating" mechanism in which the inorganic precursor condense around ordered micelle arrays (soft template). Silica based mesoporous materials were extensively studied by varying the Si sources, template molecules among other parameters [141, 142]. This methodology was also extended to the preparation of ordered mesoporous metal oxides with soft templates[143-145]. However, the use of soft template to generate ordered pores in certain chemical compositions is an easy task. So, the ordered mesoporous silicas were used as hard templates to obtain carbon-based inverse replicas[146]. Later, a similar silica replication method was used to produce other mesoporous nanowires of

platinum[147], indium oxide [148], manganese oxide, cobalt oxide, and also chromium oxide [149].

This subchapter reviews the main synthetic routes for the preparation of mesoporous materials, placing the emphasis on nanocasting, and presents an overview of literature data for the various types of mesoporous oxides with interest for this Thesis.

1.5.1 Synthetic routes and preparation methods

Figure 1.18 schematizes the two methods for the synthesis of mesoporous materials: A) soft templating and B) nanocasting.

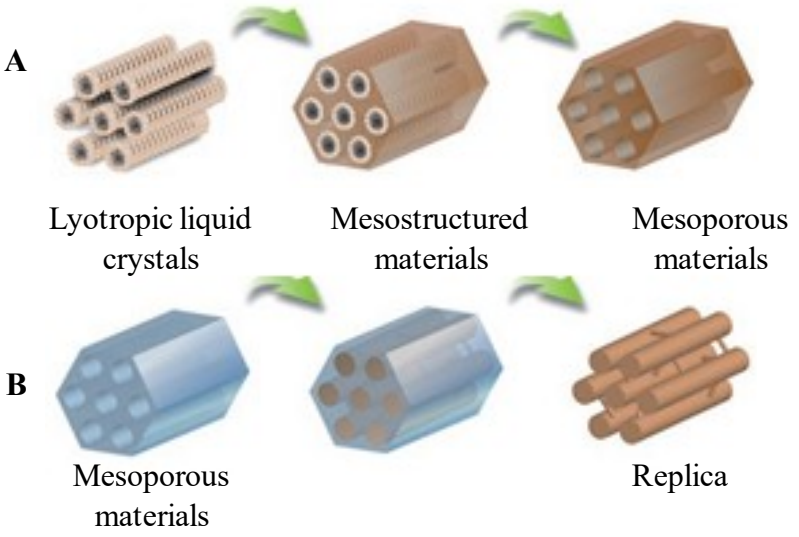

Figure 1.18 Methods to process mesoporous materials: A) soft templating and B) nanocasting.[150]

The first step of the soft templating technique is the formation of lyotropic crystals by dissolution of the structure-directing agents. After, the precursors are added and they condense around the arrays of ordered micelles. The mixture is then hydrothermally treated to consolidate the structure of the ordered mesostructure, yielding the desired mesoporous material after removal of the structure-directing agents by solvent extraction or calcination. The processes may be conducted in acidic or basic media.[150]

In the nanocasting process, the first step is the formation of a hard template (e.g. silicates or carbon) by soft templating. The precursors are then added to the mesoporous template and allowed to infiltrate inside the pores, where they are converted into the desired product for example by calcination. The final material should thus be a negative replica of the hard template. The silicate-

based templates can be removed by etching with acidic or basic solution, while carbon can be fired in oxygen atmospheres.[135, 150]

The two methodologies are significantly different in terms of:

i) Costs and resources –the soft templating is typically faster and cheaper than the nanocasting since the first step of nanocasting is the preparation of the hard template by soft template method;

ii) In terms of diversity of templates there are few hard templates that can be used;

iii) Crystal structures - the mesostructure obtained by soft templating is very dependent on temperature, type of solvent, etc., which makes the prediction of the resulting mesostructure more difficult. Moreover, certain oxide compositions are difficult to be organized by soft template. In the case of nanocasting, the mesostructure can, in principle, be easily controlled and predicted based on the mesostructure of the template. The mesostructure obtained from the soft-template technique is usually continuous whereas the nanocasted mesostructure frameworks are often discontinuous. On the other hand, the pore walls of the mesoporous materials obtained from soft-templates are usually amorphous because the temperature required for the crystallization is normally higher than the temperature that the surfactant micelles can support;

iv) Products - when the products require high processing temperature (e.g. sulfides, carbides, nitrides or borides), the nanocasting methodology is more versatile than the soft templating but there are three principal drawbacks: i) the yield of mesoporous products is low, ii) it is difficult to fully infiltrate the pores of the hard template and iii) the mechanical strength is low.[151]

The materials used in the present Thesis were prepared by nanocasting. The next sections present the principles of nanocasting and reviews literature data on some materials prepared using this technique.

1.5.2 Nanocasting

The factors influencing the nanocasting are: i) the hard template; ii) the precursors used; iii) the solvent; and iv) the impregnation method. The hard template is a key factor as it determines the structure and symmetry of the product to be formed inside the pores. Depending on the structure of the template, ordered or disordered mesostructures can be obtained. Figure 1.19 shows two examples of the nanocasting process using two different templates. In the first case (Fig. 1.19 A) the hexagonal mesostructure of template is maintained due to the existence of micropores connecting the main pore channels (circled), whereas in the second case (Fig. 1.19 B) the structure of the casted product is disordered.

Figure 1.19 Schematic representation of the nanocasting process for the cases A) with preservation and B) with loss of the hexagonal symmetry of the template in the final product.[152]

Mesostructures with different symmetries can be obtained by choosing the adequate templates. The most used templates have: i) 2-D channels (e.g. MCM-41 and SBA-15); ii) 3-D cage pores (e.g. SBA-16 and FDU-12); and iii) 3-D helix channels such as MCM-48 and KIT-6. Fig. 1.20 shows examples of such templates.

Figure 1.20 Schematic representation of the three types of templates (adapted from [151]).

The type of precursors is obviously very important. The precursors should be inert to the template, so that no reaction occurs. They also should be able to easily fill and diffuse through the pores of the mesoporous template. The capillary force, wettability and mobility of the precursor solution are very important parameters as well as the conversion temperature into the products and the volume contraction of precursors. The latter can be calculated using Eq. 1.22, and is usually of the order of 90% for the most of inorganic precursors. Such high contraction implies the need for multiple impregnation cycles in order to approach the complete filling of the pores.[135, 151]

$$V_{con} = \frac{V_{pre} - V_{pro}}{V_{pre}} \qquad (1.22)$$

The solvents play an important role on the nanocasting. The precursors must be soluble in the solvent to facilitate the infiltration in pores. Normally, high solubility of the precursor in the solvent leads to high degree of filling and enhanced infiltration efficiency. The solvents with high boiling point are not recommended because they are difficult to remove by evaporation. The most

used solvents for inorganic precursors are ethanol or water. Alternatively, tetrahydrofuran (THF) can be used for organic polymer precursors.[135, 151]

The impregnation methods play an important role too. Basically there are two methods: i) wet impregnation and ii) incipient wetness (Fig. 1.21).

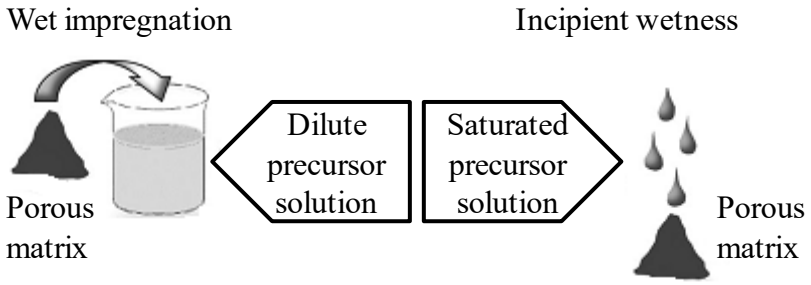

Figure 1.21 Schematic drawing of the infiltration techniques (adapted from [152]).

The wet impregnation involves the use of a diluted solution of the precursor(s) and the dispersion of the hard template into the solution. In the incipient wetness, the hard template is slowly wetted with a saturated solution of precursor(s) that to penetrate into the pores and dried before the new solution is added. Usually, the incipient wetness technique leads to higher loadings of precursors than wet impregnation, in particular when performed under vacuum to facilitate the template outgas. There are two variations of these methods. One involves the addition of molten salt precursors to the porous matrix in absence of solvent and, the other, the use of two immiscible solvents (e.g. water and hexane) and incipient wetness as impregnation method.[134, 135, 152, 153]

Due the high volume contraction Eq. 1.22 , there are three typical distributions of target products within the hard template (Fig. 1.22).

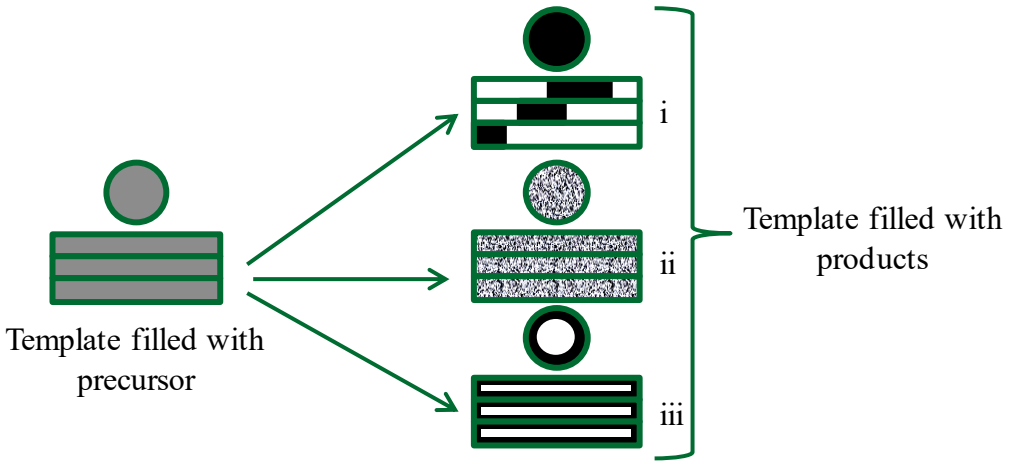

Figure 1.22 Schematic representation of different distribution of products within the template.

The target product can be aggregated in small domain on the channels of the template (i). The most order mesoporous metal oxide replicas are prepared of this way.

In second case (ii) the target product disperses fully in the pores occupying the total volume of pores. The products formed in this way show microporosity. Mesoporous carbons such as CMK-1 using MCM-48 as a hard template and CMK-3 using SBA-15 as a hard template follow this distribution.[154]

The last case (iii) the target product homogenously distributes on the interface of the mesopore channels by coating a uniform layer. It can occur when exists a strong interaction between the precursor and template or/and the amount of precursor is insufficient to fully occupy the pores. CMK-5 using SBA-15 as a hard template is synthesized in this way.[151]

The last step of the nanocasting process is the removal of the templates. There are three methods for removal of templates: i) hydrofluoric acid (HF) etching at room temperature; ii) strongly alkaline hydrothermal (NaOH) etching; and iii) calcination in air. The HF is toxic and harmful to the human body but it is more efficient than NaOH. Usually when a solution of NaOH is used requires two or more washes. The calcination in air are used for mesoporosos carbon templates.[135, 151]

1.5.3 Mesoporous oxides

Since the first reported study about the synthesis of mesoporous SiO_2 [140], many other studies were devoted to the preparation of mesoporous simple and multimetallic oxides. The synthesis of the latter is recognized as being very difficult.[144, 152, 155-157] The soft template method requires a careful control of the chemical, processing and treatment conditions on the synthesis of the mesoporous metal oxides in order to avoid the collapse of the meso-ordering during the thermal crystallization. The nanocasting has been presented as the most suitable method to obtain ordered mesoporous metal oxides.[133, 135, 158, 159] Several oxides have indeed been prepared from silica or carbon templates, but the method is not of general application as the thermochemical compatibility between the template and the precursors or the final product must be assured. The available hard templates are rather limited (mainly silica or carbon) and if they react with any of the components of the desired product, they cannot be used. The synthesis of SBA-15 and CMK-3 and their application in nanocasting has been the subject of several studies during the last years. Table 1.3 shows the principal characteristics of SBA-15 and CMK-3, both templates show a 2D hexagonal order of pores indexed at *p6mm* space group. Table 1.4 compiles literature data for mesoporous CeO_2, ZrO_2 and TiO_2 prepared by nanocasting process.

Table 1.3 Summary of the textural properties of SBA-15 and CMK-3.

Material	d_{100} (Å)[a)]	a (Å) [b)]	Wall thickness (nm)[c)]	d_p (nm)	V_p ($cm^3.g^{-1}$)	S_{BET} ($m^2.g^{-1}$)	Ref.
SBA-15	88-115[d)]	102-133	1.2-6.4	5.5-10.2	0.78-1.47	513-893	[141, 149, 160-197]
CMK-3	76-99[d)]	88-114	3.5-6.6	3.3-5.3	0.67-1.33	830-1520	[154, 185-192, 194-204]

[a)] Interplanar distance d_{100} calculated from the 2θ value of the (100) peak; [b)] lattice parameter $a=2d_{100}/\sqrt{3}$; [c)] calculated as (a-d_p); d) some obtain by extrapolation using the low angle XRD pattern available in literature.

Table 1.4 Characteristics of mesoporous ZrO_2, CeO_2 and TiO_2 prepared by nanocasting.

Oxide	Template	Precursor	Type of porosity	Crystallographic system	V_p ($cm^3.g^{-1}$)	S_{BET} ($m^2.g^{-1}$)	Ref.
CeO_2	SBA-15[a)]	$Ce(NO_3)_3.6H_2O$	2D hexagonal order	Cubic	0.15-0.52	75-164	[149, 160-168, 180, 193]
CeO_2	SBA-15	$CeCl_3.7H_2O$	2D hexagonal order	Cubic	----	----	[169]
CeO_2	CMK-3	$Ce(NO_3)_3.6H_2O$	2D hexagonal order	Cubic	0.29-0.45	104-167	[186, 187, 189, 198]
ZrO_2	SBA-15	$ZrOCl_2.8H_2O$	2D hexagonal order[b)]; 3D wormlike disordered[c)]	Tetragonal and monoclinic[d)]; tetragonal[e)]; not available[f)]	0.3-0.57	220-248	[170-172, 193]
ZrO_2	SBA-15	$Zr(OC_4H_9)_4$	---	Tetragonal	0.49	269	[184]
ZrO_2	CMK-3	$ZrOCl_2.8H_2O$	3D wormlike disordered	Tetragonal	0.21	74	[188]
TiO_2	SBA-15	$Ti(OC_4H_9)_4$	3D wormlike disordered	Tetragonal (anatase)	> 0.3	45; > 200	[181, 184]
TiO_2	SBA-15	$TiO(NO_3)_2$[g)]	2D hexagonal order	Tetragonal (rutile[h)])	0.09-0.15	30-163	[173, 174]
TiO_2	SBA-15	$TiCl_4$	2D hexagonal order	Tetragonal (anatase)	0.83	254	[166]
TiO_2	SBA-15	Titanium chloride solution[g)]	2D hexagonal order[i)]; 3D wormlike disordered[j)]	Tetragonal (anatase)[k)]; tetragonal (anatase and rutile)[l)]; tetragonal (anatase) and monoclinic (TiO_2(B))[m)]	0.15-0.35	83-317	[173, 175-177, 182, 183]
TiO_2	SBA-15	$Ti(SO_4)_2$[g)]	3D wormlike disordered	Tetragonal (anatase)	----	----	[173]
TiO_2	SBA-15	$Ti(OCH(CH_3)_2)_4$[g)]	3D wormlike disordered	Tetragonal (anatase)	----	----	[173]
TiO_2[n)]	SBA-15	$TiOSO_4$	2D hexagonal order	Tetragonal (anatase)	0.18;0.22	174;179	[178, 179]
TiO_2	CMK-3	$TiCl_4$	3D wormlike disordered	Tetragonal (rutile)	0.71	142	[188]

[a)] Obtained using microwave-digest, [149]; [b)] from, [170, 172]; [c)] from [171, 193] and with monodispersed nanoparticles, [171]; [d)]from, [170, 193]; [e)] from, [172]; [f)] from, [171]; [g)] prepared *in situ*; [h)] contaminated with the anatase phase at calcination temperature equal to 300 and 600 ºC, [173]; [i)] from [173, 175-177, 182] ; [j)] from, [183] for low impregnation circles; [k)] from, [173, 175, 177, 183]; [l)] from, [176, 182, 183]; [m)] from, [173, 183]; [n)] alcohol thermal reaction.

As shown in Tables 1.3 and 1.4, in general, the S_{BET} of the obtained mesoporous oxides, although still relatively high (100 - 400 $m^2.g^{-1}$), are lower than that of the templates (above 600 $m^2.g^{-1}$ for both silica- or carbon-based materials). Exceptions to this behavior are: i) the CeO_2 obtained following ref.[167]; ii) the TiO_2 calcined at 600 ºC using nitrate as a titanium precursor and SBA-15 [173]; iii) the TiO_2 obtained using SBA-15 (note that the SBA-15 was obtained by extraction) [181]; iv) the TiO_2 prepared based in the procedure present in ref.[183] when impregnation circle are equal to 8; and v) the ZrO_2 (CMK-3 as a template) obtaining by procedure present in ref.[188]. In terms of templates, the SBA-15 prepared using the procedure presented in refs.[161, 181, 186, 194, 195] are the exception.

Table 1.3 shows clearly the dependence of the S_{BET} and V_p of the SBA-15 on the synthetic procedure. The values of S_{BET} and V_p are sensitive to experimental conditions.

Most of the nanocasted products are highly crystalline with small domains of ordered porosity and d_p (often below 5 nm), being particularly suitable to promote the desired mesoscopic effects. The nanocasting method is retained as the prime approach to produce the desired mesoporous oxides for this work.

However, as mentioned above, the main limitation of nanocasting is the potential chemical interaction between the template and the final product or with the precursor. For example, the nanocasting of ordered mesoporous ZrO_2 using silica template seems to be feasible but at expenses of maintaining a significant amount of silicon in the final product (for example Si:Zr atomic ratio corresponding to 0.36[170]). The same happens in the case of TiO_2 using a silica template (Si:Ti = 0.031[174]). If the material is washed with a solution of NaOH 2 M during 18 h, the Si:Ti decrease but the mesostructure is partially destroyed. This means that Si-O-Ti cross-links are responsible for the order of the mesoporous. In case of CeO_2 formed using the silica template only residual amounts of Si are detected (Si:Ce = 0.14[162]), but the presence of Si-O-Ce crosslinks was not analyzed.

This may in principle be avoided by using carbon instead of SiO_2 as template[186-188, 198], although at expenses of additional synthetic steps as most carbon templates are obtained by replicating SiO_2 templates.

2

Materials and methods

This chapter is divided in nine sections. The first subchapter is dedicated to the nomenclature used in this Thesis. The following two describe the synthesis of templates and mesoporous oxide materials and the $BaCeO_3$. In the fourth section, the principal features of commercial oxides and of np-BZYO prepared by mechanosynthesis[7] are presented. In the fifth subchapter, the procedures used for the preparation of the pellets of oxide/electrolyte are described. The last four subchapters are dedicated to the presentation of the structural, microstructural and electrical techniques used in this work.

2.1 Nomenclature

Table 2.1 displays the nomenclature defined to the samples used in this Thesis. The oxides will be divided in two general groups: i) mesoporous oxides and ii) commercial oxides. In the first case it will used the prefix "ms-" and in the second case it will be added the indication of the size of particle, i.e. "np-" or "mp-" for nanocrystalline particles and microcrystalline particles, respectively. Additionally when more than one crystallographic phases of the oxide are present, the corresponding oxide prefix will be present. It will be used *m*, *t*, *a* and *r* for monoclinic, tetragonal, anatase, and rutile, respectively. For example, the acronym "np-*m*ZO" corresponds to the commercial nanocrystalline ZrO_2 particles with monoclinic crystallographic phase.

Table 2.1 List of acronyms of the different oxide materials used in this Thesis.

Oxide	**CeO_2**	**ZrO_2**	**8 mol% Y_2O_3 stabilized ZrO_2**	**TiO_2**	**$BaZrO_3$**	**$BaZr_{0.8}Y_{0.2}O_{2.9}$**	**$BaCeO_3$**
Acronym	CO	ZO	8YSZ	TO	BZO	BZYO	BCO

[7] Provided by Dr. Isabel Antunes, department of Materials and Ceramic Engineering, University of Aveiro.

In case of the mesoporous oxides prepared by nanocasting, it will be indicated if the template was removed or not. The oxides with template will present a suffix in the acronym indicating the name of the template (/SBA or /CMK) present in the material. The abbreviation indicating the template will appear between brackets if the template was already removed. For example, the mesoporous TiO_2 with anatase phase prepared using SBA-15 shows the acronyms ms-*a*TO/SBA and ms-*a*TO(SBA) before and after template removal, respectively.

The acronym of the oxide/electrolyte composites follows the nomenclature φ_{oxide} acronym of oxide/ acronym electrolyte, for example 0.1 ms-*a*TO(SBA)/Bz corresponds to a pellet with φ_{oxide} equal to 0.1 using Bz as electrolyte. Note that the acronyms of electrolytes were already presented in Chapter 1.

2.2 Synthesis of templates and mesoporous materials

Table 2.2 shows a list of mesoporous oxides synthesized using nanocasting process. In the next sections the synthesis of templates and materials will be described in more detail.

Table 2.2 List of oxide materials synthesized using nanocasting, including the synthetic conditions.

Precursor	Precursor addition	Hard template	Calcination temperature	Template removed	Acronym
$Ce(NO_3)_3.6\ H_2O$	Wet impregnation	SBA-15	350/550 °C in air	NaOH 2M	ms-CO(SBA)
$ZrOCl_2 \cdot 8H_2O$	Incipient wetness	SBA-15	600 °C in air	NaOH 2M	ms-*m,t*ZO(SBA)[a)]
		CMK-3	600 °C in argon	Calcination in oxygen	ms-*t*ZO(CMK)
$TiCl_3$ 12% in HCl	Incipient wetness	SBA-15	550 °C in air	NaOH 2M	ms-*a*TO(SBA)[b)]
		CMK-3	550 °C in argon	Calcination in oxygen	ms-*a*TO(CMK)
$Ba(OH)_2.8H_2O$ $Zr(OCH_2CH_2CH_3)_4$ 70% in 1-propanol[c)]	Incipient wetness	CMK-3[d)]	800 °C in argon	Calcination in oxygen	ms-BZO(CMK)
$Ba(OH)_2 \cdot 8H_2O$ $Zr(OCH_2CH_2CH_3)_4$ 70% in 1-propanol $OY_5(OCH(CH_3)_2)_{13}$	Incipient wetness	CMK-3	750 ºC-1100 °C in argon		ms-BZYO(CMK)[e)]

[a)] Both crystallographic phases are present, in similar volume percent (vol. %) see Table 3.2; [b)] the rutile phase is present but in low vol. %. see Table 3.2; [c)] the $BaCl_2.2H_2O$, $ZrOCl_2.8H_2O$ and the $Ba(NO_3)_2$, $ZrO(NO)_3.XH_2O$ were also used as precursors; [d)] the SBA-15 was used but no pure product was obtained; [e)] no product was achieved.

2.2.1 SBA-15 and CMK-3

The SBA-15 hard template was prepared by a well-established procedure described in the literature.[141] Tetraethylorthosilicate (TEOS, Aldrich, ≥ 99.0%) was used as silica source and poly(ethylene glycol)-block-poly(propylene glycol)-block-poly(ethylene glycol) (Pluronic P123, Aldrich, *purum*) as structure directing agent, in acid conditions, being removed afterwards by calcination. Typically, 4.0 g of Pluronic P123 was added to a solution with 30 g of distilled water and 120 g of 2 M hydrochloric acid (HCl, Carlo-Erba, 37%). The solution was stirred during 2 h at 35 ºC for total dissolution of the Pluronic P123. After that 8.5 g of TEOS was added drop-by-drop and left stirring for 24 h. Afterwards the solution was ultrasonicated for 5 min. Then the mixture was transferred to an autoclave and was heated at 100 ºC for 24 h. The powder was filtered and washed with warm distilled water and left to dry at 60 ºC overnight. The calcination was performed for 6 h at 540 ºC in air with heating rate of 1 ºC.min^{-1}.

The synthesis of CMK-3 was carried out by nanocasting using SBA-15 as a template and sucrose (Fluka, *purum*) as carbon source, according to the procedure previously reported[199]. The SBA-15 template was removed by washing with a 2 M sodium hydroxide (NaOH, EKA chemicals, *purum*) solution at room temperature. Typically, 1 g of SBA-15, 1.25 g of sucrose, 0.14 g of sulphuric acid (H_2SO_4, Sigma-Aldrich, 95-97%) and 5 g of distilled water were mixed together and placed in an oven at 100 ºC for 6 h, afterward the temperature was changed to 160 ºC for another 6 h. The resulting dark solid was ground and infiltrated again with 0.8 g of sucrose, 0.09 g of H_2SO_4 and 5 g of distilled water, followed by the same heat treatment. After that, the solid was heated to 900 ºC in argon atmosphere for 3 h with heating rate of 5 ºC.min^{-1}. The SBA-15 was removed at room temperature during 16 h using a solution of NaOH 2 M (16 ml of 2 M NaOH per gram of material). Finally the black solid was washed with distilled water and dried in air at 60 °C overnight.

2.2.2 Mesoporous CeO_2

The ms-CO(SBA) was obtained by wet impregnation of an ethanol (Carlo-Erba, *purum*) solution of cerium(III) nitrate hexahydrate ($Ce(NO_3)_3.6\ H_2O$, Aldrich, 99%). In a typical preparation adapted from ref.[160], 2.6 g of SBA-15 was added slowly to a solution of 3.7 g of $Ce(NO_3)_3.6\ H_2O$ in 74 ml of ethanol and mixed to form a “slurry”. The quantity of $Ce(NO_3)_3.6\ H_2O$ was calculated in order to fill 52% of V_P of the SBA-15 (V_P= 1.65 cm^3.g^{-1}). The ethanol was evaporated at 60 ºC in an oven. The white powder was calcined at 350 ºC (1 ºC.min^{-1}) during 4 h. After that, the powder was slowly added to a solution of 1.85 g of $Ce(NO_3)_3.6\ H_2O$ (to fill 26% of V_P of the SBA-15) in 74 ml

of ethanol and mixed again to form a "slurry". After, the ethanol was evaporated at 60 ºC in an oven. The resulting powder was calcined at 550 ºC (1 ºC.min^{-1}) for 5 h in air to obtain the ms-CO(SBA). The SBA-15 was suspended using a NaOH 2 M solution. 1 g of solid was washed in 16 ml of basic solution at room temperature during 16 h. The resulting powder was filtered, washed with distilled water and dried in air at 60 °C overnight. This process was repeated twice in order to achieve CeO_2 with residual amount of silica.

2.2.3 Mesoporous ZrO_2

The ms-*m,t*ZO(SBA) and the ms-*t*ZO(CMK) were obtained by nanocasting using zirconyl chloride octahydrate ($ZrOCl_2 \cdot 8H_2O$, Fluka, >99%) as oxide precursor, and SBA-15 and CMK-3 as templates, respectively. The technique applied in both cases was the incipient wetness impregnation.

The ms-*m,t*ZO(SBA) was synthesized following an adapted procedure from ref.[170] by dissolving 5.9 g of $ZrOCl_2 \cdot 8H_2O$ (to fill 95% of V_p of the SBA-15) in 14 ml of distilled water and adding it to 2.1 g of SBA-15 (V_P= 1.56 cm^3.g^{-1}). The white powder was calcined at 600 °C in air during 5 h, using heating rate of 1 ºC.min^{-1}. The removal of the SBA-15 was performed as indicated above. This process was repeated 3 times in order to achieve ZrO_2 with residual amount of silica.

The ms-*t*ZO(CMK) was prepared using 0.59 g of $ZrOCl_2 \cdot 8H_2O$ (to fill 60% of V_p of the CMK-3, V_P= 1.31 cm^3.g^{-1}) dissolved in 1.4 ml of distilled water and adding it to 0.4 g of CMK-3. The black powder was calcined at 600 °C (5 ºC.min^{-1}) in argon atmosphere for 5 h. The CMK-3 was removed by calcination at 400 ºC (5 ºC.min^{-1}) during 9 h in oxygen atmosphere and a white powder was obtained.

2.2.4 Mesoporous TiO_2

The ms-*a*TO(SBA) and the ms-*a*TO(CMK) were obtained using a process similar to that used to obtain ms-*m,t*ZO(SBA15) and ms-*t*ZO(CMK).The titanium(III) chloride solution ($TiCl_3$, Sigma-Aldrich, 12% in HCl) was applied as precursor in quantities filling 41% and 44% of the V_p for SBA-15 (V_P= 1.57 cm^3.g^{-1}) and CMK-3 (V_P= 1.31 cm^3.g^{-1}), respectively. The calcination temperature was 550 °C.

To obtain ms-*a*TO(SBA15) typically, 31.3 g of $TiCl_3$ 12% in HCl was added to 2.2 g of SBA-15 using incipient wetness technique. The HCl was evaporated at 40 ºC. For complete HCl evaporation, the solid was dried at 60 ºC in the oven. After that, the white solid was calcined at 550

°C with a heating rate of 1 ºC.min^{-1} during 5 h in air atmosphere. The SBA-15 was removed as described above. One wash was enough to obtain TiO_2 with residual amount of silica.

In a typical preparation of ms-*a*TO(CMK) 1.9 g of $TiCl_3$ 12% in HCl was added to 0.15 g of CMK-3 using incipient wetness technique. The calcination was performed at 550 ºC (heating rate of 5 ºC.min^{-1}) in argon during 5 h. The CMK-3 was removed by calcination at 400 ºC (heating rate of 5 ºC.min^{-1}) during 8 h in oxygen atmosphere.

2.2.5 Mesoporous $BaZrO_3$

Different attempts were made to produce ms-BZO(SBA) or ms-BZO(CMK) by nanocasting using SBA-15 and CMK-3 as templates, respectively. A variety of precursor combinations and solvents were also studied. In all cases the methodology applied was the incipient wetness.

In first attempt the barium chloride dihydrate ($BaCl_2.2H_2O$, Merck, *purum*) and $ZrOCl_2.8H_2O$ (1:1 molar ratio) dissolved in distilled water were added drop by drop to the SBA-15, the mixture was left in the oven for drying. After that the powder was calcined in air at different temperatures (700, 1000 and 1100 ºC). In this attempt, the precursors reacted with the template. The ms-BZO(SBA) was not obtained.

In second and third attempts, barium nitrate ($Ba(NO_3)_2$, Aldrich, 99%) and zirconium(IV) oxynitrate hydrate ($ZrO(NO)_3.XH_2O$, Sigma-Aldrich, 99% degree of hydration, ~6) in the molar ratio 1:0.68 dissolved in distilled water were added to the two templates. The powders were dried in the oven and calcined at 700 ºC in N_2 atmosphere. However in both cases, the desired oxides were not obtained.

The best conditions were found to correspond to a combination of CMK-3 with barium hydroxide octahydrate ($Ba(OH)_2{\cdot}8H_2O$, Merck, *purum*) and zirconium(IV) propoxide solution ($Zr(OCH_2CH_2CH_3)_4$, Aldrich, 70 wt% in 1-propanol) as a precursors (molar ratio Ba:Zr 1:0.68) in acetic acid (Pronalab, *purum*) in the quantities necessary to fill 95% of the V_p of the CMK-3. Typically, 0.14 g of $Ba(OH)_2{\cdot}8H_2O$ was dissolved in 0.54 ml of acetic acid. 0.13 ml of $Zr(OCH_2CH_2CH_3)_4$ 70 wt% in 1-propanol was added to the previous mixture into a solution using a syringe. The resulting clear solution was stirred at room temperature during 1 h before being dropped into 0.2 g of CMK-3 (previously dry in vacuum at 80 ºC during 4 h, V_P= 1.03 cm^3.g^{-1}). This mixture was stirred at room temperature during 5 min and left at room temperature during 24 h without stirring. The acetic acid was evaporated at 60 ºC in the oven. The impregnated black powder was calcined at 800 ºC in argon during 10 h (heating rate of 5 ºC.min^{-1}). The CMK-3 was removed by calcination at 400 ºC (heating rate of 5 ºC.min^{-1}) during 1 h under oxygen atmosphere. The obtained grayish white ms-BZO(CMK) was treated with formic acid (Merck, 98-100 %) to

remove the $BaCO_3$ impurity. Usually, 1 ml of formic acid 1M was added to 0.1 g of $BaZrO_3$ and stirred during 3 min. The powder without $BaCO_3$ was obtained by centrifugation (15 min at 3000 rot.min^{-1}), washed 3 times with distilled water. Finally, and finally dried in air at 60 °C overnight.

2.2.6 Mesoporous $BaZr_{0.8}Y_{0.2}O_{2.9}$

Based in the synthesis of the ms-BZO(CMK), two attempts were made to synthesize mesoporous ms-BZYO(CMK). Unfortunately, both approaches proved unsuccessful and a nanocrystalline $BaZr_{0.8}Y_{0.2}O_{2.9}$ produced by mechanosynthesis was retained for the subsequent studies.
Nevertheless, a description of both synthetic approaches is given here. In the first attempt, CMK-3 was used as template. The other precursors were $Ba(OH)_2{\cdot}8H_2O$, zirconium(IV) propoxide solution dissolved in acetic acid and yttrium isopropoxide oxide ($OY_5(OCH(CH_3)_2)_{13}$, Sigma-Aldrich, *purum*) dissolved in ethanol. The second attempt was similar but without ethanol. In both cases, the oxides precursors were used in the necessary amount to fill 95% V_p of the pores volume of CMK-3. The $Ba(OH)_2{\cdot}8H_2O$ was initially dried in the oven at 200°C for 19 h followed by 2 h at 80 °C in vacuum. Typically, 0.1 ml of $Zr(OCH_2CH_2CH_3)_4$ was added to 14 mg of $OY_5(OCH(CH_3)_2)_{13}$ dissolved in 1.5 ml of ethanol (in second approach the ethanol was replaced by 0.2 g acetic acid). This solution was added to 50 mg of dried $Ba(OH)_2{\cdot}8H_2O$ dissolved in 0.3 g of acetic acid. The final solution was kept in the ultrasonic bath during 5 min. Subsequently, the solution was added to 200 mg of CMK-3 powder, kept again in the ultrasonic bath for 5 min, followed by stirring (6 h and 25 min or 40 min for the first and second attempts, respectively) at room temperature, and dried at 60 ºC. The obtained powders underwent heat treatment in argon atmosphere at 900, 950, 1000 and 1100 ºC for the first attempt; and 750 and 900 ºC for the second attempt, both heating rate was equal to 5 ºC.min^{-1}. Surprisingly, in all cases only the zirconia phase could be obtained. The reasons for such failure were not further explored in the work.

2.3 Synthesis of $BaCeO_3$

The np-BCO was prepared with a process similar to that reported in [205]. The $Ba(NO_3)_2$ and $Ce(NO_3)_3.6\ H_2O$ were used as precursors and hexamethylenetetramine (HMTA) (Aldrich, 99%) as soft template. The product was obtained by calcination at 800 ºC. Typically, 50 ml of $Ba(NO_3)_2$ 0.12 M were added to 50 ml of $Ce(NO_3)_3.6\ H_2O$ 0.12 M, to which 50 ml of HMTA 0.12 M were added with stirring at room temperature. The obtained clear solution was kept at 80 ºC during 1 h and 30 min, until gaining a milky aspect. The water was evaporated at 100 ºC in the oven and the

resulting powder was calcined during 10 h at 800 ºC (heating rate of 5 ºC.min^{-1}) in order to obtain the desired np-BCO.

2.4 Commercial oxides and $BaZr_{0.8}Y_{0.2}O_{2.9}$

Several commercial oxides and one $BaZr_{0.8}Y_{0.2}O_{2.9}$ (np-BZYO) prepared by mechanosynthesis [206] were also used in this work. The principal structural and morphological features of those oxides are presented in Table 2.3. The diameters of particle (d_{par}) were calculated using the specific surface areas (d_{parBET}), XRD patterns (d_{parXRD}) and averaged measurements of 45 particles on the SEM micrographs (d_{parSEM}). The d_{parBET} values are typically larger than d_{parXRD} and d_{parSEM} values probably due to particle aggregation.

Some micrograph images, particle diameter distributions and XRD patterns of the used commercial oxides are presented in Appendix I.

Table 2.3 Summary of structural and morphological features of commercial oxides and np-BZYO.

Sample	Crystal system (cell parameters)	ρ_{oxide} (g.cm^{-3})[a)]	d_{parBET}[b)] (nm)	d_{parXRD}[c)] (nm)	d_{parSEM}[d)] (nm)	S_{BET} (m^2.g^{-1})	Source	Commercial data
np-CO	Cubic (a=5.4073)	7.26	12	26	36	66	Aldrich	d_{par} <25 nm ρ=7.13 g.cm^{-3}
np-*m*ZO	Monoclinic (a=5.1541 b=5.2155 c=5.316)	5.82	71	22	45	15	Tosoh	----
np-8YSZ	Cubic (a=b=c=5.1356)	6.47	75	19	----	12	Tosoh	ρ=5.9 g.cm^{-3}
np-*a*TO	Tetragonal (anatase) (a=b=3.7924 c=9.5304)	3.88	186	50	94	8	Merck	----
mp-*r*TO	Tetragonal (rutile) (a=b=4.5922 c=2.9578)	4.27	428	----	694[e)]	3	Alfa Aesar	----
mp-BZO	Cubic (a= 4.1911)	6.26	263	45	56[e)]	4	Aldrich	d_{par} <10 μm ρ=5.52 g.cm^{-3}
np-BZYO	Cubic (a=4.2176)	6.10	191	17	----	5	Mechanosynthesis	----

[a)] Calculated using the lattice parameters; [b)] calculated through the equation: $d_{par} = \frac{6}{S_{BET}\rho}$ considering the spherical shape of the particles where S_{BET} corresponds to specific surface area and ρ is the density; [c)] crystallite size obtained through the Scherrer equation: $d_{parXRD} = \frac{k_{sf}\lambda_{Cu}}{FWHM\cos(\theta)}$ where k_{sf} corresponds at dimensionless shape factor, λ_{Cu} is the wavelength of the X-ray (Cu Kα radiation, λ = 1.5406 Å), FWHM is full width of peak at half maximum in radians and θ is the Bragg angle; [d)] calculated based in diameter of 45 particles, using the Image J and Excel programs (see histograms present in appendix I); [e)] aggregates.

2.5 Preparation of oxide/electrolyte composites

Several pellets of oxide/electrolyte composites with oxide volume fraction (φ_{oxide}) between 0.1 and 0.4 were prepared. The φ_{oxide} was estimated through Eq. 2.1.

$$\varphi_{oxide} = \frac{V_{oxide}}{V_{oxide} + V_{electrolyte}} = \frac{m_{oxide}\rho_{oxide}\rho_{electrolyte}}{\rho_{oxide}\left(m_{oxide}\rho_{electrolyte} + m_{electrolyte}\rho_{oxide}\right)} \quad (2.1)$$

where, $\rho_{electrolyte}$ is the density of the electrolyte (Table 1.2), and ρ_{oxide} is the theoretical density of the oxides calculated using the lattice parameters (Tables 2.3, 3.2 and 3.3).

Before preparing the mixtures, the components were dried in order to remove adsorbed water, the oxides at 500 °C during 5 h, and the triazole at 110 °C during 16 h, the benzimidazole had no adsorbed water and was used as is. In a typical preparation, the oxide and the electrolyte powders were mixed in the desired proportion in ethanol during 15 min in an agate mortar, followed by drying at 60 °C. These mixtures were compacted in the form of disks with 8 or 10 mm of diameter (Fig. 2.1) by applying uniaxial (13-20 MPa, 3 min) and isostatic (200 MPa, 15 min) pressure.

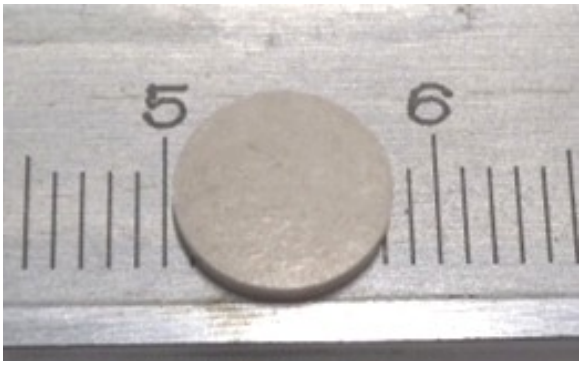

Figure 2.1 Oxide/electrolyte pellet.

2.6 Structural and microstructural characterization

The structural and microstructural characterization of the prepared materials were performed by: density measurements, X-ray diffraction (XRD), Fourier transform infrared spectroscopy (FTIR), transmission electron microscopy (TEM), scanning electron microscopy (SEM) coupled with energy-dispersive X-ray spectroscopy (EDS), thermogravimetry and differential thermal analyses (TG/DTA), N_2 physisorption isotherms. These techniques are briefly described in the following sections.

2.6.1 Density

The density measurements permit to determine the densification of pellets expressed as the ratio between the apparent (ρ_{pellet}) and the theoretical densities (ρ_{theo}) (Eq. 2.2).

$$Densification\,(\%) = \frac{\rho_{pellet}}{\rho_{theo}} \times 100 \tag{2.2}$$

ρ_{pelett} was obtained by the relationship between mass of pellet (m_{pellet}) and volume of the pellet (V_{pellet}). The V_{pellet} was calculated using the geometrical dimensions considering the cylindrical shape of the pellet (Eq. 2.3):

$$\rho_{pellet} = \frac{m_{pellet}}{V_{pellet}} = 4\frac{m_{pellet}}{\pi d_{pellet}^2 l} \tag{2.3}$$

where, m_{pellet} was measured using an analytical balance, the diameter of pellet (d_{pellet}) and the thickness of pellet (l) was measured using a micrometer screw gauge.
The theoretical density of the pellet (ρ_{theo}) was obtain though the Eq. 2.4.[207]

$$\rho_{theo} = \varphi_{oxide}\rho_{oxide} + \varphi_{electrolyte}\rho_{electrolyte} = \varphi_{oxide}\rho_{oxide} + (1-\varphi_{oxide})\rho_{electrolyte} \tag{2.4}$$

where φ_{oxide} is obtained using Eq. 2.1.

2.6.2 X-ray diffraction

X-ray diffraction (XRD) is used to identify crystalline phases or a repeating organization within amorphous materials. In the case of mesoporous silica and carbon materials, it allows to verify the presence of ordered porosity and unit cell parameters.

In XRD, the X-ray beam focuses in the sample and the photons are scattering in the 2θ angle. When the constructive interference from X-rays scattered occurs by the atomic planes in a crystal, a diffraction peak is observed. The condition for constructive interference from planes with an interplanar distance d is given by Bragg's law (Eq. 2.5):[208]

$$n_{\mathrm{p}}\lambda_{\mathrm{Cu}} = 2d\ sen(\theta) \tag{2.5}$$

where, n_{p} is the number of the plane that reflects the X-rays, λ_{Cu} is the wavelength of the X-ray (for a copper XRD ampoule - Cu Kα - is equal to 1.5406 Å), and θ is the Bragg angle.

As each material has a specific set of interplanar distances, it is possible to determine composition and crystalline phase of the material by comparison with database published by *Joint Committee on Powder Diffraction - International Centre for Diffraction Data* (*JCPDS-ICDD*).

The ideal XRD pattern consists of narrow, symmetrical, according to a well-defined unit cell but in real the XRD peaks are broad due to mainly three factors: i) instrumental effects, ii) crystallite size and iii) lattice strains. The former are associated to the apparatus and experimental procedure (packing of powders in the sampler). The others are related to the materials. The small crystallites (nanocrystallite) produce broad peaks, since the low probabilities of all crystallographic planes to produce the same diffraction peak profile. On the other hand the lattice strains affect the XRD pattern since the interplanar distance is not the same for different particles. Strain effects can be reduced by mechanical grinding.[209, 210]

In case of mesoporous materials, the low angle XRD measurement allows to characterize the structural arrangement of the ordered pores as long as the distance between them is compatible with Eq. 2.5. To give an example useful for this Thesis, a hexagonal distribution of mesopores is displayed in Fig. 2.3. This pores structure can be described by the space group *p6mm*, where the most intense reflection is the one corresponding to the (100) plane. The (100) plan can be used to estimate the lattice parameter (a) through the use of Eq. 2.6. The Fig. 2.2 also shows the molecular-scale periodicity represented by the interplanar distance d_{001}.

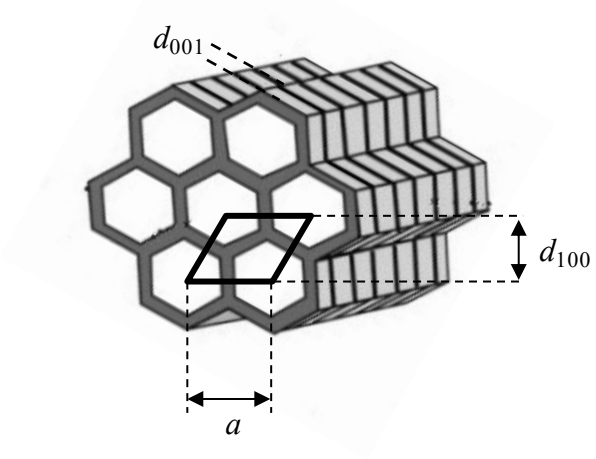

Figure 2.2 Schematic representation of the hexagonal arrangement of pores and the molecular-scale periodicity of the pore walls of Ph-PMO (adapted from [211]).

$$a = \frac{2d_{100}}{\sqrt{3}} \tag{2.6}$$

The high angle patterns were collected between 10 to 80° (2θ), with a step of 0.02° and with a scan rate 3º.min^{-1} on a Rigaku diffractometer using Cu-Kα radiation filtered by Ni (λ_{Cu}=1.5406 Å) and on Phillips X'pert MPD diffractometer between 20 to 70° (2θ) with a step size of 0.03º and step time of 2 s. These patterns provide information essentially on the crystallographic phase. The lattice parameters, the full width at half maximum (FWHM) of the peak and percentage of the different phases were calculated using POWDER CELL® program (version 2.4).[212]

The comparative high inter-pore distances implied the need of collecting patterns in a low angle. These were collected on a Bruker D8 Discover diaffractometer (the work was carried out in University of Minho, Guimarães, Portugal, by Dr Stanislav Ferdov), using Cu-Kα radiation, between 0.4 and 15° (2θ), with a step of 0.04° and step time of 1 s and collected on Phillips X'pert MPD diffractometer between 0.855 to 2.995 ° (2θ) with a step size of 0.01º and step time of 3 s.

2.6.3 Fourier transform infrared spectroscopy

Fourier transform infrared spectroscopy (FTIR) allows the identification of different chemical groups due to the interaction of the molecules or atoms with electromagnetic radiation in a process of molecular vibration. An infrared spectrum is commonly obtained by passing infrared radiation through a sample and determining what fraction of the incident radiation is absorbed at a particular

energy. The energy at which the peaks in an absorption spectrum appear corresponds to the frequency of vibration of the different functional groups of the molecule.

There are two modes for obtain a FTIR spectrum, transmission and reflectance. The transmission method is based upon the absorption of infrared radiation at specific wavelengths. In reflectance mode, the infrared beam is reflected by the material. The reflectance methods can be divided in four spectroscopies: attenuated total reflectance spectroscopy (ATR), specular reflectance spectroscopy, diffuse reflectance spectroscopy and photoacoustic spectroscopy. In this work, the ATR spectroscopy was used, which is based in the fact that when a beam of radiation passes from a more dense medium (ATR crystal) to a less dense medium (sample), a reflection occurs.[213]

The FTIR-ATR spectroscopy gives complementary information about the composition of material. In the case of oxides obtained by nanocasting, this technique allows to identify the presence of the template or of species resulting from the reaction between template and precursors. The FTIR-ATR spectra were collected using a FTIR Brucker Tensor 27 with a diamond ATR crystal. The spectra were collect with 256 scan and 4 cm^{-1} resolution using the powders directly.

2.6.4 Transmission electron microscopy

Transmission electron microscopy (TEM) has been utilized for observation of the nanostructures. It is an important technique for mesoporous materials characterization. It allows seeing the pores, their arrangement and the crystallinity of materials by using high-resolution transmission electron microscopy (HR-TEM) and selected-area electron diffraction (SAED), respectively. In TEM, the electrons are emitted from a filament and accelerated by a high voltage (usually 100-300 kV). The resulting electron beam is focalized onto the samples by electromagnetic fields (through electromagnetic lenses), when the incident beam interact with sample and different signals are produced and detected.[214]

In the literature there are many examples of the TEM characterization of mesoporous oxide materials. For example Li *et al* [163] used the TEM for characterization of mesoporous CeO_2 obtain by nanocasting (Fig. 2.3).

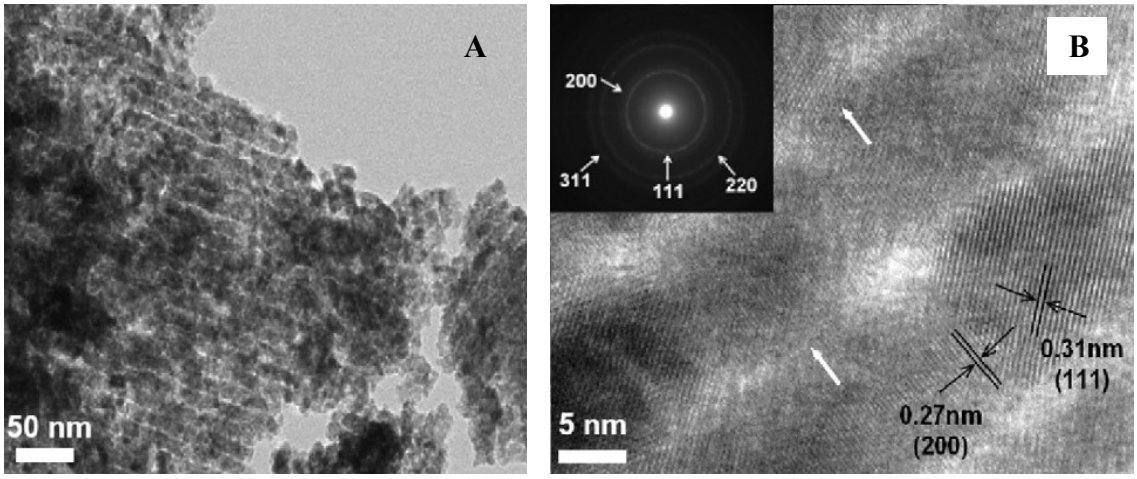

Figure 2.3 TEM micrographs of mesoporous CeO_2 [163].

Figure 2.3 A suggests that the pores are ordered. By HRTEM (Fig. 2.2 B), it is possible to identify the inter-planar distances indexed to the (200) and (111) planes of the pure cubic structure of CeO_2. The inset of Fig. 2.2 B shows the SAED rings corresponding to the (111), (200), (220) and (311) reflections of the CeO_2.

In the present work, the inter-planar distances were measured on the TEM micrographs and compared to the XRD results, using the software Image J (version 1.45s) [215].

The samples were analyzed in the form of powders placed on holey carbon film supported by 400 mesh copper grid (Agar Scientific). The sample preparation involved the dispersion of the powders in ethanol during 2 min in an ultrasonic bath, after which the grid was dipped and subsequently dried at room temperature for several hours. The TEM analyses were carried out on a Hitachi H9000-NA microscope operating at 300 kV and Jeol JEM 2100 operating at 200 kV and equipped with an Orius CCD camera from Gatan, EDS detector (Oxford Link) and a double tilt (±25°) sample holder (the work was carried out at the Renewable Energy Research Institute, University of Castilla-la Mancha, Albacete, Spain, by Dr Jesús Canales-Vázquez).

2.6.5 Scanning electron microscopy

Scanning electron microscopy (SEM) is the other electron microscopy technique used for the characterization of the prepared materials. In SEM, the electrons are accelerated with voltages from 1 kV up to 25 kV. The electron beam is scanned over the material. The images produced by SEM are secondary or backscattered electron images, since the signals change with surface topography, and give information about topography thickness.[216, 217]

The secondary electrons emission allows obtaining images with high resolution, they have low energy (<50 eV) independent of the primary beam and resulting of inelastic (not interact with the material atoms) collisions with beam electrons and material. The backscattered electrons depend of the primary beam the energy. These electrons result from the elastic scattering. So the backscattered electrons depend of material composition (atomic number), topography and crystal orientation.[217]

Due the low resolution it is impossible to observe the pore system of a mesoporous material, but it is a useful technique for morphological analyses. In case of this work allows us to confirm the densification of pellets.

In addition to SEM micrograph, the energy-dispersive X-ray spectroscopy (EDS) in SEM was used during this work to obtain elemental analysis of the materials. This technique is based on the detection of X-ray photon emitted due inelastic interaction with electrons primary beam and surface atoms of the material. The energy of X-ray photon is unique for each atomic transition and to the element. The X-ray photons that reach the detector are counted (in detector) and allow the representation of the number of counts *versus* X-ray energy. The peaks correspond to the specific decays of specific elements. The elements of material are quantified by comparison the peak intensity obtained from a reference standard in same conditions.[208, 217]

For SEM analyses, specific aluminum holders were used as supports to the samples. The templates and oxides are powders were deposited on carbon conductive tape (Ted Pella, 8 mm). The oxide/electrolyte pellets were glued to the holders using conductive carbon cement (Agar Scientific). In both case it was necessary to cover the samples with carbon using a vacuum evaporator (Emitech K 950 x).

The SEM/STEM micrographs were obtained using a Hitachi SU-70 microscope, equipped with a Quantax 400 EDS detector from Bruker. The acceleration voltage was kept between 4 to 15 kV.

2.6.6 Thermogravimetry and differential thermal analyses

Thermogravimetry (TG) and differential thermal analyses (DTA), usually performed simultaneously, consist on the measurement of mass and local temperature changes of a sample during heating at a constant rate.

In TG, the thermobalance detects the mass change during the heating. The results represent the mass variation as a function of the temperature.

In DTA, it is observed the effect of the temperature variation on the sample, i.e., if the sample absorbs or release energy when heated due to endothermic or exothermic events. The temperature change recorded in DTA can thus be correlated with the exothermic (sample temperature higher

than reference) or endothermic (sample temperature is lower than reference) processes occurring in the sample.

So using these techniques the temperature of the decomposition or/and the formation of products can be determined.[218] The TG and DTA analyses were performed at same time using a SETARAM-LABYS with heating rate of 5 ºC.min^{-1} under argon or air, using calcined Al_2O_3 as reference. The TG analyses for electrolytes and composites were made using a Shimadzu TGA 50 with heating rate of 10 ºC.min^{-1} N_2 atmosphere (20 mL.min^{-1}).

2.6.7 N_2 physisorption isotherms

A N_2 adsorption isotherm is obtained by measuring the amount of N_2 adsorbed when the relative pressure is increased up to one at a constant temperature. The N_2 desorption isotherms are achieved by measuring N_2 removed as the relative pressure is reduced back to zero.

Since the shape of N_2 physisorption isotherms reflect the characteristics of the pore structure, the physical sorption isotherms can be classified into six types (Fig. 2.4) as defined by the International Union of Pure and Applied Chemistry (IUPAC).[219]

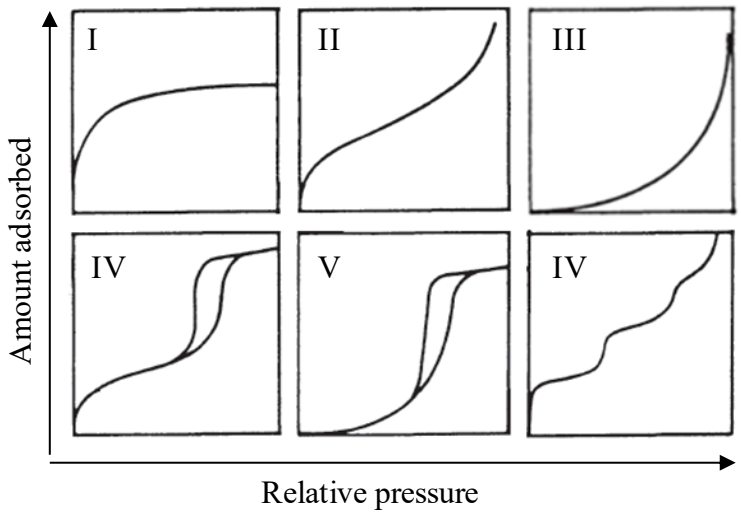

Figure 2.4- Types of physisorption isotherms.[219]

Mesoporous materials display type IV isotherms. The principal characteristics are the presence of hysteresis loop and for a low relative pressure the isotherm is similar to the isotherm type II. For high relative pressure, the adsorption rapidly increases due to the capillary condensation into the mesopores. The isotherm gives the information about the surface area and an approximation of pore size distribution.[220]

To calculate the specific surface area, the most used method is the Brunauer, Emmett and Teller (BET). This method assumes the multilayer molecular adsorption of gases. Isotherm can be expressed by Eq. 2.7,[221, 222]

$$\frac{P}{n_{ad}\left(P^0 - P\right)} = \frac{1}{n_m c} + \frac{c-1}{n_m c}\frac{P}{P^0} \tag{2.7}$$

where, n_{ad} are the moles of gas adsorbed (in case of this work N_2) on 1 g of adsorbent. n_m is the monolayer capacity. P and P^0 represent the equilibrium and saturation pressures, respectively. c is an experimental constant, which is dependent of the net heat produced by the adsorption of molecules in the monolayer.[219, 222]

For assessment of the pore size distribution, the Kelvin equation (Eq. 2.8) is usually used. This equation relates the relative pressure (P/P^0) at which condensation occurs with radius of curvature of the meniscus (r_m):[220]

$$\ln\frac{P}{P^0} = \frac{-2\gamma V_L}{RT}\frac{1}{r_m} \tag{2.8}$$

where, R is the ideal gas constant, T is the absolute temperature, γ and V_L are the surface tension and molar volume of the liquid, respectively.[220]

The r_m is related with the pores size using mathematical approximations. For mesoporous materials, the most used method for pore size evaluation is the Kruk, Jaroniec and Sayari (KJS). This model was developed by M. Kruk and M. Jaroniec in 1997 using MCM-41 silica material as model. The KJS method is based on the Barrett-Joyner-Halenda (BJH) algorithm which assumes that cylindrical shape of pores and allows obtaining the pore size using the physisorption isotherms. It is also possible to obtain the V_p through BJH algorithm.[223-226]

N_2 physisorption isotherms were collected at 77 K using a Gemini II-2370-Micromeritics equipment. Before the measurements, all oxides were degassed at 300 °C for at least 2 h, whereas CMK-3 was treated at 120 °C (for a minimum of 2 h). The data was analyzed to extract the S_{BET} by the BET method admitting multilayer coverage. The pore size distribution (PSD) and Vp were calculated with the adsorption branch using the BJH method, with the KJS approximation.

The BJH adsorption cumulative volume of pores was used to determine the amount of the precursor used for the template impregnation.

2.7 Thermodynamic predictions

When nanocasting was used for the preparation of mesoporous materials, the compatibility between template and precursors or products plays an important role. So it is useful to predict by thermodynamic calculations if a certain template is likely to react with a certain precursor under the adopted synthetic conditions. Chemical equations describing potential reactions involving the template materials and the final product or the corresponding precursors were written in order to calculate the Gibbs free energy (G) changes associated to those reactions as a function of temperature.

The change of of Gibbs free energy (ΔG) of a chemical reaction can be expressed by Eq. 2.9:

$$\Delta G = \Delta H - T\Delta S \qquad (2.9)$$

where ΔH and ΔS are the difference of enthalpy and entropy between the reaction products and the reactants. If ΔG is negative the reaction can occur spontaneously.[227]

In this work, several thermodynamic calculations were performed using the databases (FACT53) and the reaction module of the FactSage 6.1 commercial software.[228] This software allows obtaining the the Gibbs free energy and enthalpy changes as function of temperature for various reactions involving the templates and precursors or the desired products.

2.8 Zeta potential measurements

The surface charge of the particles determines the space charge layer properties, and it is thus of paramount importance for this study. The variation of the surface charge in contact with the electrolytes was studied by measuring the zeta potential.

When charged particles are dispersed in aqueous or other polar media, the ions with opposite charge are attracted while the ions with similar charge are repelled and form a double layer (gray in Fig. 2.5). This double layer can be divided in two parts: i) the Stern layer, where ions are strongly attached to the surface of the particle; and ii) part of the diffuse layer (the part between Stern layer and slipping plane), where the ions are less attached due to the increasing distance to the charged surface of the particles. The zeta potential (ξ) is the electrical potential difference between the charge surface and the final of double layer (slipping plane).[229]

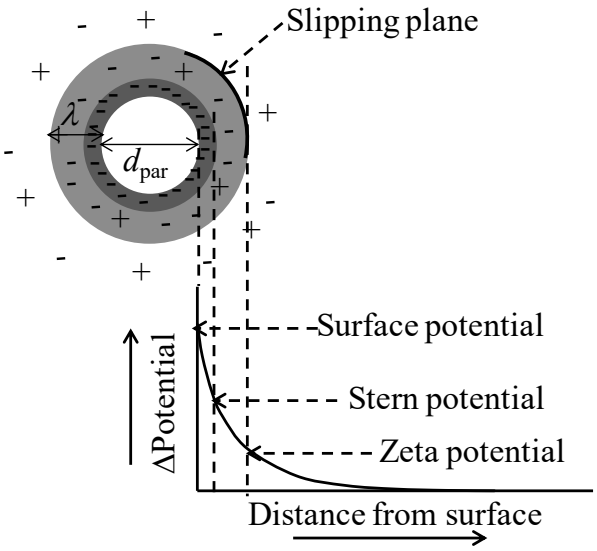

Figure 2.5 Schematic representation of the ξ (adapted from [229]).

The zeta potential depends on three factors: i) pH; ii) ionic strength of the medium; and iii) concentration of particles. The pH is the most important factor due to the high concentration of charged species found at high or low pH, which immediately will interact with the surface charges. When a particle with negative zeta potential is placed into a basic solution, the zeta potential becomes more negative due the adsorption of the excess negative species in solution to the charged surface. The opposite occurs if the pH is acid. The isoelectric point pH(I) corresponds to the pH value at which the zeta potential is equal to zero. So zeta potential value is only meaningful if pH value is known.

The ionic strength of the medium is important since the Debye length depends of concentration of ions in medium (see Eq. 1.16). Finally the zeta potential depends of the number of particles i.e. depends of the double layer. In a concentrated system, the double layer can be overlapped and the value of zeta potential is not correct. In low concentration the measure of mobility of the particles is complicated and their conversion to zeta potential can be incorrect.[230]

The zeta potential is usually measured using electrophoresis. This method is based on the measurement of the velocity of particles under an applied electrical. This velocity is referred to as electrophoretic mobility (U_E), which means that ξ is dependent of the electrophoretic mobility. The Henry equation (Eq. 2.10) shows this dependence:

$$U_E = \frac{2\varepsilon\,\zeta\, f(\alpha_H)}{3\eta} \tag{2.10}$$

where, ε is the dielectric constant; $f(\alpha_H)$ is a Henry's function and η is the viscosity. The $f(\alpha_H)$ depends of the radius of particle (R_s) and the thickness of Debye length (λ). So this function can be defined by Eq. 2.11 if $\alpha_H = \lambda^{-1} R_s < 1$ and by Eq. 2.12 if $\alpha_H > 1$.

$$f(\alpha_H) = \left(1 + \frac{1}{16}\alpha_H^2 - \frac{5}{48}\alpha_H^3 - \frac{1}{96}\alpha_H^4 - \frac{1}{96}\alpha_H^5 - \left[-\frac{1}{8}\alpha_H^4 - \frac{1}{96}\alpha_H^6\right]\exp(\alpha_H)\int_{\infty}^{\alpha}\frac{e^{-t}}{t}dt\right) \tag{2.11}$$

$$f(\alpha_H) = \left(\frac{3}{2} - \frac{9}{2}\alpha_H^{-1} + \frac{75}{2}\alpha_H^{-2} - 330\,\alpha_H^{-3}\right) \tag{2.12}$$

For $f(\alpha_H)$, two values are generally used as approximation 1 or 1.5. The value 1.5 corresponds to the Smoluchowski approximation ($\lambda^{-1}R_s \rightarrow \infty$) and 1 corresponds to the Huckel approximation ($\lambda^{-1}R_s \rightarrow 0$).[229, 231]

There are various techniques to measure the mobility of the particles such as rotating prism; rotating grating; and laser electrophoretic scattering. The latter is the mostly used, namely by the laser doppler method.[230]

In this work, the electrophoretic mobility was measured on a Zetasizer Nano Series apparatus equipped with red laser (λ_r=633 nm), using the universal 'dip' cell or the folded capillary. The technique used was the laser doppler velocimetry (LDV) in combination with the phase analysis light scattering (PALS) to obtain the mobility of particles. The conjugation of these techniques is known as M3-PALS and it is patented by Malvern.[229] The M3-PALS technique consists in application of the two reverse fields. A fast field gives an accurate determination of the mean of mobility and a low reverse field gives better resolution, but the mobility values are shifted by the effect of electro-osmosis. The two values are subtracted to determine the electro-osmotic flow. To obtain the Zeta potential, the Smoluchowski approximation was used. This approximation applies to aqueous and polar solutions.[229]

The ζ measurements of oxide/electrolyte mixtures suspended in aqueous potassium nitrate (KNO_3, Panreac, *purum*) solutions were performed according the procedure reported in literature [124].

For the measurements, 5 mg of the oxide powders (previously fired at 500 °C during 5h) were suspended in 250 ml or 100 ml of 0.001 M KNO_3 solution, which is assumed as an inert electrolyte [232], and put in ultrasonic bath during 30 min. Well-defined amounts of solutions of the various electrolytes under study, Iz (Sigma-Aldrich, 98%), Bz (Aldrich, 98%), Tz (Aldrich, 98%) and Py (Aldrich, 98%) also in 0.001 M KNO_3 were added to the oxide suspension with a syringe in order

to obtain a systematic characterization of the ζ as a function of the φ_{oxide}. The prepared suspensions were sonicated during 2 min after each addition of electrolyte and before measuring the electrophoretic mobility.

2.9 Electrochemical impedance spectroscopy

The electrochemical impedance spectroscopy (EIS) was used to perform a detailed electrical characterization of the protonic conductivity of the oxide-electrolyte composites. The technique consists on applying to the material a periodic sinusoidal voltage *V(t)* with amplitude V_0 and angular frequency (ϖ) (Eq. 2.13), and the measurement of the resulting current *I(t)* (Eq. 2.14),

$$V(t) = V_0 \sin(\varpi t) \tag{2.13}$$

$$I(t) = I_0 \sin(\varpi t + \phi_i) \tag{2.14}$$

where, ϕ_i is the phase angle between the voltage and the current. The impedance (*Z*) (Eq. 2.15) is the ratio between the voltage and the current

$$Z(t) = \frac{V(t)}{I(t)} = \frac{V_0 \sin(\varpi t)}{I_0 \sin(\varpi t + \phi_i)} = Z_0 \frac{\sin(\varpi t)}{\sin(\varpi t + \phi_i)} \tag{2.15}$$

where, Z_0 is the amplitude. The representation of *Z* in the time domain is complex, requiring the solution of a system of differential equations. Instead, it is easier to adopt the representation of *Z* as a complex function with a real *Z´* and imaginary *Z´´* parts (Eq. 2.16):

$$Z(\omega) = Z' + iZ'' = |Z|\cos(\phi_i) + i|Z|sen(\phi_i) \tag{2.16}$$

where, *i* is the imaginary number ($i = \sqrt{-1}$).*Z(ϖ)*, which can be plotted in the complex plane (or the Argand diagram) as a vector,[233] usually as a set of vectors measured at determined frequency ($f = \varpi/2\pi$) between mHz and MHz. The Nyquist plots shown in Fig. 2.6 depict the impedance of a few typical electrical circuit elements and their associations.

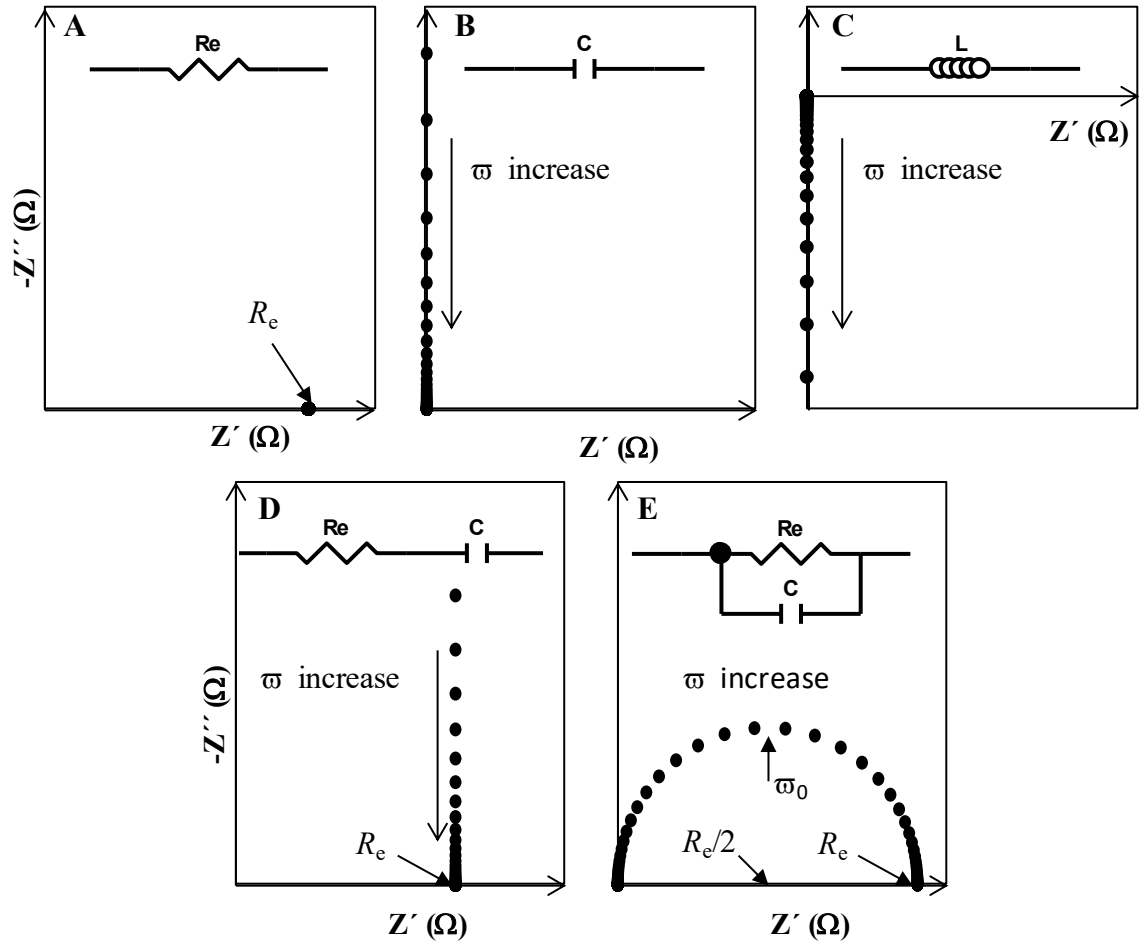

Figure 2.6 Nyquist plots of: A) resistor; B) capacitor; C) inductor; D) resistor and capacitor in series (RC series); and E) resistor and capacitor in parallel (RC parallel).

The resistor (Fig.2.6 A) shows only a real contribution ($Z(\varpi) = R_e$ where R_e is the resistance) independent of ϖ. The capacitor (Fig.2.6 B) shows only an imaginary contribution dependent of ϖ according to $Z(\varpi) = -i\varpi C$, where C corresponds to the capacitance. The inductor (Fig. 2.6 C) is similar do the capacitor, but with the opposite signal ($Z(\varpi) = i\varpi L$, L is the inductance).

The total impedance of an electrochemical system often resembles the behavior of a combination of electrical elements in circuits such as the association of a resistor and a capacitor (RC), either in series ($Z(\varpi) = R_e + 1/i\varpi C$, Fig. 2.6 E) or in parallel ($Z(\varpi) = 1/Re + i\varpi C$, Fig. 2.6 F).[234]

The parallel RC circuit is one of the most common observations, which justifies some additional comments. The total impedance of such circuit is given by

$$\frac{1}{Z(\varpi)} = \frac{1}{R_e} + \frac{1}{\frac{1}{i\varpi c}} = \frac{1}{R_e} + i\varpi c \Leftrightarrow Z(\varpi) = \frac{R_e}{1 + i\varpi R_e c} = \frac{R_e}{1 + (\varpi R_e C)^2} - i\frac{\varpi R_e^2 C}{1 + (\varpi R_e C)^2} \quad (2.17)$$

As depicted in Fig. 2.6 E, the Nyquist plot shows a semicircle with amplitude R_e centered in $Z' = R_e/2$. The imaginary part of the impedance reaches a maximum at the relaxation frequency ϖ_0. This frequency is characteristic of each process in an electrochemical cell and is a function of the resistance and the capacitance according to

$$\varpi_0 = \frac{1}{R_e C} \quad (2.18)$$

Usually when the Nyquist plot displays more than one semicircle, this implies that more than one process is occurring in the cell. The separation of the processes is possible when the relaxation frequencies are different. One example is the system schematized in Fig. 2.7 A consisting of an agglomeration of conducting electrolyte particles and corresponding series and parallel interfaces (indicated by the arrows). The total impedance is the result of three contributions: i) the contribution of electrolyte grain (R_g green arrow); ii) the contribution of electrolyte grain boundary (red arrows, solid and dashed correspond to perpendicular $R_{gb\perp}$ and parallel $R_{gb\parallel}$ contribution, respectively); and iii) the electrochemical reactions at the electrodes (blue arrows). The two former contributions correspond to resistance of the system and they appear at high values of frequency. The latest contribution corresponds to the electrode or electrolyte/electrode interface polarization phenomenon, which appears at low values of frequency. The system can be described using the equivalent circuit presented in Fig. 2.7 B, which is simplified by omitting the electrode contribution.

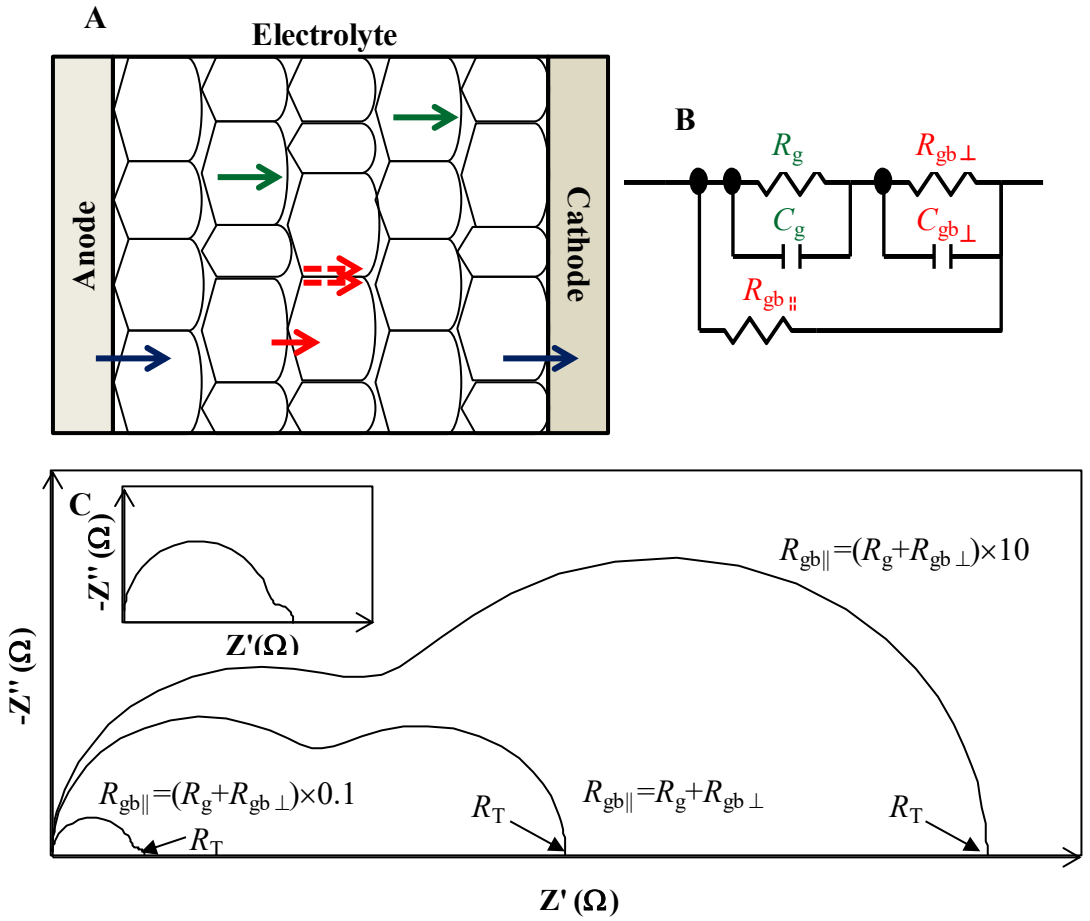

Figure 2.7 A) Schematic system showing the three contributions; B) possible equivalent circuit of the Fig. 2.6 A; C) Nyquist plot showing the influence of $R_{gb\parallel}$ in the impedance. The inset show the magnification of the plot corresponding to $R_{gb\parallel}= (R_g+ R_{gb\perp})\times0.1$.

The total resistance of the circuit (R_T) can be obtained using the following equation:

$$R_T = \frac{(R_g + R_{gb\perp})R_{gbll}}{R_g + R_{gb\perp} + R_{gbll}} \qquad (2.19)$$

Figure 2.7 C illustrates the influence of the parallel branch on the total impedance. When the transport occurs preferentially along the parallel interfaces, the overall amplitude of the semicircles decreases, which the biggest changes observed in the low frequency range. A similar behavior is expected for the nanoionic composites studied in this Thesis, where proton the charge transport should be determined essentially by conducting interfaces.

One additional feature observed in the Nyquist plots of real systems is that the impedance semicircles are usually significantly depressed due to the non-homogeneity in the system caused

by, for example, roughness and porosity of surface. In this case it is useful to replace the capacitor by a constant phase element (CPE) (Fig. 2.8).

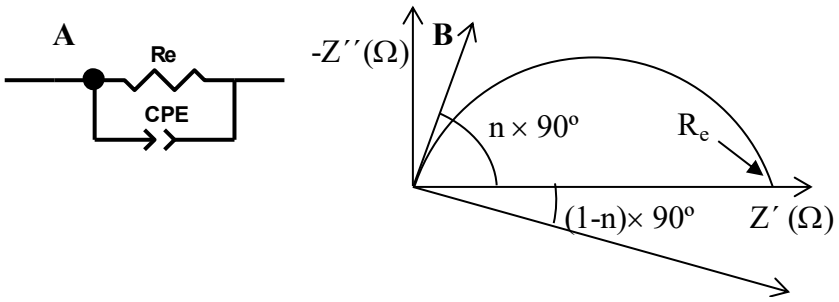

Figure 2.8 A) Resistor and CPE in parallel (R||CPE); B) Nyquist plot of a R||CPE.

The impedance of CPE is given by Eq. 2.20:

$$Z_{CPE}(\varpi) = \frac{1}{Y_0 (i\varpi)^n} \tag{2.20}$$

where Y_0 is the admittance and n is the CPE exponent that characterizes the phase shift ($n = 1\text{-}2\theta_i/\pi$; θ_i corresponds to depressed angle). The relaxation frequency (ϖ_0) can be related to n and Y_0 by the Eq. 2.21:

$$\varpi_0 = (R_e Y_0)^{1/n} \tag{2.21}$$

considering the Eq. 2.18, it is possible to obtain the true capacitance using Eq. 2.22:

$$C = R_e^{1-n/n} Y_0^{1/n} \tag{2.22}$$

The total impedance of the equivalent circuit composed by R||CPE is given by Eq. 2.23:

$$Z(\omega) = \frac{R_e}{1 + \left(\frac{i\varpi}{\varpi_0}\right)^n} \tag{2.23}$$

The center of the depressed semicircle is located at (1–n)×90° below the real axis.

Figure 2.9 depicts the experimental apparatus used for the EIS measurements. It consists of a closed chamber surrounded by a heating cartridge controlled by a proportional-integral-derivative (PID) controller (Eurotherm 3216). One stainless steel vessel mounted on a rack, filled with silica gel particles (3-6 mm with cobalt chloride indicator, Panreac) and a gas flow controller are the other components of the system.

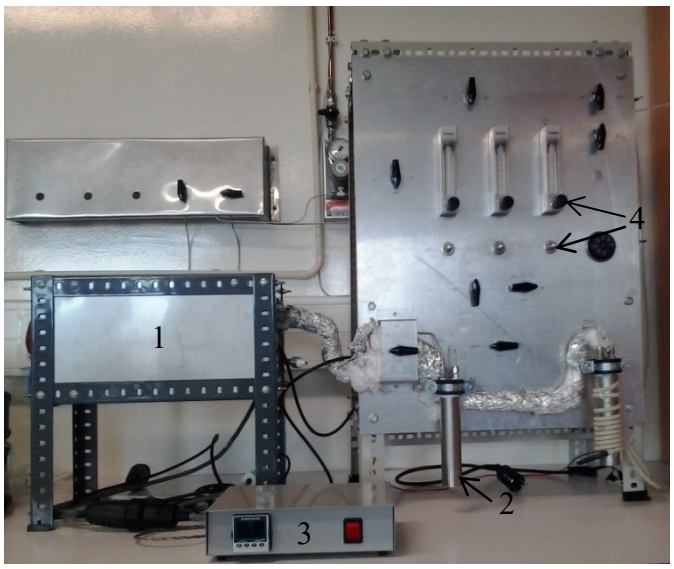

1- Climatic chamber
2- Vessel with silica
3- PID temperature controller
4- Gas flow controllers

Figure 2.9 Apparatus for EIS measurements used in this work.

The measurements were performed in air or N_2 under dry conditions (0% relative humidity within the senor detection limits). To obtain dry conditions, the atmospheric air stream, generated by an electric pump and controlled by a gas flow controller (8 $L.h^{-1}$), was driven through the steel vessel with silica gel before entering in the climatic chamber. The flow rate was kept during 15 h at 40 ºC. Afterwards, the air flow was replaced by N_2 from line (8 $L.h^{-1}$) and left for more 30 min at 40 ºC to fill the chamber (when the measurements were performed in dry air, this step was not necessary). Finally, the flow rate was decreased to 4 $L.h^{-1}$. Both the temperature and the relative humidity were constantly monitored near the sample using a Rotronic HC2-IC102 probe (equipped with a Pt100 resistance thermometer and a Hygromer®IN1 capacitive humidity sensor).

The disk-shaped samples were covered in both sides with silver paste (Agar Scientific) electrodes, which were annealed at 60 °C overnight. The sample holder used for measurements (Fig. 2.10) consists of an alumina tube with 4 platinum wires enabling the measurement of three pellets simultaneously. The pellets were placed on top of a platinum foil serving as a common bottom electrode, and each connected on top to separate platinum. Each pellet could be measured independently by changing the external connections to the meter, using a pseudo 4-electrode configuration. The meters were either a VersaSTAT 4 - Princeton Applied Research or an

AUTOLAB PGSTAT 20 potentiostats equipped with frequency response analyzer (FRA) modules for impedance measurements.

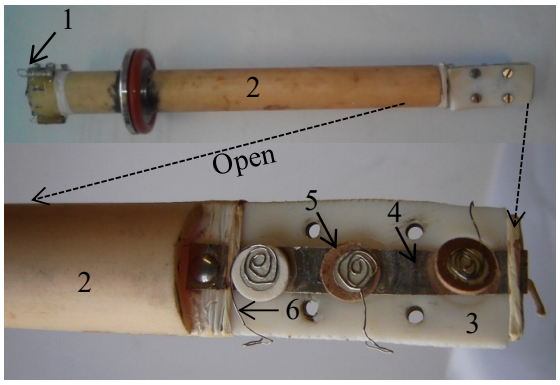

1- Local to connected the electrode
2- Alumina tube
3- Teflon support
4- Platinum tape
5- Pellet
6- Platinum wire

Figure 2.10 Sample holder used in this work.

The spectra were collected between 40 ºC and 110 ºC for Tz composites, and 40 ºC and 160 ºC for Bz-based materials, always below the melting point of these electrolytes. The test signal amplitude was varied in the range from 100 to 500 mV.

The conductivity of the samples was estimated from the impedance spectra using the amplitude of semicircle present in Nyquist plot or as the addition of the amplitudes of the semicircles, through the Eq. 2.24 collected in dry air or N_2 using the software ZView version 3 (Scribner Associates):

$$\sigma = \frac{l}{R_e A} \tag{2.24}$$

where, R_e is the resistance given by the amplitude of semicircle in the EIS spectra (or by addition of the amplitudes of semicircles when more than one semicircle was present). l is the thickness of samples and A is the surface area of the electrodes.

3

Synthesis and characterization of oxide dopants

This chapter is divided in three sections. The first describes the preparation and characterization of the hard templates SBA-15 and CMK-3. The second and most important section describes the preparation of various mesoporous oxides by nanocasting. The third reports an attempt to obtain $BaCeO_3$ by soft-templating. The characterization of materials was based on a battery of methods such as XRD, FTIR-ATR, TEM, SEM, and N_2 physisorption isotherms used to assess composition, structure and microstructure. These were complemented with TG analysis and thermodynamic predictions in order to gain insight on the thermochemical compatibility between the oxide and the template material.

3.1 Mesoporous templates

Two hard templates were used: SBA-15 and CMK-3. The CMK-3 was prepared using SBA-15 as hard template.

The XRD patterns of SBA-15 and CMK-3 (Fig. 3.1) confirm the *p6mm* hexagonal structure of both hard templates.[141, 199] The three peaks can be indexed to the (100), (110) and (200) reflections of the *p6mm* hexagonal structure.

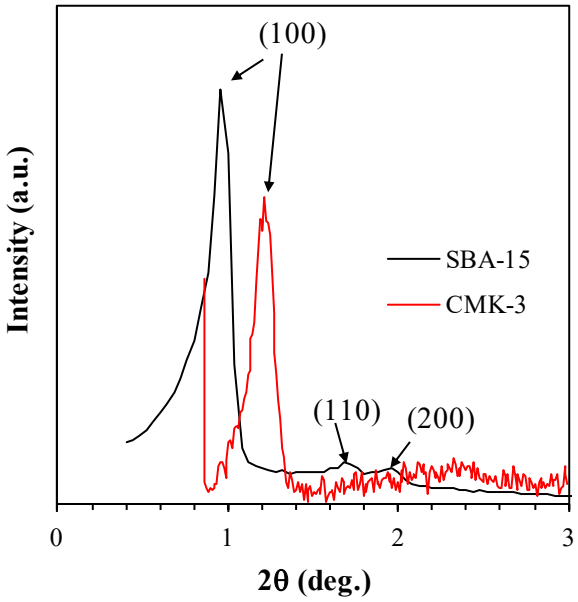

Figure 3.1 Low angle XRD patterns of SBA-15 and CMK-3. The peaks are indexed to the *p6mm* hexagonal space group. The red line corresponds to CMK-3 and the black line corresponds to SBA-15.

The corresponding interplanar distances (d_{100} = 92 and 72 Å for SBA-15 and CMK-3, respectively) and lattice parameters (a =106 and 83 Å for SBA-15 and CMK-3, respectively) are presented in Table 3.1, showing good agreement with literature (see Table 1.3).

Figures 3.2 A and B show the TEM micrographs of the SBA-15 and CMK-3, respectively, depicting the expected ordered porosity. CMK-3 corresponds to a negative replica of SBA-15. The expected hexagonal pore order is confirmed by the insets showing micrographs taken along the direction parallel to the channels, with the obtained d_{100} values in good agreement with those obtained by XRD (see Table 3.1 below).

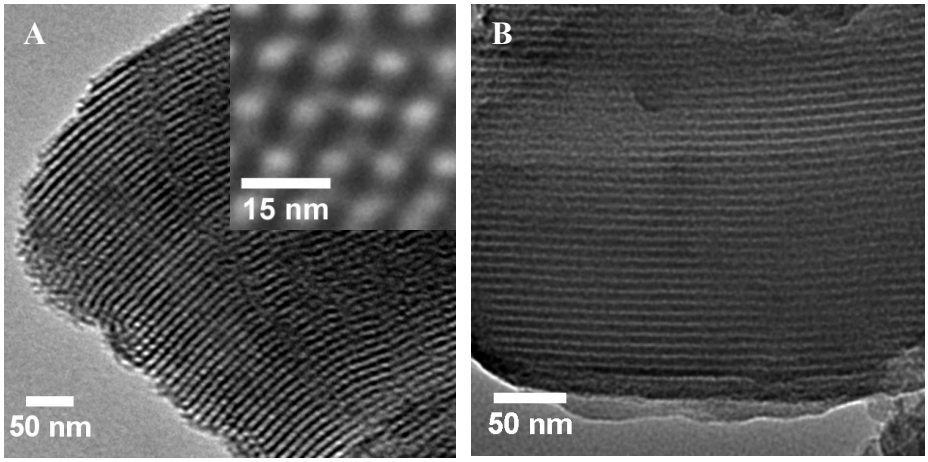

Figure 3.2 TEM micrographs of A) SBA-15 and B) CMK-3 viewed down the 100 zone axis. The inset in A) depicts the hexagonal structure of the pores viewed along [001].

The N_2 physisorption isotherms of the SBA-15 and CMK-3 shown in Fig. 3.3 A are of type IV (according to the IUPAC classification [219]), usually observed for conventional mesoporous materials, indicating mesopores of uniform size with narrow PSD (Fig. 3.3 B).

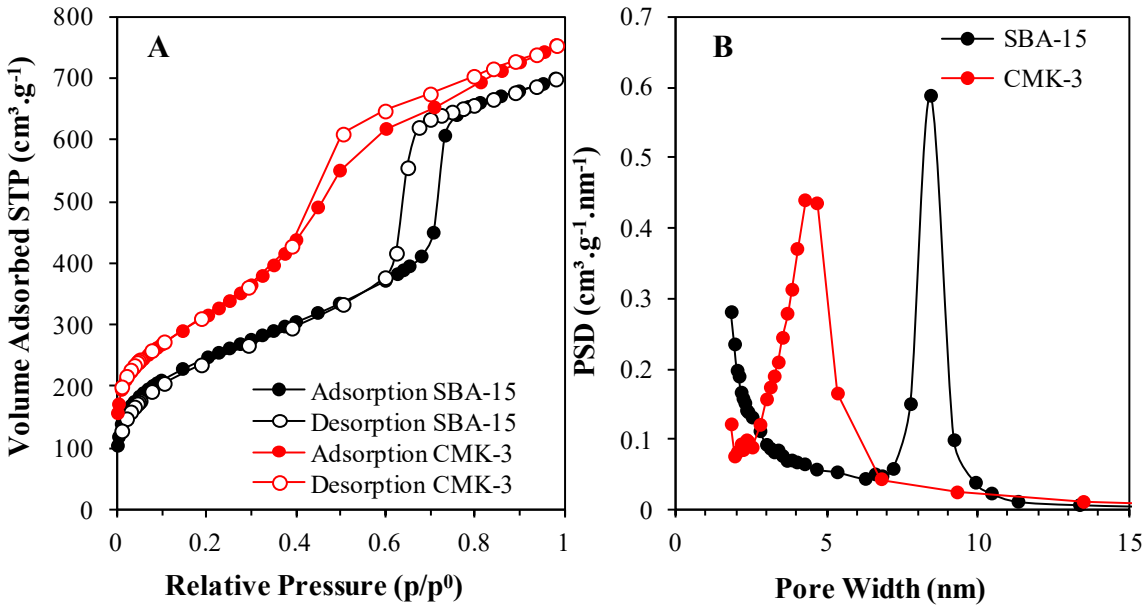

Figure 3.3 Typical N_2 physisorption isotherms (A) and PSD (B) for SBA-15 and CMK-3 materials used in this Thesis.

The sharp increase in adsorption at relative pressure between around 0.5 and 0.7, respectively for CMK-3 and SBA-15, can be attributed to capillary condensation in the mesoporous. The PSD (Fig.

3.3 B) shows a narrow peak d_p about 8.5 nm and 4.3 nm for SBA-15 and CMK-3, respectively, which are in agreement with literature (see Table 1.3).[128, 152]

Table 3.1 lists typical textural properties of the SBA-15 and CMK-3 hard templates. Contrary to TEM, the data obtained from the N_2 physorption studies (S_{BET} and V_p) tend to show some dispersion from batch to batch. Nevertheless, the results are in good agreement with the intervals found in literature data (see Table 1.3).

Table 3.1 Typical textural properties of templates SBA-15 and CMK-3

Sample	d_{100} [a] (Å)	a [b] (Å)	d_{100} [c] (Å)	a [c] (Å)	d_p [d] (nm)	V_p ($cm^3.g^{-1}$)	S_{BET} ($m^2.g^{-1}$)
SBA-15	92	106	~90	~ 100	6.8-9.3	1.16-1.65	829-1205
CMK-3	72	83	~ 69	----	4.3-4.7	1.03-1.33	904-1108

[a] Calculated by XRD using Bragg's Law; [b] considering hexagonal arrangement of pores ($a = 2d_{100}/\sqrt{3}$); [c] calculated by TEM; [d] considering the maximum of PSD distribution.

3.2 Mesoporous oxides using hard templates

Table 3.2 compiles the textural properties of the materials synthesized in this work using nanocasting using the procedure presented in Chapter 2. Note that in some experiments the d_{parXRD} is higher than d_{par} obtained with other techniques. This result can be attributed to the instrumental effects [209] and to low definition of the peaks.

Table 3.2 Summary of the structural and textural properties of mesoporous oxides prepared using nanocasting.

Acronym	Crystal system (cell parameters Å)	Type of porosity	ρ_{oxide} [a] ($g.cm^{-3}$)	d_{parXRD} [b] (nm)	d_{parTEM} [c] (nm)	d_{parBET} [d] (nm)	d_p (nm)	V_p ($cm^3.g^{-1}$)	S_{BET} ($m^2.g^{-1}$)
ms-CO(SBA)	Cubic (a= 5.4122)	2D hexagonal order	7.24	7.6	~ 9	5.6	3.4-3.7	0.23	149
ms-*m,t*ZO(SBA)	Monoclinic (55.3 vol. %) (a= 5.1176, b= 5.1725, c= 5.304; β =99.2°)	3D wormlike disordered	5.93	15.5	~ 5	----	4.0-4.7	0.32	194
	Tetragonal (44.7 vol. %) (a=b= 3.5896, c= 5.1528)		6.19	6.1					
ms-*t*ZO(CMK)	Tetragonal (a=b= 3.5971, c= 5.1742)	3D wormlike disordered and 2D hexagonal order	6.14	6.9	~ 5 and ~ 12	4.4	4.7-6.8	0.48	220
ms-*a*TO(SBA)	Tetragonal (anatase 94.5 vol. %) (a=b= 3.7857, c= 9.5107)	3D wormlike disordered	3.91	14.8	~ 5	----	3.5-3.9	0.36	142
	Tetragonal (rutile 5.5 vol. %) (a=b= 4.5908, c= 2.9617)		4.27	16.0					
ms-*a*TO(CMK)	Tetragonal (anatase) (a=b=3.7849, c= 9.5105)	3D wormlike disordered and 2D hexagonal order	3.91	17.0	10-12 or more	8.0	3.4-6.8	0.50	191
ms-BZO(CMK) [e]	Cubic (a=4.1895)	3D wormlike disordered	6.27	17.8	~ 7	----	2.8-5.4	0.11	41

[a] Calculated using the lattice parameters; [b] crystallite size obtained through the Scherrer equation; [c] d_{par} obtained using TEM micrographs ; [d] considering the spherical shape of the particles; [e] with small amount of t-ZrO_2.

3.2.1 Mesoporous CeO_2

Figure 3.4 shows the XRD patterns of the materials before (ms-CO/SBA) and after template removal (ms-CO(SBA)). All peaks can be perfectly indexed as pure cubic phase of CeO_2 with lattice parameter of 5.4122 Å (space group $Fm\bar{3}m$).

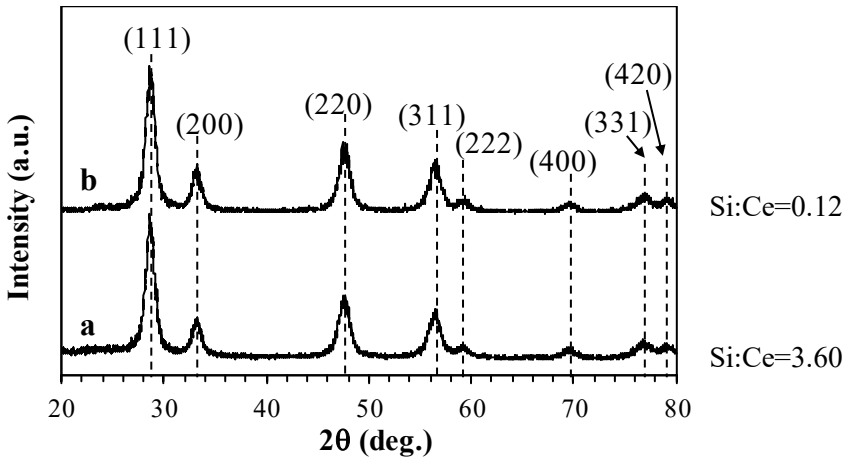

Figure 3.4 XRD patterns of: a) ms-CO/SBA and b) ms-CO(SBA) after two washing steps. The peaks are indexed according to the $Fm\bar{3}m$ cubic space group. The atomic ratios Si:Ce for each material are also provided on the side.

In the mixture ms-CO/SBA, the atomic ratio Si:Ce = 3.60 determined by EDS is in good agreement with the nominal stoichiometry (Si:Ce = 3.37). However, EDS suggests that a trace amount of Si may still be present. In fact, the atomic ratio Si:Ce=0.12 was the lowest obtained in all series of batches, some of them submitted multiple washing cycles. The Si could be just physically retained within the pores or chemically bounded to ceria.

Figure 3.5 displays the FTIR-ATR spectra of the same materials present in Fig. 3.4, including the spectrum of SBA-15 for comparison. The spectra contain only the bands typical for SiO_2 and CeO_2.The bands at 1230 and 1040 cm^{-1} can be assigned to the Si–O–Si asymmetric stretching. The band around 970 cm^{-1} corresponds to the Si–OH stretching. The band at around 806 cm^{-1} can be attributed to the Si–O–Si symmetric stretching. Finally, the band at around 434 cm^{-1} is due to the O–Si–O bending mode. In this zone of the spectrum, the band near 400 cm^{-1} corresponds to the Ce-O stretching mode.[163, 170]

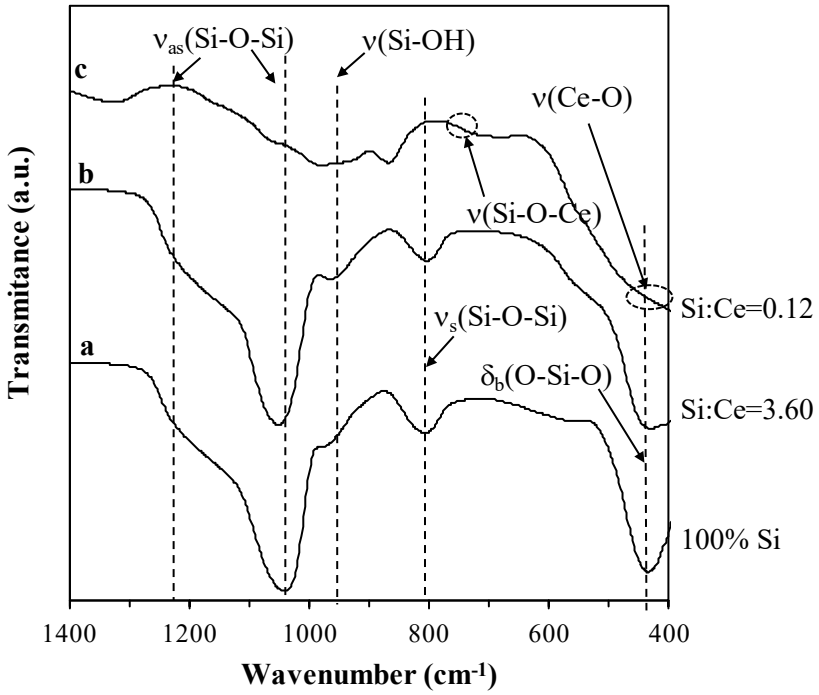

Figure 3.5 FTIR-ATR spectra of: a) SBA-15; b) ms-CO/SBA; and c) ms-CO(SBA). Si:Ce atomic ratios are also shown. The captions for Si-O-Ce in spectrum c shows the expected location of the corresponding band at ~797 cm^{-1}.

The absence of bands corresponding to SiO_2 in the final product (Fig. 3.5 spectrum c) suggests that SiO_2 can be mostly removed by washing twice the sample with NaOH 2 M. The potential chemical interaction via formation of Si-O-Ce cross links is also unlikely, judging by the absence of typical bands around 797 cm^{-1}.[235]

The TEM micrographs of materials (Fig. 3.6) confirm the formation of CeO_2 inside of pores of SBA-15 with cubic crystal structure. The estimated volume contraction of 0.91 calculated using Eq. 1.22, indicates that not all pores of the template could be filled (filled regions correspond to the darker areas in Fig. 3.6 A).The inset of Fig. 3.6 C shows the hexagonal distribution of nanorods with diameter around 9 nm similar to the d_p of SBA-15.

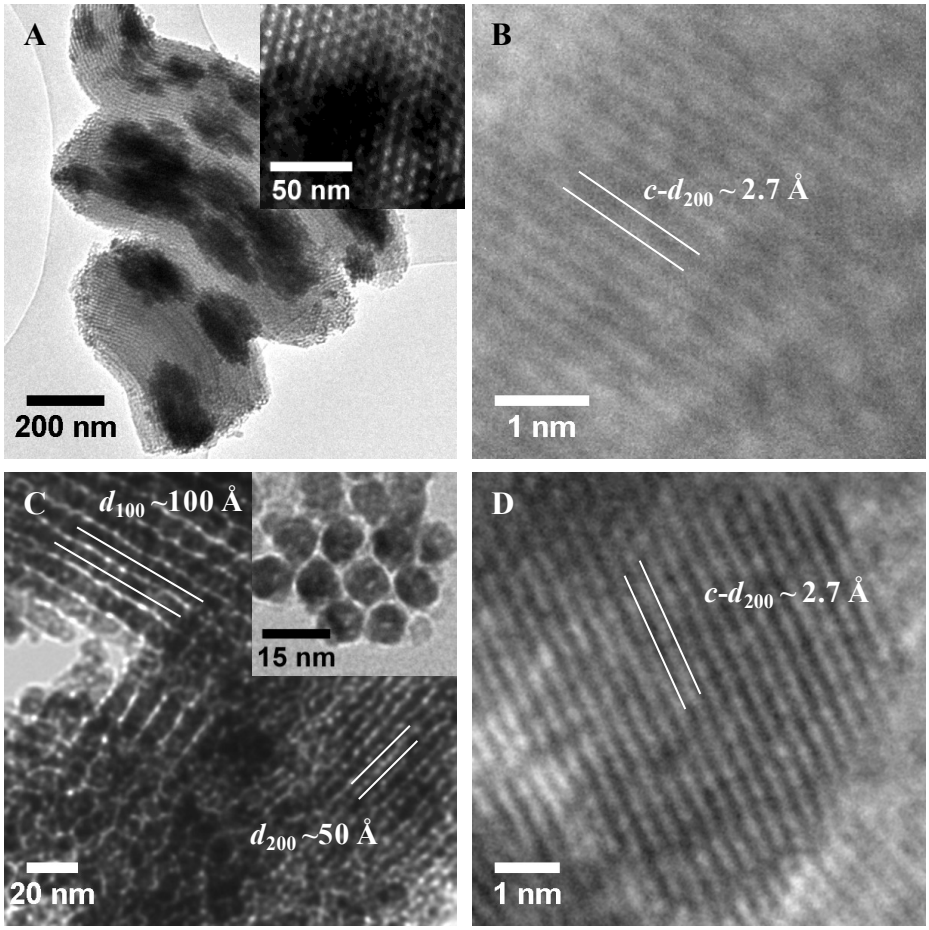

Figure 3.6 TEM and and HRTEM micrographs of: A) and B) ms-CO/SBA; and C) and D) ms-CO(SBA). The hexagonal structure of the template pores and of the ceria nanorods are shown in the insets.

The *d*-spacings in Figs. 3.6 B and D refer to the CeO_2 crystal structure correspond to the (200) plane of the CeO_2 cubic fluorite structure (c-d_{200}~ 2.7 Å**)**. In Fig. 3.4 C the *d*-spacings can be indexed to the (100) and (200) reflection of the *p6mm* hexagonal structure of the rods (d_{100}~ 100 Å and d_{200}~ 50 Å, respectively).

The N_2 physisorption isotherms obtained for the ms-CO(SBA) material show the typical type IV isotherm (Fig. 3.7 A) and a narrow PSD (Fig. 3.7 B).

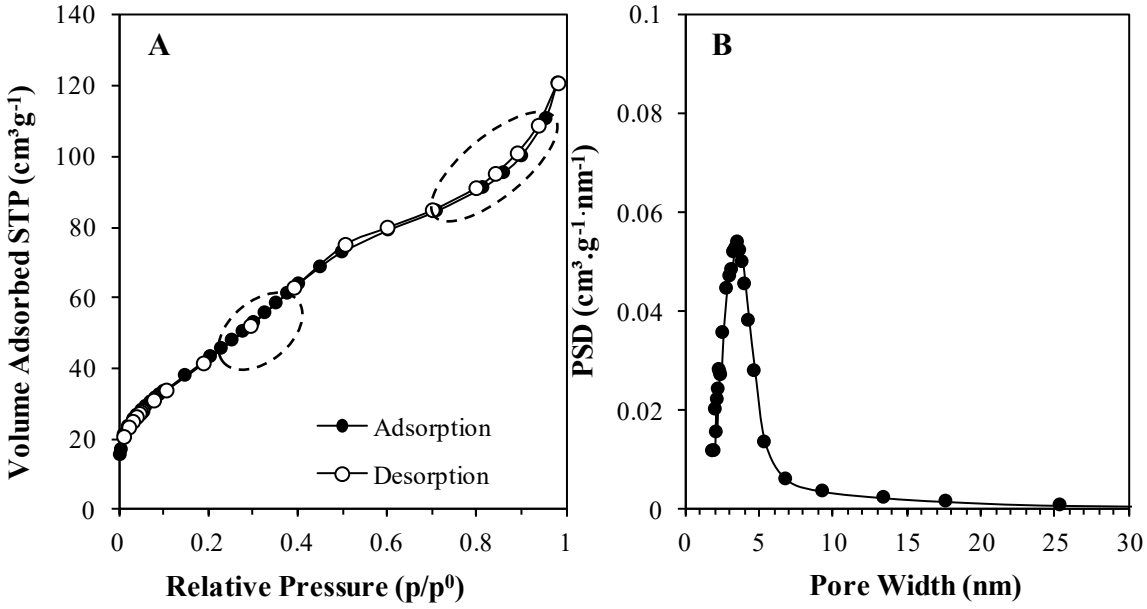

Figure 3.7 A) N_2 physisorption isotherms for CeO_2 and B) corresponding PSD.

The sudden increase in the adsorption for p/p0 > 0.7 is not due to structural mesoporosity, but is most likely related with condensation of nitrogen in the interstitial space between particles. The PSD data (Fig. 3.7 B) suggests d_p to be in the range 3.4-3.7 nm without evidence for the interparticle porosity. The specific surface area calculated from the adsorption branch of the isotherm is 149 $m^2.g^{-1}$ with a pore volume of 0.23 $cm^3.g^{-1}$.

3.2.2 Mesoporous ZrO_2

Contrary to CeO_2, the chemical reaction between zirconia and silica is indeed predicted, as shown by the Gibbs free energy calculations displayed in (Fig. 3.8). The Gibbs free energy for the formation of $ZrSiO_4$ from ZrO_2 and SiO_2 is negative for temperatures as high as 900°C, well above the firing temperature used in this work to precipitate the ZrO_2 which is 600 °C (further details in section 2.2.3). The thermodynamic calculations also suggest a more favorable reaction of $ZrCl_4$ with SiO_2 than the competing process of the formation of ZrO_2.

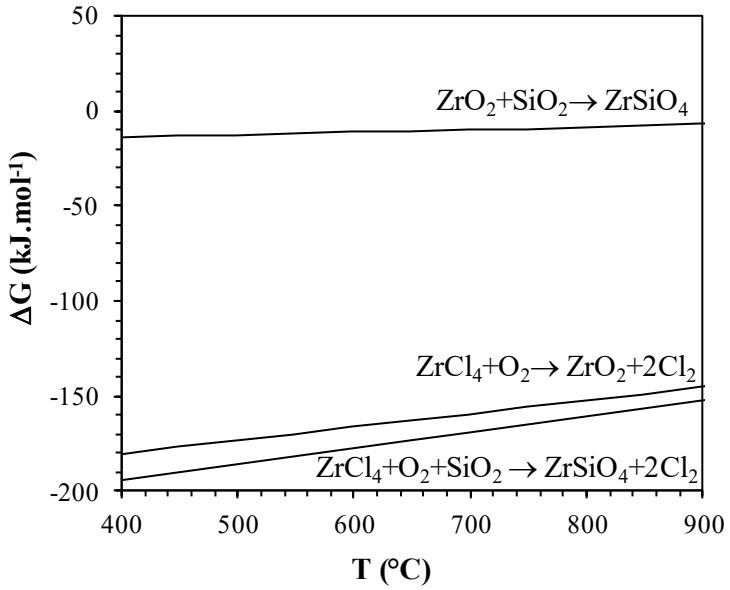

Figure 3.8 Thermodynamic predictions of the Gibbs free energy for several reactions involving the SBA-15 and the ZrO_2 product or the zirconium precursor.

Therefore, two types of mesoporous ZrO_2 were prepared using SBA-15 (ms-*m,t*ZO(SBA)) and CMK-3 (ms-*t*ZO(CMK)) as templates following the procedures described in Chapter 2. Figure 3.9 shows the XRD patterns of these two ZrO_2 samples collected along the various synthetic steps.

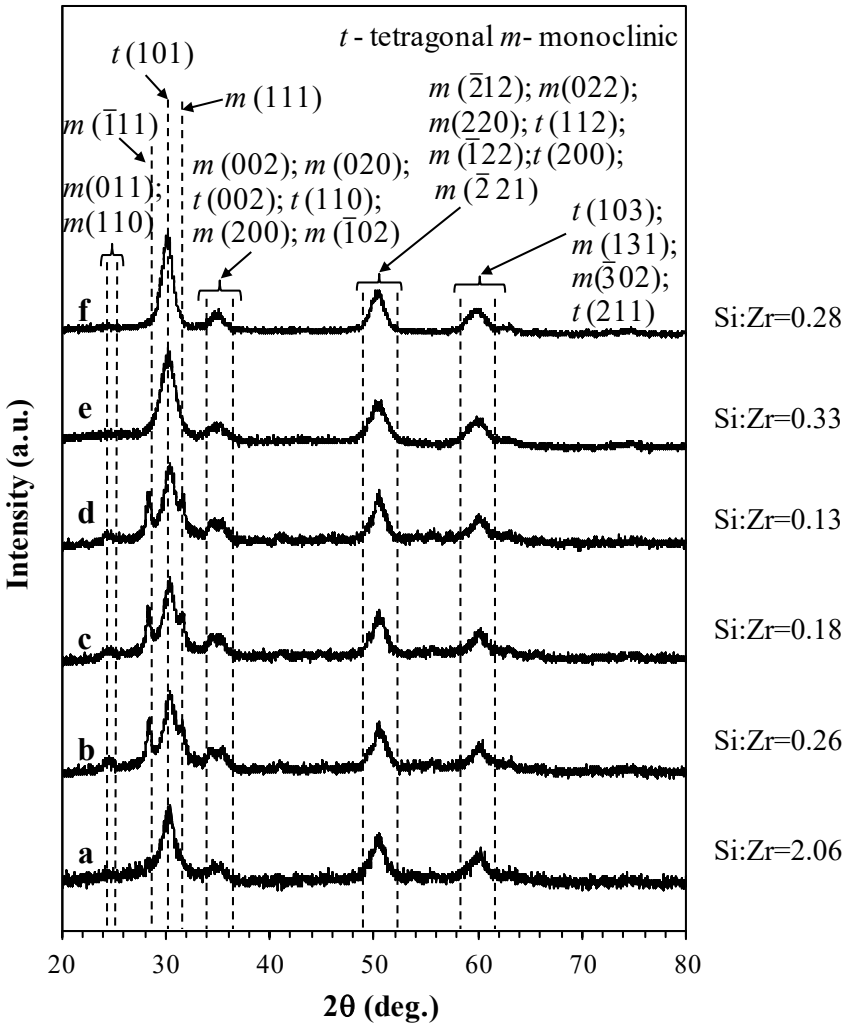

Figure 3.9 XRD patterns of: a) ms-*t*ZO/SBA; b-d) ms-*m,t*ZO(SBA) after washing 1, 2 and 3 times, respectively; e) ms-*t*ZO/CMK and f) ms-*t*ZO(CMK). The peaks are indexed according to the $P4_2/nmc$ and $P2_1/c$ space groups of the tetragonal and monoclinic zirconia polymorphs, respectively. The Si:Zr atomic ratios determined by EDS are also displayed.

The patterns of both initial oxide-template mixtures (patterns a and e) show only the reflections of tetragonal zirconia. This phase is mostly retained after washing, with the patterns indexed onto the space group $P4_2/nmc$ yielding lattice parameters $a=b=3.5896$ and $c=5.1528$ Å and $a=b=3.5971$ and $c=5.1742$ Å for ms-*m,t*ZO(SBA) and ms-*t*ZO(CMK), respectively. However, the pattern of the zirconia prepared with the SBA-15 template (patterns b-d) also include peaks of monoclinic zirconia, which can be indexed on the $P2_1/c$ space group with lattice parameters a= 5.1176, b= 5.1725, c= 5.304Å and with β=99.2°. A simple refinement of these patterns using POWDER CELL® yields a mixture of 55.3 vol.% monoclinic and 44.7 vol.% tetragonal phases.

One possible explanation for this difference could be the chemical interaction between the SiO_2 template and zirconium species. Indeed, the persistence of Si is confirmed by EDS, even after three washing cycles.

The atomic ratio Si:Zr = 2.06, determined by EDS, for mesoporous ZrO_2 before SBA-15 removal (ms- *t*ZO/SBA) mixture is in a good agreement with the initial stoichiometry (1.90). After the first washing treatment, the ratio decreases to Si:Zr = 0.26, subsequent washing lead to value close to Si:Zr = 0.13. Following the evolution of the XRD patterns a through d and the corresponding Si:Zr ratio shown in Fig. 3.9, one clearly observes (particularly after the first washing) the decreasing fraction of tetragonal ZrO_2 with decreasing Si content which suggests that Si is playing a key role in stabilizing the tetragonal polymorph.

In ms-*t*ZO/CMK and ms-*t*ZO/(CMK) materials, the Si:Zr atomic ratio is similar before and after removal of the CMK-3 (0.33 and 0.28, respectively) (Fig. 3.9 patterns e and f). In fact, the starting CMK-3 contained SiO_2 that could not be totally washed out. FTIR-ATR spectra were also collected at the various stages of the synthesis in order to find any evidence for the presence of non-crystalline phase, in particular one indicating possible chemical interaction between Si and Zr (and O) atoms that could possibly explain the persistent Si in the final mesoporous ZrO_2 products.

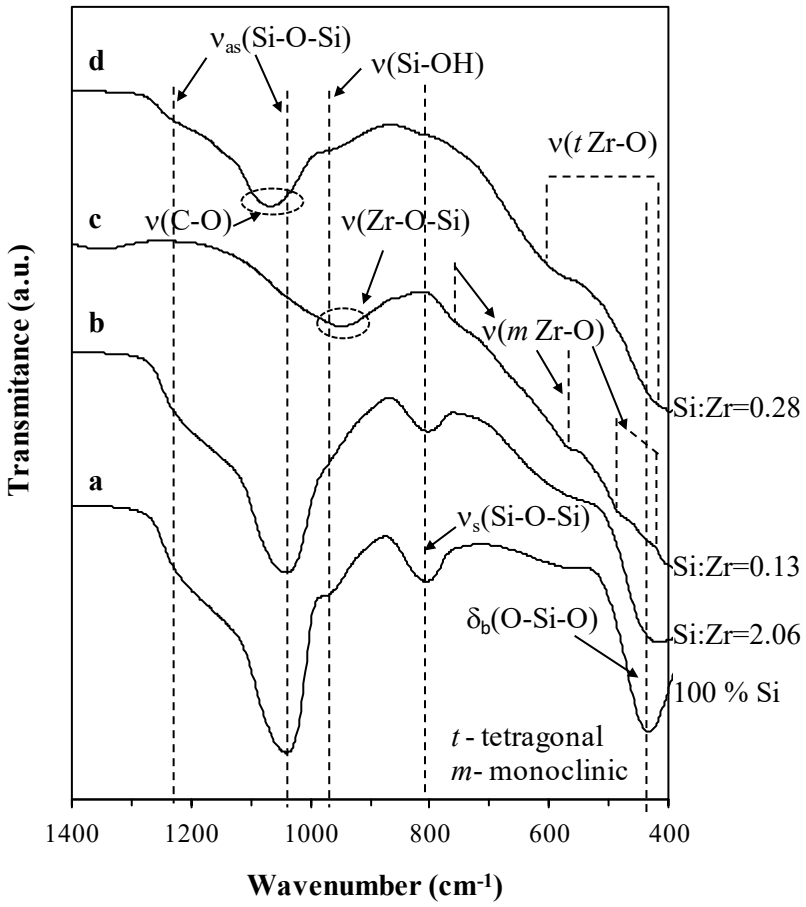

Figure 3.10 FTIR-ATR spectra of a) SBA-15; b) ms-*t*ZO/SBA; c) ms-*m,t*ZO(SBA); and d) ms-*t*ZO(CMK). The Si:Zr atomic ratios determined by EDS are also shown.

The FTIR-ATR spectrum of the ms-*t*ZO/SBA mixture (Fig. 3.10 spectrum b) is dominated by the SiO_2 bands (described in last section) which disappear in the nominally pure ms-*m,t*ZO(SBA) product. The characteristic stretching vibrations of monoclinic ZrO_2 are displayed in the spectrum at 744, 570, 486 and 390 cm^{-1} (Fig. 3.10 spectrum c). The peaks corresponding to the tetragonal phase, namely the shoulder around 600 cm^{-1} and the broad band around 400 cm^{-1}, are not evident. It is possible that they are overlapped with the peaks assigned to the monoclinic phase.

However, the most relevant feature of spectrum c is the fairly broad band centered at *ca*. 950 cm^{-1}, which can be due to the stretching vibration of the Zr-O-Si cross link.[170, 236-238] While no direct evidence for the formation of compounds, such as zirconium silicate (which is show ahead is thermodynamically favorable), could be found by XRD, the FTIR-ATR data strongly suggests the existence of a chemical bonds between Zr and Si.

In the case of ms-*t*ZO(CMK), FTIR-ATR shows stretching vibration bands corresponding to tetragonal ZrO_2, and one distinctive band centered at about 1066 cm^{-1}, which is associated to the stretching vibration of C–O bonds,[237-239] this indicating the partial oxydation of carbon after

firing in oxygen at 400 °C. The band at 950 cm^{-1} ascribed to the Zr-O-Si cross links in ms-*t*ZO/(SBA) is less clear in the case of ms-*t*ZO/(CMK), maybe due to the fact that the silicon was covered by the carbon thus preventing the reaction between the SiO_2 and zirconium metal precursor. The role of carbon on the stabilization of the tetragonal/cubic phase of ZrO_2 is not clear. Fig. 3.11 shows TEM and HRTEM micrographs of the ZrO_2 before and after removal of the SBA-15 template.

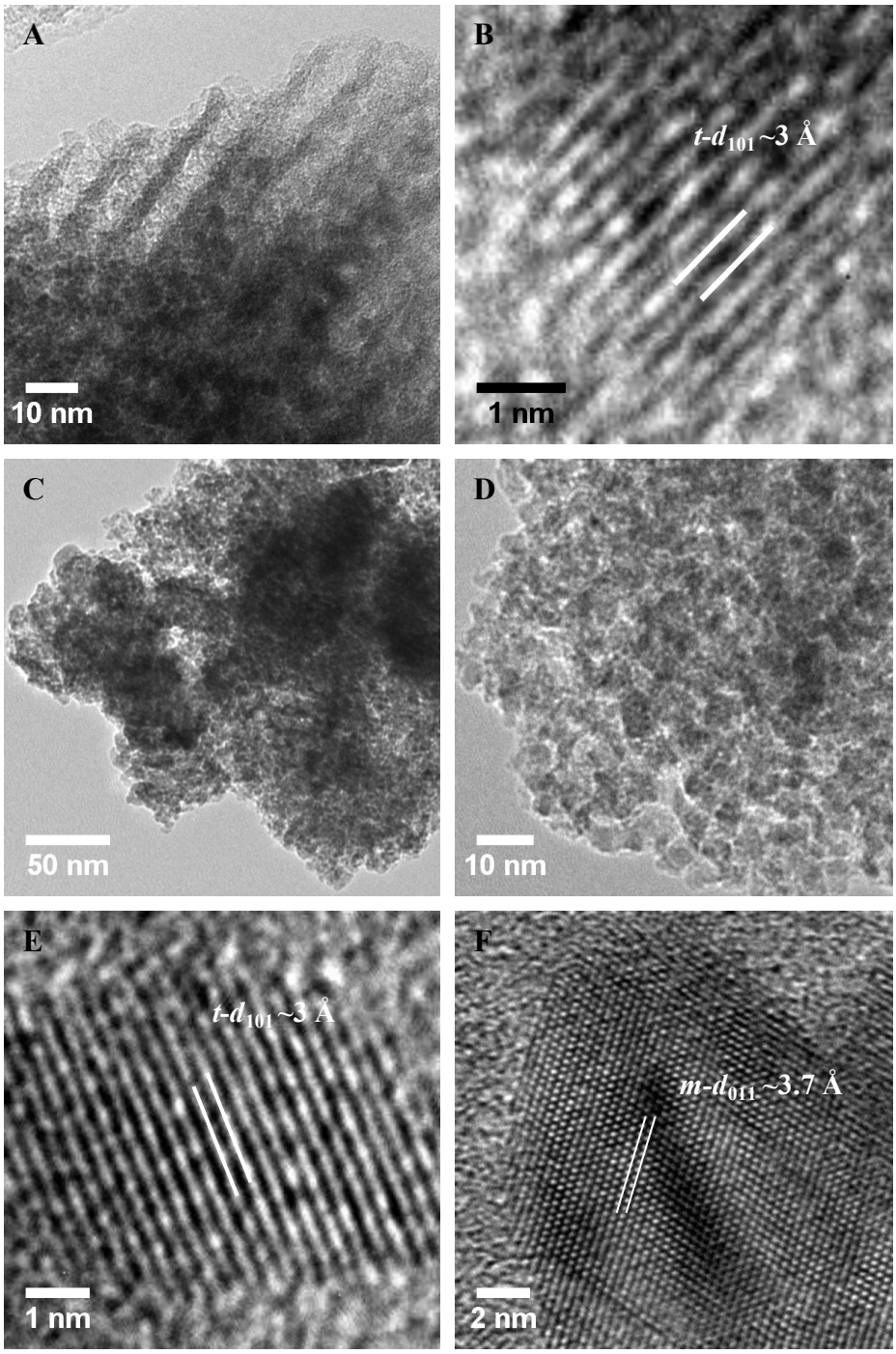

Figure 3.11 TEM and HRTEM micrographs of A), B) ms-*t*ZO/SBA and C-F) ms-*m*,*t*ZO(SBA).

The micrographs for ms-*t*ZO/SBA reveal the oxide within the pores of the SBA-15 (Figs. 3.11 A and B). High resolution TEM indicates that the ZrO_2 in the pores has predominantly the tetragonal (or cubic phase), in full agreement with the XRD data (Fig. 3.9 pattern a). The removal of the SBA-15 (Figs. 3.11 C and D) leads to a disordered mesoporous ZrO_2 probably due to cleavage of Si-O-Zr bonds. The ZrO_2 nanoparticles have a diameter in the order of 5 nm or smaller (Fig. 3.11 D), and correspond to a mixture of tetragonal (Fig. 3.11 E) and monoclinic (Fig. 3.11 F) phases. Apparently, the monoclinic nanoparticles are somewhat larger and exhibit a higher degree of crystallinity compared to the tetragonal crystallites, which are rather disordered. The phase mixture is also confirmed by XRD analyses (Fig. 3.9 pattern d). While the monoclinic phase would be the expected phase at room temperature for pure ZrO2, the extremely small particle size (5 nm) can contribute to metastabilize the tetragonal phase at room temperature.[170, 240]

The *d*-spacings in Figs. 3.11 B and E refer to the ZrO_2 crystal structure can be indexed to the (101) plane of the pure tetragonal structure for ZrO_2 (d_{101}~ 3 Å**)**, whereas in Fig. 3.11 F the measured *d*-spacing can be assigned to the d_{001}~ 3.7 Å of the monoclinic phase.

Figure 3.12 shows TEM micrographs of the ZrO_2 prepared with the CMK-3 template after burning out the carbon.

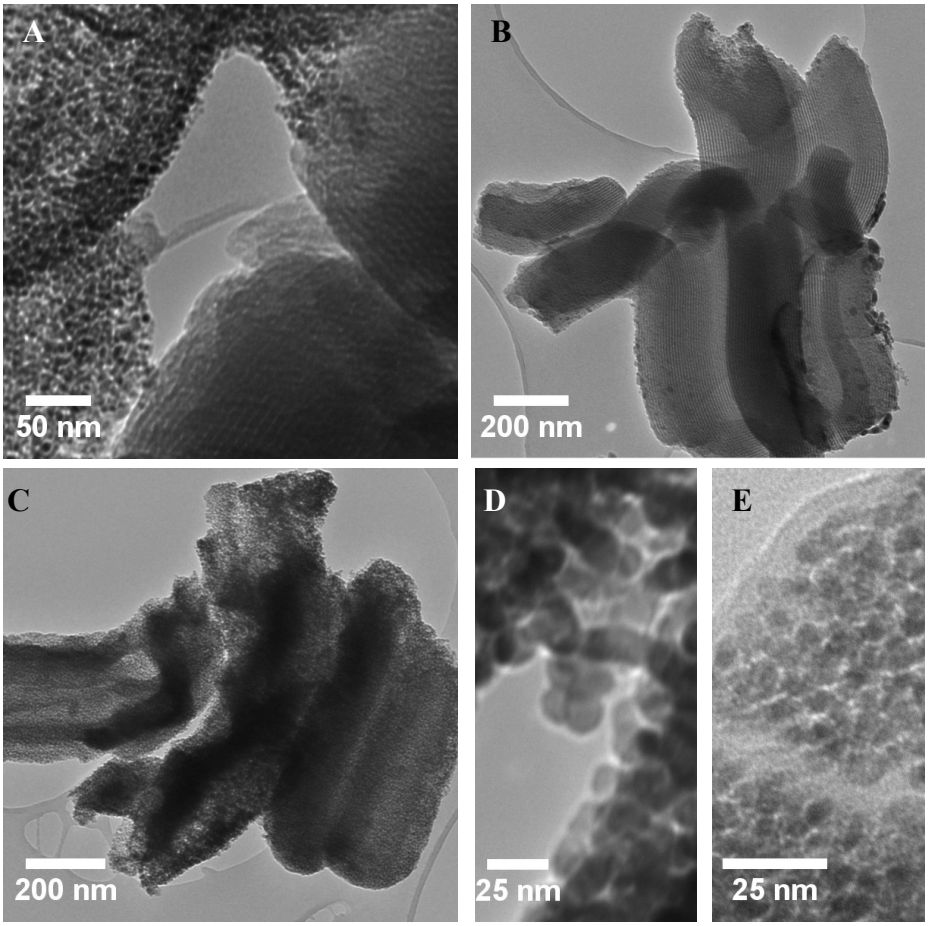

Figure 3.12 TEM micrographs of the ms-*t*ZO(CMK) taken at different magnifications.

The sample ms-*t*ZO(CMK) was less homogeneous than ms-*m,t*ZO(SBA), showing ordered areas with morphology similar to the CMK-3 and/or SBA-15 (Fig. 3.12 B), and more disordered regions such as in the center of Fig. 3.12 C. In case of disordered particles, there are two types, some are clearly larger with approximately 12 nm in diameter (Fig. 3.12 D) and others with diameters around 5 nm (Fig. 3.12 E). The high value corresponds to almost 3 times the d_p of the template (Table 3.1), suggesting that the microrods in the ordered CMK-3 mesostructure were broken allowing grain growth to occur. The presences of particles with lower diameter suggest that they are formed in the pores of the CMK-3.

Figure 3.13 presents the N_2 physisorption isotherms and corresponding PSD for materials obtained using both templates. Both are type IV typical of mesoporous materials.

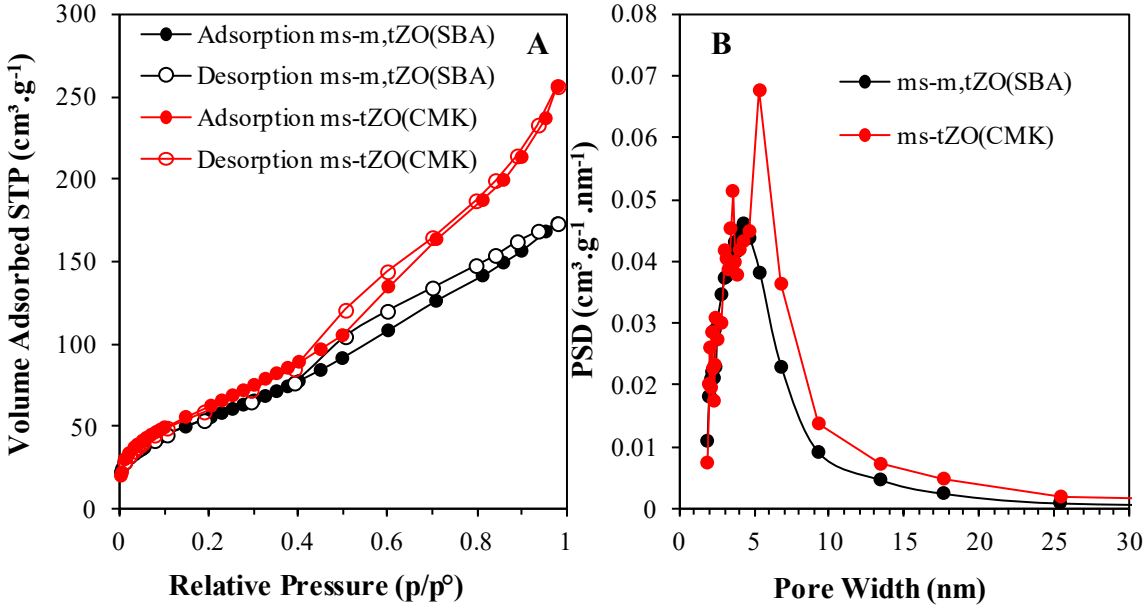

Figure 3.13 A) N_2 physisorption isotherms for ZrO_2 prepared using both templates and B) corresponding PSD.

The S_{BET} and V_p values for ms-*m,t*ZO(SBA) are 194 $m^2.g^{-1}$ and 0.32 $cm^3.g^{-1}$, respectively, whereas the corresponding PSD (Fig. 3.13 B) points to a d_p value between 4.0 and 4.7 nm, without evidence for the interparticle porosity. The PSD data (Fig. 3.13 B) suggests d_p to be in the range 4.7-6.8 nm, with S_{BET}=220 $m^2.g^{-1}$ and V_p= 0.48 $cm^3.g^{-1}$ for ms-*t*ZO(CMK). For ms-*t*ZO(CMK), the d_{parBET} is similar to the d_{parTEM} of the smaller particles with around 5 nm.

3.2.3 Mesoporous TiO_2

Although it has not been possible, so far, to thermodynamically predict the formation of titanium silicates (no data on titanium silicates available in FactSage 6.1), the relative proximity of the physico-chemical properties of TiO_2 and ZrO_2 would suggest the occurrence of such reaction. Therefore, the approach adopted to obtain mesoporous TiO_2 was similar to that used for ZrO_2 by testing the effect of the template composition. Figure 3.14 shows the XRD patterns of materials obtained using SBA-15 and CMK-3. All peaks of the materials before and after template removal can be indexed as the tetragonal anatase phase of TiO_2 with lattice parameters a=b= 3.7857 or 3.7849 Å and c= 9.5107 or 9.5105 Å ($I4_1/amd$ space group) for TiO_2 obtained from the SBA-15 or CMK-3, respectively. Additionally when the SBA-15 was used as template, the XRD patterns show the peaks characteristic of the tetragonal rutile phase of TiO_2 (about 5.5 vol.%), which can be indexed to $P4_2/mnm$ space group with lattice parameters a=b= 4.5908 and c=2.9617 Å.

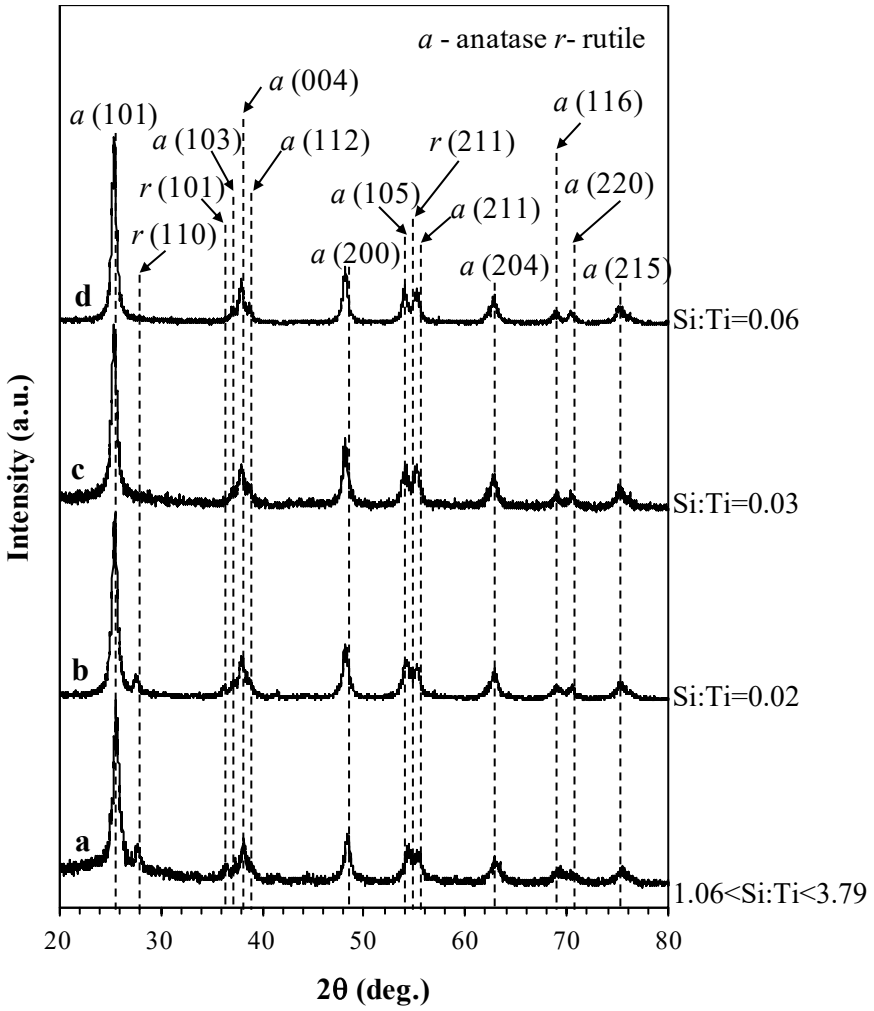

Figure 3.14 XRD patterns of a) ms-*a*TO/SBA, b) ms-*a*TO(SBA), c) ms-*a*TO/CMK and d) ms-*a*TO(CMK). The peaks are indexed according to the $I4_1/amd$ and $P4_2/mnm$ space groups of the tetragonal anatase and rutile, respectively The Si:Ti atomic ratio determined by EDS are also shown.

The Si:Ti atomic ratio determined by EDS on various regions of the sample varies between 1.06 and 3.79, which indicates a somewhat variable degree of impregnation of the template material. However, when the template was removed, the presence of Si is residual (Si:Ti= 0.02) and similar all over the sample, thus confirming the efficiency of the washing with NaOH 2 M.

As observed for ms-*t*ZO(CMK), ms-*a*TO(CMK) shows a residual quantity of Si (Si:Ti= 0.06) resulting from the SBA-15 template used to prepare the CMK-3.

The FTIR-ATR analysis of these powders was also carried out, with the results presented in Fig. 3.15.

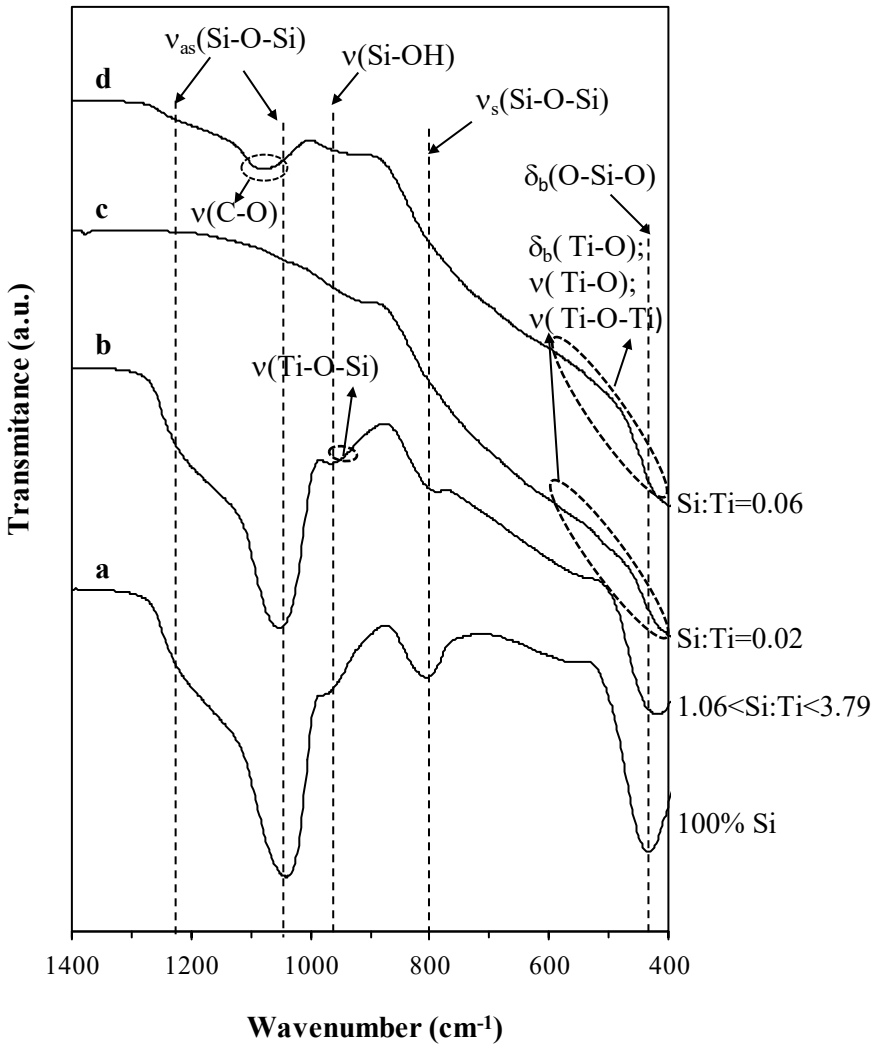

Figure 3.15 FTIR-ATR spectra of: a) SBA-15; b) ms-*a*TO/SBA; c) ms-*a*TO(SBA); and d) ms-*a*TO(CMK).

The bands observed in the TiO_2 materials are analogous to those in ZrO_2 (Fig. 3.10). The spectrum of ms-*a*TO/SBA mixture (Fig. 3.15 spectrum b) is dominated by the SiO_2 bands, while in the ms-*a*TO(SBA) the distinctive feature is the strong band below 700 cm^{-1} corresponding to various vibrations modes of TiO_2.[241-246] One may argue about the presence of one band around 900-970 cm^{-1} due to the stretching vibration of Si-O-Ti linkages, but the intensity is extremely low for ms-*a*TO(SBA) and hardly discernible for ms-*a*TO(CMK). Although the potential chemical interaction between Ti and Si cannot be totally ruled out, its evidence is considerably weaker than for the zirconia–based materials.

Figure 3.16 presents TEM micrographs of TiO_2 products with and without the templates.

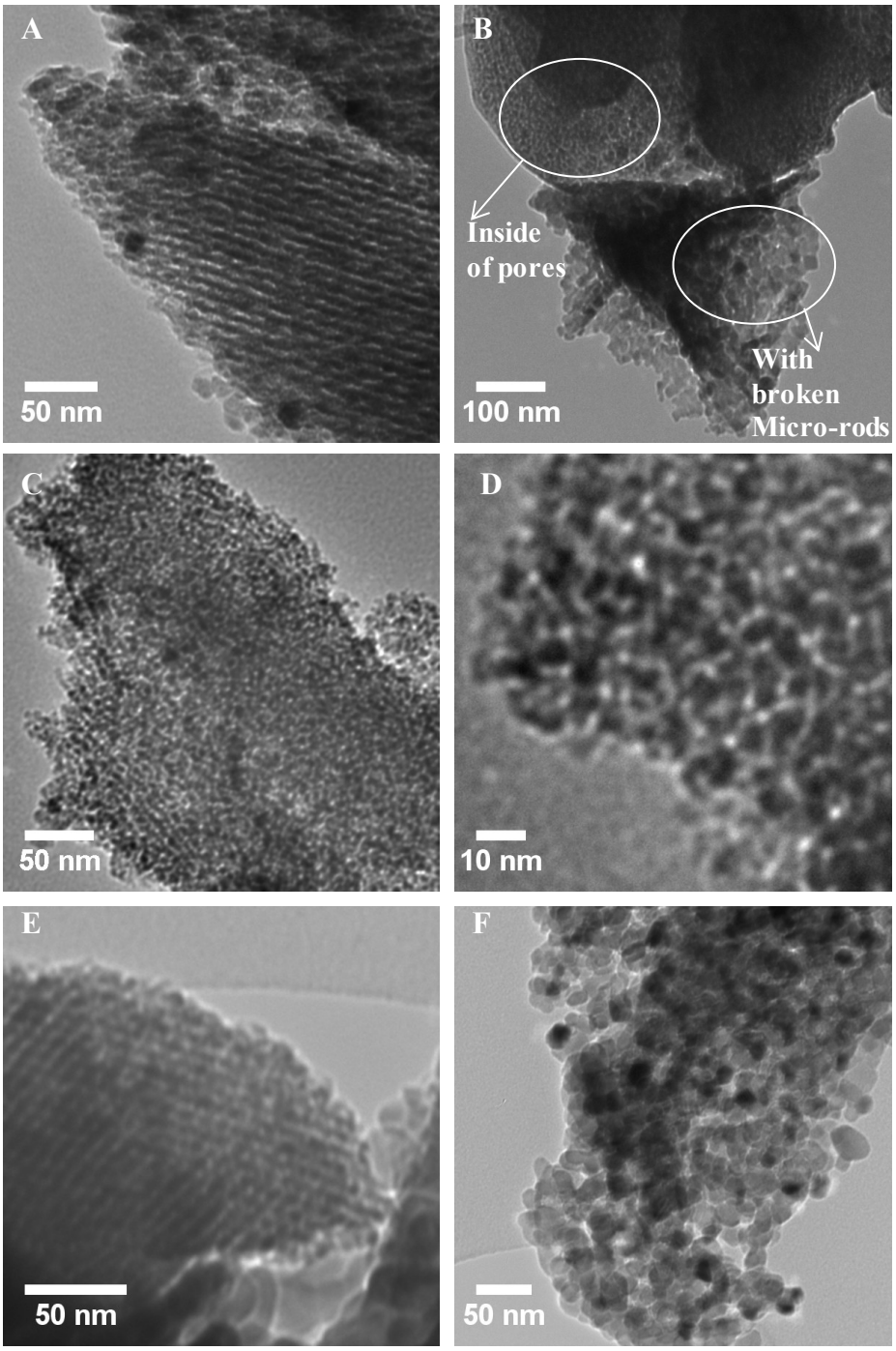

Figure 3.16 TEM micrographs: of A) ms-*a*TO/SBA; B) ms-*a*TO/CMK; C-D) ms-*a*TO(SBA); and E-F) ms-*a*TO(CMK). In B the top circle represents the material obtained inside the pores and bottom circle the material obtained when the micro-rods break.

The TEM micrographs of the ms-*a*TO/SBA and ms-*a*TO/CMK fired mixtures (Figs. 3.16 A and B) confirmed the effectiveness of the impregnation method and the crystallization of TiO_2 nanoparticles inside the pores. However in case of ms-*a*TO/CMK, besides the particles formed

inside the pores, it is possible to observe other, larger particles. These particles may result from the breaking of the template microrods responsible for maintaining the ordered porosity in the CMK-3. After removal of the SBA-15 template (Figs. 3.16 C and D), the particles are disordered and d_{par} is around 5 nm slightly lower than the pore diameter of SBA-15 used as template. In the case of ms-*a*TO(CMK) and as for ms-*t*ZO(CMK), the sample was not homogeneous. Figure 3.16 E displays agglomerate of nanoparticles of ms-*t*ZO(CMK) with morphologic arrangement similar to the template (CMK-3). Disordered particles are observable with diameter considerable higher than the CMK-3 average pore size, i.e., the particles have diameter around 10-12 nm or higher. The diameter is not easy to measure because the particles are overlapped.

The N_2 physisorption isotherms of the TiO_2 are of type IV for both templates (Fig. 3.17 A).

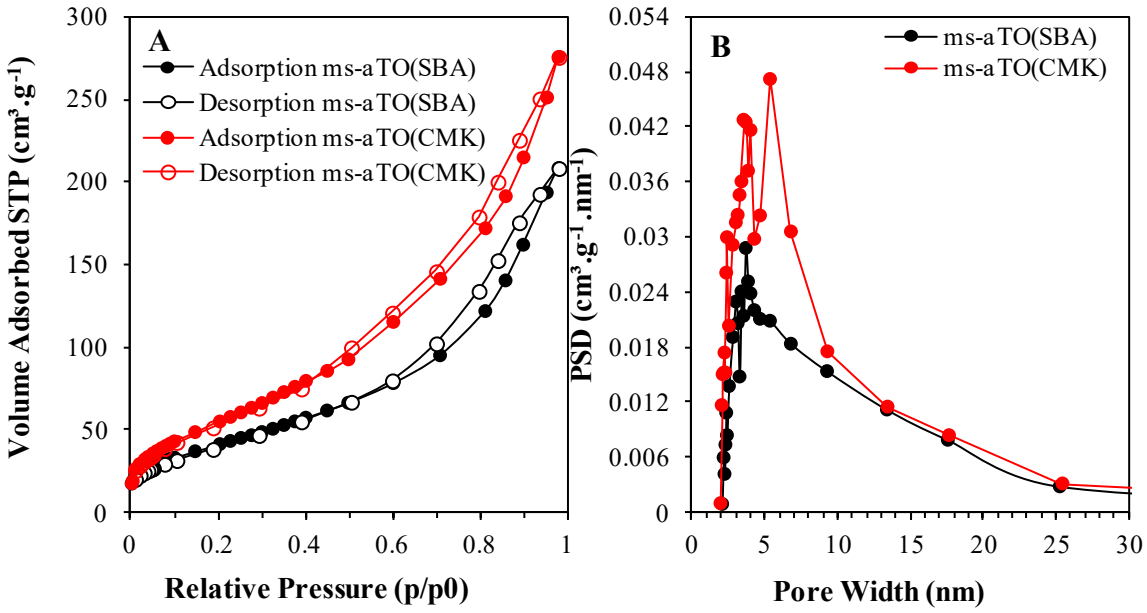

Figure 3.17 A) N_2 adsorption and desorption isotherms of the TiO_2 for materials using both templates collected at -196 ºC; and B) corresponding PSD.

The PSD (Fig. 3.17 B) show peaks at 3.5-3.9 nm and 3.4-6.8 nm for TiO_2 obtained from the SBA-15 and CMK-3, respectively. The estimated S_{BET} values are 142 and 191 $m^2.g^{-1}$, respectively for TiO_2 using SBA-15 or CMK-3 as templates, with V_p= 0.36 and 0.50 $cm^3.g^{-1}$ respectively. In case of ms-*a*TO(CMK), the d_{parBET} is smaller than d_{parTEM}, probably as a consequence of the inhomogeneity of the sample.

3.2.4 Mesoporous $BaZrO_3$

In face of the observed chemical interaction between zirconia and silica when preparing the mesoporous ZrO_2, one guesses that the same problem would arise on attempting to prepare mesoporous $BaZrO_3$ with SBA-15 template. In fact, the thermodynamic calculations indicate that the formation of $ZrSiO_4$ is indeed favorable, but the reaction between BaO and ZrO_2 yielding $BaZrO_3$ has a more negative Gibbs free energy change and is thus more favorable. However, the formation of barium silicates has the most negative free energy change, thus being the most likely reaction (Fig. 3.18).

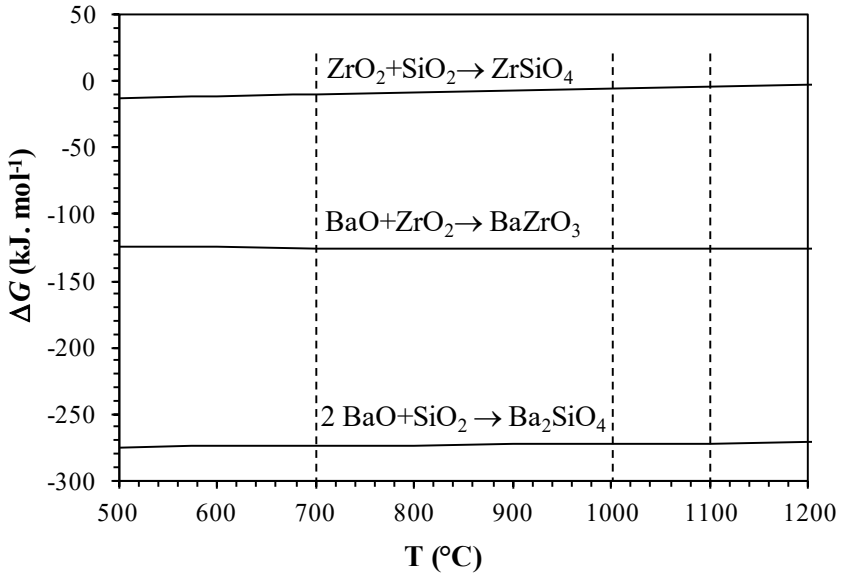

Figure 3.18 Estimation of the Gibbs free energy as a function of temperature for several chemical reactions involving the SiO_2 hard template and barium and zirconium oxides. The dashed lines indicate the firing temperatures used in the various syntheses.

Therefore, several experiences involving different oxide precursors and templates were performed in order to select the best conditions to obtain mesoporous barium zirconate. The first attempt to prepare ms-BZO(SBA) was based on the impregnation of SBA-15 with $BaCl_2.2H_2O$ and $ZrOCl_2.8H_2O$ precursors. The XRD patterns obtained after calcination in air at different temperatures show the formation of tetragonal phase of ZrO_2 ($P4_2/nmc$ space group, ICDD PDF data file 01-079-1767) as predominant product (Fig. 3.19) up to 1000 ºC. With the increase of the firing temperature to 1100 ºC, extensive chemical reaction between barium, zirconium and the SBA-15 tends to occur leading to the barium zirconate silicate $Ba_2Zr_2Si_3O_{12}$ ($P2_13$ space group, ICDD PDF data file 00-025-1466) and the crystallization of tetragonal SiO_2 ($P4_12_12$ space group, ICDD PDF data file 01-082-0512).

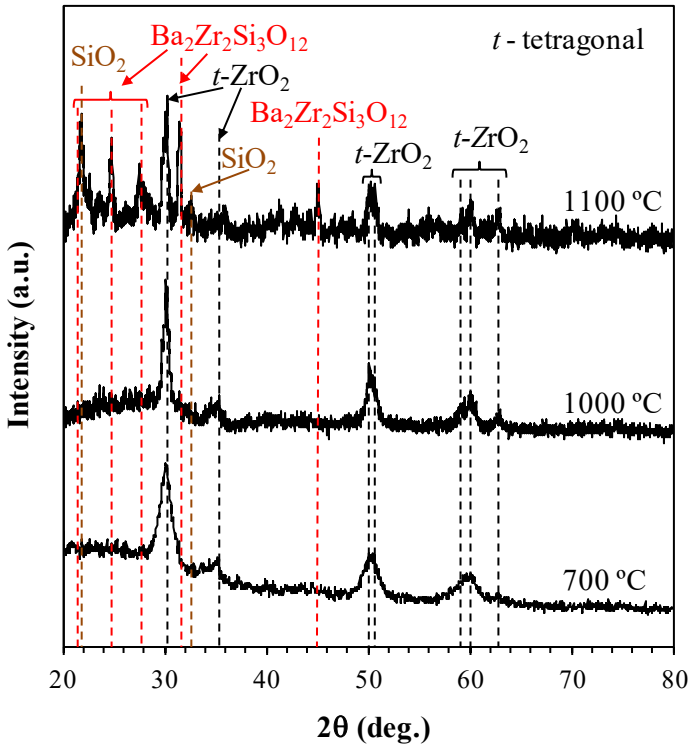

Figure 3.19 XRD patterns of ms-BZO-Cl/SBA samples fired in air at the indicated temperatures.

On a the second attempt, $Ba(NO_3)_2$ and $ZrO(NO)_3{\cdot}xH_2O$ (in this case $x \sim 6$) precursors were used with SBA-15 to try to lower the firing temperature down to 700 °C thus minimizing the formation of the undesired silicates. However, this temperature is still too high and the barium silicate (orthorhombic phase, *Pmcn* space group, ICDD PDF data file 04-011-2153) is the predominant phase formed (possibly also zirconia), as shown by the XRD pattern a in Figure 3.20. This result ends up confirming the thermodynamic predictions.

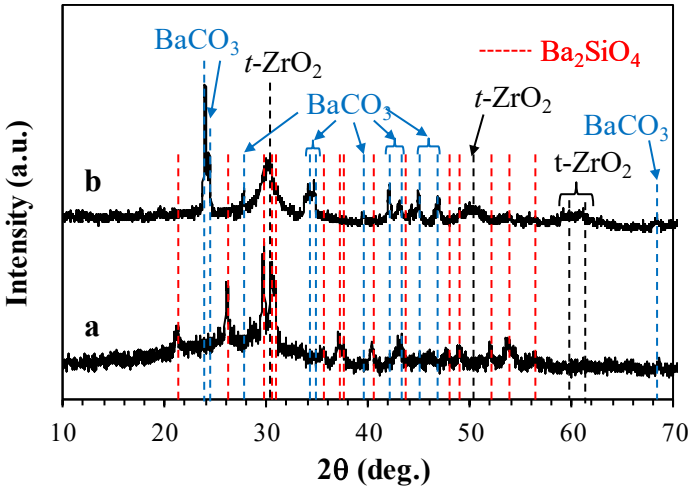

Figure 3.20 XRD patterns of a) ms-BZO-NO_3/SBA and b) ms-BZO-NO_3/CMK fired at 700 °C in N_2 atmosphere.

CMK-3 was used as template with nitrate precursors on a third attempt to avoid silicate formation. In this case, $BaCO_3$ (orthorhombic phase, *Pmcn* space group, ICDD PDF data file 00-005-0378) was the main reaction product (Fig. 3.20 pattern b). A likely explanation for the formation of the carbonate is the existence of CO_2 resulting from the oxidation of the template, which then may react with barium oxide formed after decomposition of the nitrate (Eqs. 3.1 and 3.2).

$$C + O_2 \rightarrow CO_2 \tag{3.1}$$

$$BaO + CO_2 \rightarrow BaCO_3 \tag{3.2}$$

The ZrO_2 (tetragonal phase, $P4_2/nmc$ space group, ICDD PDF data file 01-079-1770) was also generated during the synthesis due to excess of unreacted zirconium.

In order to assess the temperatures at which the relevant events of such complex reactions occur, one performed simultaneous thermogravimetric and differential thermal analyses of these two mixtures with the results shown in Fig. 3.21.

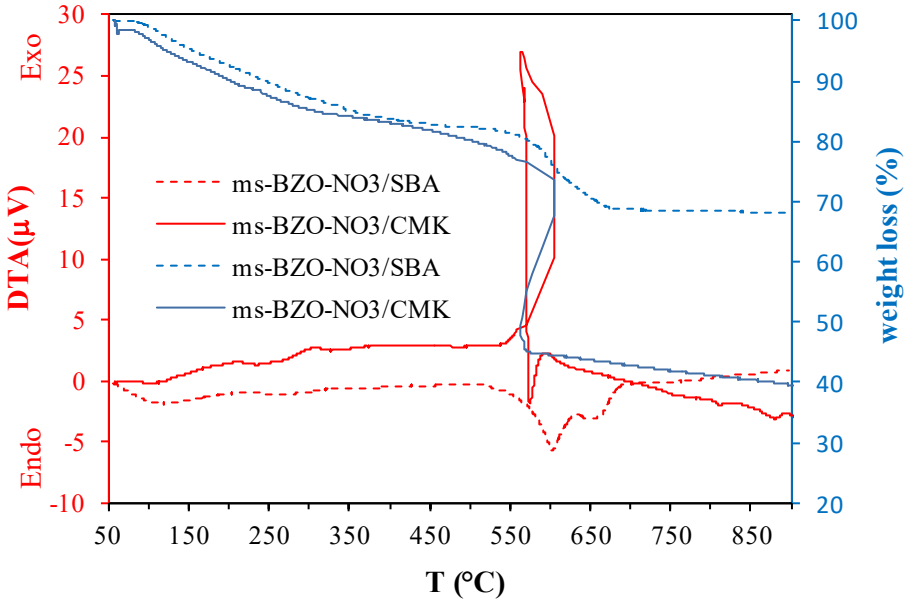

Figure 3.21 TG/DTA curves collected in argon atmosphere for as-prepared ms-BZO-NO_3/SBA (dashed lines) and ms-BZO-NO_3/CMK (solid lines).

Up to approximately 550 °C both mixtures display the same behavior, with a weight loss of about 20-25% of the initial mass that is associated to the release of hydration water and the decomposition of the zirconium nitrate (expected above 100 °C). Above this temperature, the sample prepared with SBA-15 features an endothermic event with a peak temperature at 600 °C that can be attributed to the decomposition of the barium nitrate, followed by a second endothermic

peak at ~660 °C, both accounting for an additional 10% weight loss. No more changes are apparent up to 900 °C. In the case of ms-BZO-NO_3/CMK, a very sharp exothermic peak is announced at 550 °C which is accompanied by a weight loss of about 30%. This exothermic phenomenon triggers an event strongly endothermic that even leads to a noticeable cooling of the sample (almost 50 °C). This is probably due to the fast formation of a volatile organic compound resulting from the reaction of N, C and O. This exothermic reaction provides the necessary energy to form $BaCO_3$ (Eq. 3.2).

On a fourth attempt it was thus necessary to avoid the presence of nitrogen in the initial precursors. CMK-3 was used in combination with $Ba(OH)_2.8H_2O$ and $Zr(OCH_2CH_2CH_3)_4$. Thermal analyses confirm that the strong exothermic event is no longer present. The weight loss observed up to 400 °C can be ascribed to the dehydration of the barium hydroxide (initially octahydrate). There are sequences of endothermic events up to 400 °C probably due to the release of volatiles. The subsequent exothermic peak at approximately 700 °C suggest that ZrO_2 or $BaZrO_3$ (or both) may form at this temperature, with previous decomposition of the carbonated ions. However, the strong deviation from the DTA base line may actually hide further exothermal features at lower temperatures, namely at ~350 °C, as it actually seems to be the case in face of the XRD results presented in Fig. 3.23.

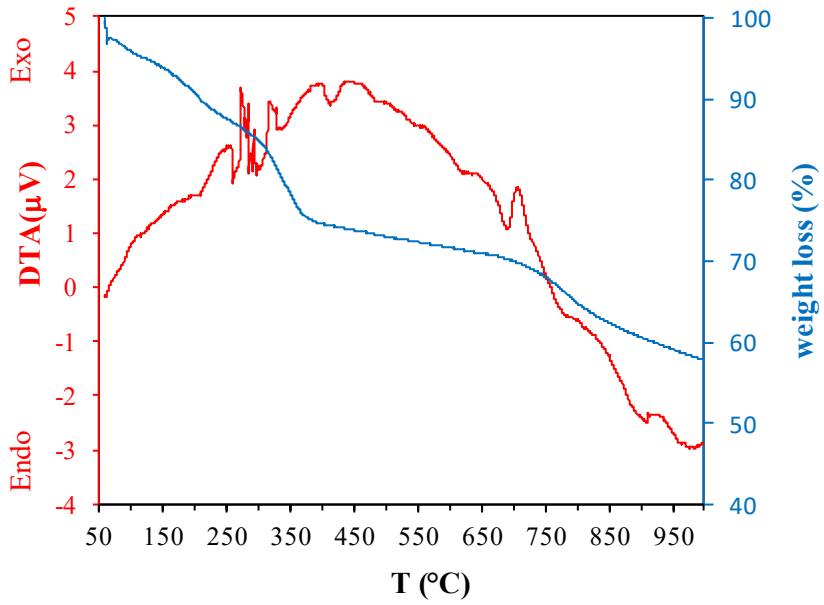

Figure 3.22 TG/DTA curves for ms-BZO/CMK sample collected in argon atmosphere.

The phase evolution under variable temperature is complex, with formation of various intermediates (Fig. 3.23).

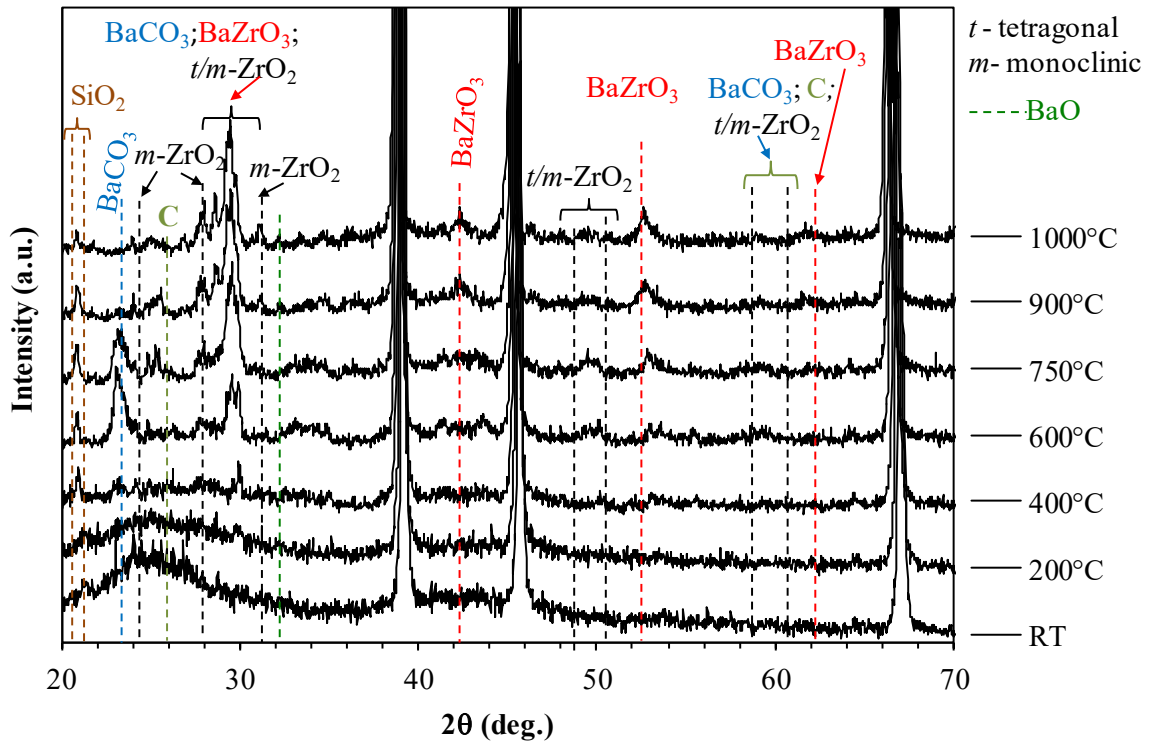

Figure 3.23 Variable temperature XRD patterns of ms-BZO/CMK acquired in vacuum (~10^{-5} atm of O_2). The shaded areas correspond to the platinum peaks from the sample holder.

Zirconia (tetragonal phase, $P2_1/c$ space group, ICDD PDF data file 01-089-6976), $BaCO_3$ (orthorhombic phase, *Pmcn* space group, ICDD PDF data file 04-015-3213) and SiO_2 ($P4_12_12$ space group, ICDD PDF data file 01-082-0512) residually present in the CMK-3 seem to be the first phases to crystallize in the range 400-600 °C. The first evidence for the formation of $BaZrO_3$ (cubic phase, $Pm\bar{3}m$ space group, ICDD PDF data file 04-005-9664) appears at 600 °C (paired to traces of carbon, $P6_3/mmc$ space group, ICDD PDF data file 04-015-2407). The $BaZrO_3$ cubic phase is clearly established in the pattern collected at 750 ºC, where the intensity of the $BaCO_3$ reflections start to decrease. The pattern collected at 900 ºC seems to possess the highest amount of $BaZrO_3$ .The $BaCO_3$ peaks eventually disappear at 900 ºC, where in turn BaO reflections show up ($Fm\bar{3}m$ space group, ICDD PDF data file 04-006-6634), most likely due to the decomposition of $BaCO_3$. Also at 900 ºC the monoclinic ZrO_2 ($P2_1/c$ space group, ICDD PDF data file 00-007-0343) are detected. Simultaneously with the increase in firing temperature (more evident from 900 °C to 1000 °C)the SiO_2 decrease probably by reaction with barium and zirconium leading to $Ba_2Zr_2Si_3O_{12}$. However the peak corresponding to the $Ba_2Zr_2Si_3O_{12}$ is not evident since it is hidden by background.

This result is confirmed by the XRD patterns collected at room temperature of samples fired at the target temperatures for a longer time (Fig. 3.24). The XRD patterns of the powders fired in argon

atmosphere are clearly dominated by the $BaZrO_3$ reflections with minor contributions of $BaCO_3$, C and ZrO_2 of variable intensity. The amount of ZrO_2 decreases with the increase of temperature from 750 °C to 900 °C, whereas the inverse happens in the case of $BaZrO_3$. The peaks corresponding at crystalline SiO_2 are evident at 900 ºC. The broad peak around 45º suggests the presence of $Ba_2Zr_2Si_3O_{12}$ due the reaction with residual SiO_2, zirconium and barium. And also the presence of and $BaCO_3$ formed by the reaction of barium oxide with carbon dioxide (eq. 3.2).

The XRD pattern collected on the powder fired at 400 °C in oxygen confirmed that the $BaZrO_3$ is retained after template removal, but still showing a non-negligible amount of $BaCO_3$ (Fig. 3.24 pattern c). It is perhaps important to notice that the color of powder changed from black to grayish white powder.

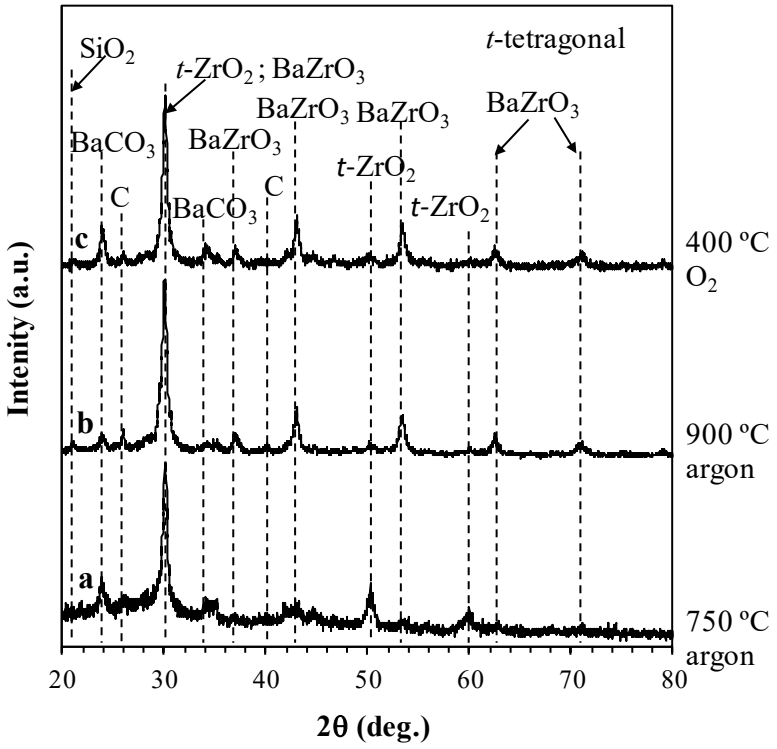

Figure 3.24 XRD patterns of ms-BZO/CMK heat treated at: a) 750 °C; b) 900 °C under argon; and c) after subsequent treatment at 400 °C under oxygen rich atmosphere to form ms-BZO(CMK).

The presence of these impurities suggests that the firing conditions are critical and need to be improved.

Taking into account the results obtained in the last attempt ($Ba(OH)_2.8H_2O$ and $Zr(OCH_2CH_2CH_3)_4$ precursors on CMK-3), the synthesis was repeated with firing at an intermediate temperature (800 ºC) and a final chemical treatment in formic acid for $BaCO_3$ removal. Figure 3.25 shows the XRD patterns during the different stages of this synthesis.

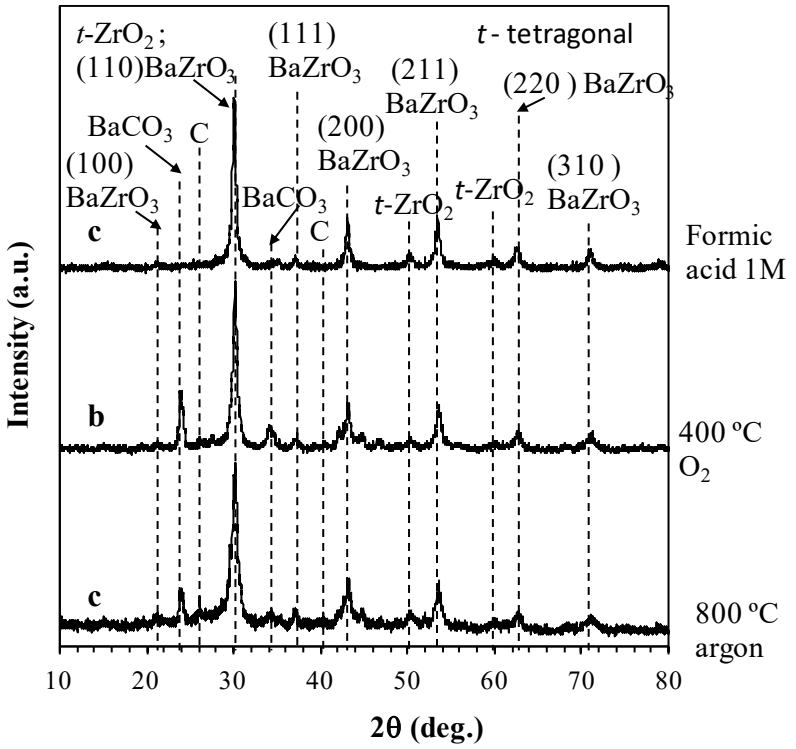

Figure 3.25 XRD patterns of subsequently treated samples during preparation of $BaZrO_3$: A) ms-BZO/CMK (800 °C/ 10 h/ argon); B) ms-BZO(CMK) with carbonates (400 ºC/ 1 h/ O_2) and C) ms-BZO(CMK) (3 min/ formic acid 1M). The peaks indexed according to the space group $Pm\bar{3}m$ of the cubic phase of $BaZrO_3$ are also shown.

The treatment in argon at 800 °C produces the expected $BaZrO_3$ powder with trace amounts of $BaCO_3$, ZrO_2 and C. The carbon and the zirconia reflections almost fully disappear after firing in oxygen, while $BaCO_3$ is efficiently removed by the final treatment in formic acid. The final cubic phase of $BaZrO_3$ was indexed in the $Pm\bar{3}m$ space group with a=4.1895 Å.

Figure 3.26 shows the FTIR-ATR spectra of the ms-BZO(CMK) before (spectrum a) and after washing with formic acid (spectrum b).

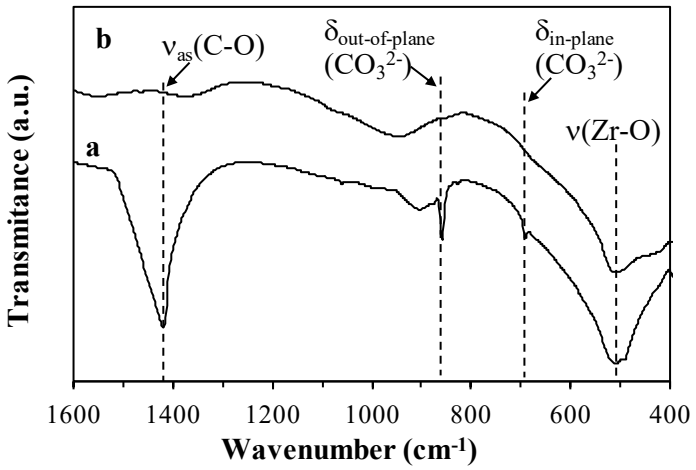

Figure 3.26 The FTIR-ATR spectra of a) ms-BZO(CMK) and b) ms-BZO(CMK) washed with formic acid.

Both FTIR-ATR spectra shows the band around 510 cm^{-1} assigned to the stretching vibration of metal oxygen (Zr-O) in the perovskite phase.[247] Additionally in spectrum a of ms-BZO(CMK) one observes the characteristic bands at 692 cm^{-1} and 859 cm^{-1} corresponding to the bending vibration modes of in-plane and out-of-plane CO_3^{2-}, which denote the presence of $BaCO_3$. These bands disappear after washing the solid with formic acid. Finally, one notes the strong band at 1420 cm^{-1} is the asymmetric stretching vibration of C-O bonds.[248]

The carbonate-free ms-BZO(CMK) maintains the disordered mesoporosity with a d_{parTEM} of around 7 nm. The d_{parTEM} is slightly larger than the d_P of CMK-3 used as template. However this difference may reflect the lack of accuracy on the measurement of the aggregated particles (Fig. 3.27 A). It is believed that the ms-BZO(CMK) was formed inside of the pores of CMK-3 becoming agglomerated after the removal of the template. The ms-BZO(CMK) shows an isotherm type IV typical of mesoporous materials (Fig. 3.27 B).

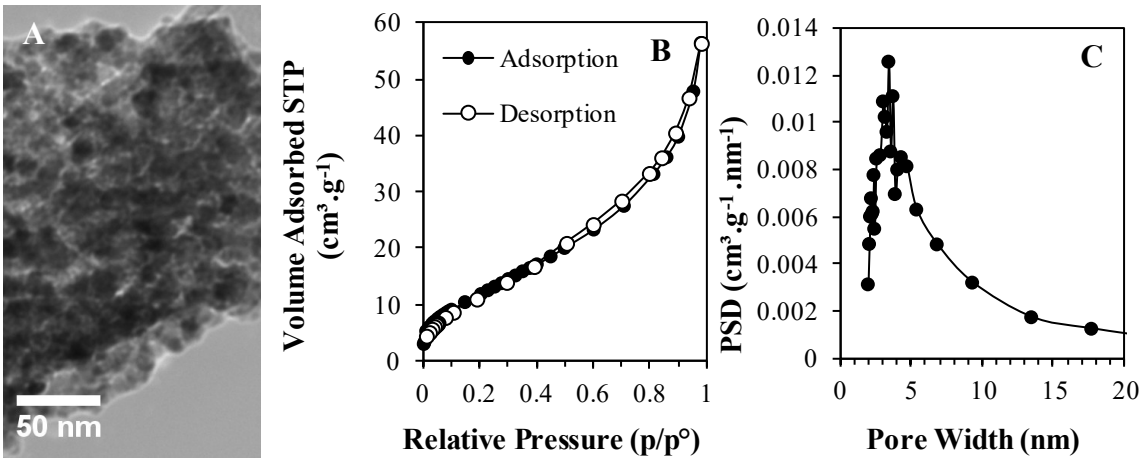

Figure 3.27 A) TEM micrograph; B) N_2 physisorption isotherms collected at -196 °C; and C) PSD of ms-BZO(CMK).

The calculated S_{BET} (41 $m^2.g^{-1}$) and V_p (0.11 $cm^3.g^{-1}$) while the PSD data suggests d_p to be in the range 2.8-5.4 nm (Fig. 3.27 C).

As in the cases of other casted oxides using CMK-3 the final product shows a residual amount of silicon determined by EDS (molar ratio Ba:Zr:Si 1:1.59:0.23).

3.3 $BaCeO_3$ by soft templating

$Ba(NO_3)_2$ and $Ce(NO_3)_3.6H_2O$ were used as oxide precursors for the synthesis of $BaCeO_3$ using a soft template route with hexamethylenetetramine (HMTA). Figure 3.28 shows the XRD patterns of the product before and after calcination at 800 ºC.

Before calcination, the XRD pattern (Fig. 3.28 pattern a) shows several peaks, which are difficult to assign. The main crystallographic phase seems to be cubic $Ba(NO_3)_2$ ($Pa\bar{3}$ space group, ICDD PDF data file 01-071-3824). Other possible phases are triclinic phase of $Ce(NO_3)_3.6H_2O$ ($P\bar{1}$ space group, ICDD PDF data file 00-031-0335), orthorhombic $BaCO_3$ (*Pmcn* space group, ICDD PDF data file 01-071-4900), cubic CeO_2 ($Fm\bar{3}m$ space group, ICDD PDF data file 01-071-4807), orthorhombic $BaCeO_3$ (*Pbnm* space group, ICDD PDF data file 01-070-1429), cubic BaO ($Fm\bar{3}m$ space group, ICDD PDF data file 01-074-1228) and cubic $(NH_4)_3Ce_2((NH_4)_9$, ($P4_132$ space group, ICDD PDF data file 00-047-0811). After calcination at 800 ºC, the most intense peaks can be indexes as orthorhombic $BaCeO_3$ (*Pbnm*) with lattice parameters *a*=6.2300, *b*=6.1978 and *c*=8.7628 Å. Other peaks can be indexed to cubic phase of CeO_2 ($Fm\bar{3}m$ space group) and orthorhombic phase of $BaCO_3$ (*Pmcn* space group).

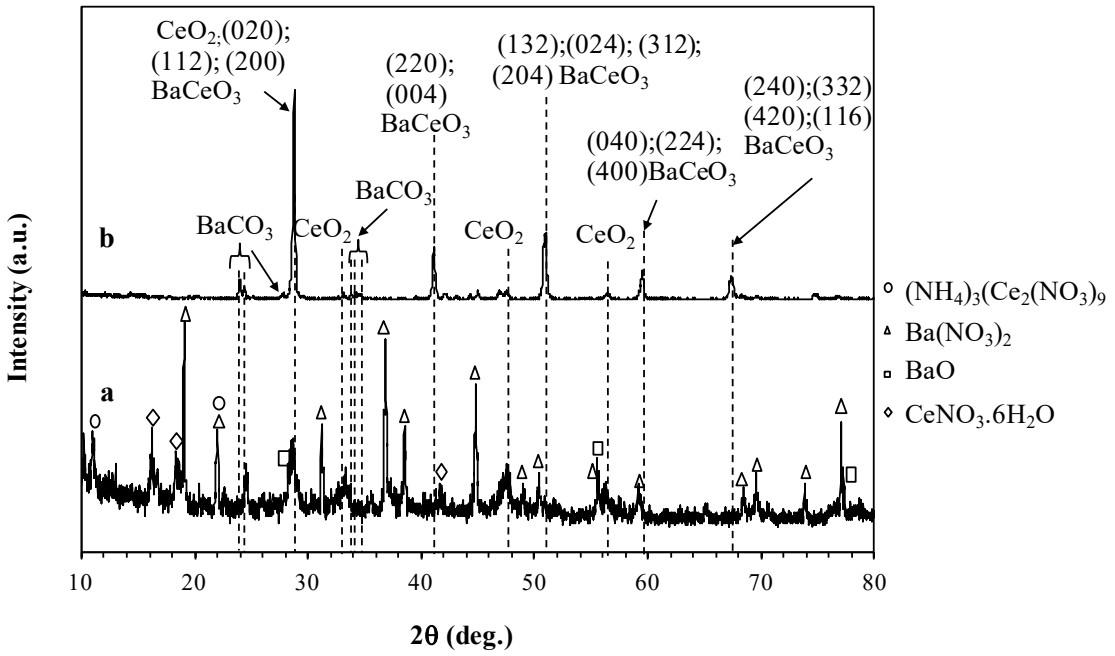

Figure 3.28 XRD pattern of the np-BCO: a) before calcination and b) after calcination at 800 °C. The peaks indexed according to the orthorhombic $BaCeO_3$ *Pbnm* space group are also shown.

Table 3.3 presents the structural and textural properties of the resulting sample.

Table 3.3 Summary of the structural characterization of np-BCO material.

Acronym	Crystal system (cell parameters Å)	ρ_{oxide} [a)] ($g.cm^{-3}$)	d_{parXRD} (nm) [b)]	S_{BET} ($m^2.g^{-1}$)
np-BCO[a)]	Orthorhombic (a= 6.2300, b= 6.1978,c= 8.7628)	6.41	49.8	16

[a)] Contaminated with CeO_2 and $BaCO_3$; [b)] using the Scherrer equation.

Fig. 3.29 displays the FTIR-ATR spectra of HMTA template and np-BCO material. The np-BCO material shows the expected band at around 400 cm^{-1} corresponding to the Ce-O stretching vibration of the $BaCeO_3$ and CeO_2 [163, 249] (spectrum b). Note the absence of any of the HMTA bands used as soft template (detailed in spectrum a). This absence suggests that the template was efficiently removed by calcination. The presence of trace amounts of $BaCO_3$ in the final product is also confirmed by FTIR-ATR.

The TEM micrograph (Fig. 3.29 C) shows the non-homogeneous character of the prepared np-BCO formed by agglomerates. It is however possible to distinguish a dominating pattern of particles with

d_{parTEM} around 50 nm that correspond to $BaCeO_3$, in accordance with d_{parXRD} values extracted from the XRD patterns.

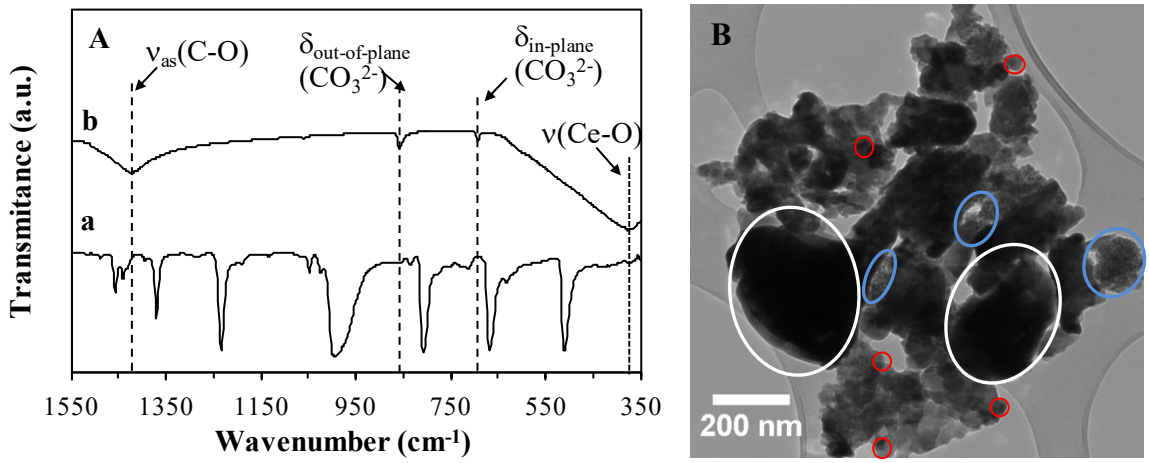

Figure 3.29 A) FTIR-ATR spectra of a) HMTA and b) np-BCO. B) TEM micrograph of np-BCO. In B the white, blue and red circles correspond to big particles, clusters of small particles and a particles with diameter around around 50 nm.

4

Zeta potential measurements of oxide/electrolyte mixtures

This chapter presents a study of the variation of the surface charge of oxides in contact with the electrolytes using the ξ measurements. The eleven different oxides in combination with four electrolytes were used to obtain the systematic characterization of the ζ as a function of the φ_{oxide}. Figure 4.1 shows these data.

Before any comment on the observed trends, it is important to notice the dispersion in the ζ values for the pure oxides (φ_{oxide}=1). For example the ζ measured for np-*m*ZO varies from -2 mV for the Iz series to about 25 mV for Py. Somewhat smaller variability, but still significant, is observed for ms-CO(SBA) and np-8YSZ. The slight variability observed for the remaining cases may be considered normal within the natural dispersion associated to ζ measurements. Several attempts, including controlling the temperature of ultrasonic bath and testing the meter with standard reference solutions, were made to obtain reproducible results for the cases of ms-CO(SBA), np-*m*ZO and np-8YSZ, but with limited success.

Possible reasons for the observed dispersion of ζ for φ_{oxide}=1 may be the instability of the oxides in the solutions at the mentioned pH. Indeed, Pourbaix diagrams suggest that Ce^{3+} (which is known to exist in nominal CeO_2) tends to dissolve at pH=5.5. The ZrO_2 may form ZrO^{2+} in a pH range close to 5-6, which is indicative of chemical instability. The TiO_2, on the other hand, is stable from pH=2 to about 8.5, which seems to correlate well with the consistent ζ values measured for the 3 types of TiO_2 tested.[250]

The instability of the suspension may lead to sedimentation and/or flocculation of oxide particles when the pH of the suspension is close to the isoelectric point (pH(I)), potentially impacting the reproducibility of the measurements. Moreover, several ionic species resulting from the dissociation of water and the electrolyte molecules may affect the pH of the suspensions. Table 4.1 lists the pH of the various electrolytes in the suspending media.

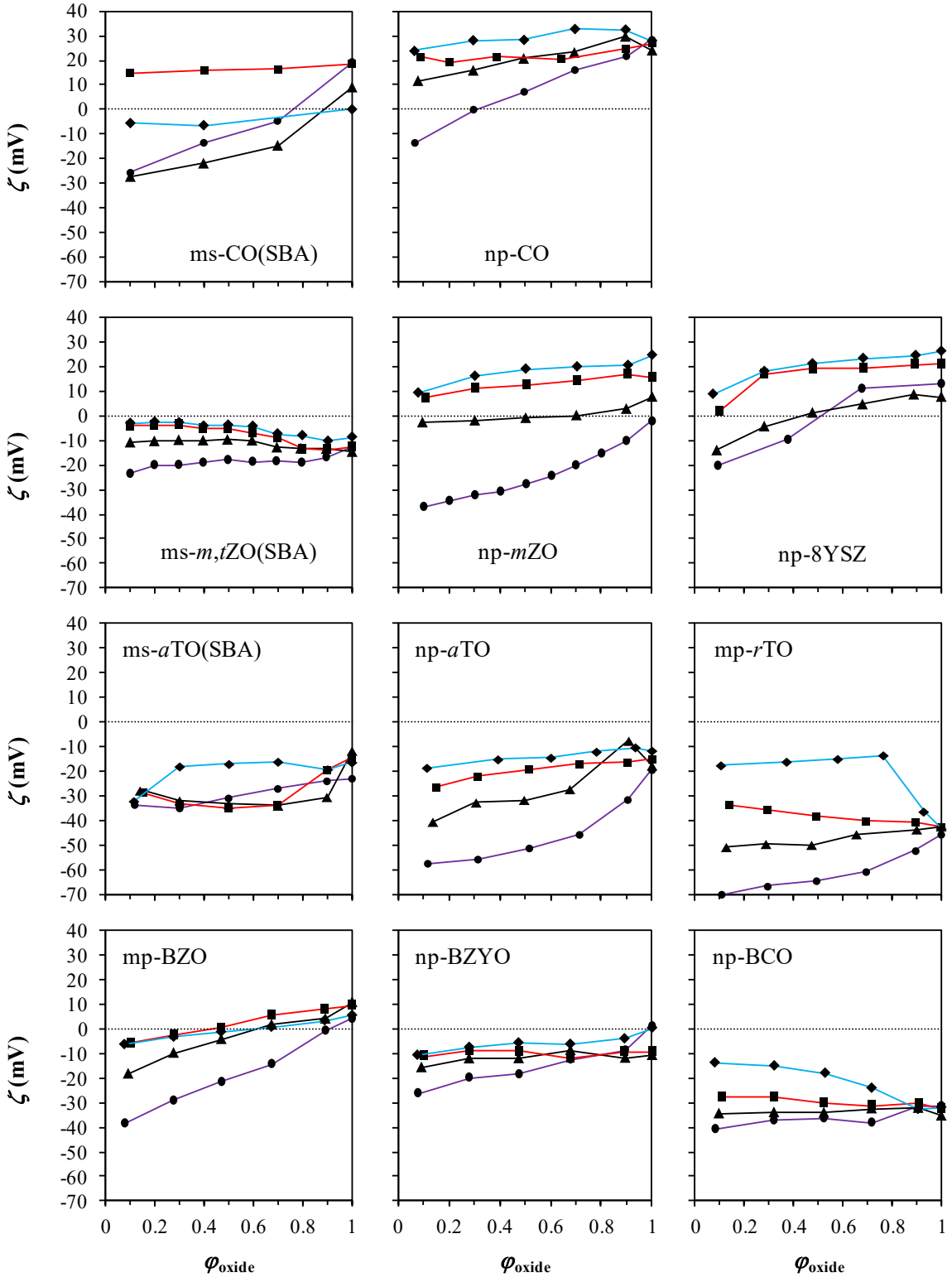

Figure 4.1 Evolution of ζ of the oxide particles in suspensions as a function of the φ_{oxide} for: ●/ purple line-Iz, ▲/black line-Bz, ■/red line-Tz and ◆/blue line-Pz.

Table 4.1 pH of the 0.001 M KNO_3 solution and of 100 mL of the same solution containing 10 mg of the various electrolytes.

Electrolyte	KNO_3	Iz	Bz	Tz	Pz
pH	5.5	8.5	7.0	5.6	5.6

The pH of the buffer KNO_3 solution is close to 5.5, which increases with additions of the various electrolytes. This increase is marginal for Tz and Pz, but for Bz and Iz it shows a direct correlation with increasing pK_a (see Table 1.2), or an increase of the concentration of hydroxyl anions in solution. The effect of the powder additions to the pH of these solutions is shown in Table 4.2, which also includes the corresponding ζ values.

Table 4.2 ζ of the oxide-electrolyte mixtures in 0.001 M KNO_3 solutions and corresponding pH obtained for $\varphi_{oxide} = 1$ and $\varphi_{oxide} = 0.1$.

Composition		$\varphi_{oxide} = 1$		$\varphi_{oxide} = 0.1$	
Oxide	**Electrolyte**	**ζ (mV)**	**pH**	**ζ (mV)**	**pH**
ms-CO(SBA)	Iz	19	5.5	-26	7.7
	Bz	9	5.5	-27	6.4
	Tz	19	5.4	15	5.3
	Pz	0.1	5.5	-6	5.5
np-CO	Iz	28	5.3	-14	7.7
	Bz	24	5.4	12	6.6
	Tz	27	5.7	21	5.6
	Pz	28	5.4	24	5.5
ms-*m*,*t*ZO(SBA)	Iz	-13	5.6	-24	7.7
	Bz	-15	5.8	-11	6.5
	Tz	-13	5.7	-4	5.6
	Pz	-9	5.2	-3	5.1
np-*m*ZO	Iz	-2	5.2	-37	7.6
	Bz	8	5.3	-3	6.4
	Tz	15	5.3	7	5.4
	Pz	25	5.4	9	5.3
np-8YSZ	Iz	13	5.3	-20	7.8
	Bz	8	5.3	-14	6.4
	Tz	21	5.3	2	5.2
	Pz	26	5.1	9	5.2
ms-*a*TO(SBA)	Iz	-23	5.9	-34	7.9
	Bz	-12	5.8	-28	6.5
	Tz	-14	5.8	-29	5.7
	Pz	-16	5.8	-32	5.6

(continues)

Table 4.2 (continues)

Composition		φ_{oxide} = 1		φ_{oxide} = 0.1	
Oxide	**Electrolyte**	**ζ (mV)**	**pH**	**ζ (mV)**	**pH**
np-*a*TO	Iz	-19	5.4	-57	7.9
	Bz	-18	5.4	-41	6.4
	Tz	-15	5.4	-26	5.4
	Pz	-12	5.3	-19	5.4
mp-*r*TO	Iz	-46	5.0	-70	7.5
	Bz	-42	5.2	-51	6.3
	Tz	-43	5.1	-34	5.2
	Pz	-43	5.2	-18	5.3
mp-BZO	Iz	4	5.6	-39	7.9
	Bz	11	5.6	-18	6.5
	Tz	10	5.5	-6	5.5
	Pz	5	5.4	-6	5.4
np-BZYO	Iz	1	6.2	-26	8.0
	Bz	-11	6.3	-16	6.8
	Tz	-9	6.4	-11	6.2
	Pz	0.2	6.3	-11	6.3
np-BCO	Iz	-32	8.1	-41	8.3
	Bz	-35	7.8	-35	7.0
	Tz	-32	8.7	-28	6.9
	Pz	-32	7.6	-14	6.7

The data in Table 4.2 show that the pH values of the initial oxide suspensions (φ_{oxide}=1) are in the range from 5 to 5.9 for most oxides, with mp-*r*TO distinctively on the lower end of this range and ms-*a*TO(SBA) (a mix of anatase and rutile, see Table 3.2) on the upper range. Both mp-BZYO and np-BCO increase the basicity of the medium (pH values of 6.2-6.4 and 7.6-8.7, respectively) as expected from the basic character of the Ba-containing oxides. Despite the many factors affecting electrophoretic measurements, the ζ values for the various oxides are in the expected range considering the pH(I) of these systems (shown in Table 4.3).

The pH of the pH(I) is inversely proportional to the electronegativity.[251, 252] Therefore, one expects for the binary oxides under study CeO_2 to show the highest pH at the pH(I), TiO_2 the lowest, and ZrO_2 should occupy an intermediate position. Consequently, for the pH of the KNO_3 solution (~5.5) the two types of CeO_2 display the highest ζ (Table 4.1), which are clearly in the positive range due to the higher pH(I), whereas the three TiO_2 show the most negative ζ due to the lower pH(I). With respect to CeO_2-based samples, ms-CO(SBA) has less positive ζ than np-CO and also shows a wider dispersion in the measurements carried out in suspensions made from the

same powder batch, in the same conditions. Differences may be due to different pH(I) resulting from smaller ms-CO(SBA) particles (Table 3.2), and possibly also due to changes in the surface composition associated to the dissolution of Ce^{3+}, in agreement with the Pourbaix diagram of cerium.[250]

Table 4.3 Literature pH(I) data for various oxides.

Oxide	pH(I)	Observation	Ref.
CeO_2	6-9	30 mV ≥ ξ ≥ -7 mV for 4 ≤ pH ≤ 8[a)]	[253-258]
ZrO_2	3-8	0.16 C.m^2 ≥ Surface charge≥ -0.02 C.m^2 for 4 ≤ pH ≤ 8[b)]	[251-255, 257-261].
8YSZ	6-9	46 mV ≥ ξ ≥ -40 mV for 5.5 ≤ pH ≤ 9[c)]	[253, 254, 262-264]
***a*TiO_2**	4-7	0 mV ≥ ξ ≥ -23 mV for 4 ≤ pH ≤ 8[d)]	[253-255, 257, 258, 260, 261, 265]
***r*TiO_2**	3-7	0.08 C.m^2 ≥ Surface charge≥ -0.09 C.m^2 for 4 ≤ pH ≤ 8[e)]	[253-255, 257-261]
SiO_2	2-4	0 C.m^2 ≥ Surface charge≥-0.12 C.m^2 for 4 ≤ pH ≤ 8[f)]	[251, 252, 254, 255, 257-261]
$BaZrO_3$	~5.5	14 mV ≥ ξ ≥ -39 mV for 4 ≤ pH ≤ 8[g)]	[253, 258, 266]
$BaCeO_3$	4-8	ξ≈0 for 4≤pH≤8[h)]	[267]

[a)] Taken from [256] using np-CO as oxide in water; [b)] taken from [259] using *m*ZrO_2 as oxide and 0.001 M KNO_3 as inert electrolyte; [c)] taken from [262] using np-8YSZ as oxide in water; [d)] taken from [265] using *a*TiO_2 as oxide in water; [e)] taken from [259] using *r*TiO_2 as oxide and 0.001 M KNO_3 as inert electrolyte; [f)] taken from [259] using SiO_2 as oxide and 0.001 M KNO_3 as inert electrolyte; [g)] taken from [266] using $BaZrO_3$ as oxide and 0.001 M KCl; [h)] using 0.01 M KNO_3 as inert electrolyte.

The two commercial zirconias (np-*m*ZO and np-8YSZ) display a significant dispersion of the measured ζ, which nonetheless is clearly positive, as expected from a pH(I) higher than the pH of the suspension. The ms-*m*,*t*ZO(SBA) prepared in this Thesis behaves quite differently from the two commercial nanopowders by displaying consistently negative ξ values. The differences suggest that the pH(I) of the ms-*m*,*t*ZO(SBA) suspension is lower than the pH of the suspension. This may indeed result from the presence of Si-O-Zr cross links on the surface of the material (Fig. 3.10). Silica is a fairly acidic oxide and the Si-O may thus enhance the acidic character of the ms-*m*,*t*ZO(SBA) in comparison to np-*m*ZO and np-8YSZ, bringing the pH(I) closer to pH=2-4, which is the pH(I) for SiO_2 (Table 4.3).

TiO_2 should have the lowest pH(I) of the tested binary oxides and indeed one observes the lowest ξ values for the three titanias. Moreover, the rutile powder has ξ slightly below -40 mV, while the

two anatase powders have ξ between -10 and -20 mV. One can again explain this difference by resorting to published pH(I) values, which tend to be smaller for the rutile (Table 4.3).

The behavior of the multicationic oxides (mp-BZO, np-BZYO and np-BCO) is also consistent with known pH(I) data. $BaZrO_3$ should have pH(I) close to pH=5.5 (Table 4.3) and indeed sufficiently close to zero ξ measured for mp-BZO seems to confirm this, considering the pH=5.4-5.6 of the corresponding suspension. The np-BZYO displays ξ values also close to zero, although slightly negative, which is in good agreement with the slightly higher pH of the suspension (6.2-6.4). Differences may also be due to the presence of yttria, the particle size or the presence of impurities such as $BaCO_3$, or also the sample dissolution (particularly Ba^{2+} in the case of mp-BZO due to the slightly acidic pH)[253]. The np-BCO has the second lowest set of ξ values (only mp-*r*TO is lower), which may be explained by the pH(I) at pH≈4 (Table 4.3), clearly lower than the basic pH of the suspension, measured between 7.6 and 8.7. It should be noticed that besides the difference of 1 pH unit observed amongst the various suspensions, the ξ values are highly reproducible, which denotes a stable suspension.

Except for the np-BCO, the pH of the initial suspension remains basically unaltered with the addition of Tz and Pz, whereas for additions of Iz and Bz the pH increases to about 8 and 6.5, respectively. This is the general behavior observed for pure electrolyte solutions, denoting the effect of the electrolyte dissociation. This effect is also apparent in the case of np-BCO, but showing an opposite trend since the initial pH of the suspensions (7.6 – 8.7) is closer to the pH of the Iz and Bz solutions.

Despite the dispersion observed in the noticed cases, it is possible to identify clear trends in the evolution of ζ with incremental additions of the oxides to the various electrolytes depicted in Fig. 4.1. The general picture is that of a decrease of ζ with increasing fraction of the electrolyte (or decreasing φ_{oxide}) in the suspension, which can only be explained by assuming anion adsorption at the oxide surface. It is also apparent that the magnitude of the effect is distinctively larger for Iz and Bz. The self-dissociation constants of these compounds are 3 to 4 orders of magnitude lower than those of Tz or Pz (Table 1.2). This means that the concentration of the ionic species in the bulk (c_∞) (or, in other words, the ionic strength of the medium) is also orders of magnitude higher for Py and Tz. The much higher ionic strength in the latter compresses the Debye length to a point where the space charge region almost disappears and, hence, no measurable differences in ζ can be detected.

There are few exceptions to this tendency where ζ increases with increasing electrolyte fraction, notably for mp-*r*TO and np-BCO in Tz and particularly in Py, where the effect is marked. A hint for this trend is also suggested for ms-*m*,*t*ZO(SBA). One may speculate with reasonable confidence

that the reason for this behavior is linked to the pH(I) of the suspensions. Indeed, mp-*r*TO and np-BCO suspensions have the most negative ξ values, which is indicative of an pH(I) at pH much lower than the pH of the suspension. The Pz and Tz have the lowest pK_a of the 4 electrolytes (Table 1.2), which means the increase of positively charged species in solution may neutralize some of the adsorbed negative ions, thus making more positive the surface charge.

5

Structure, microstructure and stability of nano-ionic composites

Considering that from the viewpoint of surface charge, Iz and Bz for one side, and Pz and Tz for the other, seem to represent two different behaviors, only two of the four initial electrolytes were selected for the subsequent phases of the study. This chapter is thus focus on the study of mixtures of Bz and Tz with various oxides, namely CeO_2, ZrO_2, TiO_2, $BaZrO_3$ and $BaCeO_3$.

This chapter is divided in three subchapters in which the detailed characterization of the structure, microstructure and stability of the oxide/electrolyte composite pellets is presented. All subchapters begin with the analysis of the pure electrolytes to help discussion.

5.1 Structure and composition

Figure 5.1 compares the XRD patterns obtained for the composites before and after the EIS measurements. The XRD patterns for the fresh powders are also presented.

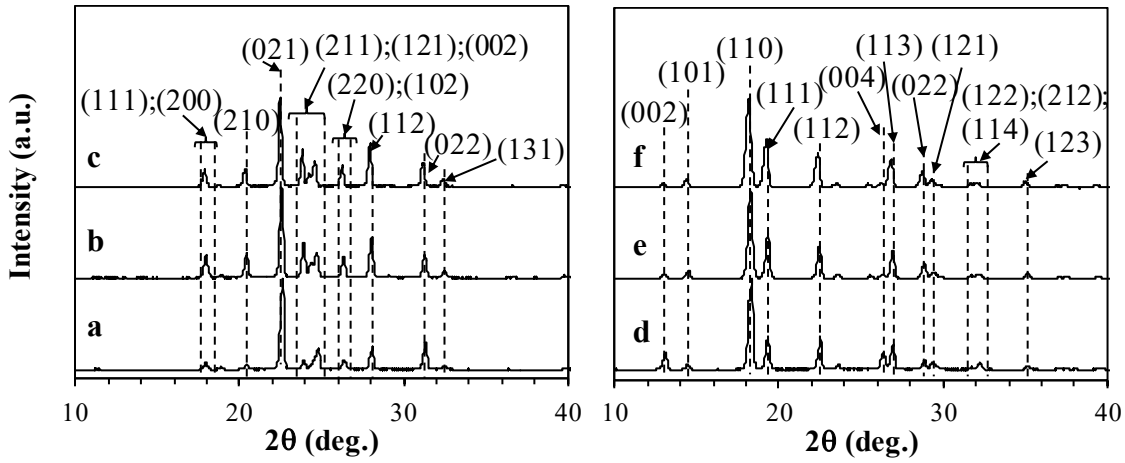

Figure 5.1 XRD patterns of: a) Tz powder; b) Tz pellet before EIS measurements; c) Tz pellet after EIS measurements; d) Bz powder; e) Bz pellet before EIS measurements; and f) Bz pellet after EIS measurements. The Tz and Bz patterns are indexed according to the orthorhombic *Pbca* and $Pc2_1n$ space groups, respectively.

The patterns of the Tz series can be indexed as the pure orthorhombic *Pbca* space group. The Bz is also orthorhombic, but with space group $Pc2_1n$.

The lattice parameters estimated by Rietveld refinement of these patterns are represented graphically in Fig. 5.2.

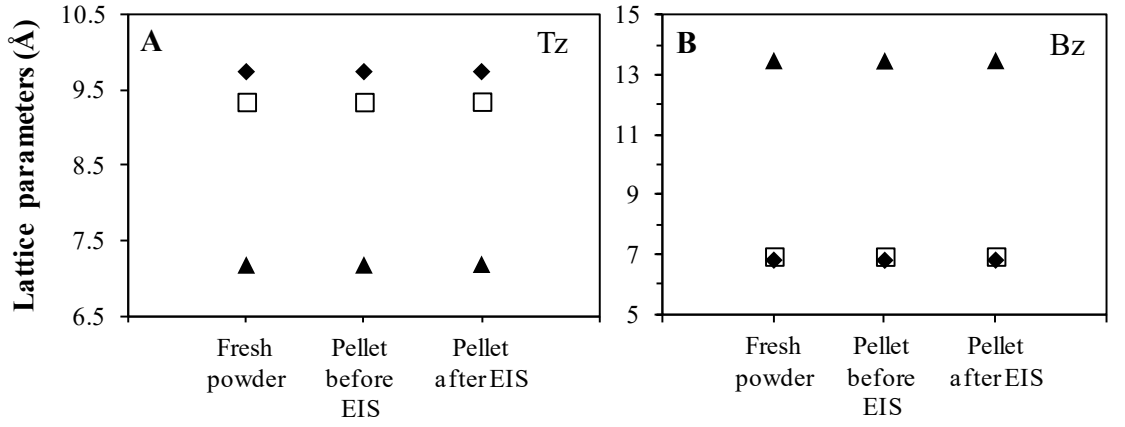

Figure 5.2 Graphical representation of lattice parameters (◆-*a*, □-b and ▲-*c*) vs sample for A) Tz and B) Bz.

No evident structural changes were detected after making a pellet and after EIS measurements for both electrolytes.

Figure 5.3 shows the comparison of the FTIR-ATR spectra of the pure electrolytes, fresh powders and pellets after EIS measurements in dry air (at temperatures up to 105 and 120 ºC for Tz and Bz, respectively).

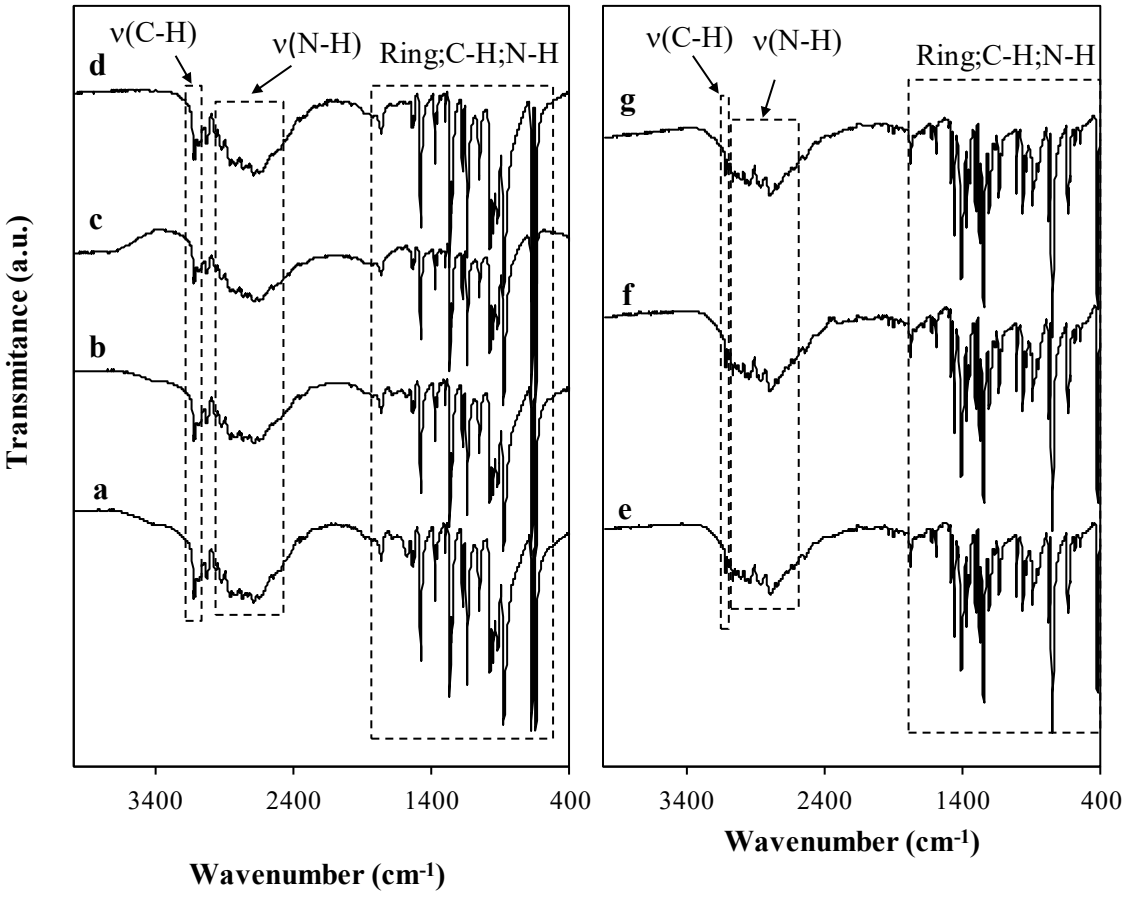

Figure 5.3 FTIR-ATR spectra of: a) Tz (fresh powder); b) Tz (fresh powder after 16 h at 110ºC); c) Tz (pellet); d) Tz (pellet) after EIS measurements; e) Bz (fresh powder); f) Bz (pellet); and g) Bz (pellet) after EIS measurements.

The FTIR-ATR spectra (Fig. 5.3) show the same characteristic vibrational bands during all process for both electrolytes. As depicted in Fig. 5.3 both spectra are very similar. It is possible to identify: i) two very close bands between 3130-3096 cm^{-1} that correspond to the stretching mode of C-H; ii) continuous transmittance over a very wide range corresponding to the characteristic vibrational bands of the N-H about 2551-3095 cm^{-1} for Tz and about 3063-2540 cm^{-1} for Bz; and iii) the vibration modes corresponding to ring stretching and *in-* and *out-* of plane deformation vibrations appear at frequencies between 1800 cm^{-1} and 350 cm^{-1} [268].

Taking into account the composites, the pellets np-CO and ms-*a*TO(SBA), using Tz and Bz as electrolytes, were used as a representative example for XRD and FTIR characterization. The Pourbaix diagrams suggest the dissolution of Ce^{3+} while the TiO_2 is stable.

Figure 5.4 depicts the comparative XRD of the pellets of the np-CO/Tz and ms-*a*TO(SBA)/Tz composites before/after EIS measurements up to 110 ºC. The XRD for pure oxides are also represented for comparison. The EIS measurements were performed in N_2.

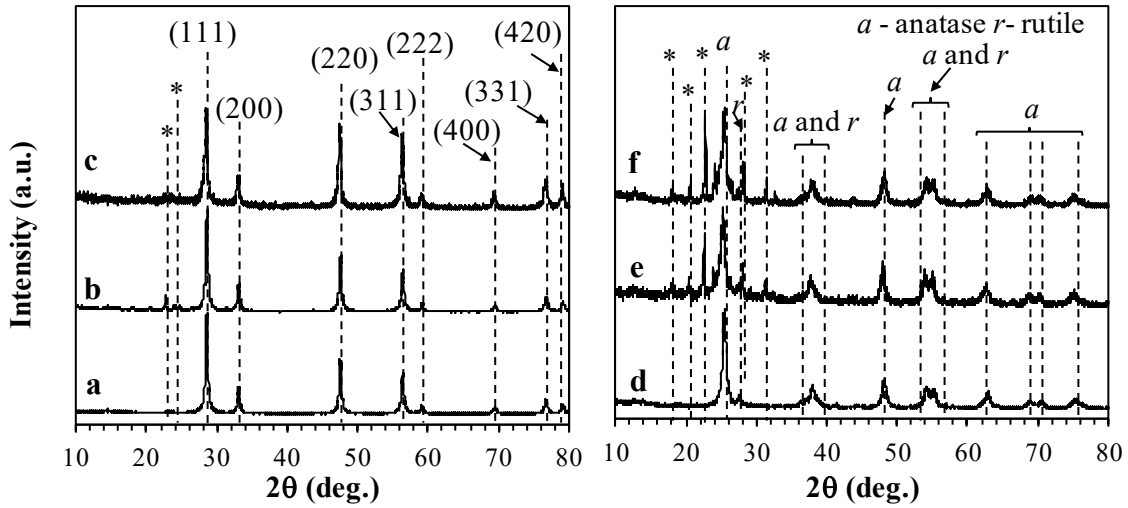

Figure 5.4 XRD patterns of: a) np-CO commercial powder; b) 0.2 np-CO/Tz before EIS measurements; c) 0.2 np-CO/Tz after EIS measurements; d) ms-*a*TO(SBA) powder; e) 0.3 ms-*a*TO(SBA)/Tz before EIS measurements; and f) 0.3 ms-*a*TO(SBA)/Tz after EIS measurements. The peaks indicated with * correspond to diffraction peaks of Tz. The peaks are indexed according to the cubic phase *Fm*$\bar{3}$*m* space group in patterns a-c.

In pellets of the np-CO/Tz composite, the diffraction peaks assigned to Tz are masked by the background and only the most intense diffraction peaks can be detected, due to the saturation of signal. This saturation occurs in result of the higher crystallity of the oxide in comparison to the Tz. In XRD of np-CO/Tz composites, the most intense peaks can be indexed to the pure cubic phase (*Fm*$\bar{3}$*m* space group) of CeO_2. The others peaks can me indexed to the orthorhombic phase of the Tz, except for np-CO powder.

In the XRD patterns of ms-*a*TO(SBA)/Tz pellets, the peaks can be assigned to: i) the tetragonal anatase phase of TiO_2 ($I4_1/amd$ space group) and ii) tetragonal rutile phase ($P4_2/mnm$ space group). The orthorhombic phase of the Tz is only absent from the XRD pattern of ms-*a*TO(SBA) powder (Fig. 5.4 pattern d).

Figure 5.5 shows the graphical representation of the unit cell volume of the materials present in Fig. 5.4. The data for fresh Tz are also shown for comparison proposes.

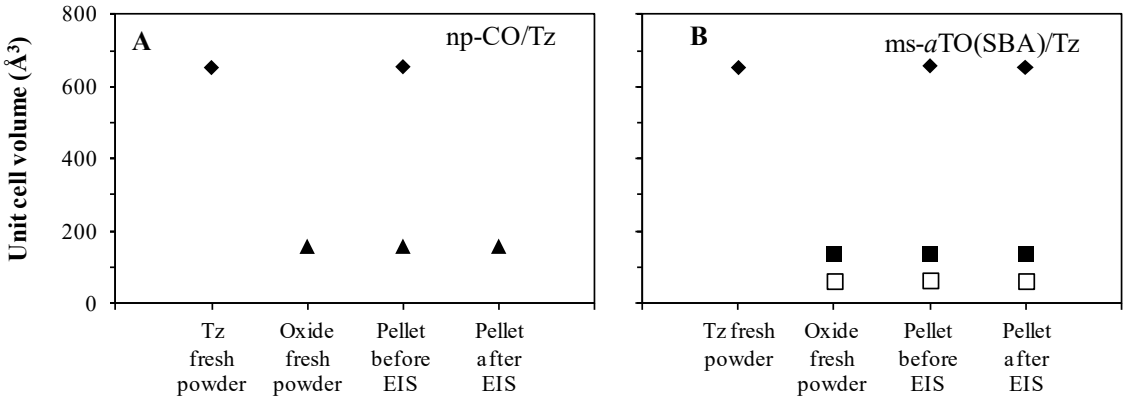

Figure 5.5 Graphical representation of unit cell volume (◆- orthorhombic phase of Tz , ▲-cubic phase of CeO_2, ■-tetragonal anatase phase of TiO_2 and □- tetragonal rutile phase TiO_2 vs sample for A) np-CO/Tz and B) ms-*a*TO(SBA-15)/Tz.

The unit cell volume is almost the same for separated fresh powders and for pellets of the mixture of the materials. This result confirms that no structural alteration during the mixture of materials, pelleting and after EIS measurements for both composites.

The vol. % different phases calculated using POWDER CELL® is present in 5.1.

Table 5.1 Volume fraction of the different phases for pellets of CO and TO with Tz obtained before and after the EIS measurements.

		Pellet before EIS measurements	Pellet after EIS measurements
0.2 np-CO/Tz	**np-CO**	18.6	----
	Tz	81.4	----
0.3 ms-*a*TO(SBA)/Tz	**Anatase**	29.7	29.7
	Rutile	1.5	1.5
	Tz	68.8	68.8

As shown in Table 5.1 the vol. % different phases are in agreement with the expected for all pellets. Note that in case of pure ms-*a*TO(SBA), the vol. % anatase and rutile are equal to 94.5 and 5.5%, respectively (Table 3.2).

Figure 5.6 shows the comparative XRD of the pellets of the np-CO/Bz and ms-*a*TO(SBA)/Bz composites before/after EIS measurements up to 160 ºC.

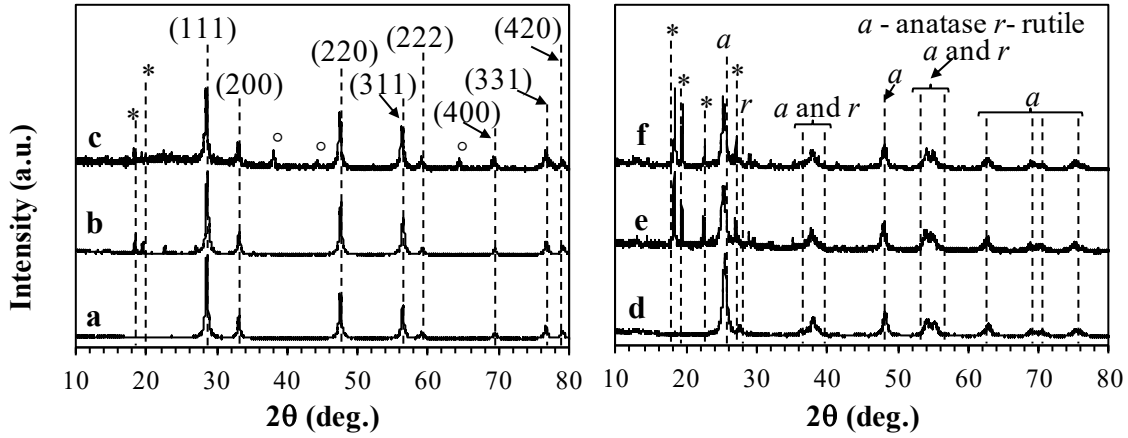

Figure 5.6 A) XRD pattern of: a) np-CO commercial powder; b) 0.2 np-CO/Bz before EIS measurements; c) 0.2 np-CO/Bz after EIS measurements; d) ms-*a*TO(SBA) power; e) 0.3 ms-*a*TO(SBA)/Bz before EIS measurements; and f) 0.3 ms-*a*TO(SBA)/Bz after EIS measurements. Peaks indicated as * correspond to diffraction peaks of Bz. Peaks indicated as ° correspond to diffraction peaks of Ag used for electrodes. The peaks are indexed according to the cubic phase $Fm\bar{3}m$ space group in patterns a-c.

The peaks in previous XRD patterns (Fig. 5.6), corresponding to the oxides, can be indexed as the same phases present in Fig. 5.4. The peaks of the Bz can be indexed at orthorhombic phase of the Bz (space group $Pc2_1n$).

Figure 5.7 represents the unit cell volume as a function of the samples represented in Fig. 5.6. The data for fresh Bz are also presented for comparison.

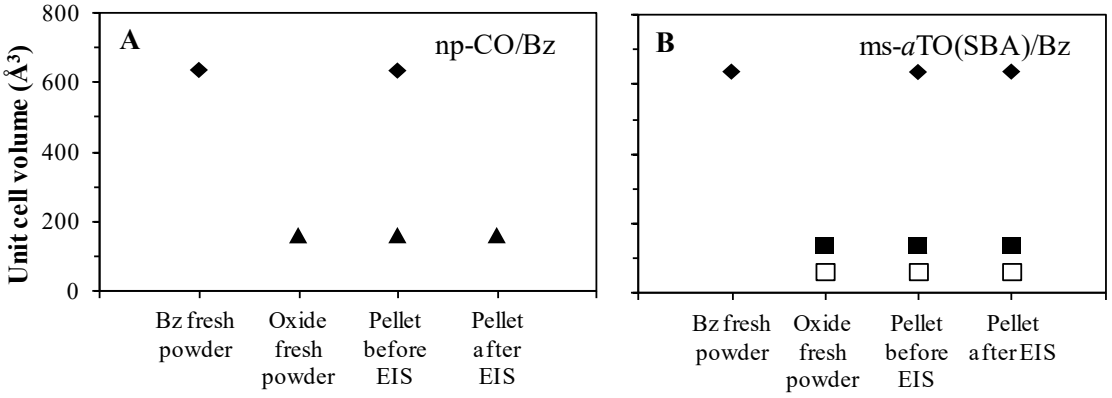

Figure 5.7 Graphical representation of unit cell volume (◆- orthorhombic phase of Bz , ▲-cubic phase of CeO_2, ■-tetragonal anatase phase of TiO_2 and □- tetragonal rutile phase TiO_2 vs sample for A) np-CO/Bz and B) ms-*a*TO(SBA-15)/Bz.

As for the Tz composites, no structural differences are detected in case of Bz composites. The unit cell volume is similar for composites and for fresh powders. Table 5.2 shows data for the vol. % of different phases calculated using POWDER CELL®, which are in accordance with the expected nominal composition.

Table 5.2 Volume fraction of the different phases for pellets of CO and TO with Bz obtained before and after the EIS measurements.

		Vol. %	
		Pellet before EIS measurements	**Pellet after EIS measurements**
0.2 np-CO/Bz[a)]	**np-CO**	17.6	----
	Bz	82.4	----
0.3 ms-*a*TO(SBA)/Bz	**Anatase**	29.6	29.6
	Rutile	1.7	1.7
	Bz	68.7	68.7

[a)] In pellet 0.2 np-CO/Bz the peaks indexed to Ag were not considered.

Figure 5.8 shows the FTIR-ATR spectra of the composites samples with Tz. The FTIR-ATR spectra of composites with Bz are shown in Fig. 5.9.

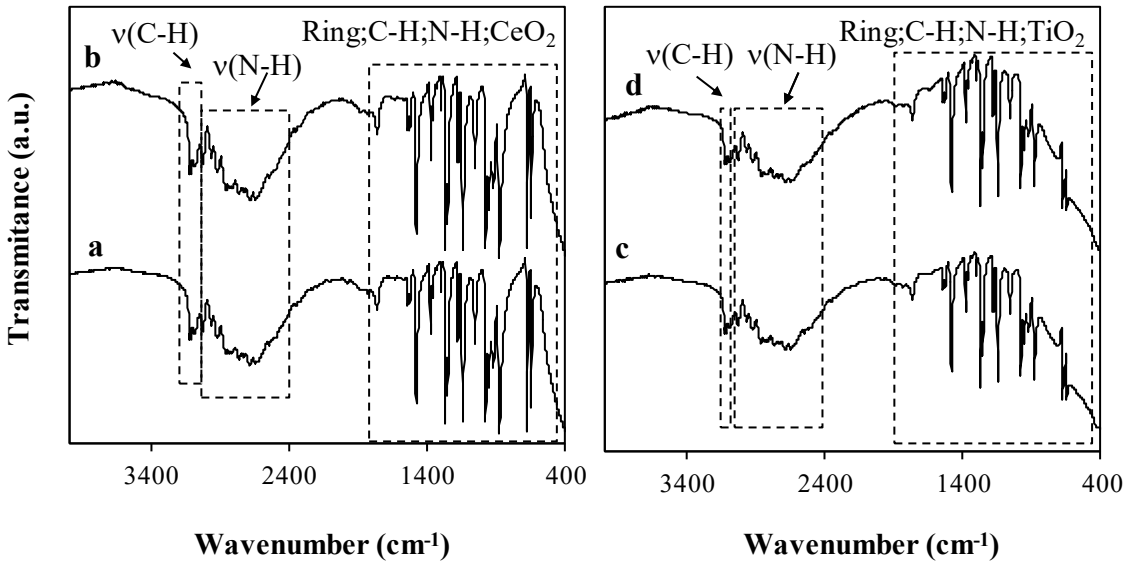

Figure 5.8 FTIR-ATR spectra of: a) 0.2 np-CO/Tz before EIS measurements; b) 0.2 np-CO/Tz after EIS measurements; c) 0.3 ms-*a*TO(SBA)/Tz before EIS measurements; and d) 0.3 ms-*a*TO(SBA)/Tz after EIS measurements;

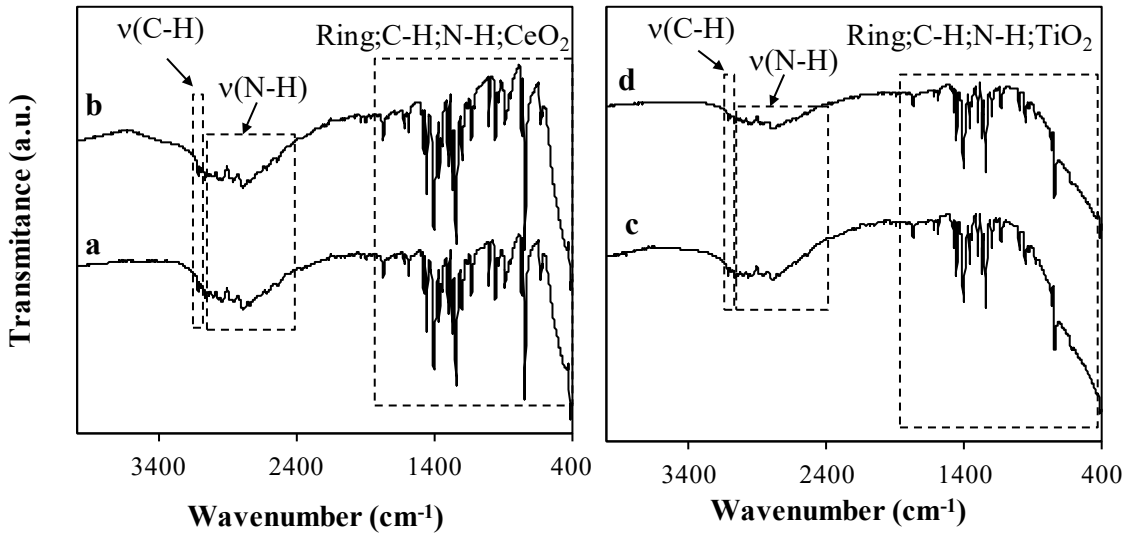

Figure 5.9 FTIR-ATR spectra of: a) 0.2 np-CO/Bz before EIS measurements; b) 0.2 np-CO/Bz after EIS measurements; c) 0.3 ms-*a*TO(SBA)/Bz before EIS measurements; and d) 0.3 ms-*a*TO(SBA)/Bz after EIS measurements.

The FTIR-ATR spectra of composites with both electrolytes show the bands corresponding to the vibrational modes of the oxides and the electrolytes without reaction (see analysis and Fig. 5.3, Fig. 5.10, and Fig. 3.15 spectrum c). The same characteristic vibrational bands are present during all process for both oxides.

The bands corresponding to the vibrational modes of water are not present in all spectra. As it is known that the oxides under study are very hygroscopic, this result suggests that the electrolytes prevent the adsorption of water.

Figure 5.10 shows the comparative FTIR-ATR spectra of the pure np-CO from commercial powder to pellet after EIS measurements (maximum temperature of 160 ºC in N_2).

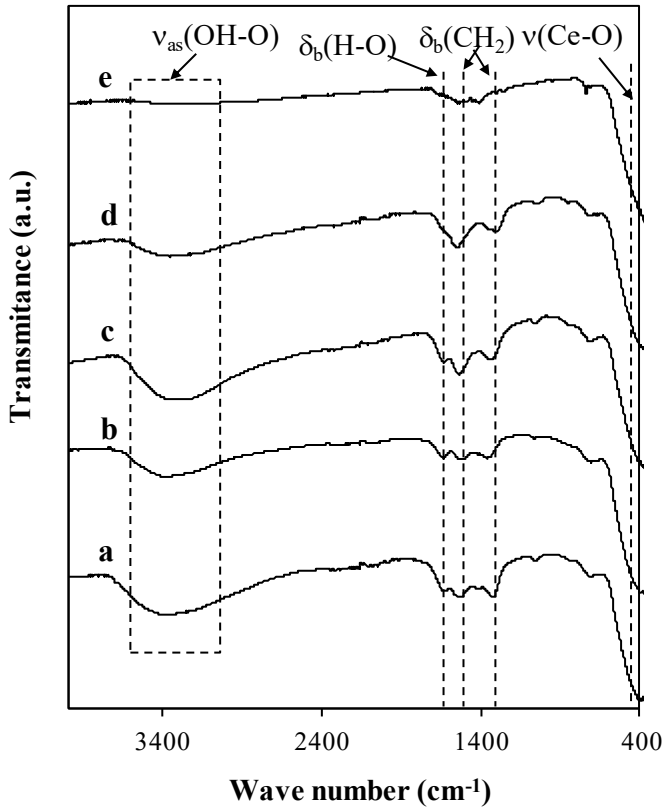

Figure 5.10 FTIR-ATR spectra of: a) np-CO (commercial powder); b) np-CO (commercial powder) after drying at 500 ºC; c) np-CO pelleted before EIS measurements; d) np-CO pelleted after 15 h at 40 ºC under dry air; and E) np-CO (pellet) after EIS measurements

The FTIR-ATR spectra (Fig. 5.10) exhibit a strong broad band ~ 400 cm^{-1} which is due to the υ (Ce–O) mode. Additionally, these FTIR-ATR spectra show two bands corresponding to the bending modes of CH_2 at ~1526 and ~1319 probably due to the presence of organic impurities.[163, 269, 270]

The FTIR-ATR spectra of the np-CO commercial powder, after drying at 500 ºC, and np-CO pellet before EIS measurements (Fig. 5.10 spectra a-c) show the bands corresponding to vibrational modes of water: i) the broad band at ~3350 cm^{-1} due to the asymmetrical O-H-O stretching and ii) the band at ~1630 cm^{-1} due to the O-H scissor bending mode associated to water bending. These bands are expectable since the CeO_2 is a very hygroscopic oxide. However when the pellet was left at 40 ºC under drying air, these bands are almost invisible. After EIS measurements, the bands associated to the vibrational modes of water are not present in the FTIR-ATR spectra.[270] The absence of these bands, confirms that the EIS measurements were performed under anhydrous conditions.

5.2 Microstructure and densification

Figure 5.11 shows SEM micrographs of the cross-section of freshly fractured pellets of pure Tz and Bz before and after the EIS measurements. One can observe the original filament-type microstructure of Tz, which originates a compact monolith observable on a second plane in Fig. 5.11 A. No major changes were identified after the heat treatment applied during the electrical measurements, as suggested by comparison of the latter figure with Fig 5.11 B. The Bz pellet displays a rather conventional aspect of a compact monolith, albeit the presence of some large pores apparent after EIS measurements and that are indicative of viscous flow at the measuring temperature. It should be noticed that those measurements were performed both in dry air and N_2 atmospheres, and no visible differences could be detected in the samples before and after the measurements.

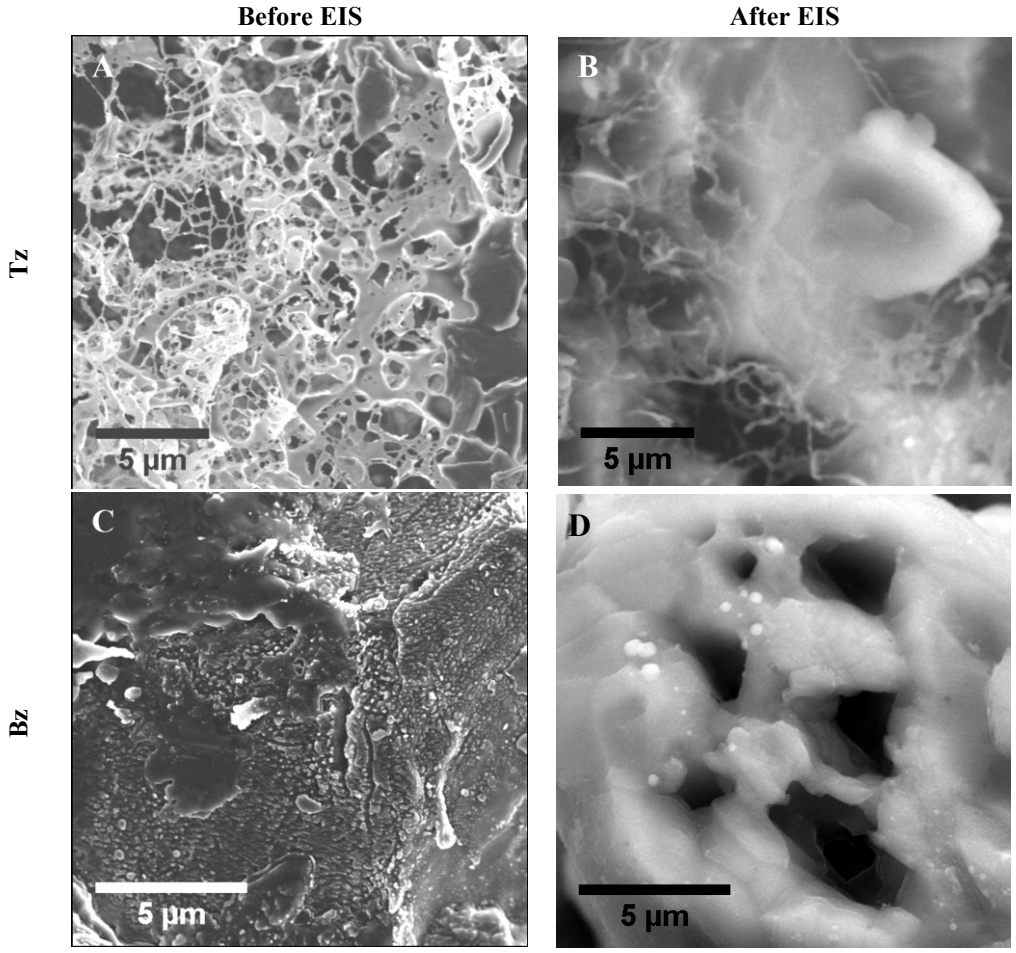

Figure 5.11 SEM micrographs for A), B) Tz and C), D) Bz before and after EIS measurements in dry air at 105 and 120 ºC, respectively.

Figure 5.12 shows representative SEM micrographs of pellets of composites containing Tz and Bz mixed with np-*a*TO. Both fresh samples and for samples submitted to high temperature treatments during EIS measurements are considered. The cross-section SEM micrographs, after breaking the pellets, confirm that the pellets are dense before and after EIS measurements and no morphological alteration in the oxide particles was detected. The electrolytes surrounding the oxide particles can be seen in detail in Fig. 5.12 B.

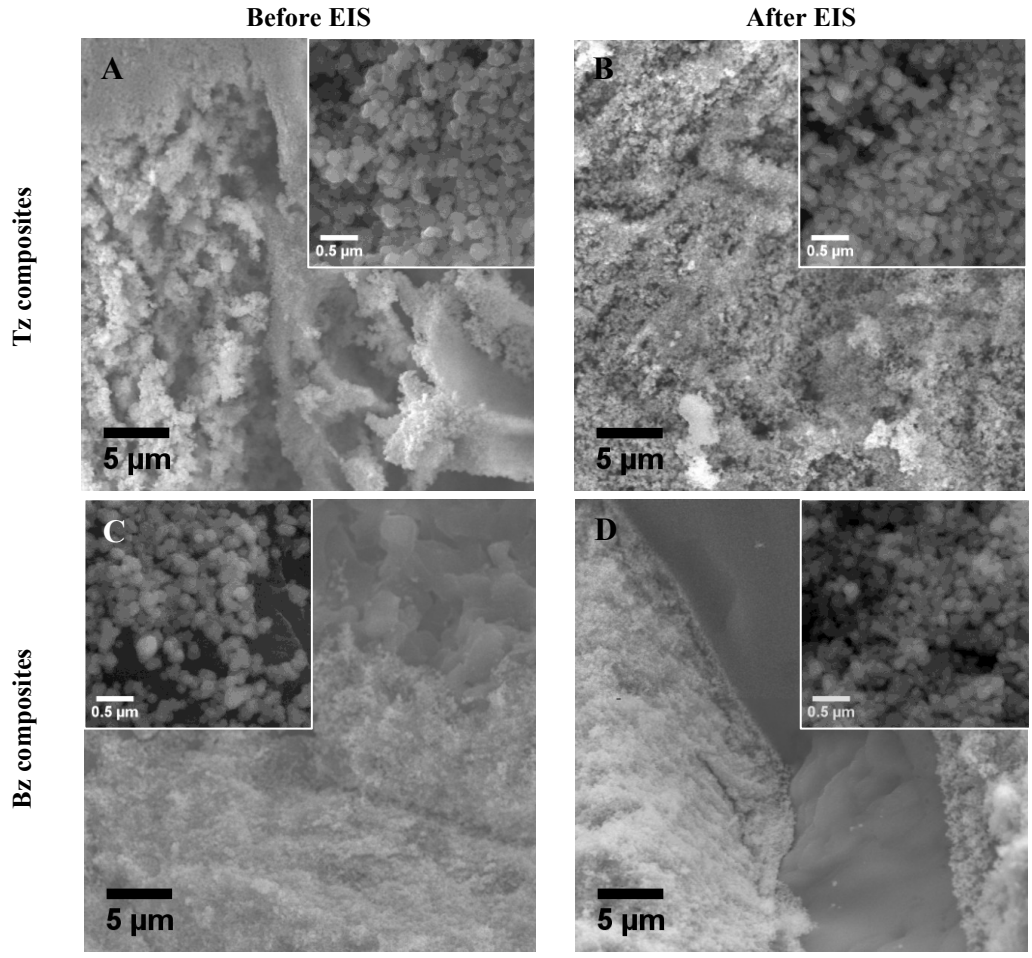

Figure 5.12 SEM micrographs for: A), B) 0.3 np-*a*TO/Tz and C), D) 0.4 np-*a*TO /Bz before and after EIS measurements in N_2 up to 110ºC and dry air up to 120 ºC, respectively. The insets show the magnification of respective SEM micrographs.

To the best of our knowledge, it is the first time that this kind of mixtures is prepared. The fabrication of the pellets for the electrical measurements implies the use of pressure, which may induce mechanochemical transformations or reactions of the individual components (especially Bz and Tz), or between them. In fact, some of the oxides may not be completely stable in the pH conditions of the electrolytes and/or under an applied electrical field.

The pellets were obtained with high densification, after applying uniaxial and isostatic pressures. Figure 5.13 shows the variation of densification (calculated through Eq. 2.2) for all pellets.

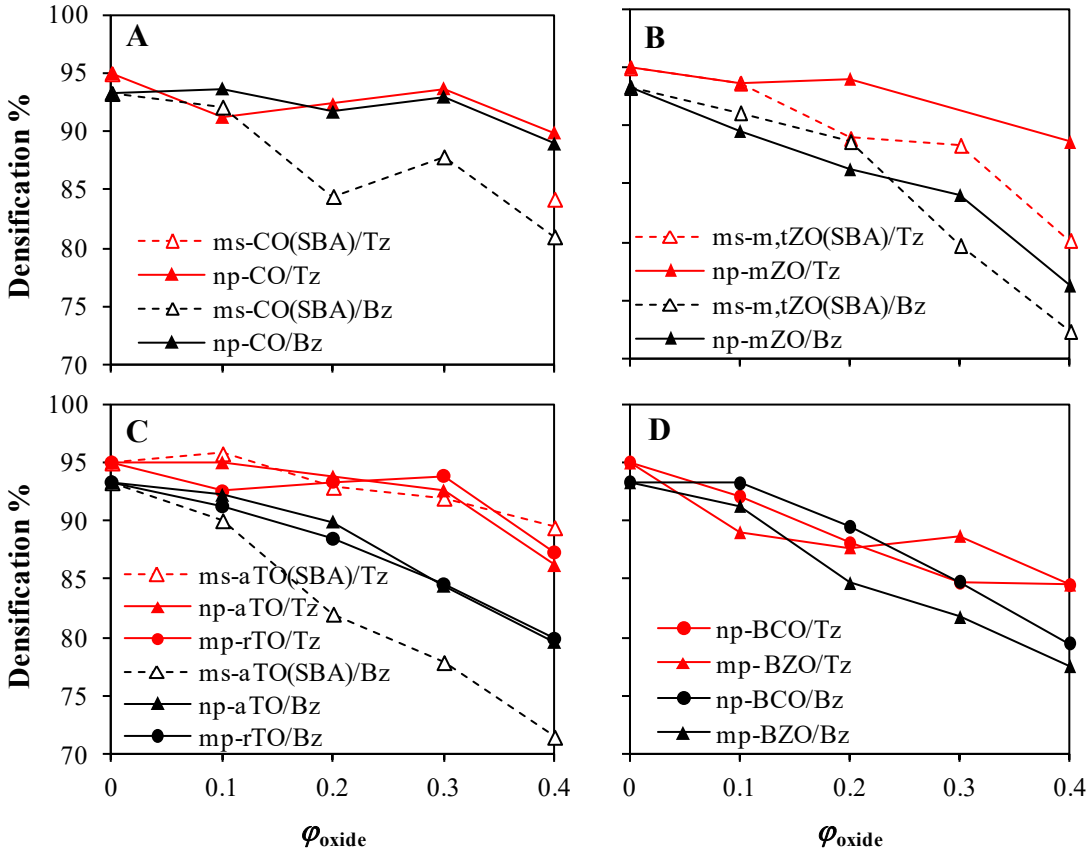

Figure 5.13 Graphical representation of the densification of the pellets of: A) CeO_2; B) ZrO_2; C)TiO_2; and D) np-BCO and mp-BZO composites in electrolytes under study, as function of the φ_{oxide} .

We first noticed that the fairly high densification achieved for both pure electrolytes, with Tz showing slightly higher values than Bz. Pellets of the pure non-mesoporous oxide powders obtained simply by applying pressure yield densifications close to 50%, which are common values in comparison to literature.[271]

In general, we can observe that the densification decreases with the increase of φ_{oxide}. As happened in case of the pure electrolytes, the densification of the composites with Bz are lower than the composites with Tz. Considering the mesoporous oxides, it possible to observe that the densification of the composites with Tz is higher than the densification of the composites with Bz. This suggests that the Tz fills better the pores than the Bz.

5.3 Thermal stability

Figures 5.14 A and B show the TGs for the electrolytes under study to evaluate their thermal stability. Before the TG analysis, the Tz was left in the oven at 110 ºC during 15 h.

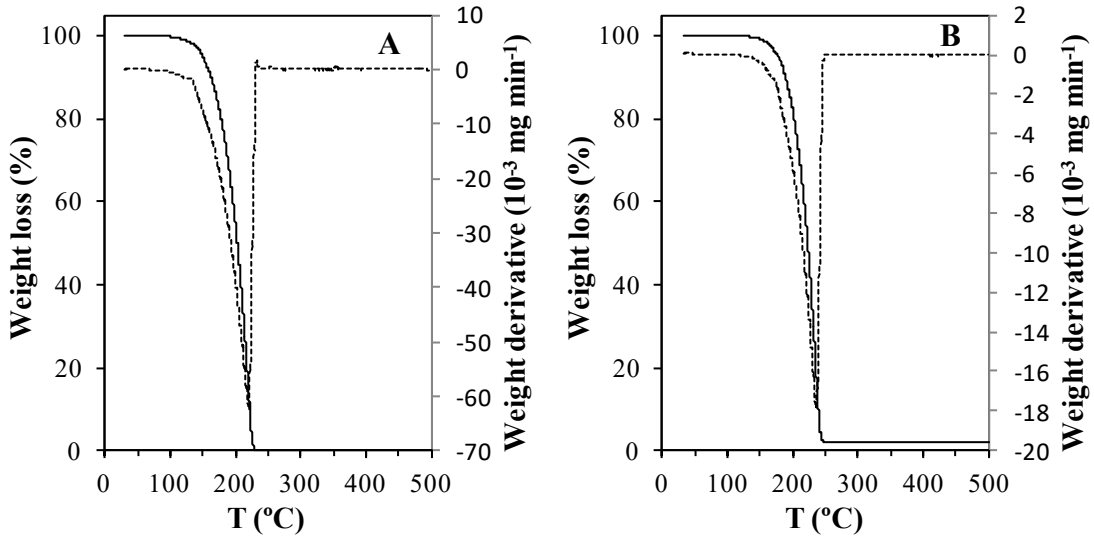

Figure 5.14 TG (full lines) and derivative (dotted lines) curves of A) Tz and B) Bz. The TG analyses were performed under N_2 atmosphere.

As shown in Fig. 5.14, both electrolytes evaporated during the TG analyses. This behavior was reported in literature using similar electrolytes.[272]

The Tz evaporates between around 165 and 226 ºC with rapid weight loss at 221 ºC while Bz evaporates between around 195 and 242 ºC with rapid weight loss at ~236 ºC.

This information was useful to evaluate the weight percentage of the electrolytes existing in the pellets of oxide/electrolyte composites. In other words, it can be assumed the mass lost during the heating corresponds to the evaporation of the electrolytes. So comparing the TG data for the pellets of composite oxide/electrolyte after the EIS measurements with the TG data of the pellets before EIS measurements (using the same batch), it is possible to know if there was electrolyte evaporation during the heating. This loss is not expected since the maximum temperature of the EIS measurements was settled up to 110 and 160 ºC for Tz and Bz, respectively.

Figure 5.15 shows the TG analyses for 0.3 ms-*a*TO(SBA) and 0.3 mp-BZO using both electrolytes as representative examples.

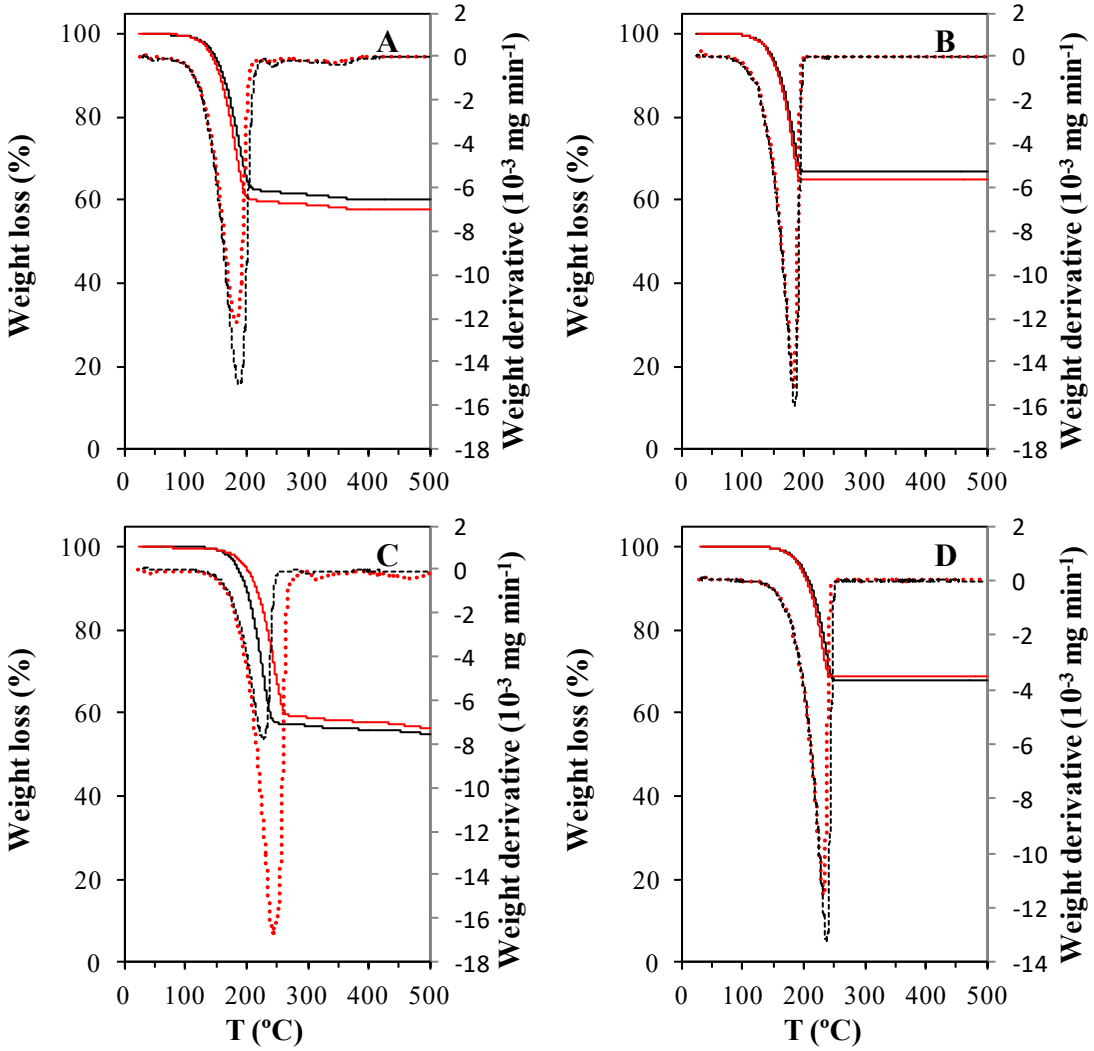

Figure 5.15 TG (full lines) and derivative (dotted lines) curves of: A) 0.3 ms-*a*TO(SBA)/Tz; B) 0.3 mp-BZO/Tz; C) 0.3 ms-*a*TO(SBA)/Bz; and D) 0.3 mp-BZO/Bz. Pellets before (black lines) and pellets after EIS measurements (red lines). The TG analyses were performed under N_2 atmosphere.

The TG data of the composites in Fig. 5.15 confirm the absence of mass loss during the EIS measurements. The fraction of mass lost in heating up to 500 °C is in accordance with the expected and corresponds to the mass of electrolyte in the oxide/electrolyte composite (Table 5.3). Table 5.3 also presents the temperature range of the evaporation of the electrolyte in the composites and for pure electrolytes.

Table 5.3 Values of: mass fraction, volume fraction and temperature range of the evaporation for electrolytes.

Sample	Conditions [a)]	Mass fraction of electrolyte [b)]	Volume fraction of electrolyte [c)]	Temperature range of the evaporation (ºC)
Tz	Fresh powder [d)]	1	1	165-226
0.3 ms-*a*TO(SBA)/Tz	Before	0.40	0.65	149-208
	After	0.42	0.67	143-199
0.3 mp-BZO/Tz	Before	0.33	0.69	144-193
	After	0.35	0.71	141-190
Bz	Fresh powder	1	1	195-242
0.3 ms-*a*TO(SBA)/Bz	Before	0.45	0.72	186-239
	After	0.44	0.71	199-259
0.3 mp-BZO/Bz	Before	0.32	0.71	189-243
	After	0.31	0.70	187-240

[a)] The EIS measurements performed up to 110 or 160 ºC for Tz or Bz composites, respectively; [b)] obtained through the analysis of the TG dada; [c)] the volume fraction was calculated taking into account the densities of electrolytes and oxides present in Tables 1.2, 2.3 and 3.2; [d)] the Tz was left in the oven at 110 ºC during 16 h before TG analysis.

As shown in Table 5.3 the mass fraction of electrolytes corresponds to a volume fraction equal to 0.7. In general the evaporation temperature of the oxides slightly decreases in presence of the oxide.

6 Electrical behavior of nano-ionic composites

This chapter is divided into two subchapters. The first subchapter starts with the characterization of the individual components of the nanocomposites. Thereafter the preliminary impedance spectroscopy data collected, for electrolytes, in dry air and N_2 are presented and compared to justify the measuring conditions selected for the subsequent electrical characterization of the materials. The second subchapter is dedicated to the characterization of oxide/electrolyte composites. It is divided in three main sections. First, the impedance data collected in dry air and N_2 for composites are presented. Section 6.2.1 is dedicated to the electrical characterization of np-CO in Tz and Bz. In section 6.2.2 the data for ms-CO(SBA) are compared with the data for np-CO. The influence of oxide composition on the conductivity is studied in section 6.2.3, using composites based in cerium oxide. This is followed by a comparison of the results obtained for various oxides (ZrO_2 TiO_2, np-BCO, and mp-BZO).

6.1 Characterization of the individual components

Figure 6.1 shows a comparative Arrhenius plot of the conductivity of np-CO powder compacts prepared in this Thesis, with conductivity for the other relevant oxides extrapolated from literature data measured on dense ceramic samples at high temperatures.[273-277] All materials show extremely low conductivity at temperatures below 200 °C. In all cases also, electronic charge carriers and particularly electron holes are expected to be the dominant charge carriers in dry oxidant or moderately reducing conditions. The activation energy is close to 100 kJ mol^{-1} (or slightly higher) for all cases, except for the ZrO_2 nanotubes, where the lower value (~43 kJ mol^{-1}) is ascribed to preferential transport along the surface at temperature lower than 450 °C, whereas at higher temperatures the activation energy approaches 100 kJ mol^{-1} which is typical for bulk transport.[274] On the same ground, one could in principle exclude the possibility for a surface transport for the nanocrystalline CeO_2 tested in this Thesis, given the high E_a measured for the np-CO powder compact (130 kJ.mol^{-1}). However, as for ZrO_2,[274] the higher conductivity for the

np-CO powder compact is higher than for a CO ceramic, obviously less porous and with much smaller grain boundary density (Fig. 6.1), suggests that the contribution of surface transport cannot be totally ruled out in these materials at temperatures of the order of 100 °C or lower. In fact, ceria easily adsorbs water, which is lost at temperatures close to 400 °C.[278] Nanocrystalline ceria is able to retain adsorbed even under nominally dry atmospheres in the range 300 – 600 °C.[279] It is not totally unexpected the observation of protonic conductivity in ceria-based nanoceramics under wet atmosphere at room temperature.[280, 281] Therefore, surface proton transport in np-CO may not be impossible, despite the pretreatment at 500 °C of the CO nanopowders.

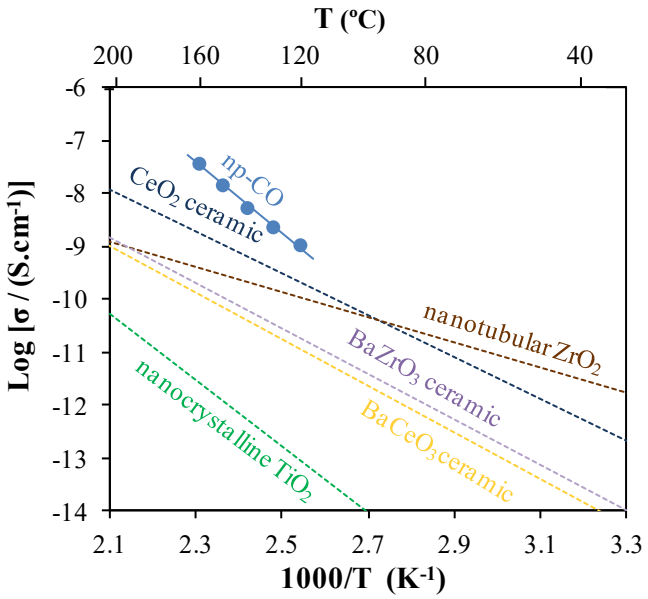

Figure 6.1 Arrhenius plots of the conductivity of a np-CO powder compact compared to literature data obtained by extrapolation to low temperature for the various oxides tested in this work, namely blue - CeO_2 ceramic,[273] brown - nanotubular ZrO_2 films, [274] green – nanocrystalline TiO_2 (grain size 260 nm),[275] yellow - $BaCeO_3$ ceramic,[276] and purple - $BaZrO_3$ ceramic.[277] Data collected in air except for np-CO and ZrO_2 nanotubes where N_2 was used.

The conductivity of the electrolytes was measured at temperatures below their melting (Table 1.2). To prevent the pellet degradation, the measurements were initially performed in dry air in the range from 40 °C to 105 ºC for pure Tz, and between 40 °C and 120 ºC for Bz. After that the measurements were performed in N_2 and the maximum of temperature was increased to 110 ºC for Tz, and 160 ºC for Bz. Electrodes made of silver paste or platinum/carbon were tested in order to obtain the best adhesion to the pellet surface, which being a powder compact was not fully mechanically stable. In summary, three pellets of Tz and four of Bz were tested using various combinations of electrodes and atmosphere, and the obtained results are displayed in the Arrhenius plots of Figs. 6.2. Bz shows lower conductivity than the Tz up to 110 ºC because the self-

dissociation constant for Bz is about 3 orders of magnitude lower than the self-dissociation constant for Tz (Table 1.2). This means that there are less protons available for the conduction in Bz.

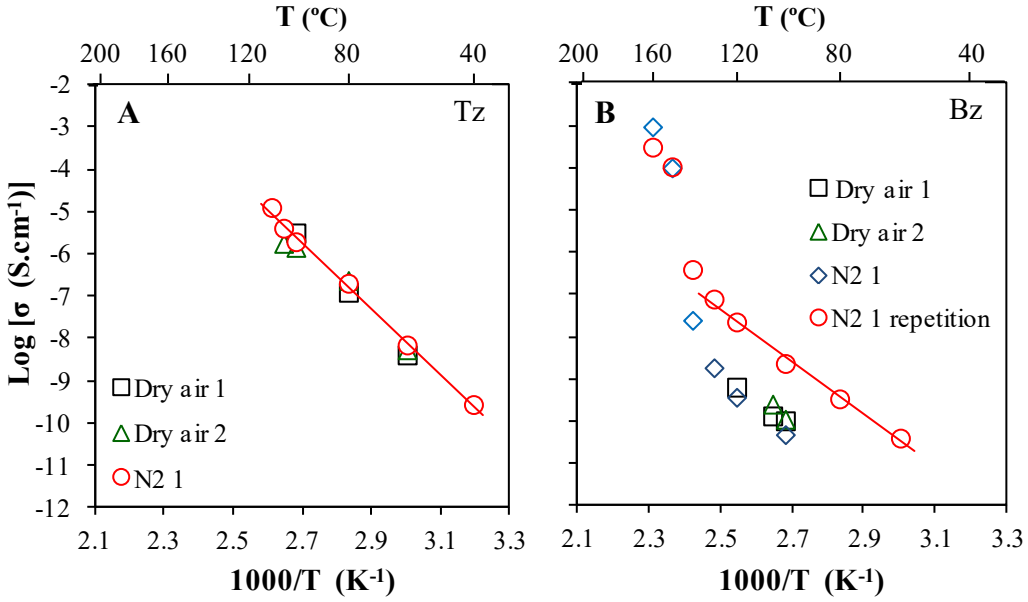

Figure 6.2 Arrhenius plots of the conductivity of A) Tz and B) Bz in dry air and N_2 atmospheres. Measurements identified with 1 and 2 were performed on samples with silver paste and platinum/carbon/Nafion electrodes, respectively

The data measured in N_2 for Bz show an Arrhenius behavior up to 130 ºC (E_a=122 kJ.mol^{-1}). Near the melting point of Bz the conductivity increases spectacularly, in agreement with the literature [92]. The same effect it also expected for Tz [93], but not observed in the Fig. 6.2 A simply because the melting point of Tz (ca. 120ºC) was not attained. The E_a = 152 kJ.mol^{-1} is slightly higher than for Bz, but all in all comparable and suggesting similar conduction mechanisms, different only in the concentration of charge carriers which, as mentioned, is higher in Tz. Contrary to the oxides with predominant electronic transport, both Tz and Bz are electrolytes and therefore intrinsic ionic conductors. No major differences in conductivity are observed when using either Ag or Pt/C electrodes, and thus the former was retained for all subsequent measurements. In this regard, one notes the SEM micrographs confirming that the viscosity of the silver paint is sufficiently high to prevent the impregnation of the porous powder compacts pellets (Fig. 6.3).

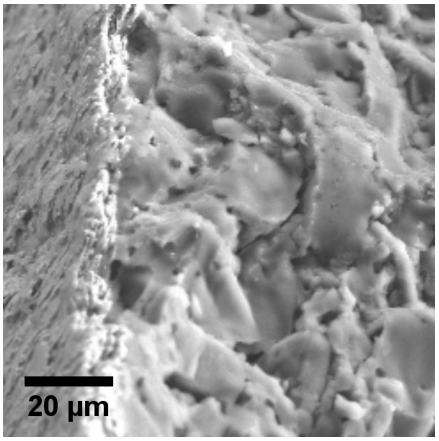

Figure 6.3 SEM micrographs of a Bz pellet showing the silver electrodes on top, collected after EIS measurements at 120 °C.

6.2 Characterization of oxide/electrolyte composites

The same experimental protocols were tested in selected samples looking for potential effect of the atmosphere on the composites. Measurements carried out in dry air and N_2 yielded virtually identical results (Fig. 6.4). This demonstrates that the slightly reducing N_2 atmosphere does not introduce any major change in the conductivity (possible for e.g. CeO_2), while it allows more stable conditions for the organic electrolytes by precluding oxidation. Also noteworthy is that all measurements were carried out in nominally dry conditions to minimize the contribution of water protons to the conductivity.

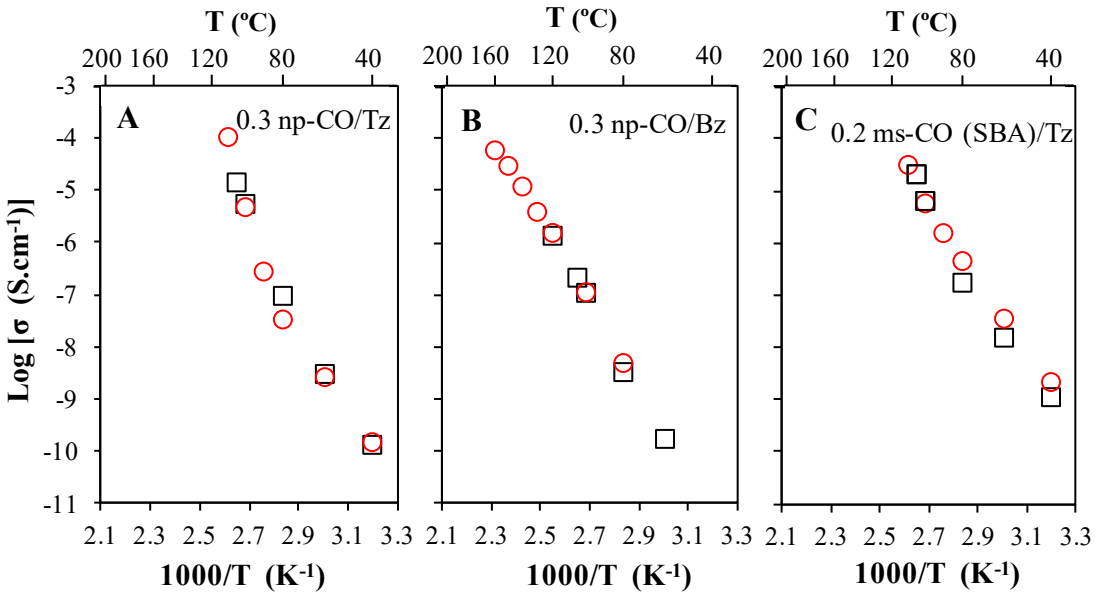

Figure 6.4 Arrhenius plots of the conductivity of composites A) 0.3 np-CO/Tz, B) 0.3 np-CO/Bz and C) 0.2 ms-CO(SBA-15)/Tz measured in dry air and N_2.

Nevertheless, experimental constraints of availability of gas dictated that composites based in ms-CO(SBA)/Tz, ms-CO(SBA)/Bz, np-*a*TO/Bz and mp-*r*TO/Bz were characterized in dry air.

Another preliminary note for the interpretation of the impedance spectra is convenient at this point. In some cases, the Nyquist plots for the composite show more than one contribution. As an example, Fig.6.5 A displays spectra with distinct contributions appearing at high frequency (HF), intermediate frequency (IF) and low frequency (LF). It can be seen that both the HF and IF contributions are independent of the test signal amplitude, thus suggesting they are related to the ohmic resistance of the material. On the contrary, the LF contribution is heavily affected by the applied voltage, which strongly suggests that it is linked to the electrode processes. However, the interpretation of some of the spectra may be even be more complex, with the IF region showing also some dependence on the signal amplitude (Fig. 6.5 B) or on an applied DC bias. In the following section dedicated to the electrical characterization of np-CO using different electrolytes, one retains as a first description of the impedance spectra simple equivalent circuits comprising a series of two or three parallel R||CPE subcircuits, in order to obtain resistance, capacitance and relaxation frequency values characterizing the evolution of each one of these contributions with the composition of the composite and the temperature.

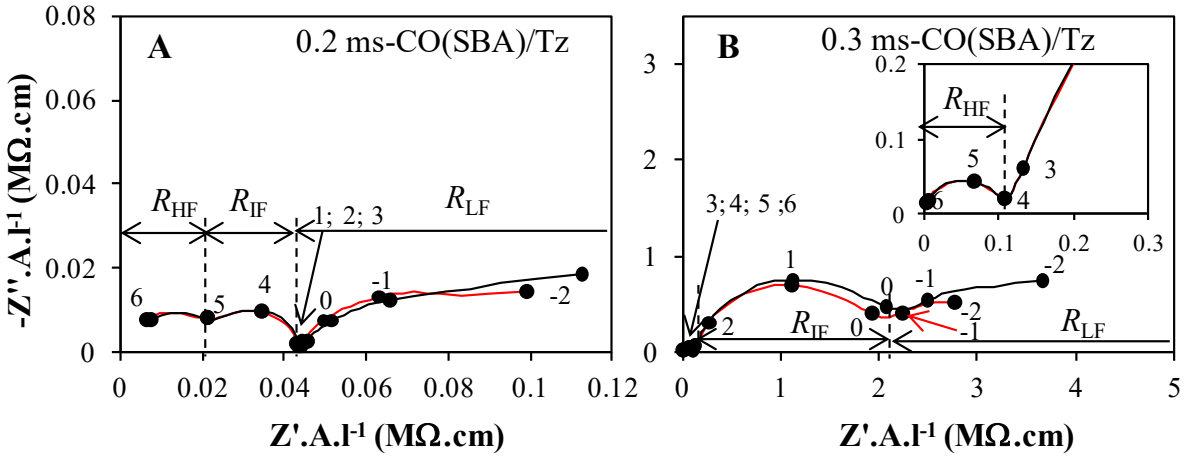

Figure 6.5 Nyquist plots of A) 0.2 ms-CO(SBA)/Tz collected at 105 ºC and B) 0.3 ms-CO(SBA)/Tz collected at 80 ºC, using test signal amplitude of black - 0.1 V and red - 0.3 V. The numbers represent powers of 10 of frequency in Hz.

6.2.1 Nano CeO_2 with triazole and benzimidazole

Figure 6.6 shows Nyquist plots normalized to the maximum of the real component of the impedance of np-CO/Tz composites. This representation hides the decrease of the magnitude of the impedance with increasing temperature, which is the typical semiconducting behavior found in the materials tested in this Thesis, but it allows a direct comparison of the influence of φ_{oxide} on the shape of the spectra. It can be seen that the pure Tz pellet shows one single semicircle through the entire temperature range. There is an obvious shift of this semicircle towards higher frequencies with increasing temperature due to the inherent semiconducting nature of this essentially ionic conductor (the resistance decreases leading to an increase of ω according to Eq. 1.18). The addition of the ceria nanoparticles leads to the onset of a second contribution in the impedance spectra of the composites. These two semicircles, strongly overlapping for low oxide contents, get clearly separated for φ_{oxide}=0.3 and φ_{oxide}=0.4, and tend to be more clearly distinguished at intermediate temperatures. Their relative magnitude varies significantly with both temperature and composition. At temperatures above 90 ºC a third contribution appears as a tail at low frequencies, which can be attributed to the electrode impedance.

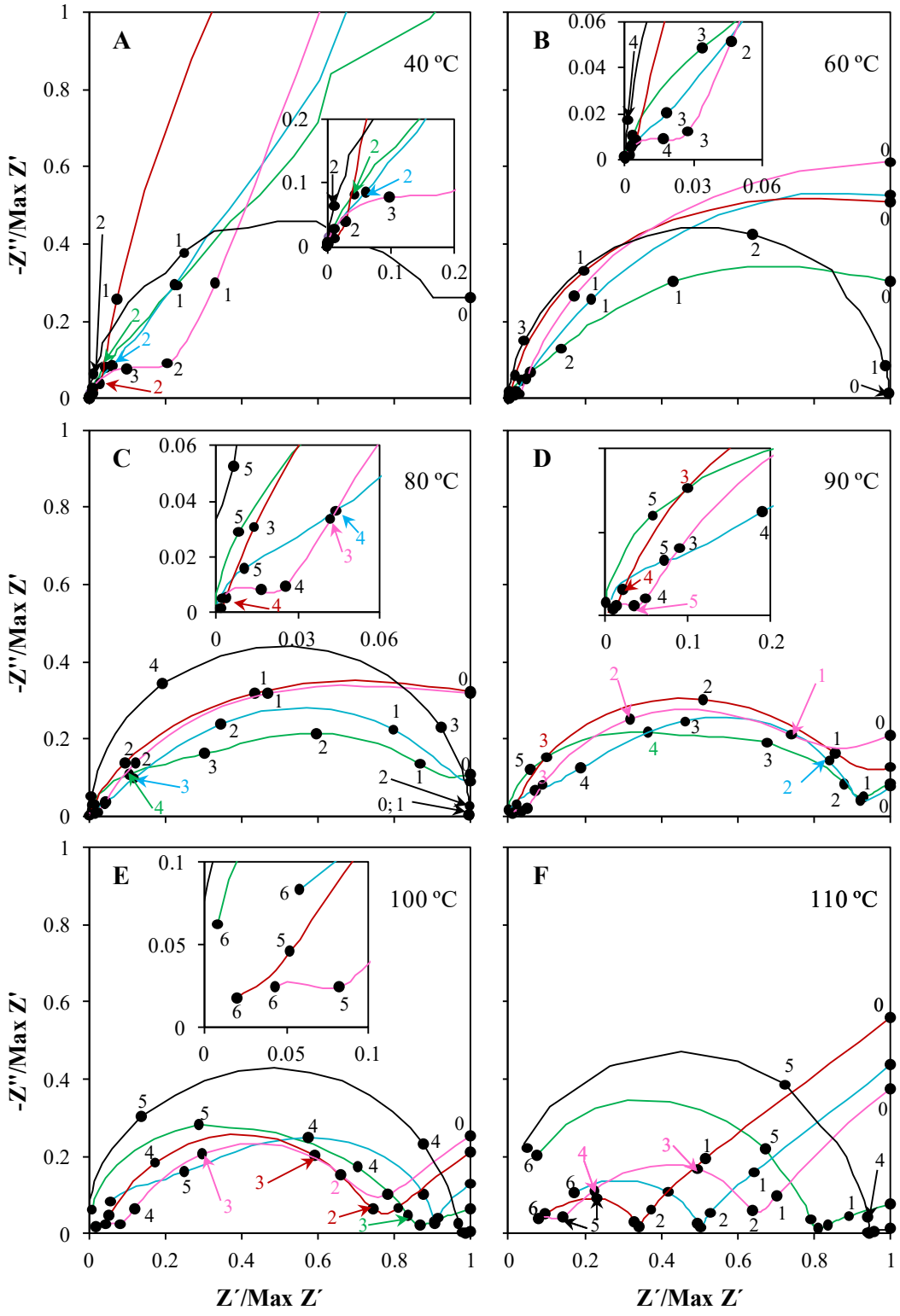

Figure 6.6 Normalized Nyquist plots of the np-CO/Tz composites at various temperatures for black-φ_{oxide}=0 , green-φ_{oxide}=0.1, blue-φ_{oxide}=0.2, red-φ_{oxide}=0.3 and pink-φ_{oxide}=0.4. The small numbers represent powers of 10 of the frequency in Hz.

Fitting the spectra of composites in Fig. 6.6 to the equivalent circuit comprising two R||CPE elements, one fitting the HF contribution and another fitting the IF one, is relatively straightforward. The evolution of the resistance, capacitance and relaxation frequency are plotted as function φ_{oxide} in Fig. 6.7, excluding the LF electrode impedance for clarity.

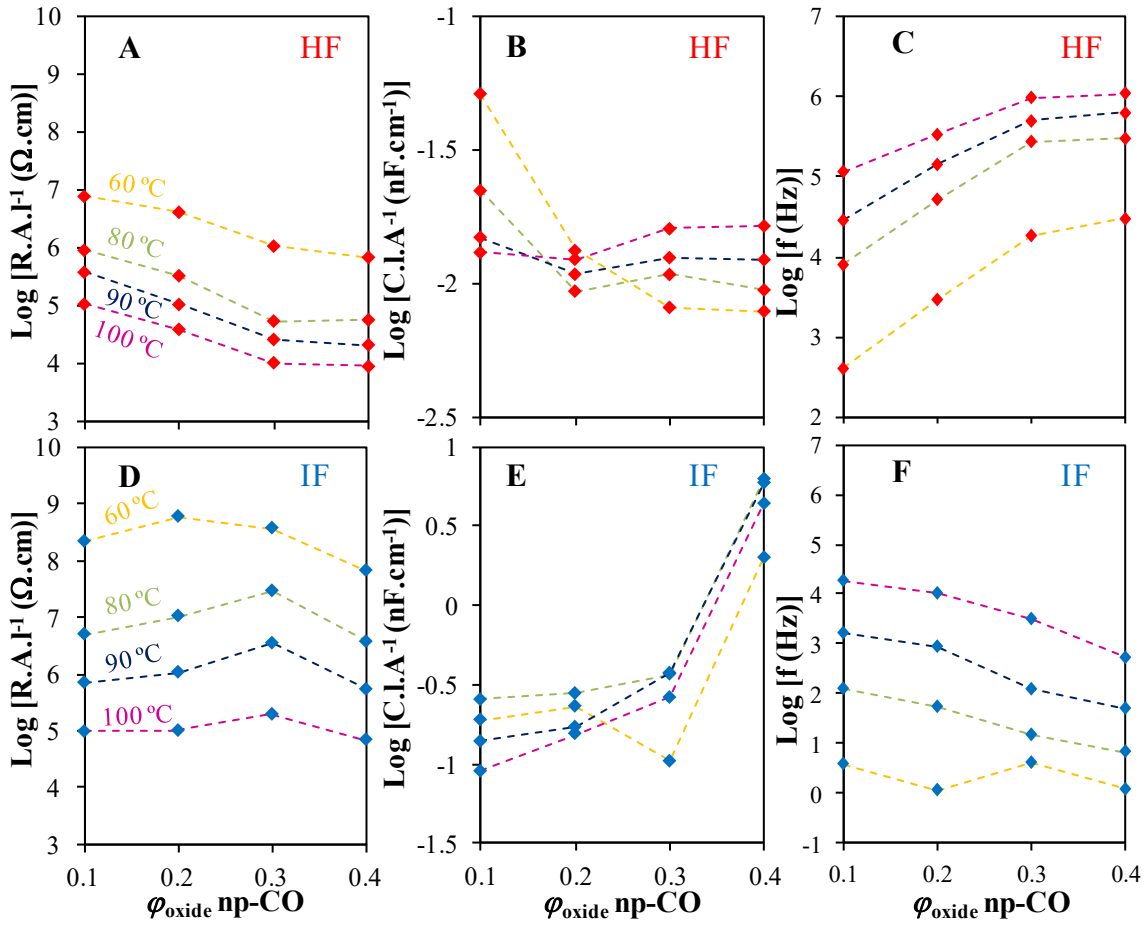

Figure 6.7 Evolution the resistance, capacitance and relaxation frequency of the HF and IF contributions as function of φ_{oxide} for the np-CO/Tz composites at yelow-60 ºC, green-80 ºC, blue-90 ºC and pink-100 ºC.

As shown in Fig. 6.7, R_{HF} decreases progressively by one order of magnitude with the addition 30%-40% ceria particles. R_{IF} displays a different tendency, featuring a maximum for about 20%-30% np-CO, but the overall variation is smaller than for R_{HF}, not exceeding 5 times. Also noteworthy is that R_{IF} is generally larger than R_{HF}, although differences decrease with increasing temperature. The stronger temperature dependence of R_{IF} is indicative of higher activation energy (effect to be addressed subsequently in this Thesis). As for the resistance, the capacitance of the IF contribution is higher than that of HF. Both C_{HF} and C_{IF} show an obvious compositional effect, the former decreasing and the latter increasing with increasing np-CO content, respectively. The compositional trends exhibited by the relaxation frequency reflect the impact of the ceria content

according to Eq. 2.21. The increase of ω_0 at HF is determined by the decrease of both R_{HF} and C_{HF} observed with increasing φ_{oxide}, whereas at IF ω_0 decreases essentially due to the increase of C_{IF} (Fig. 6.7).

The behavior of benzimidazole-ceria composites displays very similar trends to their triazole counterparts, although the two impedance contributions appear with a stronger overlapping. This can be seen in Fig. 6.8, which shows the normalized Nyquist plots for different φ_{oxide} at different temperatures.

The shape of the impedance spectra changes upon addition of the oxide particles, progressively leading to the appearance of 2 semicircles with peak frequencies different from the original single semicircle of pure Bz. The separation between these contributions is hardly discernible for φ_{oxide}=0.1 and φ_{oxide}=0.2, but the slight asymmetry and depression of the spectra clearly demonstrates the onset of new phenomena.

The np-CO/Bz composites with $\varphi_{oxide}\geq$0.3 do reveal the two distinct HF and IF semicircles. Due to the different activation energies, the separation of the two semicircles is best appreciated at temperatures in the range 100 °C - 130 °C. These major differences between Bz and Tz-based composites are determined by the much higher electrical resistivity of Bz, which precluded precise measurements at the temperatures lower than 80 °C. For this reason also, the np-CO/Bz composites show ω_0 at frequencies lower than Tz-based materials.

Due to the higher resistances and the stronger overlapping between the semicircles, the fitting of the spectra with the two R||CPE series circuit was possible only for samples with φ_{oxide}=0.3 and φ_{oxide}=0.4, which coupled to different temperature range used in the measurements preclude a systematic analysis of the data for the entire compositional range (as depicted for Tz-base materials in Fig. 6.7). The data for the composites with φ_{oxide}=0.1 and φ_{oxide}=0.2 was carried out with a single R||CPE element, which reflects an average of the two contributions.

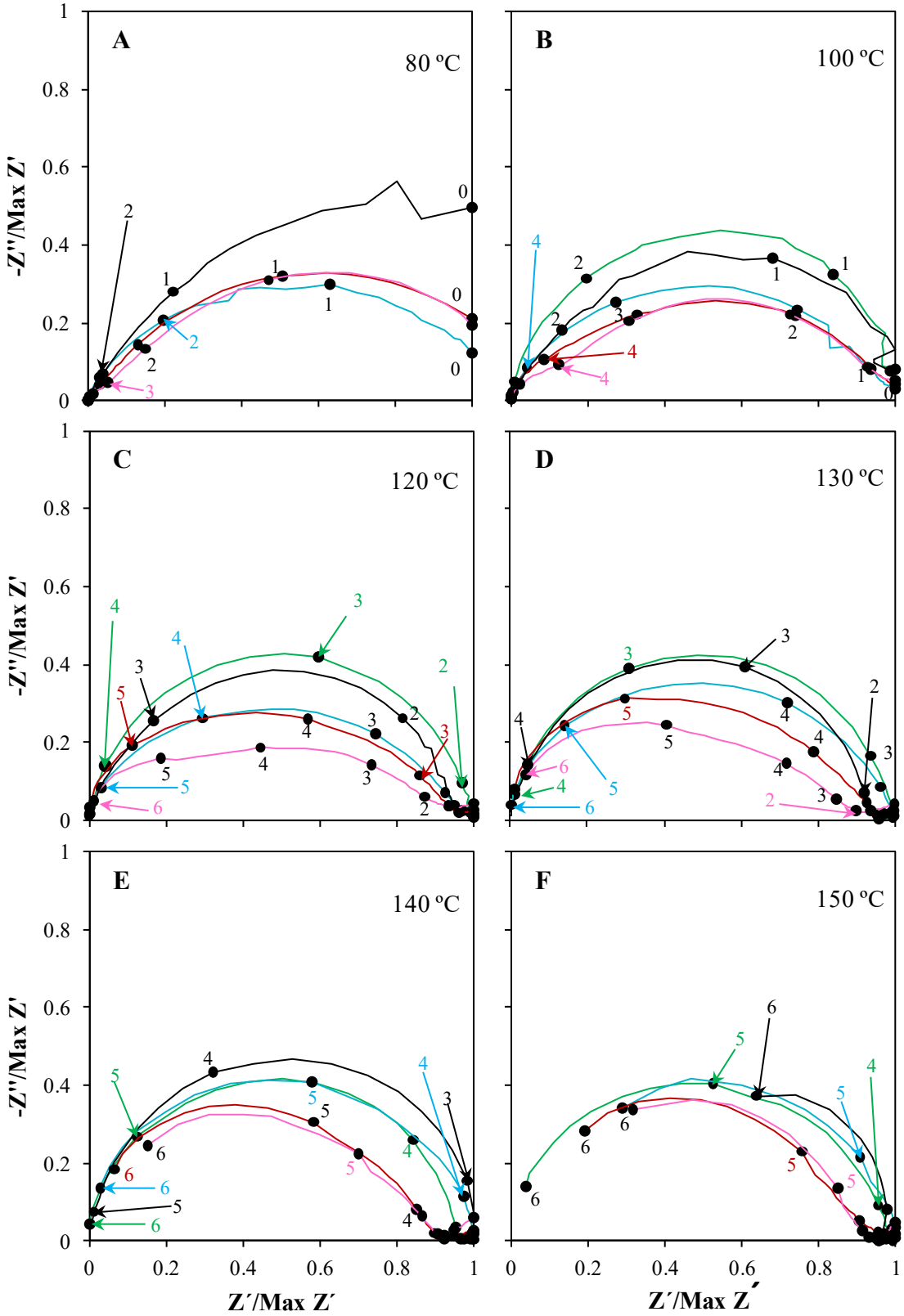

Figure 6.8 Normalized Nyquist plot of np-CO/Bz composites at various temperatures for black-φ_{oxide}=0, green-φ_{oxide}=0.1, blue-φ_{oxide}=0.2, red-φ_{oxide}=0.3 and pink-φ_{oxide}=0.4. The numbers represent powers of 10 of frequency in Hz.

The total impedance and the impedance of the partial HF and IF contributions is systematized in Figs. 6.9 and 6.10 by plotting the corresponding conductivity values (obtained through Eq. 2.24) in Arrhenius coordinates, for the Tz- and Bz-based composites, respectively. The data for the pure electrolytes and for pure ceria are also shown for the sake of comparison.

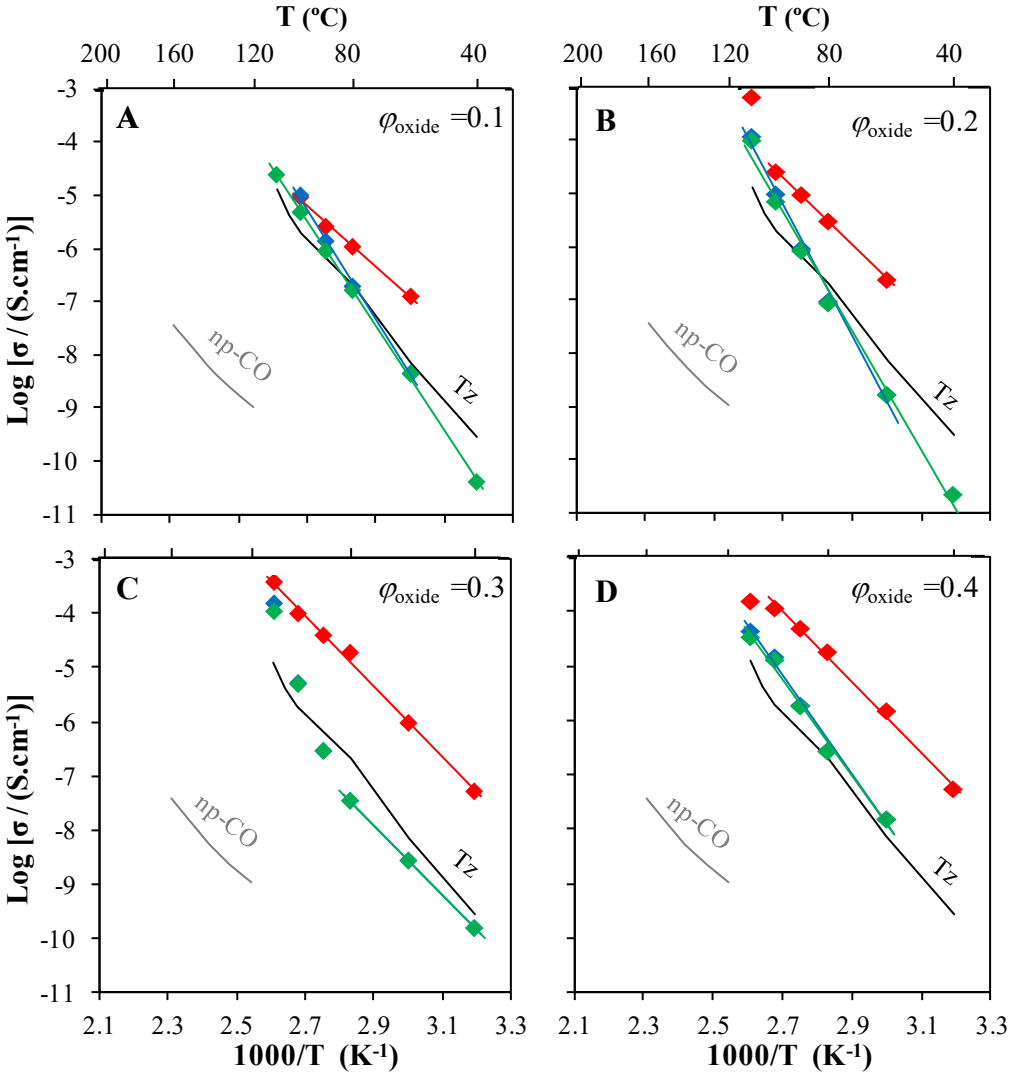

Figure 6.9 Arrhenius plots for the ◆-total conductivity and the conductivity associated to the ◆-HF and ◆-IF contributions for np-CO/Tz composites with different φ_{oxide}. Reference conductivity values for np-CO and Tz are also shown.

The figure shows a progressive increase of the total conductivity of np-CO/Tz composites with increasing ceria content at temperatures above *ca*. 80 °C. At 100 °C, the conductivity enhancement at φ_{oxide}=0.4 can be of almost one order of magnitude with respect to pure Tz, and more than five orders of magnitude in comparison to np-CO. It is also immediately apparent from these plots that the magnitude of the conductivity enhancement decreases with decreasing temperature, with only

the sample with φ_{oxide}=0.4 depicting higher conductivity than pure Tz, and this only down to 60 °C. At lower temperatures, one can guess a conductivity of the composite lower than pure Tz due to the high activation energy of the IF impedance.

. Following the previous analyses of the impedance spectra, it can be seen that the total conductivity is essentially determined by IF impedance. However, it is the HF conductivity that increases most with increasing fraction of oxide particles, and it is also this contribution with the weakest temperature dependence. In fact, for low ceria content (φ_{oxide}=0.1 and φ_{oxide}=0.2) it is the IF conductivity the contribution with the highest activation energy (even higher than pure Tz, Table 6.1). One will return to this discussion of the after analyzing the data obtained for the np-CO/Bz composites presented in Fig. 6.10.

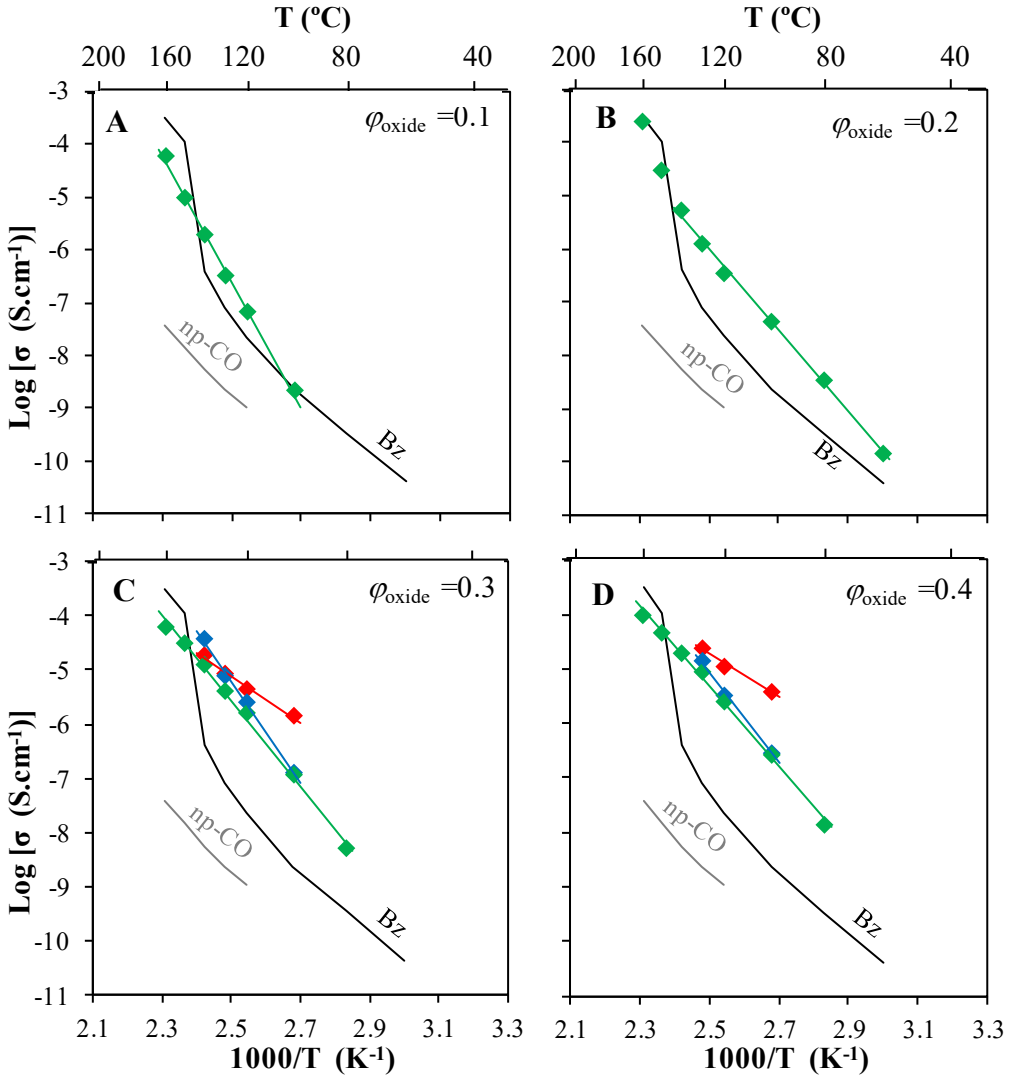

Figure 6.10 Arrhenius plots for the ◆-total conductivity and the conductivity associated to the ◆-HF and ◆-IF contributions for np-CO/Bz composites with different φ_{oxide}. Reference conductivity values for np-CO and Bz are also shown.

Like the Tz-based materials, np-CO/Bz composites depict an obvious conductivity enhancement in comparison to pure Bz, which in this case exceeds more than two orders of magnitude. Likewise, the total conductivity is mostly controlled by the IF impedance contribution, more noticeably for low oxide fractions ($\varphi_{oxide} \leq 0.2$). The HF conductivity is distinctively higher than the IF contribution, although the differences are much smaller than in the case of np-CO/Tz. In fact, both phenomena contribute nearly equally to the total conductivity at 120 °C. The increased relative contribution of the HF conductivity to the total conductivity certainly contributes to explain the greater conductivity enhancement observed for the Bz materials. Excluding the sharp increase in conductivity observed at temperatures close to the melting point of Bz, the activation energy of the various conductivities again reinforces the similarities with the np-CO/Tz composites (Table 6.1).

Table 6.1 Total electrical conductivity at 100 ºC and the activation energy for the total ($E_{a,\,total}$), HF ($E_{a,\,HF}$) and IF ($E_{a,\,IF}$) conductivity contributions of np-CO-based composites.

	σ_{total} (S·cm^{-1}) at 100 °C		E_a (kJ.mol^{-1})	
φ_{oxide}	**Tz**	**Bz**	**Tz**	**Bz**
0	2.0×10^{-6}	2.4×10^{-9}	152 [c]	122 [c]
0.1	5.0×10^{-6}	2.3×10^{-9}	112 [a] 201 [b] 191 [c]	231 [c]
0.2	7.2×10^{-6}	4.5×10^{-8}	124 [a] 238 [b] 217 [c]	149 [c]
0.3	4.9×10^{-6}	1.2×10^{-7}	128 [a] 127 [b] 127 [c]	84 [a] 183 [b] 154 [c]
0.4	1.3×10^{-5}	2.6×10^{-7}	127 [a] 177 [b] 173 [c]	78 [a] 163 [b] 144 [c]
1	1.2×10^{-10} [d]		130 [c]	

[a] $E_{a,\,HF}$; [b] $E_{a,\,IF}$; [c] $E_{a,\,total}$; [d] Obtained by extrapolation.

This mesoscopic effect agrees with the underlying Thesis of this work that the conductivity of a weak electrolyte may be enhanced by the addition of non-conductive nanoparticles leading to the formation of highly conductive space-charge regions along the particle-electrolyte interface. As shown by the Zeta potential measurements (Chapter 4), the particles surface tends to become more negative upon addition of Tz, and especially Bz due to the selective anion adsorption. Consequently, one expects the formation of a surface layer enriched in benzimidazole or triazole

cations. The observed conductivity enhancement can be explained by the existence of a sufficient number of percolating, highly conductive space-charge regions located around the ceria particles. Recalling Chapter 4 of this Thesis, the Zeta potential of the ceria particles is much lower when mixed to Bz than to Tz. This can be explained by the much lower concentration of Bz cations in the bulk of the dispersion than of Tz cations in equivalent situation, which by leading to a lower ionic strength of the Bz medium allows for an expansion of the Debye length and thus to a wider space–charge region than when the ceria particles are in contact with Tz. Therefore, one expects for the BZ composites a larger difference in conductivity between the interfacial space-charge regions and the bulk of the Bz electrolyte than in the case of the Tz-based system, in excellent agreement with results reported here.

It is important to notice that all E_a values, and particularly those for the composites (Table 6.1), are significantly higher than those normally observed for proton migration in this type of hetero-cycles above the melting temperature (e.g. 22 $kJ.mol^{-1}$ for imidazole and its composite with TiO_2 [124]). This reflects the stronger nature bounds of the crystalline phases, which in the case of Bz and Tz are predominantly covalent. Lower values are to be expected in materials with predominant ionic character.

The question remains of knowing to which phenomenon may one ascribe the HF and IF contributions to the total conductivity. In a generalized point of view, the impedance of this kind of oxide-electrolyte composites can be originated mainly from four parallel contributions, as depicted by the model schematized in Fig. 6.11. Branch I represents the contribution from the oxide particles, which may, in principle, be considered negligible since the impedance of CeO_2 at these low temperatures (<100 °C) and in the absence of humidity is much higher than that of pure Tz or Bz. Due to the low conductivity of CeO_2 (mostly electronic, as opposed to the predominant ionic transport in the two studied electrolytes), temperatures of the order of 200-300 °C are necessary to observe a bulk semicircle contribution in the impedance spectra within the frequency range available with the meter used in this work. Clearly, the bulk conductivity of ceria cannot explain neither of the two semi-circles observed in the composites contribution semicircle, hence pointing to an interfacial contribution. As such, the dominant ionic transport through the contiguous Tz or Bz electrolyte phase (branch IV) is more likely considering the higher conductivity of these phases in comparison with pure CeO_2. Yet, the conductivity of the composites is higher than that of Tz or Bz and a third possibility must be considered. This third region corresponds to the space-charge layer at the oxide/electrolyte interface with an enhanced concentration of mobile cations, which would correspond to another parallel path (branch III). Any model containing simply parallel branches cannot fit the two HF and IF contributions with distinct relaxation frequencies apparent in the impedance spectra of the composites. And in fact, for a situation where the interfacial space-

charge regions are separated by some amount of electrolyte, one may assume a fourth alternative path for ion transport where diffusion from the space-charge region of one particle to another implies diffusion over a finite length of pure electrolyte (path II in Fig. 6.11B), therefore generating one additional impedance in series with the impedance of the oxide/electrolyte interface (circuit branch II in Fig. 6.11A).

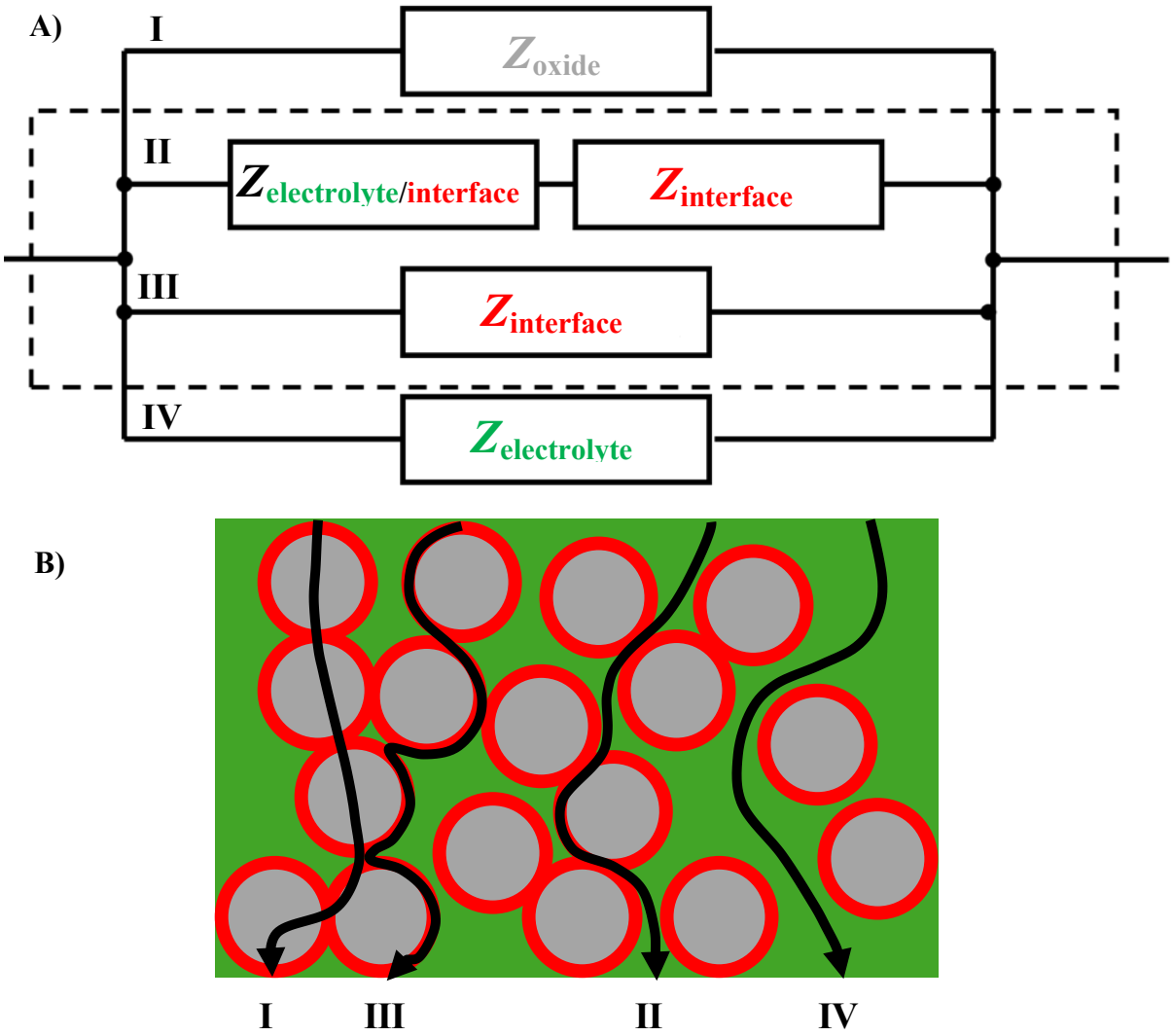

Figure 6.11 A) General equivalent circuit model grouping all the schematic situations described in B), with different contributions to the total impedance of composites comprising one electrolyte (Tz or Bz) and oxide particles, namely from the bulk of each phase, the space charge regions at the oxide/electrolyte interface and from the interfaces between them.

Assuming this model, the spectra for φ_{oxide}=0 should depict one single semicircle corresponding to $Z_{electrolyte}$. Adding a small amount of oxide nanoparticles immediately generates space-charge regions with impedance $Z_{interface}$. These regions are separated by thin electrolyte regions with an

impedance $Z_{electrolyte/interface}$. Transport across these two regions implies a series association of $Z_{interface}$ + $Z_{electrolyte/interface}$, and for small amounts of oxide nanoparticles $Z_{interface}$ should dominate the overall behavior in this branch. Subsequent increase of the fraction of nanoparticles increases the volume of space-charge regions which become increasingly percolated and thus the relative contribution of $Z_{interface}$ becomes progressively smaller with respect to $Z_{electrolyte/interface}$. Full percolation should be attained at a sufficiently high fraction of oxide particles, and the impedance should eventually be dominated by $Z_{interface}$. This provides a complete interpretation of the evolution of the impedance spectra in Figs. 6.6. and 6.8 assuming $Z_{HF} \equiv Z_{interface}$ and $Z_{IF} \equiv Z_{electrolyte/interface}$.

Going beyond the qualitative description, however, is a difficult task because in the equivalent circuit branches parallel to branch II ($Z_{interface}$ + $Z_{electrolyte/interface}$) may be active in certain situations. For example, the comparatively high conductivity of pure Tz means that branch IV in the generalized equivalent circuit of Fig. 6.11A should not be neglected. This means that the results of the fitting presented in Figs. 6.9 and 6.10 are likely to be underestimated, particularly for low particle fractions, when the charge transport through the electrolyte (path IV in Fig. 6.11 B) may represent a $Z_{electrolyte}$ value low enough to decrease the real amplitude of the semicircles in the parallel branch $Z_{interface}$ + $Z_{electrolyte/interface}$ (see Fig. 2.7 and underlying comments). Likewise, in the case of the Bz composites the value of $Z_{interface}$ in branch III (Fig. 6.11B) may also be considerably lower than the total impedance of branch II ($Z_{interface}$ + $Z_{electrolyte/interface}$), thus leading to larger differences between Z_{HF} and $Z_{interface}$, and particularly in the intermediate frequency range between Z_{IF} and $Z_{electrolyte/interface}$.

6.2.2 Influence of mesoporosity in CeO_2–based composites

The Nyquist plots presented in Fig. 6.12 show that the impedance spectra of composites with mesoporous ceria also show two contributions. In comparison to the nanocrystalline ceria, these two contributions appear clearly better resolved for the mesoporous materials. The evolution with composition follows the same patter described in the previous section for np-CO, with the two contributions appearing with increasing separation for higher ceria fractions, and again better resolved for the Tz composites in comparison to the Bz-based materials. The deconvolutions of the spectra with the series R||CPE+R||CPE equivalent circuit was possible for a broad set of conditions and the results are represented in Arrhenius coordinates in Figs. 6.13 and 6.14.

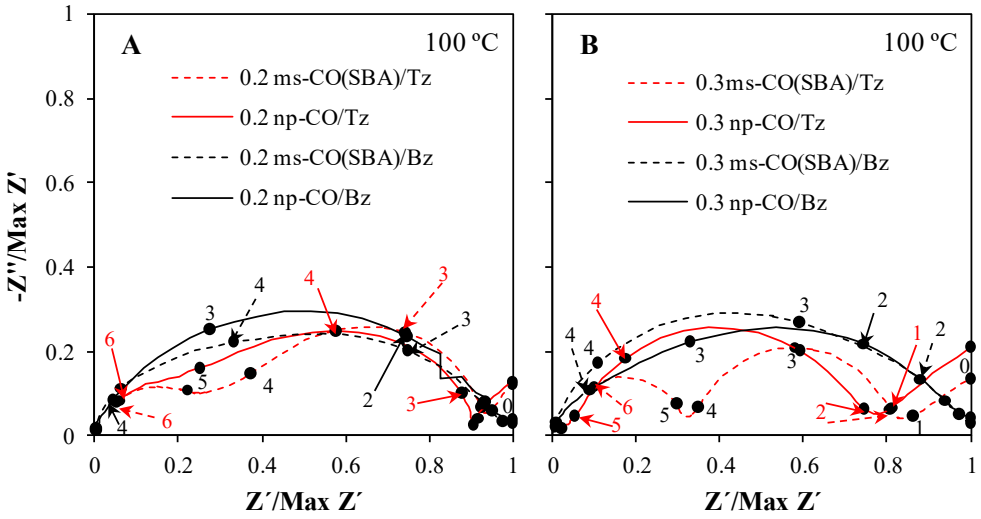

Figure 6.12 Nyquist plots obtained at 100 ºC for Tz and Bz composites containing A) 20% and B) 30% of nanocrystalline and mesoporous CeO_2.

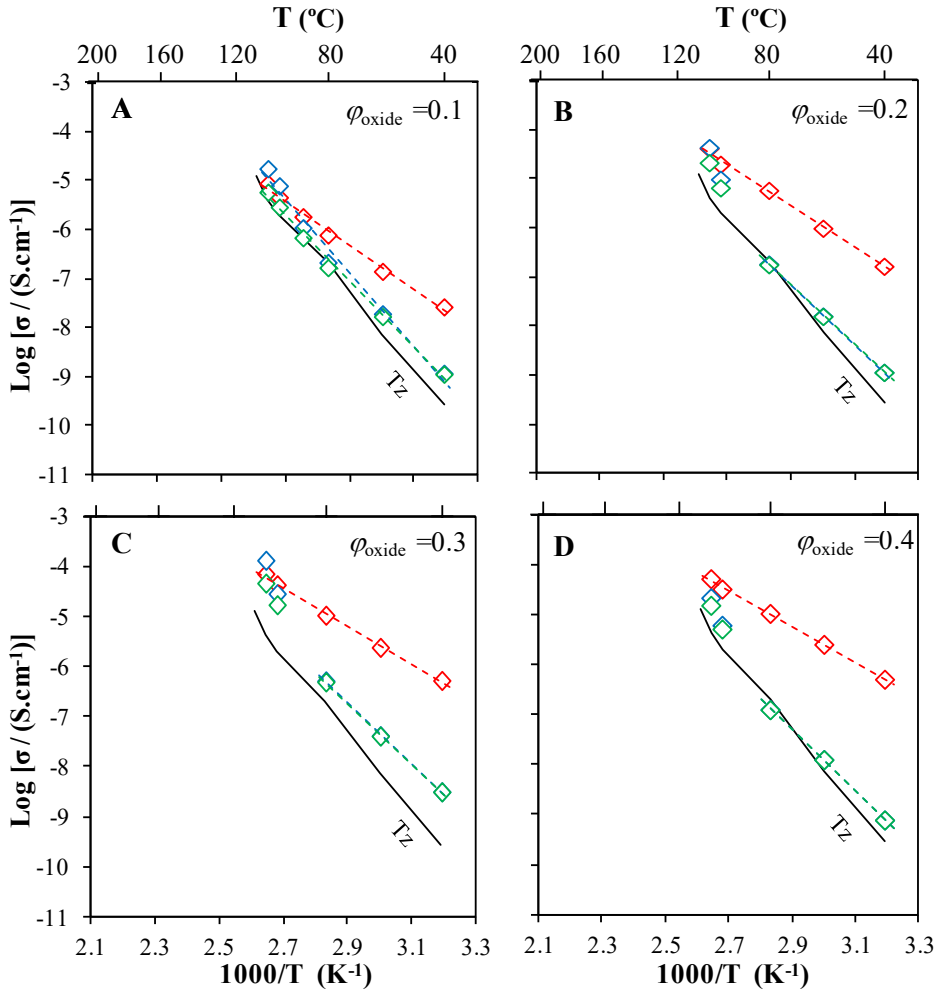

Figure 6.13 Arrhenius plots for the ◇-total conductivity and the conductivity associated to the ◇-HF and ◇-IF contributions for ms-CO(SBA)/Tz composites with different φoxide . Conductivity values for pure Tz (dark solid line) are also shown.

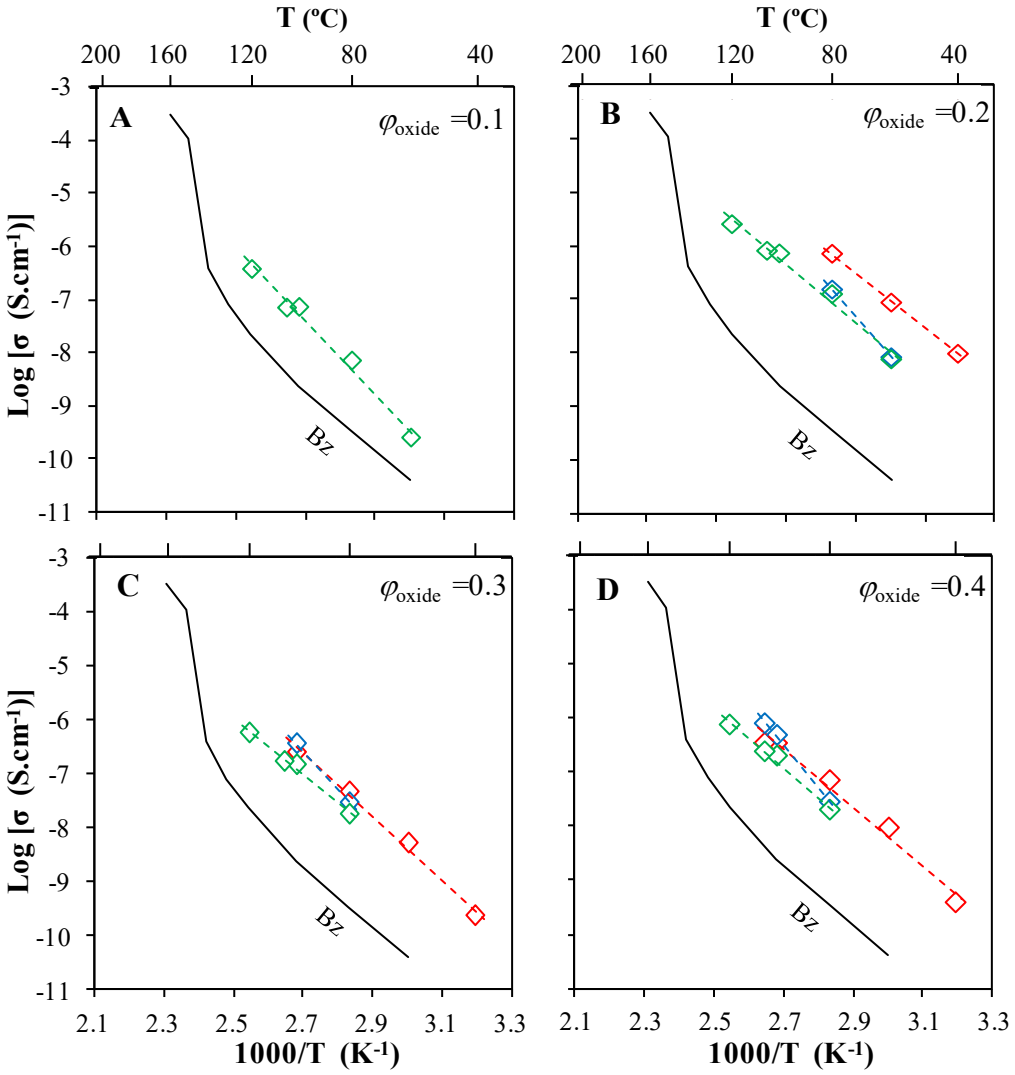

Figure 6.14 Arrhenius plots for the ◇-total conductivity and the conductivity associated to the ◇-HF and ◇-IF contributions for ms-CO(SBA)/Bz composites with different φ_{oxide}. Conductivity values for pure Bz (dark solid line) is also shown.

In general, the total conductivity for the ms-CO(SBA)-based materials is higher than for np-CO, but the difference with respect to the pure electrolytes varies in a different manner with composition for each of these cases. The maximum conductivity enhancement in the Tz materials is attained for $\varphi_{oxide=}$ 0.3, whereas for Bz materials this is apparent already for φ_{oxide}= 0.1 and 0.2. Again, one can see from the simple inspection of the above figures that the magnitude of the enhancement is clearly higher for the Bz composites.

Table 6.2 compares the activation energies of composites with ms-CO(SBA) with Tz and Bz electrolytes. The activation energy for the HF conductivity is lower than for the IF for both Tz and Bz electrolytes, but the values for Tz are distinctly lower. Moreover, they decrease with increasing

oxide fraction, reaching 66 kJ.mol^{-1} for φ_{oxide}=0.4. These values are much lower than those measured for the Tz with np-CO particles (in the range 120-130 kJ.mol^{-1} for all samples, Table 6.1), which may indicate an energetically less demanding transport mechanism in the mesopores than along the surface of the ceria nanoparticles, perhaps resulting from a less ordered (perhaps even amorphous) Tz phase within the pores. However, taking the activation energy as a fingerprint of the dominant transport mechanism, the total conductivity of the Tz composites with mesoporous ceria is controlled by the IF impedance, just as found for the ceria nanoparticles. The composites with benzimidazole display clearly higher activation energy for the two conductivity components, but in this case the similarities between $E_{a,total}$ and $E_{a,HF}$ suggest that in these composites the total conductivity of the composites is mostly determined by the interfaces. This trend is analogous to that observed for the np-CO/Bz composites, but significant differences in E_a are apparent between the two series of composites. Somewhat surprisingly (and contrary to what happens with the Tz composites), the $E_{a,HF}$ for ms-CO(SBA)/Bz is higher than for np-CO/Bz (~100 kJ.mol^{-1} vs. ~80 kJ.mol^{-1}). The reason for such behavior is not clear, but it may at least partly be due to the uncertainty in the fitting results resulting from the strong overlapping of both contributions in the case of the Bz composites.

Table 6.2 Activation energy for the total ($E_{a,total}$), HF ($E_{a,HF}$) and IF ($E_{a,IF}$) conductivity contributions of ms-CO(SBA)-based composites.

	E_a (kJ.mol^{-1})	
φ_{oxide}	**Tz**	**Bz**
0	152 [c]	122 [c]
0.1	89 [a] 146 [b] 131 [c]	134 [c]
0.2	84 [a] 119 [b] 119 [c]	102 [a] 145 [b] 107 [c]
0.3	76 [a] 120 [b] 119 [c]	115 [a] 141 [b] 103 [c]
0.4	66 [a] 120 [b] 120 [c]	100 [a] 153 [b] 108 [c]

[a] $E_{a\ HF}$, [b] $E_{a\ IF}$, [c]) $E_{a,total}$

Nevertheless, it goes without any doubt that the conductivity enhancement due to the mesoporous particles is clearly higher than that observed for equivalent volume fraction of nanoparticles, despite the higher density of the latter samples. The difference between the two composite systems is illustrated by Figure 6.15.

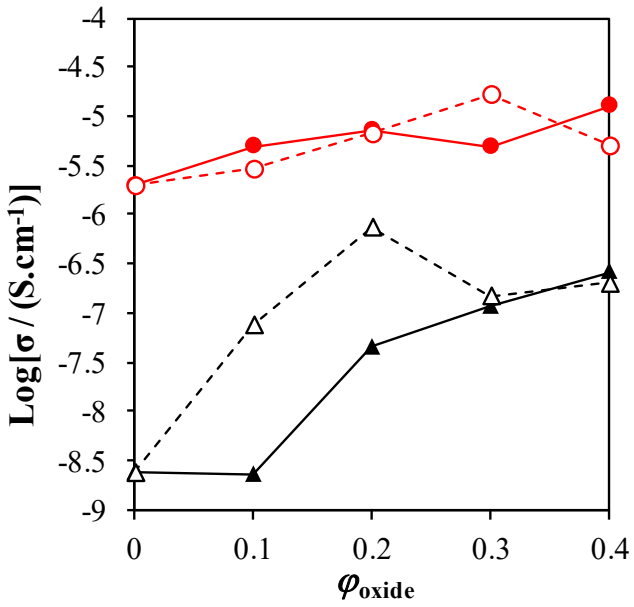

Figure 6.15 Total conductivity measured at 100 ºC as a function of the oxide volume fraction for composites with nanocrystalline (solid line) and mesoporous (dashed line) ceria particles on Tz (red) and Bz (black) electrolytes.

For the Tz-based composites the benefit of the heterogeneous doping is relatively small by the reasons invoked in the previous section, which are related to the high defect concentration in the bulk of the Tz electrolyte. Using mesoporous dopant does not change the picture much, with the actual enhancement due to doping remaining modest. This can be understood assuming again that the space-charge layer formed in the Tz at the surface of the nanoparticles or the mesopores is very thin, and certainly much smaller than the pore diameter (see Eq. 1.16 and underlying comments).

On the contrary, the initial low defect concentration in Bz allows for a quite marked mesoscopic effect of the dopant already observed for the nanoparticles. As shown in Fig. 6.15, mesoporosity strongly enhances this effect with the conductivity enhancement attaining well above two orders of magnitude for just 20 vol.% of ms-CO(SBA) particles, which is more than ten times the improvement obtained for the same amount of np-CO. Further addition of ms-CO(SBA) lead to a slight decrease of the conductivity, which could be due to the higher porosity of these samples (see Fig. 5.13).

According to Eq. 1.21, mesoporosity is leads to an increase of the conductivity of the composites because of two main factors. The first is related with the ratio of the surface area to the volume of

the dopant (Ω), with the increased of Ω leading to proportional conductivity enhancements. For the same volume of particles, Ω is essentially determined by the specific surface area. The increase in area in S_{BET} of the ceria dopant from 66 $m^2.g^{-1}$ for np-CO to 149 $m^2.g^{-1}$ for ms-CO(SBA) corresponds to an increase of Ω by 2.25 times. Figure 6.15 shows a conductivity enhancement by more than 100 times for the Bz composites with 20 vol.% ms-CO(SBA), and thus differences in the Ω value are an unlikely explanation for an effect of such magnitude. The second factor is associated to the existence of pores with size of the order of the Debye length, which allows the bulk of the pores to behave very much like the particle/electrolyte interface. In other words, the concentration of ionic defects would be strongly enhanced within the pores, hence providing preferential fast ion transport paths (Fig. 1.15 C). As shown by Fig. 1.15 B, one may expect the defect concentration at the surface of the particle to be close to 100 times higher than in the bulk. Once more recalling the analysis of the space-charge properties presented in section 1.4.1, the concentration profile (and the thickness of the space charge layer) will depend mostly on the space-electrostatic potential at the particle surface, and the higher the potential difference with respect to the bulk of the electrolyte the higher will be the concentration profile. The ms-CO(SBA) particles have stronger electrostatic interactions with Bz than np-CO (apparent in the larger Zeta potential) differences, see Fig. 4.1), which thus promote a wider space-charge layer. This combined with a diameter of pore channels close to 3.5 nm, offer the potential for the observed extraordinary enhancement of the conductivity observed when heterogeneously doping Bz with the mesoporous ceria.

While the effect is indeed extraordinary, the intrinsic low conductivity of Bz (and of Tz, for that matter) means that even when enhanced by more than two orders of magnitude, to a range between 10^{-7} $S.cm^{-1}$ and 10^{-6} $S.cm^{-1}$ (or close to 10^{-5} $S.cm^{-1}$ for composites based on Tz). The conductivity of these composites with ceria it is still insufficient for most applications, and certainly for energy conversion (desirably higher than 0.01 $S.cm^{-1}$). In the following section one explores the effect of the oxide composition combined with mesoporosity in order to assess the potential of heterogeneous doping to improve the ionic conductivity of Tz and Bz.

6.2.3 Influence of the oxide composition

Figures 6.16 show a summary of total conductivity measured at 100 °C plotted as a function of the oxide content for all the composites prepared in this Thesis, separated in two panels for Tz and Bz matrices. Each panel in the figure compares data for oxides used as conventional nanoparticles with the corresponding mesoporous counterparts (except for the BCO and BZO, where one could not obtain the oxide in the mesoporous form). The reader is referred to Appendix II for the full set of data obtained at other temperatures.

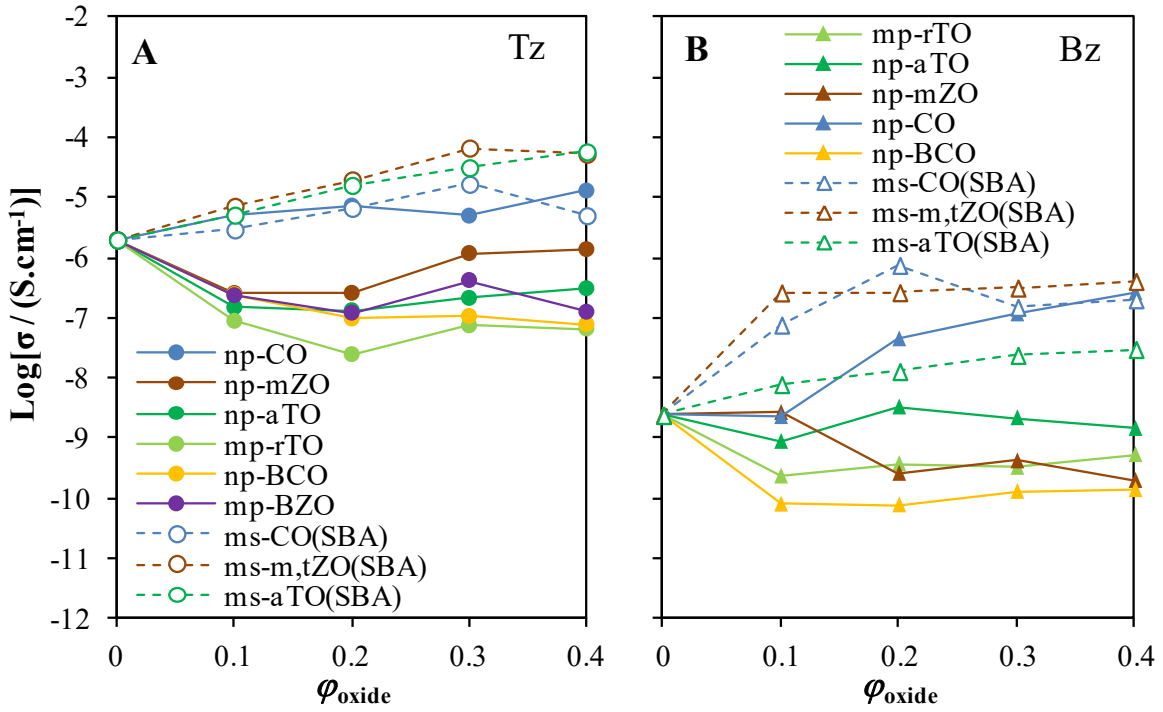

Figure 6.16 Graphic representation of the total conductivity measured at 100 ºC as a function of φ_{oxide} for: A) Tz and B) Bz.

Analogously to the behavior of the ceria-containing composites, one sees for mesoporous zirconia and titania a clear enhancement of the conductivity with respect to the pure electrolytes. As expected, the Bz composites show lower conductivity than the Tz composites for the same temperature and composition, due to the aforementioned differences in pK_a, and in good agreement with the Zeta potential measurements (see Chapter 4). In the Tz composites both zirconia and titania achieve higher conductivity than ceria, with a slight advantage for zirconia probably due to the higher specific surface area (which is 194 $m^2.g^{-1}$ for ms-*m,t*ZO(SBA),142 $m^2.g^{-1}$ for ms-*a*TO(SBA) and 149 $m^2.g^{-1}$ for ms-CO(SBA)). The slight decrease of conductivity observed for the composite with 40 vol.% mesoporous zirconia is likely to be caused by the higher porosity of this sample (Fig. 5.13 B).

Porosity, as noticed for the ceria-based materials, is likely to have greater impact on the Bz-based composites, particularly when doped with ms-*a*TO(SBA) or ms-*m,t*ZO(SBA). These composites achieve more than 20% porosity for φ_{oxide}=0.3, or close to 30% for φ_{oxide}=0.4 (Fig. 5.13). However, even with such high level of porosity, mesoporous zirconia is still very efficient in promoting a conductivity enhancement by more than two orders of magnitude for just φ_{oxide}=0.1, again better than ceria. However, adding more ms-*m,t*ZO(SBA) particles has no apparent benefit, with the conductivity reaching a plateau and converging to the values of the ceria composites. This could indeed be the result of an increasing porosity that counters the expected mesoscopic conductivity enhancement.

Porosity may also be a key factor explaining the apparent low efficiency of mesoporous titania as dopant. It should be noticed that the surface area is unlikely to explain the observed differences in face of the similarities of the values for the three mesoporous oxides. On the other hand, the weak Zeta potential changes observed for the ms-aTO(SBA) powders with Bz also suggests that titania should be a less efficient dopant than ceria to promote the formation of space-charge layers. This argument should hold also for ms-*m,t*ZO(SBA), where the changes of the Zeta potential in the presence of Bz are relatively minor, but where the conductivity enhancement is similar to that achieved with ceria.

The other and last parameter with potential effect on the space-charge concentration profile is the diameter of the mesopores. This has been found to be 3.4-3.7 nm for ms-CO(SBA) and 3.5-3.9 nm ms-*a*TO(SBA), but clearly larger for ms-*m,t*ZO(SBA), where it varies between 4.0 and 4.7 nm (Table 3.2). Small pores may lead to an excessive concentration of ions within the pore which is equivalent to a compression of the Debye layer and thus leading to smaller nano-ionic effect. On the other hand, an excessive ion concentration in small pores may also lead to stronger electrostatic interactions between ions, thus reducing their mobility and hence the conductivity. Larger pores could represent a more ideal situation on allowing a wider concentration gradient between the surface and the bulk of the pore, and weaker electrostatic interactions in the less concentrated medium.

The results observed for the mesoporous oxides should thus be the result of a complex interplay of the various factors, and cannot be simply explained in the terms of the underlying formalism presented in Section 1.4. In fact, this formalism cannot interpret the results for the conventional oxides because, with the sole exception of the ceria nanoparticles, all the other oxides lead to a significant degradation of the conductivity of the composites in comparison with the pure electrolytes. The effect tends to be somewhat larger for the Tz materials, in which series there are apparent conductivity minima for φ_{oxide}=0.2. These minima also appear in the Bz series, although not so clear. The existence such minima exclude any strong correlation with porosity, as this tends to increase monotonically with increasing φ_{oxide} (Fig. 5.13). Likewise, a simple bulk effect is not obvious as one would expect a progressive decrease of the conductivity by addition of the less

conductive oxide particles (all oxides are less conductive than Tz and Bz). The main difference between np-CO and the other powders is the high specific surface area, which is 66 $m^2.g^{-1}$ whereas for the other oxides the surface area varies from 3 to 16 $m^2.g^{-1}$ (Table 2.3 and 3.3). This would represent a Ω 5 to 20 times higher for np-CO, which obviously cannot explain the spectacular differences between this oxide and the others. The only reasonable explanation is related to the poor homogeneity of the mixtures, which precludes the efficient percolation of the interfacial particles for modest oxide contents. Some improvement is expected for higher oxide fractions, as suggested by some of the data presented in Fig. 6.16, but the values were not attained in the compositional ranges studied in this work.

7

Conclusion and outlook

A new mechanism of proton conduction based in the heterogeneous doping of weak electrolytes with oxide particles was studied. This mechanism is based on the formation of the space layers between the oxide particles and electrolyte leading to the formation of proton-enriched space-charge layers at the electrolyte/particle interface, and thus boosting conductivity with respect to the undoped electrolyte.

The first step of this work was the preparation of the hard templates, SBA-15 and CMK-3, to be used as templates. The syntheses allow obtaining SBA-15 with hexagonal arrangement of mesopores and CMK-3 with hexagonal arrays of carbon nanorods. Both templates show high S_{BET}. The CMK-3 is a negative replica of SBA-15.

The second step of the work consisted on the preparation of mesoporous CeO_2, ZrO_2, and TiO_2 materials by replication of SBA-15 silica-based hard template. However, ZrO_2 and TiO_2 showed a disordered mesostructure after removal of the template. Evidences of reaction between the silica template and the oxide precursors were found. On the contrary, an exact negative replica of the ordered SBA-15 was obtained for CeO_2, with no apparent reaction between Si and Ce.

To avoid the reaction with the silicon of the SBA-15, CMK-3 was used as template. The products obtained, ms-*t*ZO(CMK) and ms-*a*TO(CMK), were not homogeneous in terms of morphology. All mesoporous oxides prepared using SBA-15 present a residual amount of silicon, namely Si:Ce=0.12, Si:Zr=0.13 and Si:Ti=0.02. The same happened when the CMK-3 was used: Si:Zr=0.28, Si:Ti=0.06. The change of template could not prevent the remaining of silicon impurities in the material. This may be justified by diffusional problems of the washing solution during the dissolution of the hard template. As CMK-3 is prepared by replication of SBA-15, it suffers from the same.

The synthesis of the mesoporous complex multimetallic oxides $BaZrO_3$ with perovskite structure using nanocasting was attained. ms-BZO(CMK) was obtained with success, after some attempts using the two different templates and different precursors. The product obtained showed a disorder wormlike porosity. However the ms-BZYO(CMK) based in the synthesis of ms-BZO(CMK) was not obtained after several attempts.

Considering the previous data, it is necessary to optimize the synthesis mesoporous complex multimetallic oxides with perovskite using hard templates, maybe using different precursors or/and experimental procedures namely choosing different calcination temperatures for the processing. Besides the mesoporous oxides, np-BCO were prepared using soft template. It was not possible to achieve homogeneous samples in terms of morphologies.

The ζ measurements were performed to assess the difference in the surface charge of the oxides upon electrolyte addition. The instability of the suspensions of the oxides was critical for the measurements. This instability was more evident in cases of ms-CO(SBA) and commercial ZrO_2 samples leading to differences between the ζ measured for the suspensions before addition of the electrolyte. In general, ζ decreases with increasing fraction of the electrolyte, in full agreement with anion adsorption at the oxide surface. It is also apparent that the magnitude of the effect is distinctively larger for the Bz and Iz due to the lower self-dissociation constant of these electrolytes in comparison with Tz and Pz.

The pellets of oxide/electrolyte composites showed a high densification. No structure and microstructure were detected during all stages of this work.

For EIS measurements the Tz and Bz were selected as electrolytes and ms-CO(SBA), np-CO, ms-*m*,*t*ZO(SBA), np-*m*ZO, ms-*a*TO(SBA), np-*a*TO, mp-*r*TO, mp-BZO and np-BCO were used as oxides.

Independently of the used atmosphere (dry air or nitrogen), the EIS measurements gave similar results. As expected, the EIS data showed that the proton conductivity in anhydrous conditions of the oxide/electrolyte composites increases with increasing φ_{oxide} and with the mesoporosity. The mesoscopic effect is more evident in case of benzimidazole because of the low ionic concentration in the bulk. This allows a higher potential difference with respect to the dopant surface, thus extending the space-charge layer thickness and consequently the volume of the conducting interfaces. The effect is equally observed in the triazole electrolytes, but with lower magnitude. This was attributed to the high ionic strength of the medium, which compresses the Debye length thus reducing the space-charge layer.

These trends, however, are complex and not observed for all oxides. In fact, from the conventional, non-mesoporous oxides only ceria nanoparticles worked as an efficient promoter of the conductivity of the composites. All the other oxides lead to a degradation of the conductivity. The most likely explanation is related to the low surface area of the materials coupled to a poor homogeneity of the mixture.

This is even more true because if mesoporous oxides with high surface area have demonstrated an enormous potential for the development of nano-ionic materials, it is also true that the production of these materials is far from trivial and it is indeed a solution with potentially high cost.

Nevertheless, one could find a mesoscopic effect which is in general agreement with the statement that the conductivity of a weak electrolyte may be enhanced by the addition of non-conductive nanoparticles leading to the formation of highly conductive space-charge regions along the particle-electrolyte interface.

An equivalent circuit model was established to analyze the impedance spectra of such materials, where for the first time the presence of two semicirles was detected. The relevant parameters extracted from this model could be correlated with microstructural and compositional parameters, providing valuable information for the optimization of such materials.

Despite the increase on the protonic conductivity through the nano-ionic concepts, the values obtained are not yet sufficient for most applications, notably those associated to energy conversion such as fuel cells. The roadmap to improve the protonic conductivity must include the optimization of the microstructural features of non-mesoporous powders, namely in terms of particle size and how this determines the mixing efficiency, is in obvious need for future work in order to fully exploit the potential of this type of materials.

Likewise, it would be interesting to test mesoporous oxides with larger pores, which may allow broader space-charge layers and potentially higher conductivity. This was actually part of the initial work program of this Thesis and indeed zirconia and titania could be obtained with larger pore size using the carbon CMK3 hard template. Unfortunately, the production of such powders is complex and extremely time-consuming, and the test of this optimization strategy remains to be explored in future work.

The variety of the chemical nature of the oxides tested was naturally limited, but ceria emerges as an excellent candidate for future development and optimization, both as nanoparticles and as a mesoporous material. From the view point of composition, it seems that there is no advantage in going to multicomponent oxide such as the perovskites. Fluorites or other simpler structures seem a more reasonable choice, and, from these, silica appears as the immediate justification to continue the work.

Testing the materials in application is also desirable. One may envisage fuel cells if some additional conductivity can be achieved, as this type of materials are indeed interesting for operation in dry conditions. Other applications may include potentiometric sensors, supercapacitors, or others requiring proton exchange membranes. A separate study of the effect of polarization is mandatory, if possible accompanied by the search of suitable electrodes for this totally new class of electrolytes.

8

References

1. Kreuer, K.D., *Proton conductivity: Materials and applications.* Chemistry of Materials, 1996. 8(3). p. 610-641.
2. Minggu, L.J., Daud, W.R.W. and Kassim, M.B., *An overview of photocells and photoreactors for photoelectrochemical water splitting.* International Journal of Hydrogen Energy, 2010. 35(11). p. 5233-5244.
3. Mao, S.S., Shen, S.H. and Guo, L.J., *Nanomaterials for renewable hydrogen production, storage and utilization.* Progress in Natural Science: Materials International, 2012. 22(6). p. 522-534.
4. Alberti, G. and Casciola, M., *Solid state protonic conductors, present main applications and future prospects.* Solid State Ionics, 2001. 145(1-4). p. 3-16.
5. Iwahara, H., Asakura, Y., Katahira, K. and Tanaka, M., *Prospect of hydrogen technology using proton-conducting ceramics.* Solid State Ionics, 2004. 168(3-4). p. 299-310.
6. Colomban, P., *Proton conductors Solids, membranes and gels - materials and devices*. Chemistry of Solid State Materials. 2, 1992. Cambridge University Press, Cambridge.
7. Madhavan, B. and Ashok, A., *Review on nanoperovskites: materials, synthesis, and applications for proton and oxide ion conductivity.* Ionics, 2015. 21(3). p. 601-610.
8. Devanathan, R., *Recent developments in proton exchange membranes for fuel cells.* Energy & Environmental Science, 2008. 1(1). p. 101-119.
9. Kreuer, K.D., Paddison, S.J., Spohr, E. and Schuster, M., *Transport in proton conductors for fuel-cell applications: Simulations, elementary reactions, and phenomenology.* Chemical Reviews, 2004. 104(10). p. 4637-4678.
10. Nagao, M., Kamiya, T., Heo, P., Tomita, A., Hibino, T. and Sano, M., *Proton conduction in In^{3+}-doped SnP_2O_7 at intermediate temperatures.* Journal of the Electrochemical Society, 2006. 153(8). p. A1604-A1609.
11. Jin, Y., Shen, Y. and Hibino, T., *Proton conduction in metal pyrophosphates (MP_2O_7) at intermediate temperatures.* Journal of Materials Chemistry, 2010. 20(30). p. 6214-6217.
12. Kreuer, K.D., *Proton-conducting oxides.* Annual Review of Materials Research, 2003. 33. p. 333-359.

13. Winter, M. and Brodd, R.J., *What are batteries, fuel cells, and supercapacitors?* Chemical Reviews, 2004. 104(10). p. 4245-4269.
14. Zhang, L.W., Chae, S.R., Hendren, Z., Park, J.S. and Wiesner, M.R., *Recent advances in proton exchange membranes for fuel cell applications.* Chemical Engineering Journal, 2012. 204. p. 87-97.
15. Kraytsberg, A. and Ein-Eli, Y., *Review of Advanced Materials for Proton Exchange Membrane Fuel Cells.* Energy & Fuels, 2014. 28(12). p. 7303-7330.
16. Korotcenkov, G., Do Han, S. and Stetter, J.R., *Review of Electrochemical Hydrogen Sensors.* Chemical Reviews, 2009. 109(3). p. 1402-1433.
17. Stetter, J.R. and Li, J., *Amperometric gas sensors - A review.* Chemical Reviews, 2008. 108(2). p. 352-366.
18. Casciola, M. and Costantino, U., *Relative humidity influence on proton conduction of hydrated pellicular zirconium phosphate in hydrogen form.* Solid State Ionics, 1986. 20(1). p. 69-73.
19. Mellander, B.E. and Zhu, B., *High temperature protonic conduction in phosphate-based salts.* Solid State Ionics, 1993. 61(1-3). p. 105-110.
20. Korotcenkov, G., *Handbook of Gas Sensor Materials: Properties, Advantages and Shortcomings*, *Volume 1: Conventional Approaches* 2013, Springer, New York.
21. Phair, J.W. and Badwal, S.P.S., *Review of proton conductors for hydrogen separation.* Ionics, 2006. 12(2). p. 103-115.
22. Gallucci, F., Fernandez, E., Corengia, P. and Annaland, M.V., *Recent advances on membranes and membrane reactors for hydrogen production.* Chemical Engineering Science, 2013. 92. p. 40-66.
23. Iwahara, H., *Hydrogen pumps using proton-conducting ceramics and their applications.* Solid State Ionics, 1999. 125(1-4). p. 271-278.
24. Alberti, G., Casciola, M., Massinelli, L. and Bauer, B., *Polymeric proton conducting membranes for medium temperature fuel cells (110-160 degrees C).* Journal of Membrane Science, 2001. 185(1). p. 73-81.
25. Katahira, K., Kohchi, Y., Shimura, T. and Iwahara, H., *Protonic conduction in Zr-substituted $BaCeO_3$.* Solid State Ionics, 2000. 138(1-2). p. 91-98.
26. Bozkurt, A., *Application of proton conducting polymer electrolytes to electrochromic devices.* Turkish Journal of Chemistry, 2002. 26(5). p. 663-668.
27. Thakur, V.K., Ding, G.Q., Ma, J., Lee, P.S. and Lu, X.H., *Hybrid Materials and Polymer Electrolytes for Electrochromic Device Applications.* Advanced Materials, 2012. 24(30). p. 4071-4096.

28. Granqvist, C.G., *Recent progress in thermochromics and electrochromics: A brief survey.* Thin Solid Films, 2016. 614: p. 90-96.
29. Vaivars, G., Azens A. and Granqvist, C.G., *Proton conducting polymer composites for electrochromic devices.* Solid State Ionics, 1999. 119(1-4). p. 269-273.
30. Mishra, K., Hashmi, S.A. and Rai, D.K., *Nanocomposite blend gel polymer electrolyte for proton battery application.* Journal of Solid State Electrochemistry, 2013. 17(3). p. 785-793.
31. Mishra, K., Hashmi S.A. and Rai, D.K., *Studies on a proton battery using gel polymer electrolyte.* High Performance Polymers, 2014. 26(6). p. 672-676.
32. Wee, G., Larsson, O., Srinivasan, M., Berggren, M., Crispin, X. and Mhaisalkar, S., *Effect of the Ionic Conductivity on the Performance of Polyelectrolyte-Based Supercapacitors.* Advanced Functional Materials, 2010. 20(24). p. 4344-4350.
33. Gao, H. and Lian, K., *Proton-conducting polymer electrolytes and their applications in solid supercapacitors: a review.* Royal Society of Chemistry Advances, 2014. 4(62). p. 33091-33113.
34. Berger, A., Segalman, R.A. and Newman, J., *Material requirements for membrane separators in a water-splitting photoelectrochemical cell.* Energy & Environmental Science, 2014. 7(4). p. 1468-1476.
35. Klaysom, C., Marschall, R., Wang, L.Z., Ladewig, B.P. and Lu, G.Q.M., *Synthesis of composite ion-exchange membranes and their electrochemical properties for desalination applications.* Journal of Materials Chemistry, 2010. 20(22). p. 4669-4674.
36. Marschall, R., Klaysom, C., Mukherji, A., Wark, M., Lu, G.Q.M. and Wang, L., *Composite proton-conducting polymer membranes for clean hydrogen production with solar light in a simple photoelectrochemical compartment cell.* International Journal of Hydrogen Energy, 2012. 37(5). p. 4012-4017.
37. Shao, Y.Y., Yin, G.P., Wang, Z.B. and Gao, Y.Z., *Proton exchange membrane fuel cell from low temperature to high temperature: Material challenges.* Journal of Power Sources, 2007. 167(2). p. 235-242.
38. Bose, S., Kuila, T., Thi, X.L.N., Kim, N.H., Lau, K.T. and Lee, J.H., *Polymer membranes for high temperature proton exchange membrane fuel cell: Recent advances and challenges.* Progress in Polymer Science, 2011. 36(6). p. 813-843.
39. Barbir, F., *PEM Fuel Cells - Theory and practice.* 2005, ed. Dorf R.C., Elsevier Academic Press, Burlington.
40. EG&G Technical Services, Inc., *Fuel Cell Handbook*. 7th ed. 2004, US Deparment of Energy, Morgantown, West Virginia.

41. Dupuis, A.C., *Proton exchange membranes for fuel cells operated at medium temperatures: Materials and experimental techniques.* Progress in Materials Science, 2011. 56(3). p. 289-327.
42. Ye, H., Huang, J., Xu, J.J., Kodiweera, N.K.A.C., Jayakody, J.R.P. and Greenbaum, S G., *New membranes based on ionic liquids for PEM fuel cells at elevated temperatures.* Journal of Power Sources, 2008. 178(2). p. 651-660.
43. Ramaswamy, P., Wong, N.E. and Shimizu, G.K.H., *MOFs as proton conductors - challenges and opportunities.* Chemical Society Reviews, 2014. 43(16). p. 5913-5932.
44. Miura, N. and Yamazoe, N., *Development of new chemical sensors based on low-temperature proton conductors.* Solid State Ionics, 1992. 53. p. 975-982.
45. Mochizuki, K., Kikuchi, T., Sudoh, M., Ishiguro, Y. and Suzuki, T., *Performances of Fuel-Cell-Type CO Sensors Using Each of Polybenzimidazole and Nafion Membranes.* Journal of the Electrochemical Society, 2011. 158(3). p. J71-J75.
46. Yamazoe, N. and Miura, N., *Potentiometric gas sensors for oxidic gases.* Journal of Electroceramics, 1998. 2(4). p. 243-255.
47. Hibino, T. and Iwahara, H., *CO_2 sensors using $BaCeO_3$-based ceramics.* Sensors and Actuators B-Chemical, 1993. 13(1-3). p. 483-485.
48. Yajima, T., Iwahara, H., Koide, K. and Yamamoto, K., *$CaZrO_3$-type hydrogen and steam sensors: trial fabrication and their characteristics.* Sensors and Actuators B-Chemical, 1991. 5(1-4). p. 145-147.
49. Wang, J., *Selectivity coefficients for amperometric sensors.* Talanta, 1994. 41(6). p. 857-863.
50. Moattisirat, D., Poitout, V., Thome, V., Gangnerau, M.N., Zhang, Y., Hu, Y., Wilson, G. S., Lemonnier, F., Klein, J.C. and Reach, G., *Reduction of acetaminophen interference in glucose sensors by a composite nafion membrane: demonstration in rats and man.* Diabetologia, 1994. 37(6). p. 610-616.
51. Peng, Y., Wei, C.W., Liu, Y.N. and Li, J., *Nafion coating the ferrocenylalkanethiol and encapsulated glucose oxidase electrode for amperometric glucose detection.* Analyst, 2011. 136(19). p. 4003-4007.
52. Hubert, T., Boon-Brett, L., Black, G. and Banach, U., *Hydrogen sensors - A review.* Sensors and Actuators B-Chemical, 2011. 157(2). p. 329-352.
53. Lapham, D.P., Schwandt, C., Hills, M.P., Kumar, R. V. and Fray, D. J., *The Detection of Hydrogen in Molten Aluminium.* Ionics, 2002. 8(5-6). p. 391-401.
54. Bakker, E., *Electrochemical sensors.* Analytical Chemistry, 2004. 76(12). p. 3285-3298.

55. Iwahara, H., *Technological challenges in the application of proton conducting ceramics.* Solid State Ionics, 1995. 77. p. 289-298.
56. Sundmacher, K., Rihko-Struckmann, L.K. and Galvita, V., *Solid electrolyte membrane reactors: Status and trends.* Catalysis Today, 2005. 104(2-4). p. 185-199.
57. Itoh, N., Xu, W.C., Hara, S. and Sakaki, K., *Electrochemical coupling of benzene hydrogenation and water electrolysis.* Catalysis Today, 2000. 56(1-3). p. 307-314.
58. Vidakovic-Koch, T., Gonzalez Martinez, I., Kuwertz, R., Kunz, U., Turek, T. and Sundmacher, K., *Electrochemical membrane reactors for sustainable chlorine recycling.* Membranes, 2012. 2(3). p. 510-28.
59. Tao, Z., Yan, L., Qiao, J., Wang, B., Zhang, L. and Zhang, J., *A review of advanced proton-conducting materials for hydrogen separation.* Progress in Materials Science, 2015. 74. p. 1-50.
60. Yuan, X., Ma, Z., Bueb, H., Drillet, J.F., Hagen, J. and Schmidt, V.M., *Cogeneration of electricity and organic chemicals using a polymer electrolyte fuel cell.* Electrochimica Acta, 2005. 50(25-26). p. 5172-5180.
61. Granqvist, C.G., Azens, A., Hjelm, A., Kullman, L., Niklasson, G.A., Ronnow, D., Mattsson, M.S., Veszelei, M. and Vaivars, G., *Recent advances in electrochromics for smart windows applications.* Solar Energy, 1998. 63(4). p. 199-216.
62. Argun, A.A., Aubert, P.H., Thompson, B.C., Schwendeman, I., Gaupp, C.L., Hwang, J., Pinto, N. J., Tanner, D.B., MacDiarmid, A.G. and Reynolds, J.R., *Multicolored electrochromism polymers: Structures and devices.* Chemistry of Materials, 2004. 16(23). p. 4401-4412.
63. Granqvist, C.G., *Handbook of Inorganic Electrochromic Materials*. 1st ed., 1995, Elsevier, Amsterdam.
64. Pu, H.T. and Huang, P., *Studies on transparent and solid proton conductors based on $NH_4H_2PO_4$ doped poly(vinyl alcohol).* Materials Letters, 2006. 60(13-14). p. 1724-1727.
65. Pu, H., Luo M. and Yang, Z., *Transparent and anhydrous proton conductors based on PVA/imidazole/$NH_4H_2PO_4$ composites.* European Polymer Journal, 2007. 43(12). p. 5076-5083.
66. Vaivars, G., Kleperis, J. and Lusis, A., *Antimonic acid hydrate xerogels as proton electrolytes.* Solid State Ionics, 1993. 61(4). p. 317-321.
67. Liu, N., Li, W., Pasta, M. and Cui, Y., *Nanomaterials for electrochemical energy storage.* Frontiers of Physics, 2014. 9(3). p. 323-350.

68. Sarangapani, S., Tilak, B.V. and Chen, C.P., *Materials for electrochemical capacitors - Theoretical and experimental constraints.* Journal of the Electrochemical Society, 1996. 143(11). p. 3791-3799.
69. Simon, P. and Gogotsi, Y., *Materials for electrochemical capacitors.* Nature Materials, 2008. 7(11). p. 845-854.
70. Pratap, R., Singh, B. and Chandra, S., *Polymeric rechargeable solid-state proton battery.* Journal of Power Sources, 2006. 161(1). p. 702-706.
71. Zhang, L.L., Zhou, R. and Zhao, X.S., *Graphene-based materials as supercapacitor electrodes.* Journal of Materials Chemistry, 2010. 20(29). p. 5983-5992.
72. Kotz, R. and Carlen, M., *Principles and applications of electrochemical capacitors.* Electrochimica Acta, 2000. 45(15-16). p. 2483-2498.
73. Gao, H. and Lian, K., *High rate all-solid electrochemical capacitors using proton conducting polymer electrolytes.* Journal of Power Sources, 2011. 196(20). p. 8855-8857.
74. Zhang, X., Lin, Z., Chen, B., Sharma, S., Wong, C., Zhang, W. and Deng, Y., *Solid-state, flexible, high strength paper-based supercapacitors.* Journal of Materials Chemistry A, 2013. 1(19). p. 5835-5839.
75. Ahmad, H., Kamarudin, S.K., Minggu, L.J. and Kassim, M., *Hydrogen from photo-catalytic water splitting process: A review.* Renewable & Sustainable Energy Reviews, 2015. 43. p. 599-610.
76. Iwu, K.O., Galeckas, A., Kuznetsov, A.Y. and Norby, T., *Solid-state photoelectrochemical H-2 generation with gaseous reactants.* Electrochimica Acta, 2013. 97. p. 320-325.
77. Seger, B. and Kamat P.V., *Fuel Cell Geared in Reverse: Photocatalytic Hydrogen Production Using a TiO_2/Nafion/Pt Membrane Assembly with No Applied Bias.* Journal of Physical Chemistry C, 2009. 113(43). p. 18946-18952.
78. Georgieva, J., *TiO_2/WO_3 photoanodes with enhanced photocatalytic activity for air treatment in a polymer electrolyte cell.* Journal of Solid State Electrochemistry, 2012. 16(3). p. 1111-1119.
79. Jeng, K.-T., Jeng, Liu, Y.-C., Leu, Y.-F., Zeng, Y-Z., Chung, J.-C. and Wei, T.-Y., *Membrane electrode assembly-based photoelectrochemical cell for hydrogen generation.* International Journal of Hydrogen Energy, 2010. 35(20). p. 10890-10897.
80. Seger, B., Lu, G.Q. and Wang, L., *Electrical power and hydrogen production from a photo-fuel cell using formic acid and other single-carbon organics.* Journal of Materials Chemistry, 2012. 22(21). p. 10709-10715.

81. Park, H., Park, Y., Kim, W. and Choi, W., *Surface modification of TiO_2 photocatalyst for environmental applications.* Journal of Photochemistry and Photobiology C-Photochemistry Reviews, 2013. 15. p. 1-20.
82. Jang, J.S., Kim, H.G. and Lee, J.S., *Heterojunction semiconductors: A strategy to develop efficient photocatalytic materials for visible light water splitting.* Catalysis Today, 2012. 185(1). p. 270-277.
83. Aroutiounian, V.M., Arakelyan, V.M. and Shahnazaryan, G.E., *Metal oxide photoelectrodes for hydrogen generation using solar radiation-driven water splitting.* Solar Energy, 2005. 78(5). p. 581-592.
84. Nowotny, J., Sorrell, C.C., Bak, T. and Sheppard, L.R., *Solar-hydrogen: Unresolved problems in solid-state science.* Solar Energy, 2005. 78(5). p. 593-602.
85. Sarkissyan, A.G., Putnyn, E.V., Arakelyan, V.M., Aroutiounian, V.M. and Begoian, K.H., *Photoelectrochemical characteristics of photocathodes made of high-temperature superconducting ceramics.* Solar Energy Materials and Solar Cells, 1992. 28(3). p. 217-221.
86. Aroutiounian, V.M., Arakelyan, V.M. and Shahnazaryan, G.E., *Investigations of the metal-oxide semiconductors promising for photoelectrochemical conversion of solar energy.* Solar Energy Materials and Solar Cells, 2005. 89(2-3). p. 153-163.
87. Aroutiounian, V.M., Arakelyan, V. M., Shahnazaryan, G. E., Stepanyan, G. M., Turner, J. A. And Khaselev, O., *Investigation of ceramic Fe_2O_3 < Ta > photoelectrodes for solar energy photoelectrochemical converters.* International Journal of Hydrogen Energy, 2002. 27(1). p. 33-38.
88. Vijayakumar, M., Bain, A.D. and Goward, G.R., *Investigations of Proton Conduction in the Monoclinic Phase of RbH_2PO_4 Using Multinuclear Solid-State NMR.* Journal of Physical Chemistry C, 2009. 113(41). p. 17950-17957.
89. Tuckerman, M.E., Marx, D. and Parrinello, M., *The nature and transport mechanism of hydrated hydroxide ions in aqueous solution.* Nature, 2002. 417(6892). p. 925-929.
90. Agmon, N., *The grotthuss mechanism.* Chemical Physics Letters, 1995. 244(5-6). p. 456-462.
91. Dean, J.A., *Lange's handbook of chemistry*. 15th ed., 1999, McGraw-Hill, New York.
92. Kreuer, K.D., *On the development of proton conducting polymer membranes for hydrogen and methanol fuel cells.* Journal of Membrane Science, 2001. 185(1). p. 29-39.
93. Li, S.W., Zhou, Z., Zhang, Y.L., Liu, M.L. and Li, W., *1H-1,2,4-triazole: An effective solvent for proton-conducting electrolytes.* Chemistry of Materials, 2005. 17(24). p. 5884-5886.

94. Celik, S.U., Bozkurt, A. and Hosseini, S.S., *Alternatives toward proton conductive anhydrous membranes for fuel cells: Heterocyclic protogenic solvents comprising polymer electrolytes.* Progress in Polymer Science, 2012. 37(9). p. 1265-1291.
95. Maslowski, T., Drzewinski, A., Ulner, J., Wojtkiewicz, J., Zdanowska-Fraczek, M., Nordlund, K. and Kuronen, A., *Kinetic Monte Carlo simulations of proton conductivity.* Physical Review E, 2014. 90(1).
96. Chung, S.H., Bajue, S. and Greenbaum, S.G., *Mass transport of phosphoric acid in water: A H-1 and P-31 pulsed gradient spin-echo nuclear magnetic resonance study.* Journal of Chemical Physics, 2000. 112(19). p. 8515-8521.
97. Vilciauskas, L., Tuckerman, M.E., Bester, G., Paddison, S.J. and Kreuer, K.D., *The mechanism of proton conduction in phosphoric acid.* Nature Chemistry, 2012. 4(6). p. 461-466.
98. Goni-Urtiaga, A., Presvytes, D. and Scot,t K., *Solid acids as electrolyte materials for proton exchange membrane (PEM) electrolysis: Review.* International Journal of Hydrogen Energy, 2012. 37(4). p. 3358-3372.
99. Baranov, A.I., *Crystals with disordered hydrogen-bond networks and superprotonic conductivity. Review.* Crystallography Reports, 2003. 48(6). p. 1012-1037.
100. Munch, W., Seifert, G., Kreuer, K.D. and Maier, J., *A quantum molecular dynamics study of proton conduction phenomena in $BaCeO_3$.* Solid State Ionics, 1996. 86-8. p. 647-652.
101. Kreuer, K.D., *On the development of proton conducting materials for technological applications.* Solid State Ionics, 1997. 97(1-4). p. 1-15.
102. Ishihara, T., *Perovskite Oxide for Solid Oxide Fuel Cells* 2009, Springer, New York.
103. Jiao, K. and Li, X.G., *Water transport in polymer electrolyte membrane fuel cells.* Progress in Energy and Combustion Science, 2011. 37(3). p. 221-291.
104. Choi, P., Jalani, N.H. and Datta, R., *Thermodynamics and proton transport in Nafion - II. Proton diffusion mechanisms and conductivity.* Journal of the Electrochemical Society, 2005. 152(3). p. E123-E130.
105. Li, Q., Jensen, J.O., Savinell, R.F. and Bjerrum, N.J., *High temperature proton exchange membranes based on polybenzimidazoles for fuel cells.* Progress in Polymer Science, 2009. 34(5). p. 449-477.
106. Jannasch, P., *Recent developments in high-temperature proton conducting polymer electrolyte membranes.* Current Opinion in Colloid & Interface Science, 2003. 8(1). p. 96-102.

107. Pu, H.T., Meyer, W.H. and Wegner, G., *Proton transport in polybenzimidazole blended with H_3PO_4 or H_2SO_4.* Journal of Polymer Science Part B-Polymer Physics, 2002. 40(7). p. 663-669.

108. Zuo, Z.C., Fu, Y.Z. and Manthiram, A., *Novel Blend Membranes Based on Acid-Base Interactions for Fuel Cells.* Polymers, 2012. 4(4). p. 1627-1644.

109. Bozkurt, A. and Meyer, W.H., *Proton conducting blends of poly(4-vinylimidazole) with phosphoric acid.* Solid State Ionics, 2001. 138(3-4). p. 259-265.

110. Schuster, M., Meyer, W.H., Wegner, G., Herz, H.G., Ise, M., Kreuer, K.D. and Maier, J., *Proton mobility in oligomer-bound proton solvents: imidazole immobilization via flexible spacers.* Solid State Ionics, 2001. 145(1-4). p. 85-92.

111. Schuster, M.F.H., Meyer, W.H., Schuster, M. and Kreuer, K.D., *Toward a new type of anhydrous organic proton conductor based on immobilized imidazole.* Chemistry of Materials, 2004. 16(2). p. 329-337.

112. Alberti, G. and Casciola, M., *Composite membranes for medium-temperature PEM fuel cells.* Annual Review of Materials Research, 2003. 33. p. 129-154.

113. Peighambardoust, S.J., Rowshanzamir, S. and Amjadi, M., *Review of the proton exchange membranes for fuel cell applications.* International Journal of Hydrogen Energy, 2010. 35(17). p. 9349-9384.

114. Herring, A.M., *Inorganic-polymer composite membranes for proton exchange membrane fuel cells.* Polymer Reviews, 2006. 46(3). p. 245-296.

115. Maier, J., *Nanoionics: ionic charge carriers in small systems.* Physical Chemistry Chemical Physics, 2009. 11(17). p. 3011-3022.

116. Maier, J., *Pushing Nanoionics to the Limits: Charge Carrier Chemistry in Extremely Small Systems.* Chemistry of Materials, 2014. 26(1). p. 348-360.

117. Sata, N., Eberman, K., Eberl, K. and Maier, J., *Mesoscopic fast ion conduction in nanometre-scale planar heterostructures.* Nature, 2000. 408(6815). p. 946-949.

118. Maekawa, H., Tanaka, R., Sato, T., Fujimaki, Y. and Yamamura, T., *Size-dependent ionic conductivity observed for ordered mesoporous alumina-LiI composite.* Solid State Ionics, 2004. 175(1-4). p. 281-285.

119. Maier, J., *Mass storage in space charge regions of nano-sized systems (Nano-ionics. Part V).* Faraday Discussions, 2007. 134. p. 51-66.

120. Zhukovskii, Y.F., Balaya, P., Kotomin, E.A. and Maier, J., *Evidence for Interfacial-Storage Anomaly in Nanocomposites for Lithium Batteries from First-Principles Simulations.* Physical Review Letters, 2006. 96(5). p. 058302-1-058302-4.

121. Maier, J., *Ionic-conduction in-space charge regions.* Progress in Solid State Chemistry, 1995. 23(3). p. 171-263.

122. Tuller, H.L., Litzelman, S.J. and Jung, W., *Micro-ionics: next generation power sources.* Physical Chemistry Chemical Physics, 2009. 11(17). p. 3023-3034.

123. Guo, X. and Waser, R., *Electrical properties of the grain boundaries of oxygen ion conductors: Acceptor-doped zirconia and ceria.* Progress in Materials Science, 2006. 51(2). p. 151-210.

124. Beyazyildirim, S., Kreuer, K.D., Schuster, M., Bhattacharyya, A.J. and Maier, J., *Heterogeneous doping of a weak covalent electrolyte: Proton conductivity enhancement of imidazole by admixture of oxide particles.* Advanced Materials, 2008. 20(7). p. 1274-1278.

125. Fish, J.S., Li, C.P., Fehribach, J.D., Wolden, C.A., O'Hayre, R., Bunge, A.L. and Goodyer, C.E., *Poisson-Boltzmann model of space charge layer effects on conductivity in randomly distributed nanoionic composites.* Electrochimica Acta, 2012. 83. p. 454-462.

126. Maier, J., *Defect chemistry and conductivity effects in heterogeneous solid electrolytes.* Journal of the Electrochemical Society, 1987. 134(6). p. 1524-1535.

127. Hurd, J.A., Vaidhyanathan, R., Thangadurai, V., Ratcliffe, C.I., Moudrakovski, I.L. and Shimizu, G.K.H., *Anhydrous proton conduction at 150 degrees C in a crystalline metal-organic framework.* Nature Chemistry, 2009. 1(9). p. 705-710.

128. Rouquerol, J., Avnir, D., Fairbridg, C.W.E , Everett, D.H., Haynes, J.H., Pernicone, N., Ramsay, J.D.F., Sing, K.S.W. and Unger, K.K., *Recommendations for the characterization of porous solids* Pure & Appl. Chern, 1994. 66. p. 1739-1758.

129. Hoffmann, F., Cornelius, M., Morell, J. and Froba, M., *Silica-based mesoporous organic-inorganic hybrid materials.* Angewandte Chemie-International Edition, 2006. 45(20). p. 3216-3251.

130. Hogarth, W.H.J., da Costa, J.C.D., Drennan, J. and Lu, G.Q., *Proton conductivity of mesoporous sol-gel zirconium phosphates for fuel cell applications.* Journal of Materials Chemistry, 2005. 15(7). p. 754-758.

131. Hoffmann, F. and Froba, M., *Vitalising porous inorganic silica networks with organic functions-PMOs and related hybrid materials.* Chemical Society Reviews, 2011. 40(2). p. 608-620.

132. Li, W., Wu, Z., Wang, J., Elzatahry, A.A., Zhao, D., *A Perspective on Mesoporous TiO_2 Materials.* Chemistry of Materials, 2014. 26(1). p. 287-298.

133. Gu, D. and Schuth, F., *Synthesis of non-siliceous mesoporous oxides.* Chemical Society Reviews, 2014. 43(1). p. 313-344.

134. Wagner, T., Haffer, S., Weinberger, C., Klaus, D. and Tiemann, M., *Mesoporous materials as gas sensors.* Chemical Society Reviews, 2013. 42(9). p. 4036-4053.

135. Nair, M.M., Yen, H. and Kleitz, F., *Nanocast mesoporous mixed metal oxides for catalytic applications.* Comptes Rendus Chimie, 2014. 17(7-8). p. 641-655.

136. Walcarius, A., *Mesoporous materials and electrochemistry.* Chemical Society Reviews, 2013. 42(9). p. 4098-4140.

137. Ren, Y., Ma, Z. and Bruce, P.G., *Ordered mesoporous metal oxides: synthesis and applications.* Chemical Society Reviews, 2012. 41(14). p. 4909-4927.

138. Ma, Z., Zhou, B. and Ren, Y., *Crystalline mesoporous transition metal oxides: hard-templating synthesis and application in environmental catalysis.* Frontiers of Environmental Science & Engineering, 2013. 7(3). p. 341-355.

139. Yang, H.F. and Zhao, D.Y., *Synthesis of replica mesostructures by the nanocasting strategy.* Journal of Materials Chemistry, 2005. 15(12). p. 1217-1231.

140. Kresge, C.T., Leonowicz, M.E., Roth, W.J., Vartuli, J.C. and Beck, J.S., *Ordered mesoporous molecular-sieves synthesized by a liquid-crystal template mechanism.* Nature, 1992. 359(6397). p. 710-712.

141. Zhao, D.Y., Huo, Q.S., Feng, J.L., Chmelka, B.F. and Stucky, G.D., *Nonionic triblock and star diblock copolymer and oligomeric surfactant syntheses of highly ordered, hydrothermally stable, mesoporous silica structures.* Journal of the American Chemical Society, 1998. 120(24). p. 6024-6036.

142. Kleitz, F., Choi, S.H. and Ryoo R., *Cubic Ia3d large mesoporous silica: synthesis and replication to platinum nanowires, carbon nanorods and carbon nanotubes.* Chemical Communications, 2003(17): p. 2136-2137.

143. Huo, Q.S., Margolese, D.I., Ciesla, U., Feng, P.Y., Gier, T.E., Sieger, P., Leon, R., Petroff, P.M., Schuth, F. and Stucky, G.D., *Generalized synthesis of periodic surfactant inorganic composite-materials.* Nature, 1994. 368(6469). p. 317-321.

144 Yang, P.D., Zhao, D.Y., Margolese, D.I., Chmelka, B.F. and Stucky, G.D., *Generalized syntheses of large-pore mesoporous metal oxides with semicrystalline frameworks.* Nature, 1998. 396(6707). p. 152-155.

145. Yang, P.D., Zhao, D. Y., Margolese, D. I., Chmelka, B. F. and Stucky, G. D., *Block copolymer templating syntheses of mesoporous metal oxides with large ordering lengths and semicrystalline framework.* Chemistry of Materials, 1999. 11(10): p. 2813-2826.

146. Ryoo, R., Joo, S.H. and Jun, S., *Synthesis of highly ordered carbon molecular sieves via template-mediated structural transformation.* Journal of Physical Chemistry B, 1999. 103(37). p. 7743-7746.

147. Liu, Z., Sakamoto, Y., Ohsuna, T., Hiraga, K., Terasaki, O., Ko, C.H., Shin, H.J. and Ryoo, R., *TEM studies of platinum nanowires fabricated in mesoporous silica MCM-41.* Angewandte Chemie-International Edition, 2000. 39(17). p. 3107-3110.

148. Yang, H.F., Shi, Q.H., Tian, B.Z., Lu, Q.Y., Gao, F, Xie, S.H., Fan, J., Yu, C.Z., Tu, B. and Zhao, D.Y., *One-step nanocasting synthesis of highly ordered single crystalline indium oxide nanowire arrays from mesostructured frameworks.* Journal of the American Chemical Society, 2003. 125(16). p. 4724-4725.

149. Tian, B.Z., Liu, X.Y., Yang, H.F., Xie, S.H., Yu, C.Z., Tu, B. and Zhao, D.Y., *General synthesis of ordered crystallized metal oxide nanoarrays replicated by microwave-digested mesoporous silica.* Advanced Materials, 2003. 15(16). p. 1370-1374.

150. Yamauchi, Y. and Kuroda, K., *Rational design of mesoporous metals and related nanomaterials by a soft-template approach.* Chemistry-an Asian Journal, 2008. 3(4). p. 664-676.

151. Lu, A.H., Zhao, D. and Wan Y., *Nanocasting: A Versatile Strategy for Creating Nanostructured Porous Materials*. 2009, Royal Society of Chemistry, Cambrige.

152. Tiemann, M., *Repeated templating.* Chemistry of Materials, 2008. 20(3). p. 961-971.

153. Kong, A.G., Zhu, H.Y., Wang, W.J., Zhang, Q.Y., Yang, F. and Shan, Y.K., *Novel nanocasting method for synthesis of ordered mesoporous metal oxides.* Journal of Porous Materials, 2011. 18(1). p. 107-112.

154. Ryoo, R., Joo, S.H., Kruk, M. and Jaroniec, M., *Ordered mesoporous carbons.* Advanced Materials, 2001. 13(9). p. 677-681.

155. Vivero-Escoto, J.L., Chiang, Y.D., C-Wwu, K. and Yamauchi, Y., *Recent progress in mesoporous titania materials: adjusting morphology for innovative applications.* Science and Technology of Advanced Materials, 2012. 13. p. 013003-1-013003-9.

156. Makowski, P., Deschanels, X., Grandjean, A., Meyer, D., Toquer, G. and Goettmann, F., *Mesoporous materials in the field of nuclear industry: applications and perspectives.* New Journal of Chemistry, 2012. 36(3). p. 531-541.

157. Xia, Y.D. and Mokaya, R., *Hollow spheres of crystalline porous metal oxides: A generalized synthesis route via nanocasting with mesoporous carbon hollow shells.* Journal of Materials Chemistry, 2005. 15(30). p. 3126-3131.

158. Yue, W.B. and Zhou, W.Z., *Crystalline mesoporous metal oxide.* Progress in Natural Science, 2008. 18(11). p. 1329-1338.

159. Lu, A.H. and Schuth, F., *Nanocasting: A versatile strategy for creating nanostructured porous materials.* Advanced Materials, 2006. 18(14). p. 1793-1805.

160. Rossinyol, E., Arbiol, J., Peiro, F., Cornet, A., Morante, J. R., Tian, B., Bo, T. and Zhao, D., *Nanostructured metal oxides synthesized by hard template method for gas sensing applications.* Sensors and Actuators B-Chemical, 2005. 109(1). p. 57-63.

161. Tsoncheva, T., Roggenbuck, J., Paneva, D., Dimitrov, M., Mitov, I. and Froba, M., *Nanosized iron and chromium oxides supported on mesoporous CeO_2 and SBA-15 silica: Physicochemical and catalytic study.* Applied Surface Science, 2010. 257(2). p. 523-530.

162. Aranda, A., Puertolas, B., Solsona, B., Agouram, S., Murillo, R., Mastral, A.M., Taylor, S.H. and Garcia, T., *Total Oxidation of Naphthalene Using Mesoporous CeO_2 Catalysts Synthesized by Nanocasting from Two Dimensional SBA-15 and Three Dimensional KIT-6 and MCM-48 Silica Templates.* Catalysis Letters, 2010. 134(1-2). p. 110-117.

163. Li, T.T., Sun, L.B., Gong, L., Liu, X.Y. and Liu, X.Q., *In situ generation of superbasic sites on mesoporous ceria and their application in transesterification.* Journal of Molecular Catalysis a-Chemical, 2012. 352. p. 38-44.

164. Abdollahzadeh-Ghom, S., Zamani, C., Andreu, T., Epifani, M. and Morante, J.R., *Improvement of oxygen storage capacity using mesoporous ceria-zirconia solid solutions.* Applied Catalysis B-Environmental, 2011. 108(1-2). p. 32-38.

165. Yue, W. and Zhou, W.Z., *Synthesis of porous single crystals of metal oxides via a solid-liquid route.* Chemistry of Materials, 2007. 19(9). p. 2359-2363.

166. Wang, Y.G., Li, B., Zhang, C.L., Cui, L.F., Kang, S.F., Li, X. and Zhou, L.H., *Ordered mesoporous CeO_2-TiO_2 composites: Highly efficient photocatalysts for the reduction of CO_2 with H_2O under simulated solar irradiation.* Applied Catalysis B-Environmental, 2013. 130. p. 277-284.

167. Piumetti, M., Bensaid, S., Russo, N. and Fino, D., *Nanostructured ceria-based catalysts for soot combustion: Investigations on the surface sensitivity.* Applied Catalysis B-Environmental, 2015. 165. p. 742-751.

168. Wang, Y.G., Wang, Y.Q., Ren, J.W., Mi, Y., Zhang, F.Y., Li, C.L., Liu, X.H., Guo, Y., Guo, Y.L. and Lu, G.Z., *Synthesis of morphology-controllable mesoporous Co_3O_4 and CeO_2.* Journal of Solid State Chemistry, 2010. 183(2). p. 277-284.

169. Laha, S.C. and Ryoo, R., *Synthesis of thermally stable mesoporous cerium oxide with nanocrystalline frameworks using mesoporous silica templates.* Chemical Communications, 2003(17). p. 2138-2139.

170. Liu, B. and Baker, R.T., *Factors affecting the preparation of ordered mesoporous ZrO_2 using the replica method.* Journal of Materials Chemistry, 2008. 18(43). p. 5200-5207.

171. Ballem, M.A., Cordoba, J.M. and Oden, M., *Mesoporous silica templated zirconia nanoparticles.* Journal of Nanoparticle Research, 2011. 13(7). p. 2743-2748.

172. Gong, L., Sun, L.B., Sun, Y.H., Li, T.T. and Liu, X.Q., *Exploring in Situ Functionalization Strategy in a Hard Template Process: Preparation of Sodium-Modified Mesoporous Tetragonal Zirconia with Superbasicity.* Journal of Physical Chemistry C, 2011. 115(23). p. 11633-11640.

173. Yue, W.B., Randorn, C., Attidekou, P.S., Su, Z.X., Irvine, J.T.S. and Zhou, W.Z., *Syntheses, Li Insertion, and Photoactivity of Mesoporous Crystalline TiO_2.* Advanced Functional Materials, 2009. 19(17). p. 2826-2833.

174. Yue, W., Xu, X., Irvine, J.T.S., Attidekou, P.S., Liu, C., He, H., Zhao, D. and Zhou, W., *Mesoporous Monocrystalline TiO_2 and Its Solid-State Electrochemical Properties.* Chemistry of Materials, 2009. 21(12). p. 2540-2546.

175. Hwang, K.J., Shim, W.G., Jung, S.H., Yoo, S.J. and Lee, J.W., *Analysis of adsorption properties of N719 dye molecules on nanoporous TiO_2 surface for dye-sensitized solar cell.* Applied Surface Science, 2010. 256(17). p. 5428-5433.

176. Kim, S.S., Lee, H.I., Shon, J.K., Hur, J.Y., Kang, M.S., Park, S.S., Kong, S.S., Yu, J.A., Seo, M., Li, D.H., Thakur, S.S. and Kim, J.M., *Preparation of highly ordered mesoporous TiO_2 materials with crystalline framework from different mesostructured silica templates via nanoreplication.* Chemistry Letters, 2008. 37(2). p. 140-141.

177. Hwang, K.J., Yoo, S.J., Kim, S.S., Kim, J.M., Shim, W.G., Kim, S.I. and Lee, J.W., *Photovoltaic Performance of Nanoporous TiO_2 Replicas Synthesized from Mesoporous Materials for Dye-Sensitized Solar Cells.* Journal of Nanoscience and Nanotechnology, 2008. 8(10). p. 4976-4981.

178. Wang, J.G., Bian, Z.F., Zhu, J. and Li, H.X., *Ordered mesoporous TiO_2 with exposed (001) facets and enhanced activity in photocatalytic selective oxidation of alcohols.* Journal of Materials Chemistry A, 2013. 1(4). p. 1296-1302.

179. Bian, Z.F., Zhu, J.A., Wen, J., Cao, F.L., Huo, Y.N., Qian, X.F., Cao, Y., Shen, M.Q., Li, H.X. and Lu, Y.F., *Single-Crystal-like Titania Mesocages.* Angewandte Chemie-International Edition, 2011. 50(5). p. 1105-1108.

180. Ke, Y.H. and Lai, S.Y., *Comparison of the catalytic benzene oxidation activity of mesoporous ceria prepared via hard-template and soft-template.* Microporous and Mesoporous Materials, 2014. 198. p. 256-262.

181. Zhao, L. and Yu, J., *Controlled synthesis of highly dispersed TiO_2 nanoparticles using SBA-15 as hard template.* Journal of Colloid and Interface Science, 2006. 304(1): p. 84-91.

182. Serrano, D. P., Calleja, G., Pizarro and P., Galvez, P., *Enhanced photocatalytic hydrogen production by improving the Pt dispersion over mesostructured TiO_2.* International Journal of Hydrogen Energy, 2014. 39(10): p. 4812-4819.

183. Mahoney, L., Rasalingam, S., Wu, Chia-Ming and Koodali, R. T., *Nanocasting of Periodic Mesoporous Materials as an Effective Strategy to Prepare Mixed Phases of Titania.* Molecules, 2015. 20(12): p. 21881-21895.

184. Lee, J., Sugi, Y., Jeong, N. J., Seo, G. and Cho, S. J., *Novel preparation of nano-sized TiO_2 and ZrO_2 particles by nanocasting with nanoporous SiO_2 and selective dissolution*, Solid State Phenomena, 2007, Vols 124-126 p. 643-646.

185. Polrolniczak, P. and S. Kowalak, *Ordered mesoporous tin oxide and tin phosphate synthesized by nanocasting strategy.* Journal of Porous Materials, 2011. 18(6): p. 703-706.

186. Roggenbuck, J., Schafer, H., Tsoncheva, T., Minchev, C., Hanss, J. and Tiemann, M., *Mesoporous CeO_2: Synthesis by nanocasting, characterisation and catalytic properties.* Microporous and Mesoporous Materials, 2007. 101(3). p. 335-341.

187. Tsoncheva, T., Ivanova, L., Minchev, C. and Froba, M., *Cobalt-modified mesoporous MgO, ZrO_2, and CeO_2 oxides as catalysts for methanol decomposition.* Journal of Colloid and Interface Science, 2009. 333(1). p. 277-284.

188. Kang, M., Kim, D., Yi, S.H., Han, J.U., Yie, J.E. and Kim, J.M., *Preparation of stable mesoporous inorganic oxides via nano-replication technique.* Catalysis Today, 2004. 93-5. p. 695-699.

189. Tsoncheva, T., Roggenbuck, J., Tiemann, M., Ivanova, L., Paneva, D., Mitov, I. and Minchev, C., *Iron oxide nanoparticles supported on mesoporous MgO and CeO_2: A comparative physicochemical and catalytic study.* Microporous and Mesoporous Materials, 2008. 110(2-3): p. 339-346.

190. Chandrasekar, G., W.J. Son, and W.S. Ahn, *Synthesis of mesoporous materials SBA-15 and CMK-3 from fly ash and their application for CO_2 adsorption.* Journal of Porous Materials, 2009. 16(5): p. 545-551.

191. Kruk, M., Jaroniec, M., Joo, S. H. and Ryoo, R., *Characterization of regular and plugged SBA-15 silicas by using adsorption and inverse carbon replication and explanation of the plug formation mechanism.* Journal of Physical Chemistry B, 2003. 107(10): p. 2205-2213.

192. He, J.G., Ma, K., Jin, J., Dong, Z. P.,Wang, J. J. and Li, R., *Preparation and characterization of octyl-modified ordered mesoporous carbon CMK-3 for phenol adsorption.* Microporous and Mesoporous Materials, 2009. 121(1-3): p. 173-177.

193. Salvador, M.A., Canales-Vazquez, J., Ferreira, P. and Figueiredo, F. M., *Characterization of mesoporous zirconium and cerium oxides by transmission electron microscopy.* Microscopy and Microanalysis, 2012. 18: p. 81-82.

194. Roggenbuck, J., Koch G. and Tiemann M., *Synthesis of mesoporous magnesium oxide by CMK-3 carbon structure replication.* Chemistry of Materials, 2006. 18(17): p. 4151-4156.

195. Roggenbuck, J. and Tiemann M., *Ordered mesoporous magnesium oxide with high thermal stability synthesized by exotemplating using CMK-3 carbon.* Journal of the American Chemical Society, 2005. 127(4): p. 1096-1097.

196. Saini, V.K., Andrade, M., Pinto, M. L., Carvalho, A. P. and Pires, J., *How the adsorption properties get changed when going from SBA-15 to its CMK-3 carbon replica.* Separation and Purification Technology, 2010. 75(3): p. 366-376.

197. Mavrogiorgou, A., Baikousi, M., Costas, V., Mouzourakis, E., Deligiannakis, Y., Karakassides, M. A. and Louloudi, M., *Mn-Schiff base modified MCM-41, SBA-15 and CMK-3 NMs as single-site heterogeneous catalysts: Alkene epoxidation with H_2O_2 incorporation.* Journal of Molecular Catalysis a-Chemical, 2016. 413: p. 40-55.

198. Zhang, H.L., Yan, X.J. and Li, W.C., *Nanocast Ordered Mesoporous CeO_2 as Support for Highly Active Gold Catalyst in CO Oxidation.* Chinese Journal of Catalysis, 2009. 30(11). p. 1085-1090.

199. Jun, S., Joo, S.H., Ryoo, R., Kruk, M., Jaroniec, M., Liu, Z., Ohsuna, T. and Terasaki, O., *Synthesis of new, nanoporous carbon with hexagonally ordered mesostructure.* Journal of the American Chemical Society, 2000. 122(43). p. 10712-10713.

200. Huwe, H. andFroba M., *Synthesis and characterization of transition metal and metal oxide nanoparticles inside mesoporous carbon CMK-3.* Carbon, 2007. 45: p. 304-314.

201. Salgado, J.R.C., Paganin, V. A., Gonzalez, E. R., Montemor, M. F., Tacchini, I., Anson, A., Salvador, M. A., Ferreira, P., Figueiredo, F. M. L. and Ferreira, M. G. S., *Characterization and performance evaluation of Pt-Ru electrocatalysts supported on different carbon materials for direct methanol fuel cells.* International Journal of Hydrogen Energy, 2013. 38(2): p. 910-920.

202. Zhou, J., Su, W., Sun, Y., Deng, S. G. and Wang, X. J, *Enhanced CO_2 Sorption on Ordered Mesoporous Carbon CMK-3 in the Presence of Water.* Journal of Chemical and Engineering Data, 2016. 61(3): p. 1348-1352.

203. Zhang, Z.B., Zhou, Y. D., Liu, Y. H., Cao, X. H., Zhou, Z. W., Han, B., Liang, P. and Xiong, G. X., *Removal of thorium from aqueous solution by ordered mesoporous carbon CMK-3.* Journal of Radioanalytical and Nuclear Chemistry, 2014. 302(1): p. 9-16.

204. Giasafaki, D., Charalambopoulou, G., Bourlinos, A., Stubos, A., Gournis, D. and Steriotis, T l., *A hydrogen sorption study on a Pd-doped CMK-3 type ordered mesoporous carbon.* Adsorption-Journal of the International Adsorption Society, 2013. 19(2-4): p. 803-811.

205. Bhowmick, S., Basu, J., Xue, Y. and Carter, C.B., *Hydrothermal Synthesis of Nanocrystalline Barium Cerate Using Hexamethylenetetramine.* Journal of the American Ceramic Society, 2010. 93(12). p. 4041-4046.

206. Antunes, I., Brandão, A., Figueiredo, F.M., Frade, J.R., Gracio, J. and Fagg, D.P., *Mechanosynthesis of nanopowders of the proton-conducting electrolyte material Ba(Zr, Y)O_3-delta.* Journal of Solid State Chemistry, 2009. 182(8). p. 2149-2156.

207. Kaw, A.K., *Mechanics of Composite Materials*. 2nd ed., 2006, CRC Press, Boca Raton.

208. Brundle, R. C., Charles, A. E. and Shaun, W., *Encyclopedia of materials characterization materials characterization Series :Surfaces, Interfaces, Thin Films*. 1992, Butterworth-Heinemann, Boston.

209. Suryanarayana, C. and Norton, M.G., *X-Ray Diffraction A Practical Approach*. 1998, Springer Science+Business Media, New York.

210. Waseda, Y., Matsubara, E., Shinoda, K., *X-Ray Diffraction Crystallography: Introduction, Examples and Solved Problems*. 2011, Springer, New York.

211. Inagaki, S., Guan, S., Ohsuna, T. and Terasaki, O., *An ordered mesoporous organosilica hybrid material with a crystal-like wall structure.* Nature, 2002. 416(6878). p. 304-307.

212. Kraus, W. and Nolze, G., *POWDER CELL - A program for the representation and manipulation of crystal structures and calculation of the resulting X-ray powder patterns.* Journal of Applied Crystallography, 1996. 29. p. 301-303.

213. Stuart, B.H., *Infrared Spectroscopy: Fundamentals and Applications*. 2004, John Wiley & Sons, Chichester.

214. Williams, D.B. and C.B. Carter, *Transmission Electron Microscopy, A Textbook for Materials Science*. 2nd ed., 2009, Springer, New York.

215. Rasband, W.S., ImageJ, U. S. National Institutes of Health, Bethesda, Maryland, USA, http://imagej.nih.gov/ij/, 1997-2014.

216. Kjellman, T. and Alfredsson, V., *The use of in situ and ex situ techniques for the study of the formation mechanism of mesoporous silica formed with non-ionic triblock copolymers.* Chemical Society Reviews, 2013. 42(9). p. 3777-3791.

217. Goldstein, J.I., Newbury, D.E., Echlin, P., Joy, D.C., Lyman, C.E., Lifshin, E., Sawyer L., and Michael, J.R., *Scanning Electron Microscopy and X-Ray Microanalysis*. 3rd ed., 2003, Kluwer Academic, Plenum Publishers, New York.

218. Brown, M.E., *Handbook of Thermal Analysis and Calorimetry, Volume 1: Principles and practice* 1998, Elsevier, Amsterdam.

219. Sing, K.S.W., Everett, D. H., Haul, R. A W., Moscou, L., Pierotti, R. A.; Rouquerol J., and Siemieniewska, T, *Reporting physisorption data for gas solid systems with special reference to the determination of surface-area and porosity (recommendations 1984).* Pure and Applied Chemistry, 1985. 57(4): p. 603-619

220. Gregg, S.J.S. and Sing, K.S.W., *Adsorption, Surface Area and Porosity*. 2nd ed., 1982, cademic Press, London.

221. Brunauer, S., Emmett, P.H. and Teller, E., *Adsorption of gases in multimolecular layers.* Journal of the American Chemical Society, 1938. 60. p. 309-319.

222. Rodrigues, A.E., LeVan, M. D. and Tondeu, D., *Adsorption: Science and Technology*. 1989, Kluwer Academic Publishers, London.

223. Kruk, M., Jaroniec, M. and Sayari, A., *Application of large pore MCM-41 molecular sieves to improve pore size analysis using nitrogen adsorption measurements.* Langmuir, 1997. 13(23). p. 6267-6273.

224. Jaroniec, M. and Solovyov, L.A., *Improvement of the Kruk-Jaroniec-Sayari method for pore size analysis of ordered silicas with cylindrical mesopores.* Langmuir, 2006. 22(16). p. 6757-6760.

225. Mitropoulos, A.C., *The Kelvin equation.* Journal of Colloid and Interface Science, 2008. 317(2). p. 643-648.

226. Barrett, E.P., Joyner, L.G. and Halenda, P.P., *The determination of pore volume and area distributions in porous substances .1. computations from nitrogen isotherms.* Journal of the American Chemical Society, 1951. 73(1). p. 373-380.

227. Ebbing, D.D., Gammon, S.D., *General Chemistry*. 9th ed., 2007, Houghton Mifflin Company, Boston.

228. Bale, C.W., Belisle, E., Chartrand, P., Decterov, S.A., Eriksson, G., Hack, K., Jung, I.H., Kang, Y.B., Melancon, J., Pelton, A.D., Robelin, C. and Petersen, S., *FactSage thermochemical software and databases - recent developments.* Calphad-Computer Coupling of Phase Diagrams and Thermochemistry, 2009. 33(2). p. 295-311.

229. *Zetasizer Nano Series User Manual MAN 0317*. 2004. Malvern Instruments, Ltd..

230. Kissa, E., *Dispersions: Characterization, Testing, and Measurement.* Surfactant Science, No. 84, 1999, CRC Press, Austin.

231. Hiemenz. P. C. and Rajagopalan, R., *Principles of Colloid and Surface* Chemistry. 3rd ed., Revised and Expanded, 1997, Marcel Dekker, New York.

232. Rautiu, R., White, D.A., Adeleye, S.A. and Adkins, L., *The use of zeta potential measurements in inorganic ion exchange studies*.Hydrometallurgy 1995. 35(3). p. 361-374.

233. Barsoukov, E. and Macdonald, J.R., *Impedance Spectroscopy: Theory, Experiment, and Applications*. 2nd ed., 2005, Wiley, Hoboken.

234. Yuan, X., Song, C., Wang H. and Zhang J., *Electrochemical impedance spectroscopy in PEM fuel cells: Fundamentals and applications*. 2010, Springer, New York.

235. Mohamed, M.M. and Katib, S.M.A., *Ce-containing Mordenites: Synthesis, structure and reactivity towards NO and CO gases.* Microporous and Mesoporous Materials, 2006. 93(1-3). p. 71-81.

236. Zhan, Z.Q. and Zeng, H.C., *A catalyst-free approach for sol-gel synthesis of highly mixed ZrO_2-SiO_2 oxides.* Journal of Non-Crystalline Solids, 1999. 243(1). p. 26-38.

237. del Monte, F., Larsen, W. and Mackenzie, J.D., *Stabilization of tetragonal ZrO_2 in ZrO_2-SiO_2 binary oxides.* Journal of the American Ceramic Society, 2000. 83(3). p. 628-634.

238. Lee, S.W. and Condrate, R.A., *The infrared and raman-spectra of ZrO_2-SiO_2 glasses prepared by a sol-gel process.* Journal of Materials Science, 1988. 23(8). p. 2951-2959.

239. Li, H.F., Xi, H.A., Zhu, S.M., Wen, Z.Y. and Wang, R.D., *Preparation, structural characterization, and electrochemical properties of chemically modified mesoporous carbon.* Microporous and Mesoporous Materials, 2006. 96(1-3). p. 357-362.

240. Garvie, R.C., *Occurrence of metastable tetragonal zirconia as a crystallite size effect. Journal of Physical Chemistry*, 1965. 69(4): p. 1238-1243.

241. Zou, X.J., Li, X.Y., Qu, Z.P., Zhao, Q.D., Shi, Y., Chen, Y.Y., Tade, M. and Liu, S.M., *Photocatalytic degradation of gaseous toluene over TiO_2-SiO_2 composite nanotubes synthesized by sot-gel with template technique.* Materials Research Bulletin, 2012. 47(2). p. 279-284.

242. Dutoit, D.C.M., Schneider, M. and Baiker, A., *Titania-silica mixed oxides .1. influence of sol-gel and drying conditions on structural-properties.* Journal of Catalysis, 1995. 153(1). p. 165-176.

243. Bineesh, K.V., Kim, D.-K. and Park, D.-W., *Synthesis and characterization of zirconium-doped mesoporous nano-crystalline TiO_2.* Nanoscale, 2010. 2(7). p. 1222-1228.

244. Ba-Abbad, M.M., Kadhum, A.A.H., Mohamad, A.B., Takriff, M.S. and Sopian, K., *Synthesis and Catalytic Activity of TiO_2 Nanoparticles for Photochemical Oxidation of Concentrated Chlorophenols under Direct Solar Radiation.* International Journal of Electrochemical Science, 2012. 7(6). p. 4871-4888.

245. Mali, S.S., Betty, C.A., Bhosale, P.N. and Patil, P.S., *Synthesis, Characterization of Hydrothermally Grown MWCNT-TiO_2 Photoelectrodes and Their Visible Light Absorption Properties.* Ecs Journal of Solid State Science and Technology, 2012. 1(2). p. M15-M23.

246. Music, S., Gotic, M., Ivanda, M., Popovic, S., Turkovic, A., Trojko, R., Sekulic, A. and Furic, K., *Chemical and microstructural properties of TiO_2 synthesized by sol-gel procedure.* Materials Science and Engineering B-Solid State Materials for Advanced Technology, 1997. 47(1). p. 33-40.

247. Perry, C.H., McCarthy, D.J. and Rupprech. G., *Dielectric dispersion of some perovskite zirconates.* Physical Review, 1965. 138(5A). p. A 1537- A 1538.

248. Chen, L., Shen, Y., Xie, A., Zhu, J., Wu, Z. and Yang, L., *Nanosized barium carbonate particles stabilized by cetyltrimethylammonium bromide at the water/hexamethylene interface.* Crystal Research and Technology, 2007. 42(9). p. 886-889.

249. Lin, H.-L., Chiang, R.-K., Kuo, C.-L. and Chang, C.-W., *Synthesis of $BaCeO_3$ powders by a fast aqueous citrate-nitrate process.* Journal of Non-Crystalline Solids, 2007. 353(11-12). p. 1188-1194.

250. Pourbaix, M., *Atlas of electrochemical equilibria in aqueous solutions*. 2nd ed., 1974, National Association of Corrosion Engineers, Houston.

251. Butler, M.A. and Ginley, D.S., *Prediction of flatband potentials at semiconductor-electrolyte interfaces from atomic electronegativities.* Journal of the Electrochemical Society, 1978. 125(2). p. 228-232.

252. Kwon, C.W., Poquet, A., Mornet, S., Campet, G., Delville, M.H., Treguer, M. and Portier, J., *Electronegativity and chemical hardness: two helpful concepts for understanding oxide nanochemistry.* Materials Letters, 2001. 51(5). p. 402-413.

253. Kosmulski, M., *Surface Charging and Points of Zero Charge.* Surfactant Science, No. 145, 2009, CRC Press, Boca Raton.

254. Kosmulski, M., *The pH dependent surface charging and points of zero charge. VI. Update.* Journal of Colloid and Interface Science, 2014. 426. p. 209-212.

255. Kosmulski, M., *The pH-dependent surface charging and points of zero charge V. Update.* Journal of Colloid and Interface Science, 2011. 353(1). p. 1-15.

256. Berg, J.M., Romoser, A., Banerjee, N., Zebda, R. and Sayes, C.M., *The relationship between pH and zeta potential of similar to 30 nm metal oxide nanoparticle suspensions relevant to in vitro toxicological evaluations.* Nanotoxicology, 2009. 3(4). p. 276-283.

257. Kosmulski, M., *The pH-dependent surface charging and the points of zero charge.* Journal of Colloid and Interface Science, 2002. 253(1). p. 77-87.

258. Kosmulski, M., *pH-dependent surface charging and points of zero charge III. Update.* Journal of Colloid and Interface Science, 2006. 298(2). p. 730-741.

259. Fukuzaki, S., Urano H., and Nagata K., *Adsorption of bovine serum albumin onto metal oxide surfaces.* Journal of Fermentation and Bioengineering, 1996. 81(2): p. 163-167.

260. Kosmulski, M., *pH-dependent surface charging and points of zero charge. IV. Update and new approach.* Journal of Colloid and Interface Science, 2009. 337(2). p. 439-448.

261. Kosmulski, M., *pH-dependent surface charging and points of zero charge. II. Update.* Journal of Colloid and Interface Science, 2004. 275(1). p. 214-224.

262. Moghadas, S., Maghsoudipour, A., Alizadeh, M. and Ebadzadeh, T., *Investigation on rheological behavior of 8 mol% yttria stabilized zirconia (8YSZ) powder using Tiron.* Ceramics International, 2011. 37(6). p. 2015-2019.

263. Wang, Y.H., Liu, X.Q. and Meng, G.Y., *Dispersion and stability of 8 mol.% yttria stabilized zirconia suspensions for dip-coating filtration membranes.* Ceramics International, 2007. 33(6). p. 1025-1031.

264. Lee, Y.H., Kuo, C.W., Shih, C.J., Hung, I.M., Fung, K.Z., Wen, S.B. and Wang, M.C., *Characterization on the electrophoretic deposition of the 8 mol% yttria-stabilized zirconia nanocrystallites prepared by a sol-gel process.* Materials Science and Engineering a-Structural Materials Properties Microstructure and Processing, 2007. 445. p. 347-354.

265. Bueno, S., Moreno, R. and Baudin, C., *Reaction sintered Al_2O_3/Al_2TiO_5 microcrack-free composites obtained by colloidal filtration.* Journal of the European Ceramic Society, 2004. 24(9). p. 2785-2791.

266. Boschini, F., Rulmont, A., Cloots, R. and Moreno, R., *Colloidal stability of aqueous suspensions of barium zirconate.* Journal of the European Ceramic Society, 2005. 25(13). p. 3195-3201.

267. Kirby, G., Armstrong, T.R. and Armstrong, B.L., *Economic Fabrication of Membrane Materials.* 2008, Oak Ridge National Laboratory, Oak Ridge.

268. Grinshtein, V. Y., Strazdin, A.A. and Grinvalde, A. K., *Infrared absorption spectra of some c-halogenated 1, 2, 4-triazole derivatives.* Khimiya Geterotsiklicheskikh Soedinenii, 1970. 6. p. 248-258.

269. Zawadzki, M., *Preparation and characterization of ceria nanoparticles by microwave-assisted solvothermal process.* Journal of Alloys and Compounds, 2008. 454(1-2). p. 347-351.

270. Silverstein, R.M., Webster, F.X. and Kiemle, D.J., *Spectrometric identification of organic compounds*. 7th ed, 2005, Jonh Wiley & Sons, New York.

271. Chaim, R., Levin, M. Shlayer, A. and Estournes, C., *Sintering and densification of nanocrystalline ceramic oxide powders: a review 2.* Advances in Applied Ceramics, 2008. 107(3): p. 159-169.

272. Katritzky, A.R., Wang, Z., Tsikolia, M., Hall, C.D. and Carman, M., *Benzotriazole is thermally more stable than 1,2,3-triazole.* Tetrahedron Letters, 2006. 47(43). p. 7653-7654.

273. Ferreira, A.S.V., Saradha, T., Figueiredo, F.L. and Marques, F.M.B., *Compositional and microstructural effects in composite electrolytes for fuel cells.* International Journal of Energy Research, 2011. 35(12): p. 1090-1099.

274. Buyukaksoy, A., Fuerstenhaupt, T. and Birss, V.I., *First-time electrical characterization of nanotubular ZrO_2 films for micro-solid oxide fuel cell applications.* Nanoscale, 2015. 7(18): p. 8428-8437.

275. Demetry, C. and Shi, X.L., *Grain size-dependent electrical properties of rutile (TiO_2).* Solid State Ionics, 1999. 118(3-4): p. 271-279.

276. Fu, Y.-P. and Weng, C.-S., *Effect of rare-earth ions doped in $BaCeO_3$ on chemical stability, mechanical properties, and conductivity properties.* Ceramics International, 2014. 40(7): p. 10793-10802.

277. Gu, Y.-J., Liu, Z.-G., Ouyang, J.-H., Zhou, Y and Yan, F.-Y., *Synthesis, structure and electrical conductivity of $BaZr_{1-x}Dy_xO_{3-delta}$ ceramics.* Electrochimica Acta, 2012. 75: p. 332-338.

278. Laachir, A., Perrichon, V., Badri, A., Lamotte, J., Catherine, E., Lavalley, J. C., Elfallah, J., Hilaire, L., Lenormand, F., Quemere, E., Sauvion, G. N. and Touret, O., *Reduction of CeO_2 by hydrogen - magnetic-susceptibility and fourier-transform infrared, ultraviolet and X-ray photoelectron-spectroscopy measurements*. Journal of the Chemical Society-Faraday Transactions, 1991. 87(10): p. 1601-1609.

279. Kim, S., Merkle, R., and Maier, J., *Water uptake of nanocrystalline ceria: weight and conductance effects.* Solid State Ionics, 2003. 161(1-2): p. 113-119.

280. Kim, S., Anselmi-Tambtirini, U., Park, H. J., Martin, M. and Munir, Z. A,. *Unprecedented room-temperature electrical power generation using nanoscale fluorite-structured oxide electrolytes.* Advanced Materials, 2008. 20(3): p. 556-559.

281. Takamura, H. and Takahashi, N., *Electrical conductivity of dense nanocrystalline ceria under humidified atmosphere.* Solid State Ionics, 2010. 181(3-4): p. 100-103.

282. Rondão, A.I.B., Patrício, S. G., Figueiredo, F. M. L. and Marques, F. M. B., *Role of gas-phase composition on the performance of ceria-based composite electrolytes.* International Journal of Hydrogen Energy, 2013. 38(14): p. 5497-5506.

Appendix I
Characterization of commercial oxides

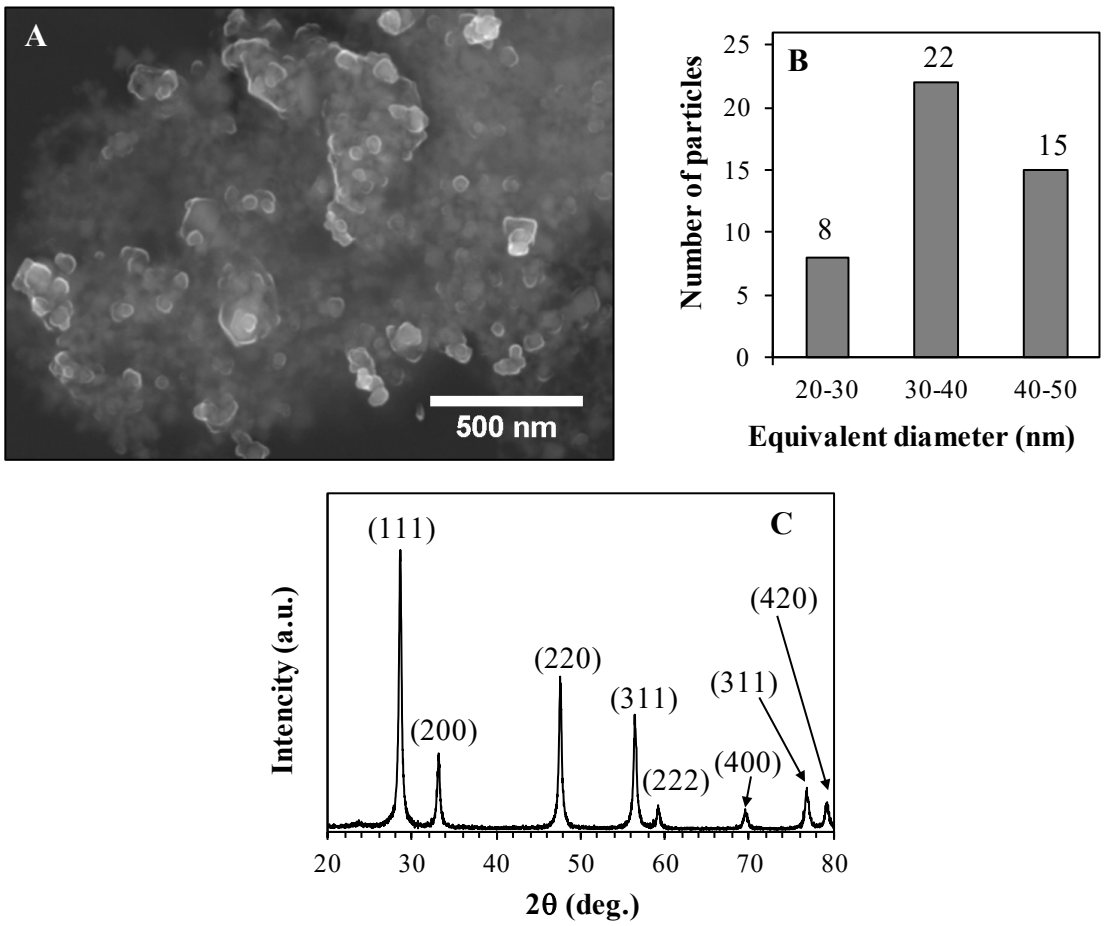

Figure I.1 Characterization of np-CO: A) SEM micrograph (adapted from [282]); B) histogram of the equivalent diameter distribution; and C) XRD pattern. The peaks are indexed according to the $Fm\bar{3}m$ cubic space group.

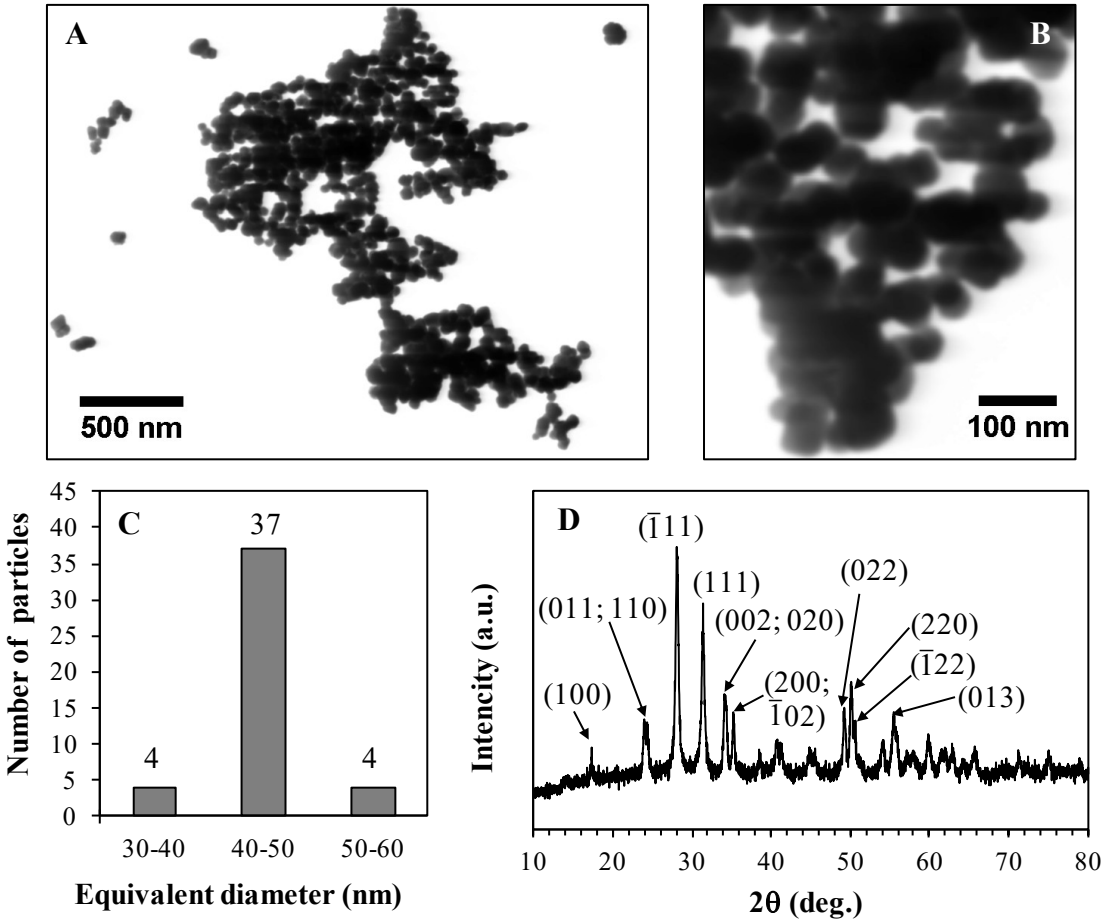

Figure I.2 Characterization of np-*m*ZO: A) and B) STSEM micrographs; C) histogram of the equivalent diameter distribution (considering Fig. I.2 A); and D) XRD pattern. The peaks are indexed according to the $P2_1/c$ monoclinic space group.

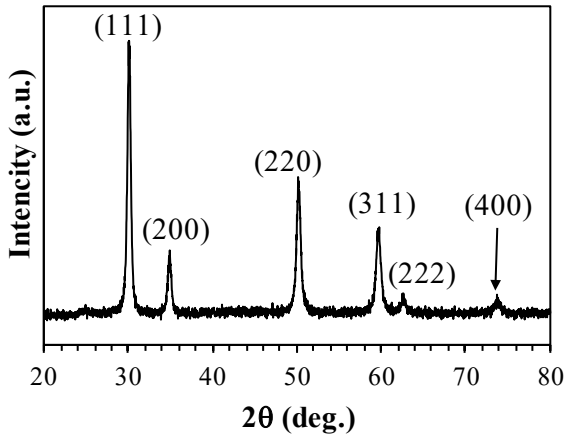

Figure I.3 XRD pattern of commercial np-8YSZ. The peaks are indexed according to the $Fm\bar{3}m$ cubic space group.

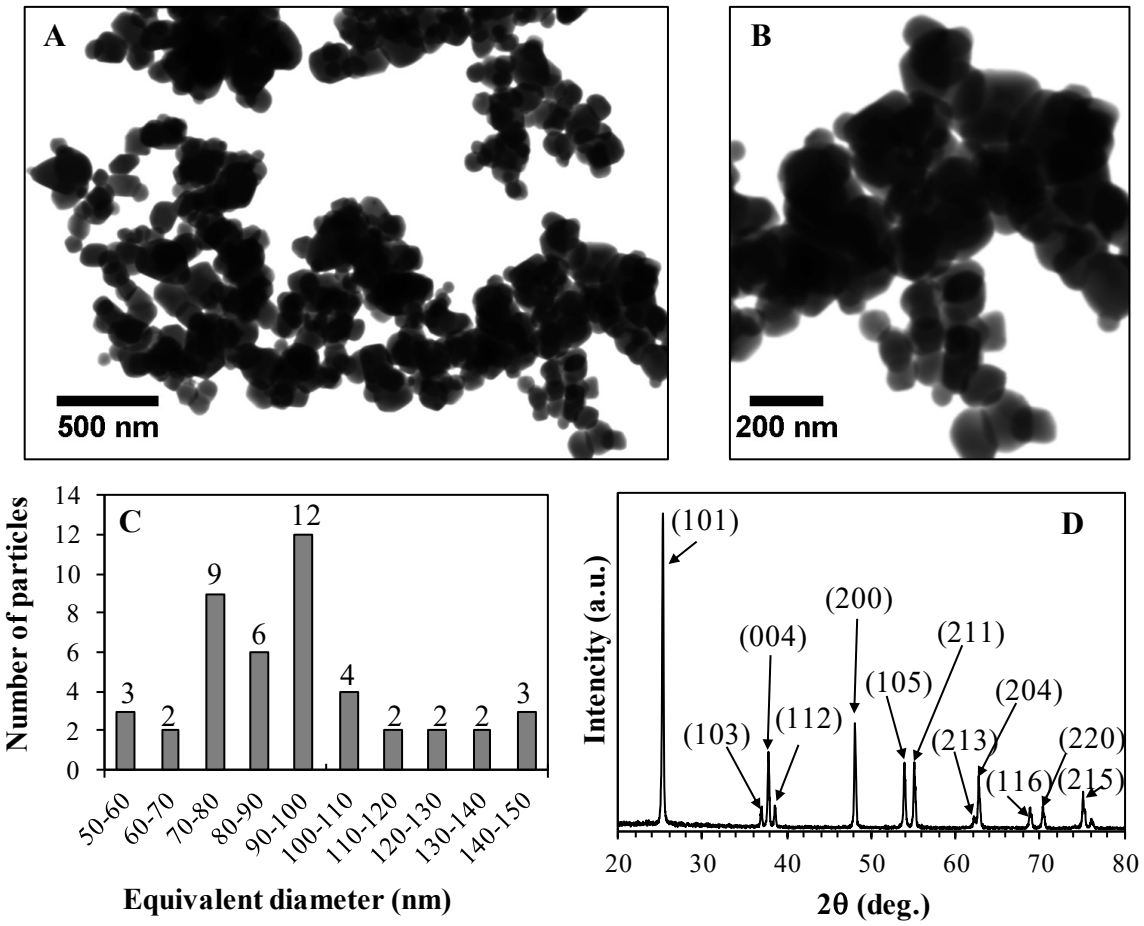

Figure I.4 Characterization of np-*a*TO: A) and B) STEM micrographs; C) histogram of the equivalent diameter distribution (considering Fig. I.3 A); and D) XRD pattern. The peaks are indexed according to the anatase $I4_1/amd$ tetragonal space group.

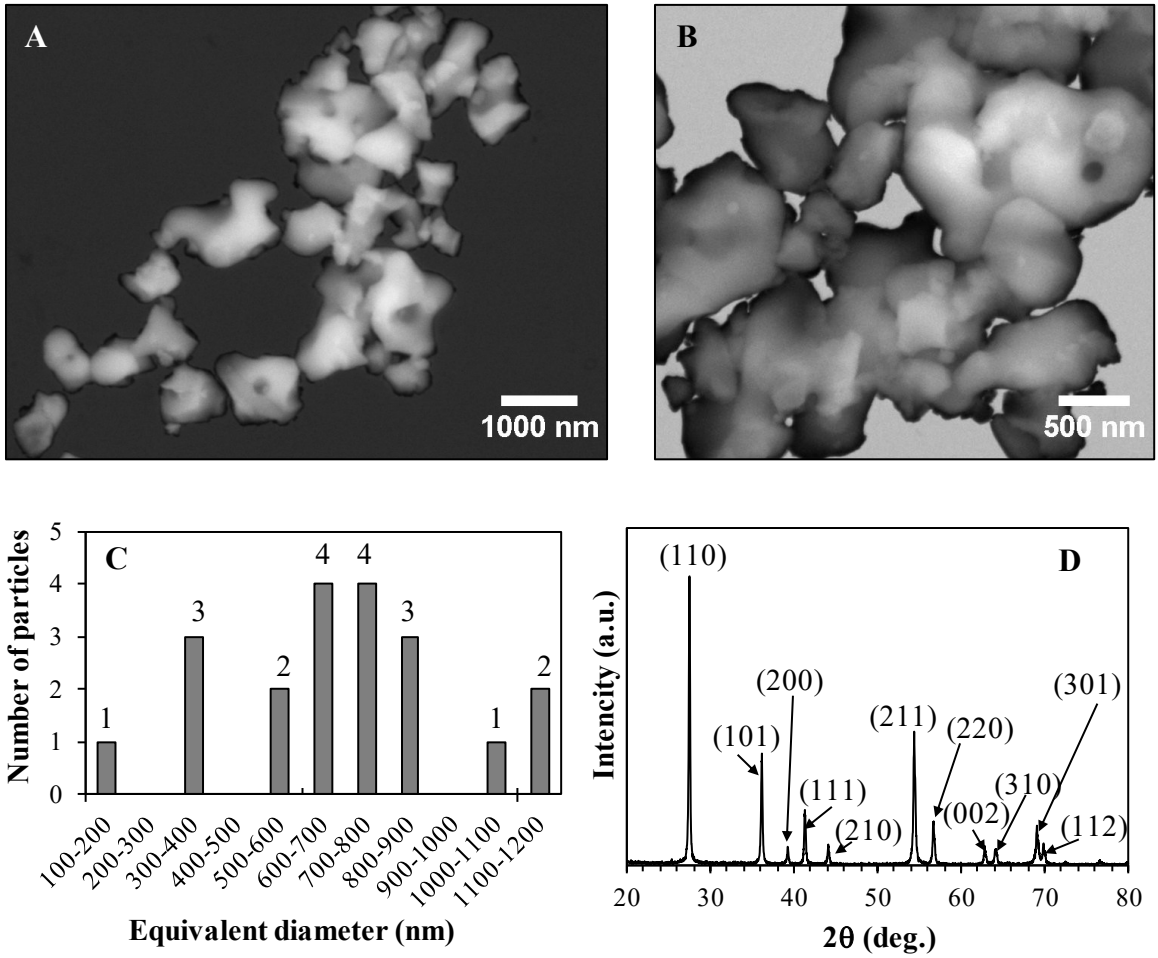

Figure I.5 Characterization mp-*r*TO; A) and B) STSEM micrographs; C) histogram of the equivalent diameter distribution (considering Fig. I.5 A); and D) XRD pattern. The peaks are indexed according to the rutile $P4_2/mnm$ tetragonal space group.

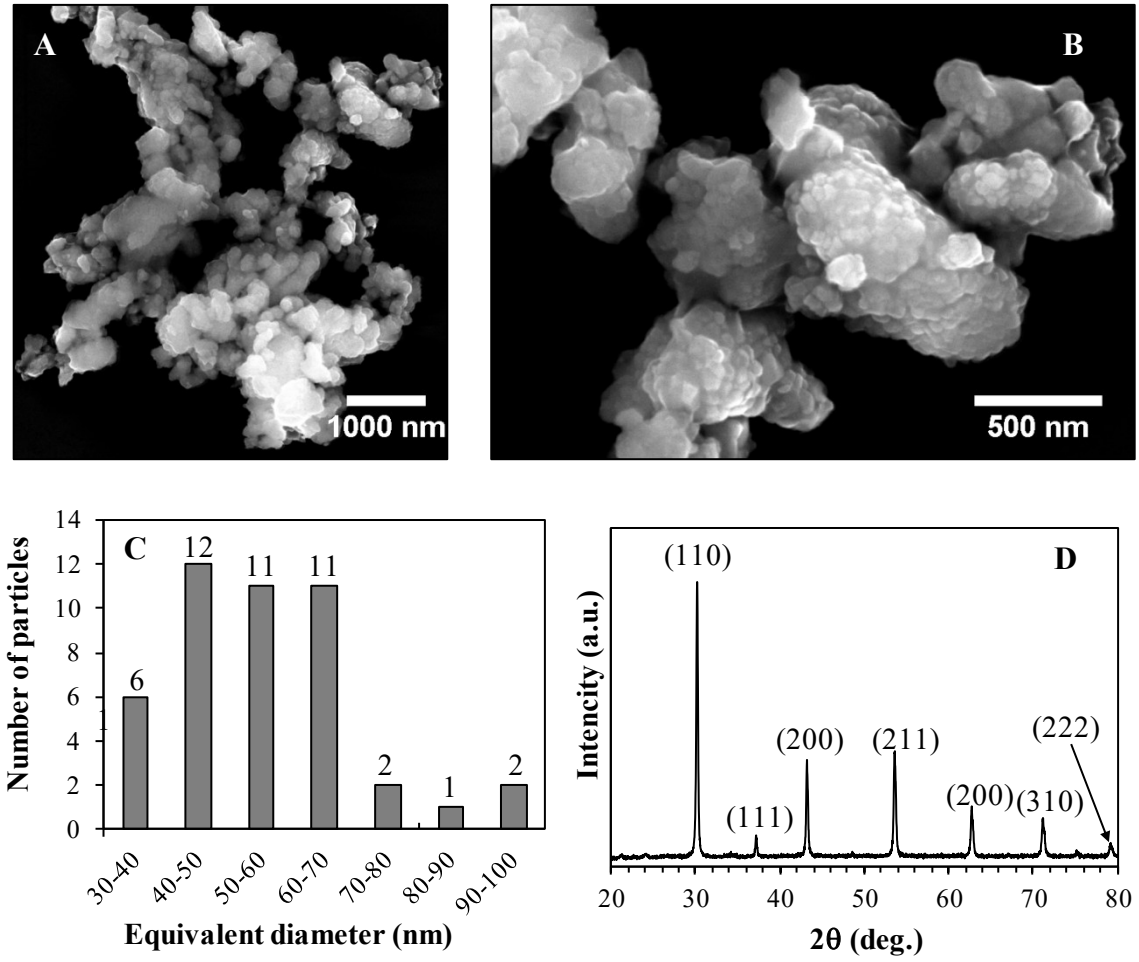

Figure I.6 Characterization mp-BZO: A) and B) STSEM micrographs; C) histogram of the equivalent diameter distribution (considering Fig. I.6 B); and D) XRD pattern. The peaks are indexed according to the $Pm\bar{3}m$ cubic space group.

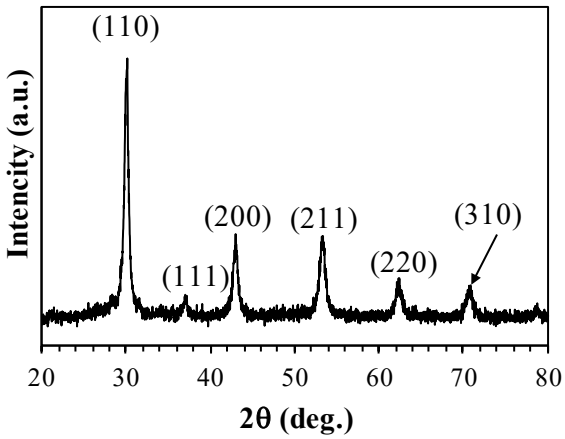

Figure I.7 XRD pattern of np-BZYO prepared by mechanosynthesis [206]. The peaks are indexed according to the $Pm\bar{3}m$ cubic space group.

Appendix II
Influence of oxide composition on the total conductivity of composites

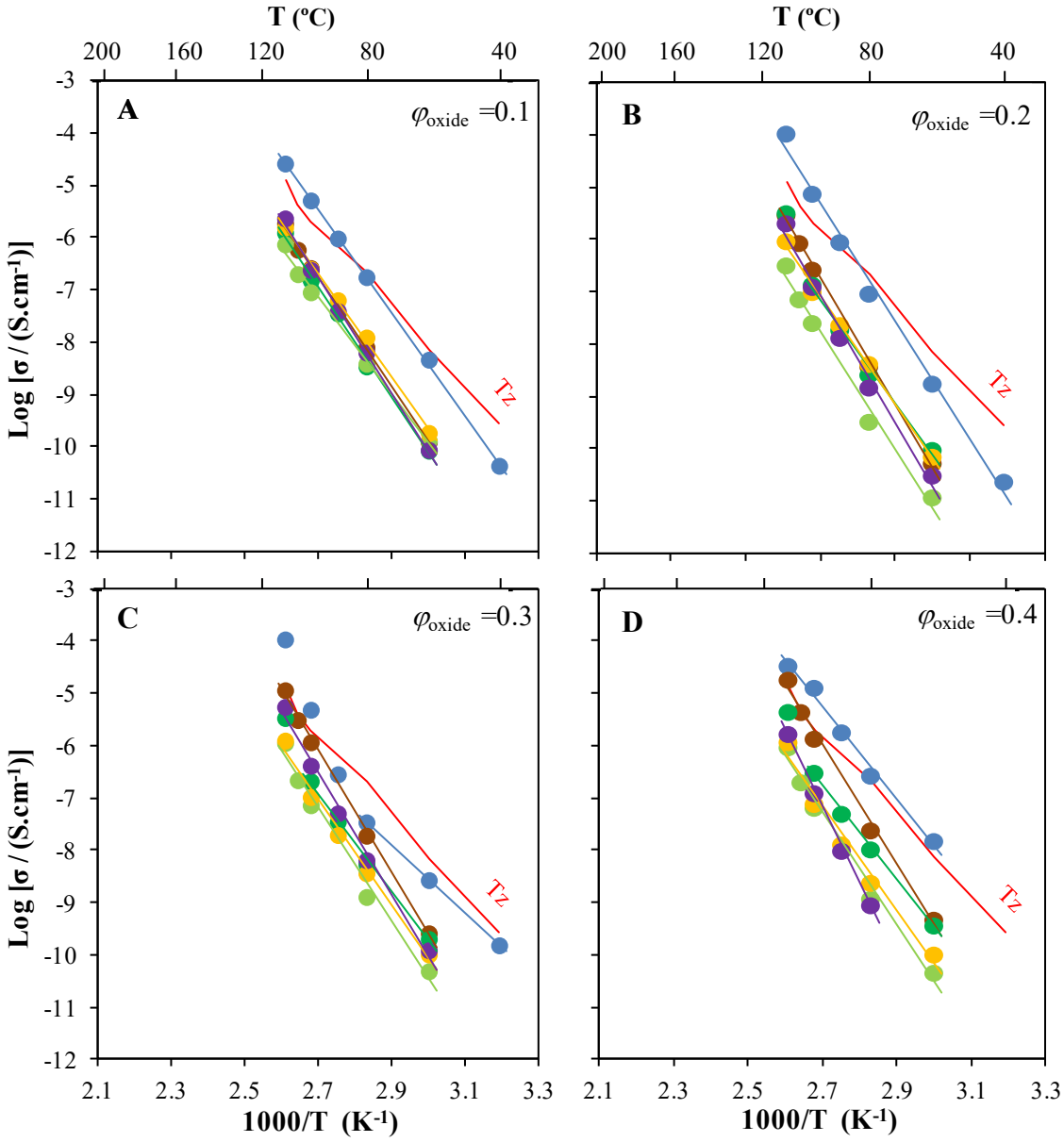

Figure II.1 Arrhenius plot for total conductivity of Tz-based composites with oxides ●-np-CO, ●-np-*m*ZO, ●-np-*a*TO, ●-mp-*r*TO, ●-np-BCO, ●-mp-BZO. The red lines are data for pure Tz.

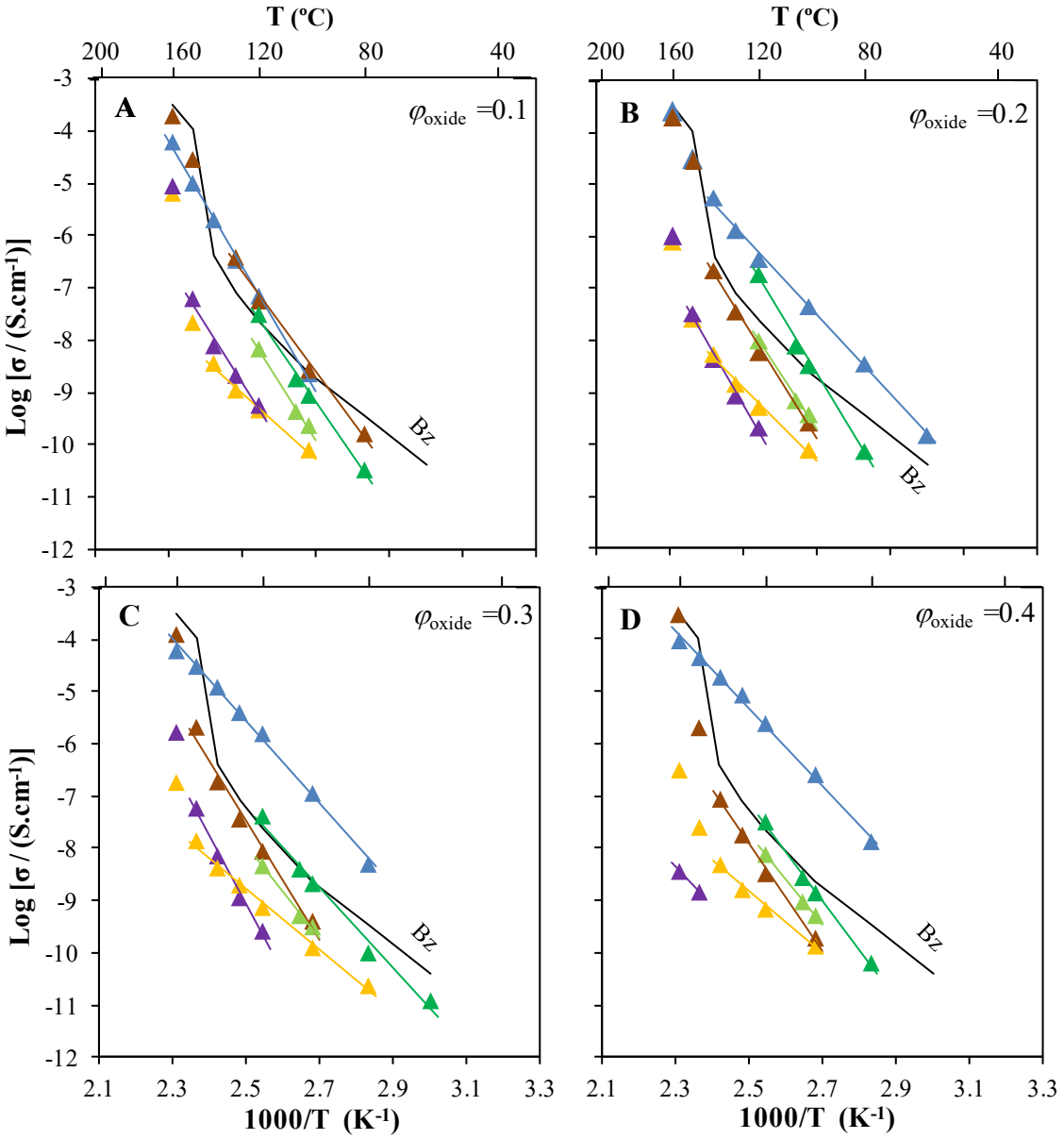

Figure II.2 Arrhenius plot for total conductivity of Bz-based composites with oxides ▲-np-CO, ▲-np-*m*ZO, ▲-np-*a*TO, ▲-mp-*r*TO, ▲-np-BCO, ▲-mp-BZO. The black lines are data for pure Bz.

Table II.1 Total conductivity and activation energy for composites based in CeO_2.

Oxide	φ_{oxide}=0.1				φ_{oxide}=0.2				φ_{oxide}=0.3				φ_{oxide}=0.4			
	σ_{total} at 100 ºC ($S\cdot cm^{-1}$)		E_a ($kJ\cdot mol^{-1}$)		σ_{total} 100 ºC ($S\cdot cm^{-1}$)		E_a ($kJ\cdot mol^{-1}$)		σ_{total} 100 ºC ($S\cdot cm^{-1}$)		E_a ($kJ\cdot mol^{-1}$)		σ_{total} 100 ºC ($S\cdot cm^{-1}$)		E_a ($kJ\cdot mol^{-1}$)	
	Tz	Bz	Tz	Bz	Tz	Bz	Tz	Bz	Tz	Bz	Tz	Bz	Tz	Bz	Tz	Bz
ms-CO(SBA)	2.9×10^{-6}	7.6×10^{-8}	89[a)] 146[b)] 131[c)]	134[c)]	6.6×10^{-6}	7.5×10^{-7}	84[a)] 119[b)] 119[c)]	102[a)] 145[b)] 107[c)]	1.7×10^{-5}	1.5×10^{-7}	76[a)] 120[b)] 119[c)]	115[a)] 141[b)] 103[c)]	5.0×10^{-6}	2.0×10^{-7}	66[a)] 120[b)] 120[c)]	100[a)] 153[a)] 108[c)]
np-CO[d)]	5.0×10^{-6}	2.3×10^{-9}	112[a)] 201[b)] 191[c)]	231[c)]	7.2×10^{-6}	4.5×10^{-8}	124[a)] 238[b)] 217[c)]	149 [c)]	4.9×10^{-6}	1.2×10^{-7}	128[a)] 127[b)] 127[c)]	84[a)] 183[b)] 154[c)]	1.3×10^{-5}	2.6×10^{-7}	127[a)] 177[b)] 173[c)]	78[a)] 163[b)] 144[c)]

[a)] $E_{a,\ HF}$; [b)] $E_{a,\ IF}$; [c)] $E_{a,\ total}$; [d)] $E_{a,\ total}$ of the pure equal to np-CO 130 $kJ\cdot mol^{-1}$.

Table II.2 Total conductivity and activation energy for composites based in ZrO_2.

Oxide	φ_{oxide}=0.1				φ_{oxide}=0.2				φ_{oxide}=0.3				φ_{oxide}=0.4			
	σ_{total} at 100 ºC ($S\cdot cm^{-1}$)		E_a ($kJ\cdot mol^{-1}$)		σ_{total} at 100 ºC ($S\cdot cm^{-1}$)		E_a ($kJ\cdot mol^{-1}$)		σ_{total} at 100 ºC ($S\cdot cm^{-1}$)		E_a ($kJ\cdot mol^{-1}$)		σ_{total} at 100 ºC ($S\cdot cm^{-1}$)		E_a ($kJ\cdot mol^{-1}$)	
	Tz	Bz	Tz	Bz	Tz	Bz	Tz	Bz	Tz	Bz	Tz	Bz	Tz	Bz	Tz	Bz
ms-*m*,*t*ZO(SBA)	7.2×10^{-6}	2.6×10^{-7}	71[a)] 179[b)] 152[c)]	72[a)] 160[b)] 123[c)]	2.0×10^{-5}	2.6×10^{-7}	88[a)] 223[b)] 200[c)]	79[a)] 170[b)] 138[c)]	6.7×10^{-5}	3.1×10^{-7}	80[a)] 246[b)] 221[c)]	83[a)] 177[b)] 116 [c)]	5.3×10^{-5}	4.0×10^{-7}	75[a)] 236[b)] 243[c)]	86[a)] 168[b)] 114[c)]
np-*m*ZO	2.5×10^{-7}	2.7×10^{-9}	203[c)]	185[c)]	2.6×10^{-7}	2.6×10^{-10}	233[c)]	218[c)]	1.2×10^{-6}	4.1×10^{-10}	227[c)]	220[c)]	1.4×10^{-6}	2.0×10^{-10}	223[c)]	199[c)]

[a)] $E_{a,\ HF}$; [b)] $E_{a,\ IF;}$ [c)] $E_{a,total.}$

Table II.3 Total conductivity and activation energy for composites based in TiO_2.

Oxide	φ_{oxide}=0.1				φ_{oxide}=0.2				φ_{oxide}=0.3				φ_{oxide}=0.4			
	σ_{total} at 100 ºC ($S \cdot cm^{-1}$)		E_a ($kJ \cdot mol^{-1}$)		σ_{total} at 100 ºC ($S \cdot cm^{-1}$)		E_a ($kJ \cdot mol^{-1}$)		σ_{total} at 100 ºC ($S \cdot cm^{-1}$)		E_a ($kJ \cdot mol^{-1}$)		σ_{total} at 100 ºC ($S \cdot cm^{-1}$)		E_a ($kJ \cdot mol^{-1}$)	
	Tz	Bz	Tz	Bz	Tz	Bz	Tz	Bz	Tz	Bz	Tz	Bz	Tz	Bz	Tz	Bz
ms-*a*TO(SBA)	5.1×10^{-6}	7.8×10^{-9}	119[a] 223[b] 191[c]	173[c]	1.6×10^{-5}	1.3×10^{-8}	128[a] 258[b] 227[c]	136[c]	3.1×10^{-5}	2.4×10^{-8}	118[a] 217[b] 188[c]	149[c]	5.8×10^{-5}	3.0×10^{-8}	116[a] 256[b] 243[c]	132[c]
np-*a*TO	1.5×10^{-7}	8.8×10^{-10}	206[c]	198[c]	1.3×10^{-7}	3.3×10^{-9}	189[c]	227[c]	2.1×10^{-7}	2.2×10^{-9}	181[c]	151[c]	3.0×10^{-7}	1.4×10^{-9}	175[c]	181[c]
np-*r*TO	8.7×10^{-8}	2.3×10^{-10}	181[c]	213[c]	2.4×10^{-8}	3.7×10^{-10}	217[c]	207[c]	7.3×10^{-8}	3.2×10^{-10}	211[c]	171[c]	6.5×10^{-8}	5.3×10^{-10}	209[c]	169[c]

[a] $E_{a,\ HF}$; [b] $E_{a,\ IF}$; [c] $E_{a,\ total}$.

Table II.4 Total conductivity and activation energy for composites based in $BaZrO_3$ and $BaCeO_3$.

Oxide	φ_{oxide}=0.1				φ_{oxide}=0.2				φ_{oxide}=0.3				φ_{oxide}=0.4			
	σ_{total} at 100 ºC ($S \cdot cm^{-1}$)		E_a ($kJ \cdot mol^{-1}$)		σ_{total} at 100 ºC ($S \cdot cm^{-1}$)		E_a ($kJ \cdot mol^{-1}$)		σ_{total} at 100 ºC ($S \cdot cm^{-1}$)		E_a ($kJ \cdot mol^{-1}$)		σ_{total} at 100 ºC ($S \cdot cm^{-1}$)		E_a ($kJ \cdot mol^{-1}$)	
	Tz	Bz	Tz	Bz	Tz	Bz	Tz	Bz	Tz	Bz	Tz	Bz	Tz	Bz	Tz	Bz
np-BCO	2.4×10^{-7}	7.9×10^{-11}	192[c]	123[c]	9.5×10^{-8}	7.7×10^{-11}	199[c]	136[c]	1.0×10^{-7}	1.3×10^{-10}	159[a] 239[b] 197[c]	115	7.7×10^{-8}	1.4×10^{-10}	153[a] 224[b] 173[c]	150[a] 165[b] 116[c]
mp-BZO	2.3×10^{-7}	----	216[c]	216[c]	1.2×10^{-7}	----	235[c]	235[c]	4.2×10^{-7}	----	227[c]	253[c]	1.2×10^{-7}	----	286[c]	----

[a] $E_{a,\ HF}$; [b] $E_{a,\ IF}$; [c] $E_{a,\ total}$.

Nomenclature

Nanocasted mesoporous oxides:

- **CeO_2**

ms-CO/SBA ⇔ CeO_2 with SBA-15
ms-CO(SBA) ⇔ CeO_2 without SBA-15

- **ZrO_2**

ms-*t*ZO/SBA ⇔ tetragonal ZrO_2 with SBA-15
ms-*m*,*t*ZO(SBA) ⇔ monoclinic and tetragonal ZrO_2 without SBA-15
ms-*t*ZO/CMK ⇔ tetragonal ZrO_2 with CMK-3
ms-*t*ZO(CMK) ⇔ tetragonal ZrO_2 without CMK-3

- **TiO_2**

ms-*a*TO/SBA ⇔ anatase TiO_2 with SBA-15
ms-*a*TO(SBA) ⇔ anatase TiO_2 without SBA-15
ms-*a*TO/CMK ⇔ anatase TiO_2 with CMK-3
ms-*a*TO(CMK) ⇔ anatase TiO_2 without CMK-3

- **$BaZrO_3$**

ms-BZO-Cl/SBA ⇔ material with SBA-15 when the chlorines were used in the synthesis
ms-BZO-NO_3/SBA ⇔ material with SBA-15 when the nitrates were used in the synthesis
ms-BZO-NO_3/CMK ⇔ material with CMK-3 when the nitrates were used in the synthesis
ms-BZO/CMK ⇔ $BaZrO_3$ with CMK-3
ms-BZO(CMK) ⇔ $BaZrO_3$ without CMK-3
ms-BZYO(CMK) ⇔ attempt to synthesized $BaZr_{0.8}Y_{0.2}O_{2.9}$ without CMK-3

Nomenclature

Commercial oxides:

- **CeO_2**

np-CO ⇔ nanocrystalline particles of CeO_2

- **ZrO_2**

np-*m*ZO ⇔ nanocrystalline particles of monoclinic ZrO_2
np-8YSZ ⇔ nanocrystalline particles 8 mol% Y_2O_3 stabilized ZrO_2

- **TiO_2**

np-*a*TO ⇔ nanocrystalline particles of anatase TiO_2
mp-*r*TO ⇔ microcrystalline particles of rutile TiO_2

- **$BaZrO_3$**

mp-BZO ⇔ microcrystalline particles of $BaZrO_3$

Other oxides:

np-BCO ⇔ $BaCeO_3$ prepared in this Thesis
np-BZYO ⇔ $BaZr_{0.8}Y_{0.2}O_{2.9}$ prepared by mechanosynthesis